

SHEAR DYNAMO, TURBULENCE, AND THE
MAGNETOROTATIONAL INSTABILITY

JONATHAN SQUIRE

A DISSERTATION
PRESENTED TO THE FACULTY
OF PRINCETON UNIVERSITY
IN CANDIDACY FOR THE DEGREE
OF DOCTOR OF PHILOSOPHY

RECOMMENDED FOR ACCEPTANCE
BY THE DEPARTMENT OF
ASTROPHYSICAL SCIENCES
PROGRAM IN PLASMA PHYSICS
ADVISER: A. BHATTACHARJEE

SEPTEMBER 2015

© Copyright by Jonathan Squire, 2015.

All rights reserved.

Abstract

The formation, evolution, and detailed structure of accretion disks remain poorly understood, with wide implications across a variety of astrophysical disciplines. While the most pressing question – what causes the high angular momentum fluxes that are necessary to explain observations? – is nicely answered by the idea that the disk is *turbulent*, a more complete grasp of the fundamental processes is necessary to capture the wide variety of behaviors observed in the night sky. This thesis studies the turbulence in ionized accretion disks from a theoretical standpoint, in particular focusing on the generation of magnetic fields in these processes, known as *dynamo*. Such fields are expected to be enormously important, both by enabling the magnetorotational instability (which evolves into virulent turbulence), and through large-scale structure formation, which may transport angular momentum in different ways and be fundamental for the formation of jets.

The central result of this thesis is the suggestion of a new large-scale dynamo mechanism in shear flows – the “magnetic shear-current effect” – which relies on a positive feedback from *small-scale magnetic fields*. As well as being a very promising candidate for driving field generation in the central regions of accretion disks, this effect is interesting because small-scale magnetic fields have historically been considered to have a negative effect on the large-scale dynamo, damping growth and leading to dire predictions for final saturation amplitudes. Given that small-scale fields are ubiquitous in plasma turbulence above moderate Reynolds numbers, the finding that they could instead have a *positive* effect in some situations is interesting from a theoretical and practical standpoint. The effect is studied using direct numerical simulation, analytic techniques, and novel statistical simulation methods.

In addition to the dynamo, much attention is given to the linear physics of disks and its relevance to turbulence. This is studied using *nonmodal* stability theory, which both provides a highly intuitive connection between global domains and the commonly studied shearing box, and suggests that transient linear growth can often be more important than spectral instability. These realizations

motivate the use of the quasi-linear models that are applied extensively throughout the turbulence and dynamo studies later in the thesis.

Acknowledgements

It has been a constant pleasure to work with my advisor and mentor, Amitava Bhattacharjee. I have very much enjoyed our discussions over the past couple of years, coming away with suggestions for fresh ways to look at problems, interesting new avenues to explore, or just a newfound excitement for our research questions. I am also indebted to Amitava for allowing me the freedom to explore what I found intriguing and exciting, both academically and geographically. My studies at Princeton have not been consistently focused on accretion disks, and I must acknowledge my former thesis advisors Hong Qin and Bill Tang. I cannot thank them enough for their understanding when I felt that our project was not going to work out, as well as for the myriad of interesting conversations that led me to appreciate some of the beauty in the geometry and mathematics of plasma physics.

I must also thank a variety of other staff at PPPL and Princeton, who each have helped make the lab such a stimulating environment in which to undertake a PhD. John Krommes has been very supportive, making time for numerous discussions that have been hugely helpful, as well as giving a very useful set of comments on this thesis. I would also like to thank Jeremy Goodman, Hantao Ji, Greg Hammett, and Jim Stone both for their help with this thesis and for a wide variety of interesting and informative conversations over the years. Nat Fisch and all of the other teaching faculty, for creating such an engaging graduate program at PPPL. Barbara – and later Beth – have always been wonderfully supportive and so friendly, with a magical ability to solve problems.

Josh and Seth, you guys have not only been fantastic housemates and friends, but were always up for a thought-provoking powwow about physics. I'll sorely miss our conversations about each other's work, current problems, or just random interesting things in physics and maths. So many other PPPL students (and postdocs) have also made the whole experience that much more enjoyable: Lee, Yao, Renaud, Jake, and all the other "theory-nubbers" have all been wonderful people to have around. For the gift of sanity through escape, I have to thank the climbing community at

Princeton. Alex, for the crazy escapades and constant reminders that too much seriousness is a sin. Dan, Ben, Kedron, and Munan for always being up for an adventure, and just being really good people. Finally, Keith and Veronica have always been so welcoming and such lovely hosts.

None of this would have been possible without the unwavering support and devotion of my parents, Vernon and Pat, and brother, Dougie. And of course, Julia, to whom I dedicate this thesis – life is so much better when shared with you.

This work was partially supported by a Charlotte Elizabeth Procter Fellowship from Princeton University, and by the US Department of Energy Grant DE-AC02-09-CH11466.

Contents

Abstract	iii
Acknowledgements	v
1 Introduction	1
1.1 Accretion disks	3
1.2 Dynamo	19
1.3 Overview of the work presented in this thesis	25
2 Nonmodal stability of the MRI	35
2.1 Introduction	35
2.2 Nonmodal stability methods	42
2.3 Equations and physical models	46
2.4 General properties	52
2.5 The dynamical importance of shearing waves	61
2.6 The relationship between the shearing wave equations and global structures	68
2.7 Nonmodal growth of the shearing wave equations	71
2.8 Summary and discussion	76
3 The MRI dynamo	81
3.1 The CE2 method and numerical implementation	83

3.2	The MRI dynamo instability	98
3.3	The saturation mechanism of the dynamo instability	103
3.4	Discussion	110
4	Nonhelical shear dynamos	113
4.1	Introduction to the magnetic shear-current effect	113
4.2	Shear dynamos	119
4.3	Equations and numerical method	123
4.4	Kinematic dynamo	129
4.5	Magnetically driven dynamo	139
4.6	Discussion and conclusions	147
5	The magnetic shear-current effect	150
5.1	Measuring the transport coefficients	153
5.2	Results – the magnetically driven dynamo	160
6	Analytic transport coefficients	168
6.1	Fundamentals of mean-field electrodynamics	171
6.2	Outline of the calculation of \mathcal{E}	179
6.3	Specific results for unstratified shear dynamos	186
6.4	Specific results for stratified accretion disks	189
6.5	Discussion and conclusions	193
7	Conclusions	196
7.1	Outlook	200
A	Chapter 2	204
A.1	Global linear MHD equations	204

A.2	Conversion between global and shearing box equations	205
A.3	Does the shearing box possess Floquet eigenmodes?	207
B	Chapter 3	211
B.1	Derivation of the equation for $\mathcal{C}(t)$	211
C	Chapter 4	213
C.1	Stochastic- α shear dynamos: some notes on previously proposed mechanisms . . .	213
D	Chapter 6	217
D.1	Equations for $\mathbf{m}^{(0)}$, $\mathbf{m}^{(1)}$, $\mathbf{b}^{(0)}$, $\mathbf{b}^{(1)}$ in Fourier space	217
D.2	List of all transport coefficients	219
D.3	The sign of $(\eta_{yx})_b^S$	225
E	VEST	228
E.1	Introduction	228
E.2	Index notation as a tool for vector calculus	231
E.3	Simplification through Levi-Civita expansions	234
E.4	Additional <i>VEST</i> functionality	240
	Bibliography	243

Chapter 1

Introduction: Disks and dynamos

The paradigm of an *accretion disk* is ubiquitous in modern astrophysics, forming the basis for our understanding of a wide variety of astrophysical systems. The general idea is that matter with even a small amount of rotation cannot directly gravitationally accrete into a central mass, due to conservation of its angular momentum. Thus a disk forms around the mass and much of the accretion is dominated by the dynamics and structure of this object. Since relatively high angular momentum transport is required to explain observed accretion rates, the central question of accretion disk theory arises: how and why does the matter accrete as fast as it does? Certainly the answer is not the molecular viscosity, since Reynolds numbers in disks are usually immense and the corresponding angular momentum transport would be far too low. An obvious panacea is turbulence, which could enhance transport by many orders of magnitude and possibly lead to accretion rates that are somewhat independent of Reynolds number. Of course, such an explanation is hardly complete and poses more questions than it answers: what is the origin of this turbulence, how does it saturate, and what is the transport in the saturated state?

Very broadly, these questions have formed the basis for the majority of the work that makes up this thesis. Because all indications are that hydrodynamic Keplerian motion is stable (Ji *et al.*, 2006; Lesur and Longaretti, 2005), I have focused on turbulence in ionized disks, as described

approximately by magnetohydrodynamics (MHD). Importantly, as realized by Balbus and Hawley (1991), the addition of even a very weak magnetic field in such a system can be dramatically important due to the *magneto-rotational instability* (MRI). This virulent instability can lead directly from quiescent laminar flow to a highly turbulent saturated state with rather high momentum transport (Balbus and Hawley, 1998). Over the past two decades this turbulence has been the subject of intense study, primarily through numerical simulation. While the basic existence of MRI turbulence in numerically realizable regimes is well-established, many controversies remain in the community, particularly relating to the scaling of transport as the Reynolds numbers (kinetic and magnetic) are increased to astrophysically relevant values. Another issue that may be of profound importance concerns the role of large-scale magnetic fields and flows in mediating transport, as well as how and why these might be generated by the MRI turbulence (Blackman, 2012). This is essentially a large-scale *dynamo*, and its study has made up a substantial portion of this thesis.

Our general approach to understanding these problems has been to focus on models that are as simple and parsimonious as possible. With this in mind, most of the work presented here studies homogeneous turbulence without the complicating factors of radial or vertical stratification – the so-called unstratified shearing box. While this model misses many important physical effects, the hope is that its study can point the way to physical interpretation and quantitative analysis techniques in more physically complete numerical setups. The unstratified shearing box has also been a common tool in theoretical studies of mean-field dynamos, and MRI turbulence is very closely related to a variety of works studying nonhelical shear dynamos (e.g., Brandenburg *et al.* 2008a; Yousef *et al.* 2008a). While the numerical setups for such studies have been very similar to those in the MRI turbulence literature, there is a difference in perspective that comes primarily from forcing the flow field. This can allow improved control over aspects of the turbulence (for example, by studying low Reynolds numbers, changing rotation, or forcing at small scales), and can be particularly helpful for studying the dynamo. A variety of the chapters in this thesis study

the dynamo in such a manner, and while the direct application to accretion disks may be lost, this has proved very helpful for isolating the fundamental field generation mechanisms at play.

In this introduction, I start by giving a very basic overview of the fundamental physics of accretion disks and some of the astrophysical objects in which they are observed. This then leads to a discussion of the basics of momentum transport in disks, the MRI, and a brief description of various local approximations for studying MRI turbulence and dynamo. Given that a reasonable portion of this work emphasizes the dynamo, I follow with an outline of formal dynamo theory, focusing particularly on mean-field theory. Finally, I shall give a detailed overview of what I consider to be the most important results presented in this thesis, explaining the work covered in each chapter and how these are related.

1.1 Accretion disks

Accretion disks form around a wide variety of astrophysical objects, from cool, mostly neutral disks around young stars, to enormously energetic active galactic nuclei. Fundamentally, we are able to study such a wide variety of systems using similar theoretical frameworks due to the enormous difficulty of removing angular momentum from the infalling matter. While the energy (e.g., gravitational binding energy, or kinetic energy) can usually be easily radiated away, there is no such mechanism for the release of angular momentum. This forces the formation of disk-like structures, the dynamics of which will govern the accretion process without necessarily being substantially influenced by their detailed origins.

It is useful to have some idea of where disks are observed in the night sky, and here I give a very basic overview of some of the main classes of objects. More information can be found in Alexander 2008 (protoplanetary disks), Remillard and McClintock 2006 (binary systems), and Krolik 1999 (active galactic nuclei).

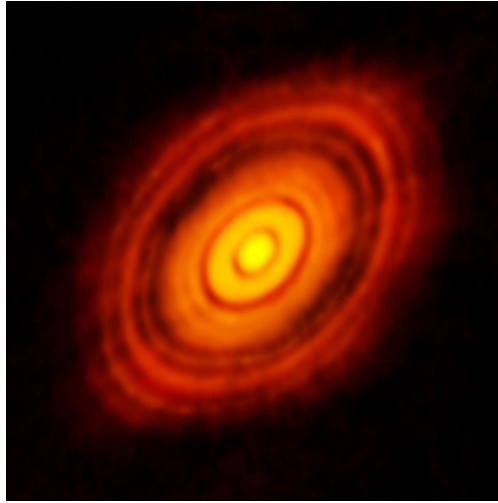


Figure 1.1: Image of the young HL Tauri star, taken at 1.28mm wavelength. The concentric rings are potentially the sites of planet formation (image credit <http://www.eso.org>)

Protoplanetary disks As a gaseous cloud condenses to form a young star, conservation of momentum causes the formation of an accretion disk. This disk will generally be relatively poorly ionized due to its coolish temperatures, and is best seen in the infrared. As the name suggests, protoplanetary disks form the environment in which planets are born and are of fundamental interest in a wide variety of subfields. With the recent completion of the Atacama Large Millimeter/submillimeter Array (ALMA), some stunning images at unprecedented resolutions have been produced, most notably of HL Tauri (ALMA Partnership *et al.* 2015, see Fig. 1.1). The very low ionization fraction in protoplanetary disks makes explaining observed angular momentum transport rates rather troublesome, and there exist “dead zones” where it is unlikely that the MRI is active. In addition, a variety of other MHD models (e.g., the Hall effect, ambipolar diffusion) are more applicable than standard MHD in most regions of the disk (Kunz and Lesur, 2013; Bai and Stone, 2013; Lesur *et al.*, 2014). The study of these models in the context of disks is in its infancy, but a variety of different behaviors are seen, much of which could not be considered turbulence in the usual sense.

Binary systems Binary disks consist of a (secondary) main-sequence star orbiting with a (primary) white dwarf, neutron star, or black hole. The star loses matter to the primary object, which subsequently forms an accretion disk as it spirals in. Emission of radiation is powered by this accretion process, and while these disks are too small to be directly imaged, a variety of spectral signatures exist that provide compelling evidence for their existence (Balbus and Hawley, 1998). Cataclysmic variables form an interesting subclass of binary disk systems in which the primary is a white dwarf, emission is mostly in the ultraviolet, and the brightness can increase enormously over a short timescale (perhaps due to instabilities of the accretion disk). X-ray binaries occur when the primary is a neutron star or black hole, which allows for hotter temperatures (due to the smaller disk radii) and correspondingly more emission in the X-ray range. Disks in binary systems are expected to be very well ionized and thus unstable to the MRI in the presence of even minute magnetic fields.

Active galactic nuclei At the center of galaxies, an accretion disk often forms around a supermassive black hole, forming an active galactic nucleus (AGN). So much energy can be released in the, often super-Eddington,¹ accretion process that the AGNs can outshine their galaxy. While general relativistic effects definitely become important very close to the event horizon, much of the physics of accretion outside of this can be studied with Newtonian gravity. These disks are very well ionized due to their high temperatures and would be expected to be unstable to the MRI. The Event Horizon Telescope project aims to image Sagittarius A*, the supermassive black hole at the center of the milky way, with unprecedented precision. A better understanding of the physics of its accretion disk will be critical for interpreting such images.

¹The *Eddington luminosity* is the limit at which (outwards) radiation pressure balances the (inwards) gravitational force, forming a theoretical upper bound on the maximum mass accretion rate. However, the limit is calculated for a spherical object and, because of their different geometry, disks can sometimes surpass this limit, thus becoming a super-Eddington accretor.

In each of the systems discussed above, it is common to observe astrophysical jets. These highly collimated beams emanate from the central object, perpendicular to the plane of the disk. While disks and jets are often examined together, I shall not discuss jets further in this thesis.

1.1.1 Basic physics of accretion

In this section I give a basic overview of the physics of momentum balance and transport in disks. More detailed information and derivations can be found in Shakura and Sunyaev (1973), Balbus and Hawley (1998), and Blaes (2004).

As mentioned previously, I shall be using fluid models – specifically magnetohydrodynamics (MHD) – exclusively in this work and these equations are a good starting point to discuss the basic processes and balances in disks. Most generally the compressible MHD equations have the form

$$\frac{\partial \rho}{\partial t} + \nabla \cdot (\rho \mathbf{u}) = 0, \quad (1.1a)$$

$$\rho \left(\frac{\partial \mathbf{u}}{\partial t} + \mathbf{u} \cdot \nabla \mathbf{u} \right) = -\nabla p - \rho \nabla \Phi + \mathbf{B} \times \nabla \times \mathbf{B} + \nabla \cdot [\rho \nu (\nabla \mathbf{u} + (\nabla \mathbf{u})^T) + \rho \zeta \delta_{ij} \nabla \cdot \mathbf{u}], \quad (1.1b)$$

$$\frac{\partial \mathbf{B}}{\partial t} = \nabla \times (\mathbf{u} \times \mathbf{B}) + \eta \nabla^2 \mathbf{B}, \quad (1.1c)$$

along with some equation of state for the pressure as a function of density (e.g., isothermal, adiabatic). Here ρ is the density, \mathbf{u} is the fluid velocity, \mathbf{B} is the magnetic field, Φ is the gravitational potential, ν is the kinematic viscosity, ζ is the bulk viscosity, and η is the resistivity (spatial variation of ν , ζ , and η is ignored). I have given the magnetic field units of $\sqrt{\rho} \mathbf{u}$ for simplicity (i.e., \mathbf{B} is really $\mathbf{B}/\sqrt{\mu_0}$) and neglected the Hall and Ambipolar terms in the induction equation. The fluid and magnetic Reynolds numbers (Re and Rm respectively) measure the range of dynamically important scales in a turbulent situation, and are defined through the ratio of inertial forces to viscous

(or resistive) forces

$$\text{Re} = \frac{\bar{u}L}{\nu}, \quad \text{Rm} = \frac{\bar{u}L}{\eta}, \quad (1.2)$$

where \bar{u} is a characteristic velocity and L is a characteristic length scale of the system. Their ratio, $\text{Pm} = \text{Rm}/\text{Re} = \nu/\eta$, is the magnetic Prandtl number. In small Pm magnetofluids, velocity structures can reach smaller scales than magnetic structures, while the opposite is true at high Pm.

Consider a disk whose mass can be neglected in comparison to that of the central object (M), such that $\Phi = -GM/R$. The zeroth-order motion of the gas in this case (neglecting radial pressure in comparison to gravity) is simply Keplerian: $u_\phi^2 = R^2\Omega^2 = GM/R$. We are primarily interested in thin disks, in which the vertical scale height H is less than the radius, $H/R \ll 1$. The pressure supports the gas against gravity in the vertical direction $\partial_z P = -GM\rho z/R^3 = -\rho\Omega^2 z$, which leads to $\rho(z) = \exp(-\Omega^2 z^2/2c_s^2)$ assuming an isothermal gas with sound speed c_s , $P = c_s^2\rho$. Thus we see that the ratio H/R scales as the ratio of the sound speed to rotation velocity, c_s/Ω , and the disk will be thin if this is small. Many of the analytical approximations in accretion disk theory arise from an expansion in H/R , including the local shearing box approximations used later in this work.

The equation for the angular momentum of the fluid is obtained by multiplying the ϕ component of the momentum equation by R (Balbus and Hawley, 1998; Blaes, 2004),

$$\frac{\partial}{\partial t} (\rho R u_\phi) + \nabla \cdot \mathcal{F} = 0, \quad (1.3a)$$

$$\mathcal{F} = \rho R u_\phi \mathbf{u} - R B_\phi \mathbf{B}_p + R \left(p + \frac{B_p^2}{2} \right) \hat{\phi} - \nu \left(\frac{R}{3} \hat{\phi} \nabla \cdot \mathbf{u} + R^2 \nabla \frac{u_\phi}{R} \right), \quad (1.3b)$$

where $\mathbf{B}_p \equiv B_R \hat{\mathbf{R}} + B_z \hat{\mathbf{z}}$. \mathcal{F} is angular momentum flux and it is worth noting that there are no sources and sinks in this (exact) equation – angular momentum can only be redistributed.² We

²Note that magnetocentrifugal winds, which may play a very important role in some accretion processes, are ignored in the ensuing discussion by neglecting the vertical component of \mathcal{F} . Such winds enable angular momentum transport in the central regions of a disk by means of a flux of matter or magnetic fields through its top and bottom; see, for example, Bai and Stone (2013).

are most interested in the radial component of the flux in steady-state conditions, since this will determine the flow of matter into the central object. To proceed, it is useful to average the R component of \mathcal{F} [Eq. (1.3b)] over z , ϕ , and a region ΔR in R (to smooth over rapid fluctuations) using the average

$$\langle f \rangle = \frac{1}{2\pi\bar{\rho}\bar{R}\Delta R} \int_0^{2\pi} d\phi \int_{-\infty}^{\infty} dz \int_{\bar{R}}^{\bar{R}+\Delta R} dR R\rho f, \quad (1.4)$$

where $\bar{\rho} \equiv \int_{-\infty}^{\infty} dz \rho$. Considering the fluctuation velocity $\tilde{\mathbf{u}} \equiv \mathbf{u} - \mathbf{U}_{\text{Kep}} = \mathbf{u} - R\Omega\hat{\phi}$, this gives

$$\mathcal{F}_R = R\bar{\rho} \left(R\Omega \langle \tilde{u}_R \rangle + \left\langle \tilde{u}_R \tilde{u}_\phi - \frac{1}{\rho} B_R B_\phi \right\rangle \right) + \nu R \left(\frac{3}{2} \Omega + \frac{\bar{\rho}}{R} \left\langle \frac{\tilde{u}_\phi}{\rho} \right\rangle - \bar{\rho} \left\langle \frac{1}{\rho} \frac{\partial \tilde{u}_\phi}{\partial R} \right\rangle \right). \quad (1.5)$$

The infall of matter is governed directly by the first term, $R^2\bar{\rho}\Omega \langle \tilde{u}_R \rangle$, since the mass accretion rate is simply

$$\dot{M} = -2\pi R\bar{\rho} \langle \tilde{u}_R \rangle. \quad (1.6)$$

The final terms govern transfer of angular momentum directly through the viscosity, and since $\tilde{u}_\phi \ll \Omega R$ (\tilde{u}_ϕ is limited by the sound speed due to shock formation), we would expect $\frac{3}{2}\nu\Omega R$ to dominate over $\nu\bar{\rho} \langle \tilde{u}_\phi/\rho \rangle$ and $-\nu R\bar{\rho} \langle \partial_R \tilde{u}_\phi/\rho \rangle$. Even so, due to the enormously large Reynolds numbers in real disks (small ν), this direct transfer is far too small to account for measured accretion rates and can be neglected entirely. Thus we see that in steady state, $\partial_t(\rho R u_\phi) = 0$, a positive $W_{R\phi} \equiv \langle \tilde{u}_R \tilde{u}_\phi - B_R B_\phi/\rho \rangle$ is required to balance $\langle \tilde{u}_R \rangle$, which is necessary for mass accretion onto the central object. Importantly, since the origin of $W_{R\phi}$ is turbulence in the disk, it could be expected to reach a nonzero limit as the viscosity is decreased to zero ($\text{Re} \rightarrow \infty$), in contrast to the viscous transfer term $3\nu\Omega R/2$. Through similar manipulations of the energy conservation equation, one can relate the disk surface emissivity Q to \dot{M} , and thus to $W_{R\phi}$ (Balbus and Hawley, 1998), giving

$$Q = \frac{3}{4} \bar{\rho} \Omega \left\langle \tilde{u}_R \tilde{u}_\phi - \frac{1}{\rho} B_R B_\phi \right\rangle, \quad (1.7)$$

where the viscous contribution has been neglected. Thus we have reduced the problem of explaining the high observed luminosities of disks (and by implication high angular momentum transport), to understanding how the excitation of turbulence can lead to nonzero correlations between \tilde{u}_R and \tilde{u}_ϕ , and/or B_R and B_ϕ .

From where does the turbulence arise? Is it possible to have a purely hydrodynamic disk transition to turbulence, or do we really require MHD? This question is not so simple as it may seem at first glance. While the local linear stability of a Keplerian shear flow is easy to calculate, illustrating that the system is linearly stable (see below), this does not *prove* that the system is nonlinearly stable to finite-amplitude disturbances. The obvious counterexample is a nonrotating shear flow, or Couette flow, which is linearly stable at all Reynolds numbers but will readily transition to self-sustaining turbulence.³ Importantly, this transition only occurs above a certain Reynolds number that is related to the nonlinear physics of the fluid, and thus is very difficult to determine theoretically. This leaves one in the awkward situation of easily being able to show that moderate Re hydrodynamic Keplerian flows are stable, but having no straightforward way to extrapolate this result to astrophysically relevant values. It was partly the analogy with turbulence in nonrotating shear flows that led many early authors (e.g., Shakura and Sunyaev 1973) to conclude that turbulence in disks should exist and be responsible for momentum transport, without any known mechanism for its production.

It is still controversial whether the problem of turbulence in Keplerian disks has been satisfactorily solved. Some of the best evidence against its existence comes from rotating Couette flow experiments (in particular Ji *et al.* 2006), which have shown that turbulence will not self-sustain in flows up to $\text{Re} \approx 10^6$. While high, this is still a long way from astrophysically relevant values ($\text{Re} \sim 10^{14}$). Careful computational studies (Lesur and Longaretti, 2005; Shen *et al.*, 2006) and a variety of heuristic arguments (e.g., Balbus and Hawley 1998, 2006) have also come to the same

³This behavior is strongly related to nonmodal linear physics, which will be discussed in the context of the MRI in Chapter 2.

conclusion, but these are limited to substantially smaller Re still. More studies, and perhaps completely new theoretical methods, are needed to satisfactorily solve this problem. As we shall see in the next section, consideration of an ionized gas completely changes this problem, bringing in the magnetorotational instability (MRI). This instability develops into turbulence with the required correlations between fluctuations, $\langle \tilde{u}_R \tilde{u}_\phi - B_R B_\phi / \rho \rangle > 0$, to cause significant outward flux of angular momentum.

1.1.2 Magnetorotational instability

Here I give a brief outline of the linear behavior of the simplest axisymmetric magnetorotational instability. Although the basic instability was derived very early in the context of liquid metals (Velikhov, 1959; Chandrasekhar, 1960), the possible consequence for turbulence in accretion disks was not realized until much later by Balbus and Hawley (1991). Subsequently, a wide variety of linear analyses of various forms have been published (e.g., Balbus and Hawley 1992; Curry *et al.* 1994; Kersalé *et al.* 2004). As part of the work in this thesis, we have also considered the linear development of the MRI, using the machinery of nonmodal stability theory. This is discussed in Chapter 2.

For the sake of simplicity, I shall make various approximations to the full MHD system [Eqs. (1.1)]. These are not entirely justified without knowing the properties of the instability *a priori*, but turn out to make little difference to the growth rate, while significantly reducing the algebraic complexity. The starting point is an application of the Boussinesq approximation to the MHD equations [Eq. (1.1)], which is valid for nearly incompressible disturbances (essentially when the disturbance velocity is substantially less than the sound speed). I shall also go further and neglect vertical variation of the disk profile and density perturbations, which removes the effects of radial and vertical stratification from the instability (this approximation changes the growth rate slightly but does not fundamentally alter in the instability). Essentially, these approximations

amount to considering an incompressible fluid with a varying density (the final dispersion relation will contain background density just as a parameter). Finally I assume that perturbations vary only in the z direction (this leads to the simplest version of the MRI), inserting the ansatz $f \sim e^{ikz-i\omega t}$ for perturbations in each variable. One then linearizes against the background flow $u_\phi = R\Omega$, and the background magnetic field is $B_z = B_{z0}$. After simple manipulations, one arrives at

$$ik\delta u_z = ik\delta b_z = 0, \quad (1.8a)$$

$$-i\omega\delta v_R - 2\Omega\delta v_\phi = \frac{1}{\rho}B_{z0}ik\delta b_R, \quad (1.8b)$$

$$-i\omega\delta v_\phi + 2\Omega\delta v_R + R\frac{\partial\Omega}{\partial R}\delta v_R = \frac{1}{\rho}B_{z0}ik\delta b_\phi, \quad (1.8c)$$

$$-i\omega\delta b_R = B_{z0}ik\delta v_R, \quad (1.8d)$$

$$-i\omega\delta b_\phi - R\frac{\partial\Omega}{\partial R}\delta b_R = B_{z0}ik\delta v_\phi, \quad (1.8e)$$

where δv_R , δb_R etc. are the perturbations and I have neglected dissipation terms for simplicity. Upon rescaling time by Ω and the magnetic field perturbations by ρ , one finds that stability of the system is determined by the eigenvalues of the matrix

$$i \begin{pmatrix} 0 & 2 & ikB_{z0} & 0 \\ q-2 & 0 & 0 & ikB_{z0} \\ ikB_{z0} & 0 & 0 & 0 \\ 0 & ikB_{z0} & -q & 0 \end{pmatrix}, \quad (1.9)$$

where $q \equiv -d \ln \Omega / d \ln R = -R/\Omega \partial_R \Omega$ (a definition that leads to $\Omega(R) \sim R^{-q}$, with $q = 3/2$ for a Keplerian disk).

Let us first examine the hydrodynamic limit [the 2×2 sub-matrix in the upper left corner of the MRI matrix, Eq. (1.9)]. In this case, the system is entirely determined by the parameter q , and

eigenvalues of the system are simply

$$\omega = \pm \sqrt{2(2 - q)}, \quad (1.10)$$

showing that the system is unstable for $q > 2$ and stable otherwise. This is the well-known Rayleigh criterion,⁴ and we see that the Keplerian disk with $q = 3/2$ is decidedly stable. Including again the magnetic field variables, the eigenvalues are

$$\omega = \pm [2 - q + k^2 B_{0z}^2 \pm (4k^2 B_{0z}^2 + (2 - q)^2)^{1/2}]^{1/2}. \quad (1.11)$$

From this, it is evident that stability requires $2 - q + k^2 B_{0z}^2 > [4k^2 B_{0z}^2 + (2 - q)^2]^{1/2}$, which is guaranteed only if $q < 0$. Thus we see that addition of *any* magnetic field changes the stability criterion from $q < 2$ to $q < 0$ and Keplerian rotation ($q = 3/2$) will be unstable. The growth rate of the MRI can be found by maximizing the imaginary part of Eq. (1.11) over $B_{0z}^2 k^2$, giving

$$\omega = iq/2, \quad (1.12)$$

which occurs when $B_{0z}^2 k^2 = (q - q^2/4)^{1/2}$.

What is happening here? While the MRI certainly requires a magnetic field to be unstable, its growth rate is completely independent of magnetic field. Physically, the resolution of this apparent conundrum arises from the fact that the energy source of the MRI is the velocity shear. That is, rather than driving the instability itself, the magnetic field acts as a mediator that allows the energy to be unlocked from the rotating shear flow. While it appears from Eq. (1.11) that B_{0z} can be as small as desired without affecting the growth rate, this is only true in the nonphysical limit of zero

⁴Note that the Rayleigh criterion is often given in terms of $R_\Omega = 2\Omega/S$ as $-1 < R_\Omega < 0$, where S is the local velocity shear and Ω is the rotation. In terms of q , $R_\Omega = -2/q$, and the upper stability limit of the Rayleigh criterion, $R_\Omega = 0$, now occurs at $q = \infty$. This singular limit has come about because in defining q , we have assumed that our velocity shear arises from a rotation.

dissipation. Any real system will always have some nonzero η , however small,⁵ and this will place a limit on the allowable k such that the MRI is eventually stabilized at sufficiently low B_{0z} . Of course, in astrophysics, dissipation coefficients are vanishingly small in comparison to the scales of the disk and the MRI should be unstable at very small wavelengths with even the smallest wisp of an imposed magnetic field, making it a particularly attractive instability for explaining turbulence in disks. On the side of large B_{0z} , the MRI can be stabilized because its required wavelength becomes too large to fit inside the physical structure of the disk.

Finally, it is worth noting that for the sake of turbulence, it is not necessarily the presence of unstable linear modes that is important, but the addition of magnetic perturbations into the system. Specifically, it is possible to excite self-sustaining turbulence with no net magnetic field, and thus no linear instability whatsoever (Hawley *et al.*, 1996). The turbulence is *subcritical* in a way similar to turbulence in nonrotating shear flows, and arises if the Reynolds numbers are high enough and the initial perturbation large enough. Interestingly, it seems that such turbulence will always eventually decay back to the laminar state (Rempel *et al.*, 2010), as is the case for hydrodynamic pipe flows (Hof *et al.*, 2006). Nonetheless, because the lifetime (or more accurately, the probability of decay after a given time) is an exponential function of Reynolds number, for reasonably large Reynolds numbers the turbulence is effectively self-sustaining.⁶ To quote an amusing example from hydrodynamic pipe flow (Hof *et al.*, 2006), to make an observation of the decay of pipe flow turbulence in a garden hose at a flow rate of 1 L min^{-1} ($\text{Re} \approx 2400$), one would require a hose of length 40 000 km and 5 years before the turbulence eventually decayed! Self-sustaining turbulence in the shearing box will be discussed in much more detail in the following section, as well as chapter 3.

⁵Note that viscosity, by itself, cannot prevent instability, although it does reduce the MRI growth rate.

⁶The size of the perturbation required to cause transition also decreases as the Reynolds numbers increase. Since there will always be some background level of perturbations in any physical or numerical system (e.g., inaccuracies in the MHD model, round-off error), there is presumably some point above which turbulence *will* self-sustain indefinitely, since if it ever decays it will be instantly re-excited.

Experimental efforts

There have been a variety of experimental efforts to observe the MRI (see, for example, Ji *et al.* 2001; Sisan *et al.* 2004; Stefani *et al.* 2006; Collins *et al.* 2014), but at the present time it has not been convincingly identified. The primary difficulty is that most experiments utilize liquid metals as their conducting fluid, and these have very high resistivities in comparison to their viscosities. This implies enormously high Re is needed to obtain even $R_m \sim 1$, which is required for the MRI to be excited (Ji *et al.*, 2001). In addition, hard wall boundaries in these experiments can create significant difficulties since a variety of other flows and instabilities are excited, and these have probably led to false claims (Sisan *et al.*, 2004; Gissinger *et al.*, 2011, 2012). Nonetheless, variants of the MRI (“Helical” and “Azimuthal” MRI, see Hollerbach and Rüdiger 2005; Liu *et al.* 2006; Hollerbach *et al.* 2010; Kirillov and Stefani 2013) have been observed (Stefani *et al.*, 2006; Seilmayer *et al.*, 2014). These are “induction-less” instabilities and thus have less stringent requirements on R_m for their observation. Finally, it is worth noting that a plasma experiment has recently been completed (Collins *et al.*, 2014) and results will presumably be forthcoming in the near future.

1.1.3 Local approximation and the shearing box

It is generally inconvenient to work with the full compressible MHD equations using global accretion disk profiles. This is particularly true for numerical simulations of turbulence due to a variety of factors such as numerical resolution constraints, boundary conditions, and the analysis of data. Indeed, although a variety of global turbulence studies have come out in recent years (e.g., Flock *et al.* 2011; Sorathia *et al.* 2012; Hawley *et al.* 2013), most of the numerical work on MRI turbulence has been carried out in the shearing box. Due to our focus on the basic theory of shearing turbulence, this has also been the case throughout this thesis (the one exception being the nonmodal

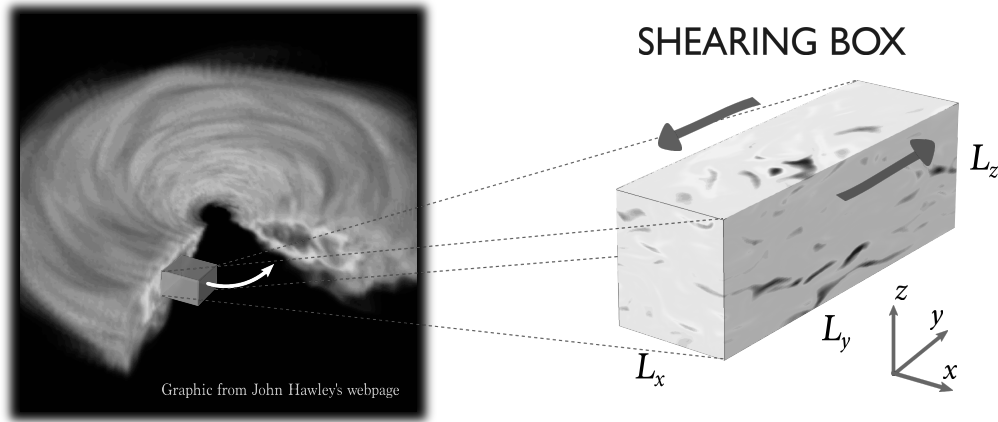


Figure 1.2: Illustration of the concept of the shearing box (figure constructed using the image of a global accretion disk from <https://www.astro.virginia.edu/~jh8h/>).

linear studies in Chapter 2). Here, I outline these approximations, including some discussion of important physical effects that might be lost in the reduction.

The basic idea of the shearing box is illustrated in Fig. 1.2. Consider a small patch of fluid that is co-rotating with the Keplerian background flow. Expanding about this patch in a Cartesian coordinate frame, one obtains a linear background velocity shear with the effects of rotation taken into account through a mean Coriolis force. Conforming to standard astrophysical conventions, we set (x, y, z) to correspond to the radial, azimuthal, and vertical directions respectively.⁷ Boundary conditions are set to be periodic in the y direction and periodic in the frame in which the background velocity vanishes – or shearing periodic – in the x direction; that is,

$$f(x, y, z) = f(x, y + L_y, z), \quad (1.13a)$$

$$f(x, y, z) = f(x + L_x, y - q\Omega L_x t, z). \quad (1.13b)$$

⁷ Note that most fluid dynamics literature uses the convention $(y, -x, z)$ instead of (x, y, z) , denoting these the shearwise, streamwise and spanwise directions.

These boundary conditions are designed to represent a series of tiled domains, each moving in a background linear shear flow and containing identical patches of turbulent flow (Balbus and Hawley, 1998).

There are two common variants on the shearing box. The first is the *stratified shearing box*, in which the vertical density profile is included along with the vertical component of gravity, with the simulation covering the entire vertical extent of the disk. Compressibility effects must be retained within the equation of motion (at least within the anelastic approximation) to account for the vertical variation. The second variant is the *unstratified shearing box* in which the background is completely homogenous and periodic boundary conditions are used in the vertical direction. This is designed to represent a small vertical patch near the center of the disk, and within this approximation it is appropriate to use incompressible fluid equations, essentially because a sound wave will necessarily cross a small domain faster than flow dynamics in the system (Umurhan and Regev, 2004). It is unclear what quantitative conclusions can be drawn from unstratified shearing box results, since there is no physically motivated outer scale to the turbulence; nonetheless, a variety of interesting dynamics can be seen, which definitely share qualitative features with more complete models. Due to its simplicity, we shall primarily consider the unstratified shearing box for the remainder of this thesis. The appropriate incompressible MHD equations, including the background shear ($\mathbf{U}_0 = -q\Omega x \hat{\mathbf{y}}$) and rotation $\Omega \hat{\mathbf{z}}$, are

$$\frac{\partial \mathbf{u}}{\partial t} - q\Omega x \frac{\partial \mathbf{u}}{\partial y} + (\mathbf{u} \cdot \nabla) \mathbf{u} + 2\Omega \hat{\mathbf{z}} \times \mathbf{u} = -\nabla p + \mathbf{B} \cdot \nabla \mathbf{B} + q\Omega u_x \hat{\mathbf{y}} + \bar{\nu} \nabla^2 \mathbf{u}, \quad (1.14a)$$

$$\frac{\partial \mathbf{B}}{\partial t} - q\Omega x \frac{\partial \mathbf{B}}{\partial y} = -q\Omega B_x \hat{\mathbf{y}} + \nabla \times (\mathbf{u} \times \mathbf{B}) + \bar{\eta} \nabla^2 \mathbf{B}, \quad (1.14b)$$

$$\nabla \cdot \mathbf{u} = 0, \quad \nabla \cdot \mathbf{B} = 0. \quad (1.14c)$$

Here $\mathbf{u} = \mathbf{u}_{si}/u_0$, $\mathbf{B} = \mathbf{B}_{si}/(u_0\sqrt{\mu_0\rho_0})$, $p = p_{si}/(u_0^2\rho_0)$, where \mathbf{u}_{si} , \mathbf{B}_{si} , p_{si} are respectively the fluid velocity, magnetic field, and pressure in SI units, and ρ_0 , μ_0 are the density (considered

constant) and the vacuum permeability. Lengths have been scaled by characteristic scale L_0 in Eq. (1.14), time is scaled by $1/\Omega$, and the velocity scale u_0 is $L_0\Omega$. As such, $\Omega = 1$ in Eq. (1.14); I have kept Ω explicitly to show more clearly how the basic MHD equations have been altered by the Coriolis force. As a reminder, the parameter $q = -d \ln \Omega / d \ln r$ embodies the radial velocity shear, with $q = 3/2$ for Keplerian rotation. The fluid and magnetic diffusivities, $\bar{\nu}$ and $\bar{\eta}$, are defined as $\bar{\nu} = \nu / (\Omega L_0^2)$, $\bar{\eta} = \eta / (\Omega L_0^2)$, where ν and η are the kinematic viscosity and resistivity of the plasma. Since parameters in the unstratified shearing box are all of order one, $\bar{\nu}$ and $\bar{\eta}$ are approximately the inverses of Re and Rm respectively (as defined with respect to the large-scale shear flow).

The shearing box in its various guises has generated significant controversy. Most notable was the discovery of Fromang and Papaloizou (2007) that turbulence in unstratified shearing boxes without net magnetic flux is not converged – a doubling of the resolution leads to a *decrease* in the level of angular momentum transport. Given the enormous Reynolds numbers of real disks, this is a particularly troubling result. The problem has later been shown to disappear so long as explicit values of the viscosity and resistivity are used and their ratio is kept fixed⁸ (Fromang, 2010); however, far from solving the problem, this result is perhaps even more confusing since it implies that MRI turbulence depends strongly on details of the microscopic dissipation, in particular the magnetic Prandtl number (Fromang *et al.*, 2007). While these problems are possibly alleviated somewhat by the addition of net flux or vertical stratification (Bodo *et al.*, 2008; Shi *et al.*, 2010; Davis *et al.*, 2010; Longaretti and Lesur, 2010; Simon *et al.*, 2011; Oishi and Mac Low, 2011; Simon *et al.*, 2012; Flock *et al.*, 2012; Bodo *et al.*, 2014), the physical origin of the Pm dependence remains unclear. Very recently, in one of the few encouraging results about unstratified shearing box turbulence since Fromang and Papaloizou (2007), Meheut *et al.* (2015) have shown that net-flux MRI turbulence does eventually converge in the low Pm limit for $Pm \lesssim 1/40$ at fixed Rm

⁸ I have also tested this convergence using the spectral code snoopy (Lesur and Longaretti 2007, see also chapter 3), and found results essentially in agreement with Fromang (2010) (who used a finite difference scheme) for the case $Pm = 8$. These results are unpublished and not included in this thesis.

(bear in mind that this value is almost certainly specific to their chosen magnetic flux and R_m). Finally, I note that shearing box turbulence also depends significantly on the chosen aspect ratio of the box. This is true in both unstratified setups with (Bodo *et al.*, 2008) or without net flux, and when vertical stratification is included (Johansen *et al.*, 2009; Simon *et al.*, 2012).

Based on the results described in the previous paragraph, it may strike the reader that the prospects of understanding MRI turbulence using the shearing box are somewhat bleak. If one is looking for quantitative answers regarding the level of turbulent angular momentum transport, this is probably true. After all, if changing the dimensions of a system that is designed to represent a “patch” of turbulence will significantly change the answer, it is difficult to convincingly ascribe importance to one particular result. A variety of other objections have been given to the shearing box (Kersalé *et al.*, 2004, 2006; Regev and Umurhan, 2008) and local disk approximations in general (Knobloch, 1992), which often center around their inability to capture global instabilities.⁹ Nonetheless, it is my view that we still have a lot to gain from studying the shearing box, even the unstratified variety. This primarily centers around understanding the basic turbulence and dynamo mechanisms, which become much more difficult to analyze as the number of physical effects included in a simulation is increased. For instance, there have been a variety of suggestions that the accretion disk dynamo requires two separate mechanisms: one for the central unstratified region, and one for the stratified areas away from the mid-plane (Blackman and Tan, 2004; Gressel, 2010). The central mechanism should be perfectly well captured by unstratified simulations and indeed is regularly observed (Lesur and Ogilvie, 2008b; Käpylä and Korpi, 2011), although it is not so coherent as its stratified cousin. As one of the major results of this thesis, I suggest that the magnetic shear-current effect (see Sec. 1.2 and chapters 4–6) is likely to be the primary driver of this dynamo.

⁹See Sec. 2 on nonmodal instability for more discussion of this. I will argue that shearing waves, which are well captured by the shearing box, are probably much more relevant to global dynamics than global spectral instabilities.

While it may at first seem troublesome that the behavior of unstratified simulations depends so strongly on the details of the computational domain, after more thought this is hardly surprising; the presence of a large-scale dynamo suggests that structures will always reach scales comparable to the domain size, and any change in box dimensions will therefore effect the saturation of these structures as well as their influence on smaller scale turbulence. Similar ideas are often discussed in terms of parasitic modes (Goodman and Xu, 1994) for net-flux simulations (Bodo *et al.*, 2008). It follows that the unstratified shearing box should never be considered as a “patch” of turbulence, but more as a simplified setup in which to study the fundamentals of the turbulence and dynamo process. The dependence of unstratified simulations on numerical resolution is perhaps more troublesome and remains an outstanding unsolved issue in the community. Since the most worrisome aspect of the effect (the decrease in turbulence level with increasing grid resolution) occurs only when the grid itself is used to dissipate small-scale turbulence,¹⁰ it seems likely that the effect is numerical in origin (although this is not a viewpoint shared by all). The dependence on magnetic Prandtl number is certainly physical, however, and is also observed in global simulations (Flock *et al.*, 2011). Understanding the cause of this effect in sufficient detail to extrapolate results to astrophysically relevant regimes with $R_m \gg 1$, $P_m \ll 1$ is probably one of the most important unsolved problems related to accretion disk turbulence.

1.2 Dynamo

Magnetic fields pervade the universe. From the scales of planets up to galaxy clusters and beyond, they are not only ubiquitous but have also proven surprisingly dynamically important in a wide variety of astrophysical and geophysical processes. Our understanding of their generation and sustenance is based primarily on the concept of a *magnetic dynamo*. In a dynamo, magnetic fields

¹⁰ It is probable that the non-convergence also exists when hyper-viscosity (i.e., dissipation terms $\sim \nu \nabla^n \mathbf{u}$ with $n \geq 4$) is used in a Fourier code (G. Lesur, personal communication, 2015).

are stretched and folded by fluid motions in such a way as to make themselves stronger, causing exponential growth of the magnetic energy. Through this process, very small seed fields – arising, for example, from the Biermann battery or kinetic instabilities – might be amplified enormously by plasma motions to the levels seen throughout the universe today.

While there are a wide variety of known laminar dynamos, or specified velocity fields that will lead to magnetic field amplification, we shall be solely concerned with the *turbulent* dynamo. Here, the fluid is considered to be turbulent, with chaotic motion across a large range of length and time scales, and its flow properties are known only in the statistical sense. Of course, this situation is far more directly applicable than laminar dynamos, which are studied mostly for the theoretical insights they can bring through simplifying the problem. I shall further break down the turbulent dynamo into the *large-scale* and *small-scale* varieties, distinguished by the length (and time) scales of the generated magnetic field, in comparison to that of the underlying turbulence. As the nomenclature suggests, for a small-scale dynamo, the scales of the amplified field will be smaller than (or comparable to) the scales in the fluid turbulence. In contrast, in a large-scale dynamo, magnetic fields are generated with scales larger than those of the fluid motions. Of course, in real turbulence this distinction may not be quite so clear-cut, and real dynamos will generally be a mix of the two. Robust large-scale mechanisms can be harder to understand than the small-scale dynamo, but are of vital importance for explaining astrophysical fields. Most prominently, the solar magnetic field is a beautiful example of a large-scale dynamo – its dipolar field, which reverses sign every 11 years, is correlated over length scales far exceeding that of the convective motions inside the sun’s interior (see Fig. 1.3).

Most studies of large-scale dynamos use the formalism of *mean-field* dynamo theory (Moffatt, 1978; Krause and Rädler, 1980). Fundamentally, this involves assuming a separation of scales between small-scale turbulence and a mean field, and calculating the average influence of the small scales on the large. This scale separation is formalized through the use of a mean-field average $\langle f \rangle$, which encodes the difference between mean fields and fluctuations; the average of a

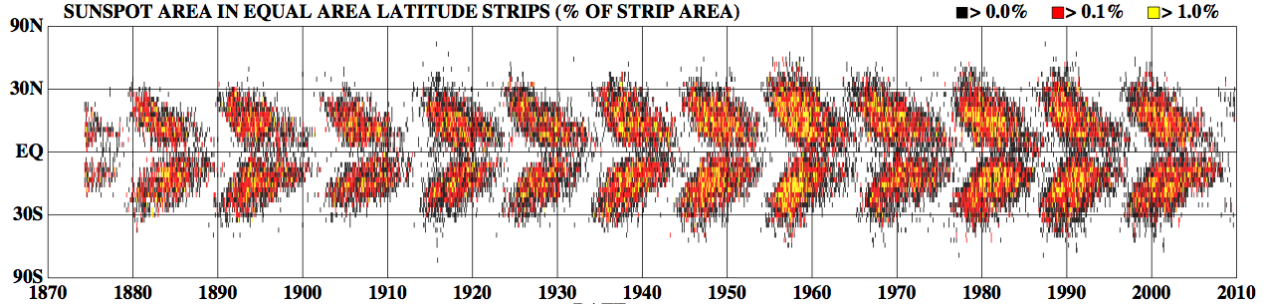


Figure 1.3: The famous “butterfly diagram” showing the 11-year period of solar activity (as measured by sunspots). Sunspot activity increases when the global dipolar field changes direction, due to the corresponding decrease in magnetic field. This 22-year cycle is highly coherent over long time periods, and is one of nature’s best known examples of large-scale dynamo action.

mean field is itself, $\langle \mathbf{B} \rangle = \mathbf{B}$, while the average of a fluctuating field vanishes $\langle \mathbf{b} \rangle = 0$ (where mean and fluctuating fields are denoted by capital and lower case letters respectively). The mean-field average should also satisfy the Reynolds averaging rules: linearity, commutativity with spatial and temporal derivatives, and that the average of a product between an average and a function is the product of the averages (i.e., $\langle \langle f \rangle g \rangle = \langle f \rangle \langle g \rangle$).

The theory proceeds by averaging the induction equation [Eq. (1.1)], giving

$$\frac{\partial \mathbf{B}}{\partial t} = \nabla \times (\mathbf{U} \times \mathbf{B}) + \nabla \times \mathcal{E} + \eta \nabla^2 \mathbf{B}, \quad (1.15)$$

where \mathbf{U} is the mean-field flow. The all-important *electromotive force* (EMF) $\mathcal{E} = \langle \mathbf{u} \times \mathbf{b} \rangle$ is nonzero due to the correlation between \mathbf{u} and \mathbf{b} and is responsible for dynamo action. The difficulty of actually solving Eq. (1.15) is belied by its simple appearance – in general one must understand how the turbulent \mathbf{u} and \mathbf{b} respond to an applied \mathbf{B} and \mathbf{U} before computing \mathcal{E} . This essentially amounts to a statistical closure for MHD that is inhomogenous in both space and time, a tremendously difficult problem that is far from being solved with any semblance of accuracy.

To study the idea of a *dynamo instability* let us consider \mathbf{B} and \mathbf{U} as a small perturbation to some pre-existing small-scale turbulence, specified by \mathbf{u}_0 and \mathbf{b}_0 . This allows us to assume the

linearity of \mathcal{E} in \mathbf{B} and \mathbf{U} (so long as $\mathcal{E}_0 = \langle \mathbf{u}_0 \times \mathbf{b}_0 \rangle = 0$). Combined with the assumption of scale separation, which permits the neglect of higher order mean-field derivatives in comparison to low orders, one can expand \mathcal{E} in a Taylor series in \mathbf{U} and \mathbf{B}

$$\mathcal{E} = \alpha \mathbf{B} + \beta \nabla \mathbf{B} + \Gamma \nabla \mathbf{U} + \dots, \quad (1.16)$$

where α , β and γ are the tensorial dynamo transport coefficients.¹¹ These coefficients must be calculated by solving for the statistics of the small-scale fields in some way and will depend on general properties of the pre-existing turbulence such as stratification, a mean rotation, or its symmetry properties. To simplify matters somewhat, much of dynamo theory has historically focused on the *kinematic* dynamo, in which one assumes the presence of small-scale velocity fluctuations, while magnetic fluctuations arise purely from the small-scale induction equation. This is motivated by situations where fluid turbulence may exist independently of any magnetic field, for instance due to convective instability in the sun. However, it transpires that the small-scale dynamo is always active in turbulence above even moderate Reynolds numbers and grows much faster than the large-scale dynamo (Boldyrev *et al.*, 2005), implying that kinetic fluctuations are probably always accompanied by magnetic fluctuations to some degree. Since much of the new work in this thesis concerns the effects of magnetic fluctuations on large-scale dynamo, I shall consider this more general situation and include magnetic fluctuations in the simple outline given here.

The α effect is the most well-studied of dynamo instabilities. A scalar α implies that a perturbation of the turbulence by a (small) constant mean field \mathbf{B} will cause the turbulence to respond in such a way such that the generated EMF is proportional to this \mathbf{B} . If we insert this into the induction equation [Eq. (1.15)] ignoring \mathbf{U} , exponential growth of the mean field is possible with the spatial form $\mathbf{B} \propto \nabla \times \mathbf{B}$. From where does such an α arise? It turns out that the *helicity* $\langle \mathbf{u} \cdot \nabla \times \mathbf{u} \rangle$ of the flow or magnetic field is fundamental to the α effect in isotropic homogenous

¹¹Note that there is no \mathbf{U} term in Eq. (1.16) because the spatially independent part of a mean flow can be removed through a Galilean transformation.

turbulence, and various closure approximations lead to (Pouquet *et al.*, 1976; Moffatt, 1978; Brandenburg and Subramanian, 2005)

$$\alpha \approx -\frac{1}{3}\tau_{\text{cor}} \langle \mathbf{u} \cdot \nabla \times \mathbf{u} \rangle + \frac{1}{3}\tau_{\text{cor}} \langle \mathbf{b} \cdot \nabla \times \mathbf{b} \rangle, \quad (1.17)$$

where τ_{cor} is a correlation time of the turbulence. Let us now examine the β term. Again considering the simplified case of homogenous isotropic small-scale turbulence, the symmetries of the problem dictate that the general tensorial expression in Eq. (1.16), $\beta \nabla \mathbf{B} = \beta_{ijk} B_{j,k}$, reduces to $-\beta_0 \nabla \times \mathbf{B}$, for the scalar β_0 . Inserting this form into Eq. (1.15) to join the α parameter leads to the simple replacement of η with $\eta + \beta_0$; that is, the β effect acts as a turbulent resistivity. As for the α effect, closure calculations lead to

$$\beta_0 \approx \frac{1}{3}\tau_{\text{cor}} \langle \mathbf{u}^2 \rangle, \quad (1.18)$$

showing that the turbulence *enhances* the standard resistivity for the large-scale field. This illustrates that dynamo instability is impossible from the β effect alone, and that any α dynamo must have sufficiently helical small-scale turbulence (i.e., have a large $\langle \mathbf{u} \cdot \nabla \times \mathbf{u} \rangle$ in comparison to $\langle \mathbf{u}^2 \rangle$), with some imbalance between kinetic and magnetic fluctuations, to be unstable. It is also worth noting that magnetic fluctuations do not contribute at lowest order to β_0 . Finally, the lesser-known Γ term (Yokoi, 2013; Yoshizawa and Yokoi, 1993), is proportional (in isotropic homogenous turbulence) to the small-scale cross-helicity, $\langle \mathbf{u}_0 \cdot \mathbf{b}_0 \rangle$. This is fundamentally different from the α and β effects, since it relies on a mean correlation between the kinetic and magnetic fluctuations, and has no kinematic equivalent.

The simplicity of the discussion in the previous paragraph hides a fundamental difficulty that has plagued mean-field dynamo theory for the past 20 years. This is the issue of α quenching (Kulsrud and Anderson, 1992; Gruzinov and Diamond, 1994). The fundamental problem is related to

the build-up of current helicity $\langle \mathbf{b} \cdot \nabla \times \mathbf{b} \rangle$ on small scales faster than the dynamo develops on large scales (Boldyrev *et al.*, 2005). As this small-scale \mathbf{b} field develops, it generates a magnetic α effect [the final term in Eq. (1.17)], which has the tendency to oppose further large-scale field generation. Importantly, because of the larger range of scales at low dissipation, this effect has a greater impact at higher Reynolds numbers, and by the most extreme estimates, the saturated large-scale field strength varies as $1/Rm$ (Brandenburg and Subramanian, 2005; Hubbard and Brandenburg, 2012). Extrapolating to astrophysically relevant values, $Rm \sim 10^{10} \rightarrow 10^{15}$, such scaling is problematic, leading to the nomenclature “catastrophic quenching.” The standard theory to describe this process is derived from the conservation of small-scale magnetic helicity¹² $h_f = \langle \mathbf{a} \cdot \mathbf{b} \rangle$ (where \mathbf{a} is the small-scale magnetic helicity, $\nabla \times \mathbf{a} = \mathbf{b}$; see Blackman and Brandenburg 2002; Blackman and Field 2002), and leads to an equation for h_f of the form

$$\frac{\partial h_f}{\partial t} = -2\mathcal{E} \cdot \mathbf{B} - 2\eta \nabla^2 h_f - \nabla \cdot \mathcal{F}, \quad (1.19)$$

where \mathcal{F} represents a flux term. Relating h_f to the α effect, one can then form a coupled set of equations for the growth of the dynamo field. Without the flux term in Eq. (1.19) one arrives at the previously discussed $1/Rm$ scaling of the saturated \mathbf{B} field; however, it is now generally thought that \mathcal{F} is of fundamental importance,¹³ allowing helicity to be removed from the active dynamo region (Vishniac and Cho, 2001; Hubbard and Brandenburg, 2012). Nonetheless, despite some confidence in the community that quenching may not be quite so catastrophic as originally thought, there are a wide variety of open issues and the physics of high Rm dynamos is far from being convincingly understood.

¹²Issues of gauge invariance certainly arise in defining a density of magnetic helicity. Since one really cares about the current helicity $\langle \mathbf{b} \cdot \mathbf{j} \rangle$ it can be reasonable to simply specify the Coulomb gauge, but a variety of other possibilities may be more useful and cleanly defined (Subramanian and Brandenburg, 2004, 2006; Candelaresi *et al.*, 2011).

¹³Interestingly, these fluxes were first studied (using the terminology “hyper-resistivity”) in the context of magnetic fields in reversed-field pinch fusion devices (Bhattacharjee and Hameiri, 1986; Boozer, 1986), where they were found to be crucial in the approach to the self-organized state and have been experimentally measured (Ji, 1999). While not explored extensively in this thesis, such connections may prove very useful for future studies of the accretion disk dynamo (Ebrahimi and Bhattacharjee, 2014).

If we relax the assumptions of isotropy and homogeneity of the background turbulence, a wide variety of other dynamo effects are possible. In particular, one loses the requirements that α and β be representable by scalar quantities. For example, one of the more commonly studied additions is that of stratification with rotation – important due to its relevance to the solar dynamo – which leads to an α effect proportional to $u_{\text{rms}}^2 \boldsymbol{\Omega} \cdot \nabla \ln(\rho u_{\text{rms}})$ in addition to off-diagonal contributions (Brandenburg and Subramanian 2005; ρ is a background density and u_{rms} is the turbulence intensity). Note that this arises without net helicity being explicitly added to the system (although one can also consider the effect to arise through helicity created by the combination of rotation and stratification). It is also possible to have a growing dynamo without any α effect at all. This is important because α is constrained to be zero by symmetries of the system in homogeneous and mirror symmetric turbulence, such as is found in the central regions of accretion disks. The most prominent of these effects, which will be the subject of a large amount of the work presented in this thesis, is the so-called “shear-current” effect. This can arise in the presence of mean shear flow, which exists in a wide variety of astrophysical objects, if a particular off-diagonal component of β_{ijk} has the correct sign. The combination of the stretching of the mean field by the flow shear (the “ Ω effect”) with this component of β_{ijk} can lead to dynamo instability even though $\alpha = 0$. In what is probably the most significant result presented in this thesis, I will argue in chapters 4–6 that magnetic fluctuations are crucial for this effect, and can be responsible for large-scale mean field generation. The significance of this result lies in the fact that it is the first example (of which we are aware) of a large-scale dynamo being driven by the saturated state of the small-scale dynamo.

1.3 Overview of the work presented in this thesis

In this section I give a detailed outline of the most important results presented in this thesis. This is intended to both highlight those results that I consider to be the most important, and to explain how the different chapters fit into the overall coherent structure of the research program. My

outline is a little unconventional, as it is presented in near reverse order from the thesis chapters themselves. The primary reason for this is to emphasize the more important results, which are presented towards the end of the thesis. This notwithstanding, given that an overarching theme of the research presented here is the importance of linear physics in understanding the turbulent situation, it is helpful to start in chapter 2 with work on the nonmodal linear stability of the MRI. This, in turn, motivates the use of the quasi-linear models presented later in the thesis.

1.3.1 The magnetic shear-current effect

I consider the most important results of this thesis to be those presented in chapters 3-6, proposing the “magnetic shear-current effect” as a mechanism for generating large-scale magnetic fields in shear flows. The suggestion is that a bath of homogeneous nonhelical *magnetic* fluctuations, influenced by the velocity shear, can cause a dynamo instability through an off-diagonal turbulent resistivity. More specifically, in response to a large-scale azimuthal magnetic field B_y , a bath of magnetic fluctuations will produce an azimuthal electromotive force \mathcal{E}_y , proportional to $\partial_z B_y$. This \mathcal{E}_y causes the generation of a radial magnetic field, which in turn amplifies the azimuthal field through stretching by the mean flow (the Ω effect), resulting in a dynamo instability. The effect rests crucially on the sign of the proportionality between \mathcal{E}_y and $\partial_z B_y$ (termed η_{yx} throughout this thesis¹⁴) – if the product $\eta_{yx}(\nabla \times \mathbf{U})_z$ is negative, the induced radial field will act to damp, rather than amplify, the azimuthal field.

Why is this dynamo mechanism interesting? I would like to give two answers to this question: the first relates to the specific case of the MRI dynamo in accretion disks, the second more generally to dynamo theory.

The MRI dynamo The central regions of accretion disks are both unstratified and lack a source of net kinetic or magnetic helicity, implying that an α effect is not possible. In addition, a

¹⁴ This is simply a component of β_{ijk} . The reason for the difference in notation will be explained in chapter 4.

variety of authors have found from simulation and theory¹⁵ that the crucial η_{yx} is of the wrong sign for a kinematic nonhelical dynamo. What then is the cause of the apparent large-scale dynamo seen in simulations? While there is the possibility that it is driven by fluctuations in the α coefficients, I would argue that the magnetic shear-current effect is a more likely candidate: MRI simulations exhibit stronger magnetic than kinetic fluctuations, the velocity shear is obviously important, and the nonlinear behavior of the effect bears strong similarities to mean-field dynamics in unstratified MRI simulations. In addition, the basic importance of η_{yx} in the MRI dynamo has been concluded from nonlinear simulation (Lesur and Ogilvie, 2008b) and perturbative calculations of the evolution of MRI modes (Lesur and Ogilvie, 2008a). The suggestion in this thesis that small-scale magnetic fields are in fact the primary driver thus ties together formal mean-field dynamo theory with these studies and explains the special importance of strong magnetic fluctuations in MRI turbulence and dynamo.

General mean-field dynamo theory As discussed in Sec. 1.2, much of mean-field dynamo theory in recent years has focused on the issue of α -quenching. This is specifically related to the adverse influence of small-scale magnetic fields on large-scale dynamo action. Since small-scale dynamos grow faster than large-scale fields above moderate Reynolds numbers, large-scale dynamos may *always* have to grow on a bath of small-scale magnetic fluctuations (Cattaneo and Hughes 2009, but see also Tobias and Cattaneo 2014). With this in mind, the magnetic shear-current effect is the first suggestion (that I know of) for a large-scale dynamo driven by small-scale magnetic fluctuations.¹⁶ Thus, in some sense, the effect is the

¹⁵The subject has been somewhat controversial. Following initial studies that found η_{yx} had the correct sign for a dynamo (Urpin, 1999, 2002; Rogachevskii and Kleeorin, 2003, 2004; Rogachevskii *et al.*, 2006; Kleeorin and Rogachevskii, 2007), others found the opposite result, both analytically (Rädler and Stepanov, 2006; Rüdiger and Kitchatinov, 2006; Sridhar and Subramanian, 2009; Sridhar and Singh, 2010; Singh and Sridhar, 2011) and numerically (Brandenburg *et al.*, 2008a; Singh and Jingade, 2015), as well as finding growth rate scalings that were inconsistent with a coherent dynamo effect (Yousef *et al.*, 2008a,b).

¹⁶The magnetic α effect can certainly drive a mean field in isolation. The key point is that its sign is opposite to that of the kinetic effect, and the small-scale dynamo grows such that the two effects cancel. While it may be possible that instabilities (for instance, the MRI in the presence of stratification, Gressel 2010; Park and Blackman 2012) would

inverse of dynamo quenching; rather than magnetic fluctuations overwhelming a desirable kinematic effect, mean field growth starts after small-scale dynamo saturation, driven by the small-scale field itself. Of course, more work is needed to better assess regimes where the effect might be dominant, or even if it continues to operate at very high Reynolds numbers; nonetheless, it is an interesting possibility that may find application across a wide variety of astrophysical objects.

Having broadly outlined why the magnetic shear-current effect might be interesting, I now explain the evidence for existence, as presented in chapters 3–6. Proving the existence and importance of a dynamo instability is tricky: numerical simulations of turbulence are necessarily noisy, one is limited in available Reynolds numbers (and thus the ability to prove a dynamo will remain active at high values), and when large-scale field growth is observed it can be difficult to show convincingly that it is not some other (possibly unknown) mechanism that is responsible. These problems are exacerbated in the magnetically driven case. In particular, due to the finite size of any numerically realizable mean-field average, the mean field will quickly come into equipartition with the turbulent bath of fluctuations, robbing the researcher of the ability to study the dynamo during a long period of exponential growth. For these reasons, we have attempted to tackle the problem from a variety of different angles, including analytically with the second-order correlation approximation, through quasi-linear theory and statistical simulation, and using direct numerical simulations. We also introduce the novel technique of using an *ensemble* of simulations to study the statistics of the mean field without taking time averages. As is standard in dynamo theory, these studies have all considered the forced problem, in which the turbulence is driven by small-scale noise, rather than the self-sustaining turbulence more directly relevant to accretion disks. This allows a more systematic study of the dynamo for a number of reasons, including the ability to

cause a magnetic α effect to overwhelm the kinematic one, this remains unclear. In contrast, the magnetic shear-current effect has a fixed sign, arising from the nonhelical part of the fluctuations.

examine lower Reynolds numbers, an increased control over the levels of magnetic and kinetic fluctuations, and the ability to straightforwardly calculate transport coefficients in some cases.

The presentation of results on the magnetic shear-current effect is organized as follows. Chapter 4 studies mean field generation at low R_m , where the small-scale dynamo is not active. While such a regime is certainly less interesting (of course, we wish to examine mean field generation due to the saturated small-scale dynamo itself), it is very helpful to fully understand the low- R_m case before moving on to less controllable situations where the small-scale field arises self-consistently through small-scale dynamo. The primary difficulty in these low- R_m studies originates from the separation of coherent and incoherent dynamo mechanisms. Here, by “coherent” mechanism I simply refer to standard mean-field dynamos, as previously discussed. In contrast, an “incoherent” mechanism results from temporal fluctuations in the transport coefficients about zero, which must occur to some degree due to the finite domain size. The aforementioned quasi-linear and statistical simulations are very helpful in separating these effects; in statistical simulation only the coherent mechanism is possible, and a comparison with simulation of an individual realization allows for a direct probe of the incoherency of the dynamo. So far as we are aware, this thesis presents the first use of such statistical simulation techniques for the study of mean-field dynamo. I shall first present kinematic results, in particular examining the effects of rotation, which nicely explain some of the numerical scalings presented in Yousef *et al.* (2008a). Following this, the magnetic effect is analyzed, using direct numerical simulation (with forcing of the induction equation) and statistical calculations to illustrate the potency of magnetic fluctuations in driving a coherent nonhelical dynamo.

With the basic existence of the effect confirmed, chapter 5 examines the important question of whether the source of magnetic fluctuations can be the small-scale dynamo itself. With the aim of showing such an effect is possible, I present ensembles of 100 kinematically driven simulations in the shearing box at higher Reynolds numbers, such that the small-scale dynamo is unstable. This use of an ensemble of simulations to study the *statistics* of a large-scale dynamo is without

precedent in previous dynamo literature (to my knowledge), but proved crucial for accurate measurement of transport coefficients and qualitative understanding. After saturation of the small-scale magnetic field, relatively strong, large-scale fields are seen to develop in most realizations, with some qualitative similarities to the dynamos observed at lower R_m in chapter 4. The difficulty, of course, is to show that this dynamo arises through a coherent shear-current mechanism, and that it is not possible kinematically. We argue that this is indeed the case by measuring the mean-field transport coefficients both before and after the saturation of the small-scale dynamo, illustrating that the crucial η_{yx} component decreases. Further arguments for the coherency of the dynamo are given through solution of the mean-field equations using the measured coefficients. The methods used to determine the transport coefficients after saturation are somewhat novel, and their accuracy is verified (before discussion of the magnetic shear-current effect) through application to lower Reynolds number kinematic dynamos.

The final piece of evidence for the magnetic shear-current effect comes from the analytic studies presented in chapter 6. This chapter describes general calculations of the dynamo transport coefficients using the second-order correlation approximation, including the effects of rotation, velocity gradients, magnetic fluctuations, and density and turbulence stratification. The primary finding is that the velocity shear contribution to η_{yx} from magnetic fluctuations is generally larger than other contributions, and is always of the correct sign to promote mean-field dynamo. Rather than seeing this as good evidence in itself (the second-order correlation approximation is decidedly approximate), the result acts as a complement to previous studies, which have each found the same sign and a similar magnitude for the effect. These studies have used a variety of techniques, including the spectral τ -approximation (Rogachevskii and Kleeorin, 2004), shear quasi-linear theory (chapter 4), and inhomogeneous shearing wave calculations (Lesur and Ogilvie 2008a; this shows the same sign, but magnetic and velocity fluctuations are not separated). Such agreement is in stark contrast to the kinematic effect, where the sign disagrees between the τ approximation (Rogachevskii and Kleeorin 2003; dynamo), the second-order correlation approximation (Rädler and

Stepanov 2006; Rüdiger and Kitchatinov 2006; no dynamo), shear quasi-linear theory (Singh and Sridhar 2011; no dynamo), and other quasi-linear theories (Urpin 2002; dynamo). This disagreement may be related to a change in sign with Reynolds number (Brandenburg *et al.*, 2008a), but this remains unclear. In any case, the hope is that the agreement between calculation methods for the magnetic effect speaks to a greater robustness in its sign and magnitude in comparison to its kinematic cousin.

Finally, it is worth mentioning the relationship of chapter 3 to the studies in the subsequent chapters outlined above. This chapter serves as motivation for study of the magnetic shear-current effect, as an introduction to the statistical and quasi-linear methods, and as a study of the dynamo instability specifically in the context of MRI turbulence. Using novel statistical simulation techniques – one solves for the *statistics*, rather than an individual realization of turbulence – the chapter’s primary results are that MRI turbulence (or the quasi-linear approximation thereof) is unstable to mean-field dynamo, and that the saturation characteristics of this dynamo bear a strong resemblance to MRI turbulence. This is somewhat surprising given the rather drastic approximations made in deriving the statistical evolution equations. Most interesting is the strong increase in the saturated turbulence level with $P_m = R_m/Re$, which is counter to naive expectations but pervasive in nonlinear simulation of MRI turbulence. Importantly, incoherent dynamos are impossible within statistical simulation, thus the mere existence of the dynamo motivates study of the magnetic shear-current effect (since the kinematic effect is too weak). More subtly, by combining the conclusions that the observed dynamo is necessarily driven by a coherent effect, with the resemblance of the saturated state to nonlinear MRI turbulence, we find compelling evidence that the mechanism for the unstratified MRI dynamo is indeed the magnetic shear-current effect.

1.3.2 Linear MRI and nonmodal growth

Our exploration of magnetorotational turbulence started with consideration of the linear system. Specifically, we wished to interpret the relationship between the global system and the shearing box, with the goal of understanding what was missing from local models and whether better alternatives might exist. These investigations led to the idea that nonmodal (or transient) linear physics is important for the MRI, despite the existence of unstable eigenmodes in many cases, and in turn the notion that linear physics could be an important driver of MRI turbulence across a wide range of wavenumbers. This turbulence drive is not predicated on the idea that eigenmodes are spectrally unstable, but rather that non-eigenmode structures may be important due to their transient growth over shorter timescales. Such ideas proved foundational for interpretation of results in subsequent work on quasi-linear turbulence and dynamo (described above). In addition, nonmodal linear theory provides a natural and intuitive connection between global linear modes and the shearing box (thus fulfilling the original aim), suggesting that, from the linear standpoint, one can expect the shearing box to capture the fundamental physics of both the axisymmetric and non-axisymmetric MRI.

Nonmodal stability theory, discussed in detail in chapter 2, studies the linear stability of systems over finite timescales. The theory is based around the basic question, what set of initial conditions will be most amplified by time t ? In the case of a system with a self-adjoint operator,¹⁷ the answer is simply the least-stable eigenmode. But, if this is not the case (as occurs more often than not), a variety of other physically meaningful structures can emerge, often with growth rates and physical characteristics far removed from the eigenmodes. Most dramatic is when a system is spectrally stable, but non-eigenmode structures can grow transiently, sometimes by many orders of magnitude. If initializing from random initial conditions, these structures can emerge out of the

¹⁷ One must specify a norm. This should be chosen as being a physically motivated measure of the size of a solution; see chapter 2 for more information.

random bath, thus becoming at least as physically meaningful as the eigenmodes even though they must eventually decay.

The primary result presented in chapter 2 is that such nonmodal growth is almost always important for the MRI, especially for non-axisymmetric modes. The structures that emerge invariably resemble *shearing waves* – time-dependent waves entrained in the background flow – in both local and global domains, independently of the imposed boundary conditions. This illustrates that, even in global domains, local stability results will most often be *more relevant* than unstable global eigenmodes for non-axisymmetric MRI modes, since the nonmodal structures can grow many orders of magnitude before the eigenmode eventually takes over. This in turn justifies the use of the shearing box (from the linear standpoint), since shearing waves are naturally compatible with shearing box boundary conditions. In addition, the nonmodal viewpoint cleanly illustrates the relationship between previous studies of global eigenmodes (which have strong dependence on boundaries, see for example, Curry and Pudritz 1996; Ogilvie and Pringle 1996) and studies of time-dependent shearing waves (e.g., Balbus and Hawley 1992; Johnson 2007), for both axisymmetric and non-axisymmetric modes.

The persistent emergence of shearing waves from spatially dependent nonmodal calculations justifies the insertion of this ansatz into the MHD equations to obtain a set of ordinary differential equations for a given wavenumber $(k_x(0), k_y, k_z)$ – the “shearing wave equations” (Balbus and Hawley, 1992). Noting that these fundamentally arise from nonmodal physics, it is helpful to again apply the nonmodal toolbox, with the view that transient growth is possible due to the system’s non self-adjointness rather than the time dependence of the shearing wave ODEs. Simple analytic calculations show that over short timescales, modes of all wavenumbers (k_y, k_z) can grow at the same rate, that of the least stable MRI mode ($\gamma = q/2$, see Sec. 1.1.2). This result, which is very different from eigenmode growth rates, suggests that turbulence could be fed through such linear growth over a wide range of scales and mode numbers, with the spectrally unstable MRI modes perhaps not so much more important than transiently growing non-axisymmetric modes. With this

in mind, I present a simple illustration of how a change in the choice of timescale affects the relative dominance of different modes, illustrating reasonable agreement with trends observed in nonlinear turbulence with changing vertical field (Longaretti and Lesur, 2010). Such compatibility between linear and nonlinear trends, which is contrary to some previous claims, motivated the exploration of a more complete statistical quasi-linear theory for the MRI dynamo, as studied in chapter 3.

1.3.3 Outline

Following this introduction, the five research chapters are organized as discussed above. Chapter 2 examines linear nonmodal theory for the MRI, which then motivates the statistical study of turbulence introduced in chapter 3. The finding that a strong coherent MRI dynamo is excited leads to the study of its linear phase in chapters 4–6, which focus on magnetic shear-current effect in the low- R_m regime (chapter 4), its excitation through small-scale dynamo (chapter 5), and its analytic study with the second-order correlation approximation (chapter 6). Each chapter has its own introduction and discussion section to reiterate the primary results and conclusions. In addition, most chapters are accompanied by an appendix, which present subsidiary results and derivations. In App. E, I include a description of the symbolic vector calculus *Mathematica* package *VEST* (Squire *et al.*, 2014), which has been used extensively for the calculations in chapter 6.

Chapter 2

Nonmodal stability of the MRI and the relationship between local and global modes

This chapter focuses on the linear behavior of the MRI, utilizing *nonmodal stability theory* to examine this well-studied subject from a somewhat different standpoint. While linear results obviously cannot be applied directly to study MRI turbulence, several of these results are suggestive that linear dynamics might play a fundamental role in the nonlinear dynamics, motivating models and techniques used throughout the remainder of the thesis. The work presented here has been published in Squire and Bhattacharjee (2014a,b).

2.1 Introduction

The linear behavior of the MRI has been extensively studied over the past 20 years. With the basic character of the axisymmetric MRI in a vertical field well established (Balbus and Hawley, 1991), these studies have both considered how more complex physical effects might change MRI growth (e.g., Kersalé *et al.* 2004; Pessah and Psaltis 2005; Hollerbach and Rüdiger 2005), and studied the variety of other MRI modes (e.g., Balbus and Hawley 1992; Curry and Pudritz 1996; Terquem and

Papaloizou 1996). Since the basic axisymmetric MRI mode is so virulent, the motivation behind the latter class of studies is that linear results might tell us something useful about the nonlinear turbulence, and a number of nonlinear scenarios have been advanced in this regard (Goodman and Xu, 1994; Lesur and Ogilvie, 2008b; Latter *et al.*, 2009; Pessah and Goodman, 2009; Kitchatinov and Rüdiger, 2010). Despite their lower growth rates, the influence of non-axisymmetric modes is very important for such theories, since Cowling's anti-dynamo theorem precludes the possibility of sustained turbulence in an axisymmetric system (Balbus and Hawley, 1998). Whether linear ideas can be useful in explaining the more complex aspects of MRI turbulence remains to be seen. While some studies have discounted the importance of linear eigenmodes in fully developed turbulence (Longaretti and Lesur, 2010), there have also been hints that linear shearing waves¹ may have substantial dynamical importance (Lesur and Ogilvie, 2008a; Heinemann *et al.*, 2011), in particular in relation to the MRI dynamo (Rincon *et al.*, 2007; Riols *et al.*, 2013).

The study of linear stability is often synonymous with the study of eigenmodes, those perturbations that grow, oscillate or decay in an exponential manner with no change in their structure over time. The motivation behind this is that over long time periods, the least stable eigenmode will emerge from general initial conditions and thus be important for any subsequent development of the system (particularly if it is unstable). However, there are many linear systems, in particular those that are not self-adjoint, that can exhibit growth that is substantially faster than that predicted by eigenvalues over intermediate timescales. This is the concept behind *nonmodal* stability theory (Trefethen and Embree, 2005), which studies the maximum possible growth (under a chosen norm) of *any* initial perturbation over a given time frame. Why might such information be useful? The most obvious reason is that even in a spectrally stable system, nonmodal effects can sometimes lead to sufficient linear growth for nonlinearities of the system to become important. This can be profoundly relevant, explaining for instance the transition to turbulence in pipe flow at relatively

¹These are linear waves that shear with the background flow, also known as Kelvin waves or spatial Fourier harmonics.

moderate Reynolds numbers, despite the lack of unstable eigenmodes (Schmid, 2007). Aside from this, there are other somewhat more subtle reasons nonmodal growth may be significant. For instance, in attempting to understand the transition from a linear regime to one where nonlinear effects are important, one may wish to anticipate the relative significance of different mode numbers. Depending on the important timescales, estimates based on eigenmode growth rates may be incorrect. Such considerations will be especially important in any linear or quasi-linear interpretation of turbulence characteristics (Farrell and Ioannou, 1994), since with strong fluctuations, growth rates over short times are almost certain to be more relevant than the $t \rightarrow \infty$ limit explored by eigenmode analyses (Friedman and Carter, 2014).

Despite the spectral instability of the MRI, this is a fruitful and natural approach, in particular illustrating that simple local shearing wave approaches (Balbus and Hawley, 1992) often have greater relevance to global models than the global eigenmodes. While the general applicability of local approximations has been noted in previous works (Terquem and Papaloizou, 1996; Papaloizou and Terquem, 1997), so far as I am aware, this work is the first to explicitly explain the connection between global and local approaches for general modes. In addition to the qualitative connection that is evident upon observing the spatial structures that appear in non-axisymmetric nonmodal calculations (e.g., Figs. 2.3 and 2.5), there is very good quantitative agreement, as evidenced by comparison of global calculations to solutions of the shearing wave equations. This connection illustrates that nonmodal techniques are also particularly natural for analysis of the shearing wave equations themselves; such methods are straightforward and easy to interpret, and are useful in considering turbulence from a quasi-linear perspective. We shall see that an appropriate choice of timescale is of enormous importance in the consideration of MRI growth rates, changing the relative importance of different modes and how this varies with parameters (e.g., background magnetic field).

Given the large number of studies of the local and global linear MRI, as well as many works on the nonmodal stability of hydrodynamic disks (e.g., Ioannou and Kakouris 2001; Yecko 2004;

Mukhopadhyay *et al.* 2005; Tevzadze *et al.* 2008; Zhuravlev and Razdoburdin 2014), it is somewhat surprising that the MRI has not been previously investigated using formal nonmodal techniques. Most studies using global domains have focused on eigenmodes for both axisymmetric (e.g., Curry *et al.* 1994; Kersalé *et al.* 2004; Mahajan and Krishan 2008) and more general non-axisymmetric (e.g., Curry and Pudritz 1996; Ogilvie and Pringle 1996; Bonanno and Urpin 2008; Goedbloed *et al.* 2010; Rüdiger *et al.* 2013) modes, usually solving for eigenmodes directly using a suitable numerical discretization. In contrast, there have also been a number of local studies (e.g., Balbus and Hawley 1992; Johnson 2007; Salhi *et al.* 2012; Mamatsashvili *et al.* 2013) that have approached the stability problem by considering the shearing wave equations. These equations certainly exhibit nonmodal growth, although this is often attributed to the explicit time dependence in the shearing wave equations, rather than an inherent property of the original local MHD model. The approach here bridges the two aforementioned methods. We shall solve the full equations on the global domain numerically, focusing on the nonmodal structures rather than the eigenmodes of the system. Since these structures resemble shearing waves, this gives an obvious justification for the use of the shearing wave equations and illustrates that they are *more relevant* than the global eigenmodes in many situations. In addition, this interpretation implies that the shearing wave equations, including the time-independent axisymmetric case, are most naturally studied using nonmodal techniques also. I give simple analytic explanation of these ideas in Sec. 2.5, where a comparison of the short-time growth rates of shearing and static structures illustrates why nonmodal structures should always resemble shearing waves.

2.1.1 A simple motivational example

To introduce ideas used in the remainder of this chapter, here I give a very simple example showing the physical origins of nonmodal growth of the simplest axisymmetric MRI. While the general idea (which is nothing but the standard Ω effect) has been discussed in previous works in a somewhat

different context (see, for example, Rincon *et al.* 2007, 2008), its presentation as a linear instability provides a useful starting point for the examination of more complicated non-axisymmetric situations later in the chapter.

Consider a magnetohydrodynamic system with a background linear shear flow and impose an initial perturbation to the magnetic field (the lack of a velocity perturbation renders the presence of a background magnetic field irrelevant). For perturbations that depend on only the vertical coordinate as $\mathbf{B}(z, t) = \mathbf{B} \exp(ik_z z)$, the induction equation,

$$\frac{\partial \mathbf{B}}{\partial t} = \nabla \times (\mathbf{U} \times \mathbf{B}) + \bar{\eta} \nabla^2 \mathbf{B}, \quad (2.1)$$

with $\mathbf{U} = (0, -qx, 0)$ becomes

$$\frac{\partial}{\partial t} \begin{pmatrix} B_x \\ B_y \end{pmatrix} = \begin{pmatrix} -\bar{\eta}k_z^2 & 0 \\ -q & -\bar{\eta}k_z^2 \end{pmatrix} \begin{pmatrix} B_x \\ B_y \end{pmatrix}. \quad (2.2)$$

This system is perhaps the simplest paradigmatic example in nonmodal stability theory, appearing in many introductory treatments due to its tendency to exhibit strong transient growth at small $\bar{\eta}k_z^2$ (Trefethen and Embree, 2005). More precisely, although the eigenvalues of the system ($-\bar{\eta}k_z^2$ repeated) indicate it is stable, in the limit $\bar{\eta}k_z^2 \rightarrow 0$ the system can grow many orders of magnitude before eventually decaying exponentially, as illustrated in Figure 2.1. Indeed, with $\bar{\eta}k_z^2 = 0$ the solution, $B_x(t) = B_x(0)$, $B_y(t) = B_y(0) - qtB_x(0)$, can grow indefinitely, the physical mechanism being simple advection of the initial perturbation by the shear (Ω effect). Of course, over long timescales this algebraic growth is dwarfed by the standard MRI (if there is a vertical background field), which can grow as $|B(t)|^2 \sim \exp(qt)$ in these units. Nonetheless, it is interesting to note that with the initial conditions $B_x(0) = -B_y(0)$ the magnetic energy growth $\partial_t \ln(B_x^2 + B_y^2)$ for Eq. (2.2) at $t = 0$ is q , the same as for the standard MRI. This result – over short timescales the

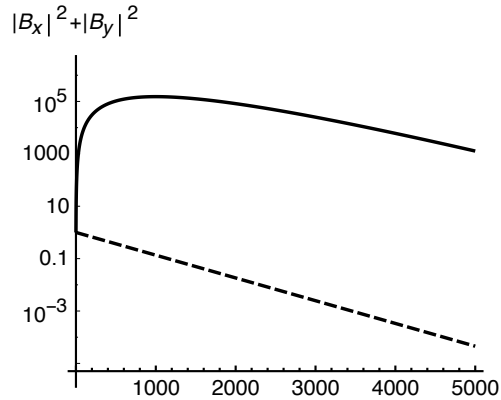


Figure 2.1: Evolution of the magnetic energy for the system Eq. (2.2) at $\bar{\eta}k_z^2 = 10^{-3}$, $q = 3/2$, comparing the solution with initial condition $B_x(0) = -B_y(0)$ (solid) and the eigenmode (dashed). Even at this somewhat modest value of $\bar{\eta}k_z^2$ the magnetic energy can grow by a factor of more than 10^5 before eventually decaying exponentially.

MRI energy growth rate is q – holds for all axisymmetric and non-axisymmetric MRI modes given an appropriate choice of initial conditions.

What is the significance of this transient growth if such perturbations eventually decay? In the case of perturbations on top of a quiescent (non-turbulent) disk, one could imagine that some nonlinear effect might become important as the azimuthal magnetic field increased in magnitude, particularly since such a field would have the radial and vertical structure of the initial perturbation if dissipation were sufficiently low. However, the question of what nonlinear mechanisms might be at work to allow for the sustenance of a turbulent state are subtle and very difficult to answer conclusively (Rincon *et al.*, 2008; Riols *et al.*, 2013, 2015) and we do not speculate on such ideas in this work. Another, less obvious, situation where the shorter time behavior of such perturbations may be of interest is if the plasma is already turbulent. If we neglect the issue of why the turbulence is sustaining in the first place, it is of note that this very simple nonmodal growth mechanism could be injecting energy into the turbulence at a rate similar to the most unstable MRI modes, since both have the same growth rate over short times. To explore these ideas more rigorously, in chapter 3 I examine the interaction of the linear MRI system with space- and time- dependent mean fields in a self-consistent quasi-linear theory (Farrell and Ioannou, 2003). The nonmodal

growth of the MRI is critical in this endeavor, and a more traditional analytic quasi-linear approach (see, for example, Sagdeev and Galeev 1969) based on eigenmode growth rates would be quite unsuitable for this problem. Finally, note that simple applications of linear nonmodal ideas to wall-bounded hydrodynamic flows (using parameterized versions of the turbulence induced viscosity) have shown that the fastest growing structures are remarkably similar to many of the large-scale structures observed in full nonlinear turbulence simulations (Butler and Farrell, 1993; Cossu *et al.*, 2008).

2.1.2 Outline

Rather than examining a particular case in detail, I have structured the chapter to survey several different ways that nonmodal methods can be useful for the analysis of the MRI. This choice was made because the techniques are useful in understanding both global (i.e., r -dependent) and simplified local versions of the MRI, as well as the connection between them. After describing the fundamentals of nonmodal stability theory and detailing the models used (Secs. 2.2 and 2.3 respectively), I give a basic explanation of the relationship between MRI eigenmodes and nonmodal structures in Sec. 2.4. This is done for non-axisymmetric modes in both local and global models with hard-wall boundary conditions, to illustrate the origins and fundamental importance of structures that shear with the background flow (shear waves). With such ubiquitous appearance of shearing wave structures, it is nice to explore in more detail why this should be the case and in Sec. 2.5 I prove within a WKB-like approximation that shearing waves grow faster than eigenmodes over short timescales. This is followed by a discussion of shearing wave equations in more general settings, including other global effects not usually captured by the local approximation. I then illustrate the utility of the local model in Sec. 2.6 by directly comparing global nonmodal structures to the shearing wave equations (see Sec. 2.3.2). This relationship between the global and local pictures implies that the shearing wave equations should themselves be interpreted from

the nonmodal standpoint and this is the purpose of Sec. 2.7. I illustrate how such an interpretation of the equations can be fruitful by showing that nonmodal linear predictions qualitatively match aspects of MRI turbulence (Longaretti and Lesur, 2010), in stark contrast to the eigenmodes.

2.2 Nonmodal stability methods

The general idea of nonmodal stability methods is to compute the maximum possible linear amplification of disturbances under some chosen norm at finite times. If the system is self-adjoint, the choice of the time is unimportant, since the most strongly amplified perturbation is always the most unstable eigenmode, with the growth rate given by its corresponding eigenvalue. If the system is not self-adjoint, the non-orthogonality of the eigenmodes allows for the possibility of *transient growth*, where the perturbations can grow substantially faster than the most unstable eigenmode over intermediate timescales (Trefethen and Embree, 2005; Schmid, 2007). This effect is most commonly studied in spectrally stable systems, since the consequences of transient growth can be especially profound in this case.

Here I give a brief overview of the methods used to calculate nonmodal growth, introducing some notation and important concepts. Unlike standard treatments, I shall allow for time dependence of the operator and norm (Farrell and Ioannou, 1996), which is necessary for application to the shearing wave equations. Note that the nonmodal approach encompasses standard normal mode analysis as a special case. Indeed, in the $t \rightarrow \infty$ limit, the fastest growing structures necessarily become the least stable eigenmodes, growing or decaying at the rate dictated by the corresponding eigenvalues.² More information and references to applications in many areas of physics

²This is of course not true if a spatial form of the disturbance is specified *before* carrying out the nonmodal analysis, as is the case for the shearing wave equations Eq. (2.22). Insertion of an ansatz in this way restricts analysis to the nonmodal growth of disturbances of the chosen form. If this chosen spatial structure is never observed in the full spatially dependent calculation, such a computation will be meaningless.

and engineering can be found in Trefethen and Embree (2005), Schmid (2007), and Camporeale (2012).

For the sake of clarity, consider the general linear system,

$$\frac{\partial U}{\partial t} = \mathcal{L}(t)U(t). \quad (2.3)$$

This system can either represent a set of spatially discretized partial differential equations (PDEs) [e.g., Eq. (2.20)], or a set of ordinary differential equations (ODEs) [e.g., Eq. (2.22)]. Eq. (2.3) has the solution $U(t) = K(t)U(0)$, where $K(t)$ is the propagator, and in the case that \mathcal{L} is time-independent $K(t) = \exp(\mathcal{L}t)$. The maximum possible amplification of the energy of U by time t is given by

$$G(t) = \max_{U(0)} \frac{\|K(t)U(0)\|_E^2}{\|U(0)\|_E^2}, \quad (2.4)$$

where $\|\cdot\|_E^2$ denotes the energy norm, which is calculated using $\|U\|_E^2 = U^\dagger \cdot M_E(t) \cdot U$ for the energy matrix $M_E(t)$ [see Eq. (2.10) below]. With a change from the energy norm to the standard 2-norm ($\|\cdot\|_2^2$) using the Cholesky decomposition

$$\|U\|_E^2 = U^\dagger \cdot M_E(t) \cdot U = U^\dagger \cdot F^\dagger(t)F(t) \cdot U = \|F(t)U\|_2^2, \quad (2.5)$$

Eq. (2.4) can be calculated as the largest singular value of the matrix

$$F(t)K(t)F^{-1}(0). \quad (2.6)$$

The initial conditions that achieve this growth are given by $F^{-1}(0)\kappa$, where κ is the right singular vector corresponding to the largest singular value. I have allowed for time dependence of the inner product since this is necessary for shearing waves in the variable choice [Eqs. (2.17) and (2.19) below]. Note that if \mathcal{L} represents the discretization of a spatially continuous operator, the matrices

$M_E(t)$ and its Cholesky decomposition $F(t)$ must be calculated using the basis functions chosen for the discretization.

For some of the analytic results presented in this chapter, we compute the growth rate at $t = 0^+$,

$$G_{\max}^+ = \max_{U(0)} \left\| U(t) \right\|_E^{-2} \frac{d}{dt} \left\| U(t) \right\|_E^2 \Big|_{t=0^+}. \quad (2.7)$$

This may be considered as a simple approximation to the maximum growth rate of structures over short times (although the definition of “short times” will depend on the problem in question). Note that for a self-adjoint system G_{\max}^+ is simply (twice) the most unstable eigenvalue growth. Differentiating $K(t)$ and changing to the 2-norm, one obtains the result

$$G_{\max}^+ = \lambda_{\max}(\Lambda + \Lambda^\dagger), \quad (2.8)$$

where $\Lambda = F\mathcal{L}F^{-1} + \partial_t F F^{-1}|_{t=0}$, and $\lambda_{\max}(A)$ denotes the largest eigenvalue of the matrix A .

Computationally, the most challenging step in the above procedures is the calculation of the propagator $K(t)$. For time-independent systems [i.e., spatial discretizations of Eqs. (2.20) and (A.1)] this is most easily calculated through the eigenspectrum by noting that in the eigenmode basis

$$K(t) = \exp(\mathcal{L}t) = \exp(\Lambda t), \quad (2.9)$$

where Λ is the diagonal matrix of eigenvalues. The Chebyshev-Tau method is used to calculate the spectrum, since this generally has very good numerical properties for fluid eigenvalue problems (Dongarra *et al.*, 1996). After truncating the spectrum to the top \mathcal{K} most unstable modes and removing spurious eigenvalues, one computes the inner product matrix $M_E(t)$ in the Chebyshev spectral basis (Reddy *et al.*, 1993) to allow application of the singular value decomposition [see Eq. (2.4)]. The number of modes \mathcal{K} should be chosen such that the results are unchanged if this is increased; usually $\mathcal{K} \approx 120$ is sufficient. The calculation of the spectrum can be rather com-

putationally challenging due to numerical errors caused by round off in the Chebyshev matrices, a problem that is exacerbated as the number of polynomials is increased (Dongarra *et al.*, 1996). Because of this I have generally restricted Reynolds numbers to less than $\sim 10^4$, ensuring that the smallest scales in the solution can be well represented by the chosen number of modes. In addition, results can be very sensitive to errors in the Cholesky decomposition used to calculate F (especially for high \mathcal{K}) and use high-precision arithmetic for this part of the calculation. I have scrutinized the numerical quality of the eigenmodes and nonmodal results using several separate methods: comparison to previous hydrodynamic results (Yecko, 2004; Mukhopadhyay *et al.*, 2005), comparison with a finite difference eigenmode solver, and regular checks that pseudo-modes were insensitive to an increase in \mathcal{K} and the number of Chebyshev modes used for the eigenvalue solver. The above process is implemented numerically using *Mathematica*. This has the advantage of allowing the derivation of the equations to be seamlessly integrated into the eigenvalue solver³ and nonmodal machinery, reducing the chances of mistakes and enabling very straightforward changes for the study of other problems.

In the case that \mathcal{L} is time dependent [i.e., the shearing wave equations, Eq. (2.22)] $K(t)$ cannot be calculated using the eigen-decomposition, since $K(t) \neq \exp(\mathcal{L}t)$. If we consider the discrete system $\partial_t U_i(t) = \sum_{j=1}^N \mathcal{L}_{ij} U_j(t)$ (where N is the dimension of the system), a simple way to calculate $K(t)$ is to evolve the system for each initial condition $\{U_n(0) = 1, U_i(0) = 0 \text{ for } i \neq n\}$, for all $n = 1 \rightarrow N$. For the shearing wave equations [Eq. (2.22)] $N = 4$, so it is computationally straightforward to calculate the propagator using this technique. While the method can in principle be used for nonmodal calculations of space- and time-dependent systems (with a suitable spatial discretization), computation of $K(t)$ can become prohibitively expensive and more sophisticated variational techniques have been developed (Schmid, 2007; Zhuravlev and Razdoburdin, 2014).

³ The eigenvalue solver `EigenNDSolve`, is implemented in a way similar to *Mathematica*'s native `NDSolve` function. One simply specifies symbolic equations and boundary conditions and identifies the eigenvalue parameter; the function handles all numerical details.

Throughout this work I use the total energy of the perturbation as the norm,

$$E = \int d\mathbf{x} (|\mathbf{u}|^2 + |\mathbf{B}|^2), \quad (2.10)$$

since it has been the standard choice for hydrodynamic studies (Reddy *et al.*, 1993). Of course, due to the background velocity, this norm does not represent the full (background plus perturbation) energy, and other choices can be well justified. Thus, I prefer to consider the norm Eq. (2.10) to be a useful measure of the size of a disturbance, rather than a physical energy. I relegate an investigation of the effects of changing norms to future work (see Zhuravlev and Razdoburdin 2014 for a more thorough discussion of this issue for hydrodynamic disks, including the effects of using a different norm).

For ease of presentation, I denote the linear solution that maximizes the energy at time t_0 , evaluated at time t as $\Gamma(t, t_0)$ and call this the *pseudo-mode*. I shall represent the norm of the pseudo-mode, $\|\Gamma(t, t_0)\|_E^2$, as $G_\Gamma(t, t_0)$. Thus $G(t)$, the maximum possible growth of any initial conditions by time t [see Eq. (2.4)], is given by $G(t) = G_\Gamma(t, t)$, and $G_\Gamma(t, t_0) < G(t) \forall t \neq t_0$.

2.3 Equations and physical models

In order to present ideas in a clear and concise manner, models are chosen to be as simple as possible while retaining the features necessary to illustrate the importance of nonmodal growth. In particular, I neglect compressibility, vertical stratification, radial density stratification and vertical gravity in both local and global calculations, and consider a rather restricted set of global field profiles for illustrative purposes. While there are many physical effects excluded by such simplifications (*e.g.*, magnetic buoyancy, density waves), the results are not intended to provide an accurate description of a real accretion disk. Very similar conclusions about the importance of transient effects would almost certainly hold in a more general model. In any case, many previous

studies (e.g., Pessah and Psaltis 2005; Rosin and Mestel 2012; Mamatsashvili *et al.* 2013) have shown that MRI growth is generally weakly affected by the introduction of more complex physical models, probably because the MRI itself is so virulent an instability.

2.3.1 Global model

The starting point is the incompressible, resistive magnetohydrodynamic (MHD) model,

$$\frac{\partial \mathbf{u}}{\partial t} + (\mathbf{u} \cdot \nabla) \mathbf{u} = -\nabla p + \nabla \times \mathbf{B} \times \mathbf{B} - \nabla \Phi + \bar{\nu} \nabla^2 \mathbf{u}, \quad (2.11a)$$

$$\frac{\partial \mathbf{B}}{\partial t} + (\mathbf{u} \cdot \nabla) \mathbf{B} = (\mathbf{B} \cdot \nabla) \mathbf{u} + \bar{\eta} \nabla^2 \mathbf{B}, \quad (2.11b)$$

$$\nabla \cdot \mathbf{u} = 0, \quad \nabla \cdot \mathbf{B} = 0, \quad (2.11c)$$

which is the incompressible version of the MHD disk equations given in Eq. (1.1). In Eq. (2.11), as for the remainder of the thesis, we use dimensionless variables; $\mathbf{u} = \mathbf{u}_{si}/u_0$, $\mathbf{B} = \mathbf{B}_{si}/(u_0\sqrt{\mu_0\rho_0})$, $p = p_{si}/(u_0^2\rho_0)$, $\Phi = \Phi_{si}/(u_0^2\rho_0)$, where \mathbf{u}_{si} , \mathbf{B}_{si} , p_{si} , Φ_{si} are respectively the fluid velocity, magnetic field, pressure, and gravitational potential in SI units, and u_0 , ρ_0 , and μ_0 are a characteristic velocity, the density (considered constant for simplicity), and the vacuum permeability. Lengths have been scaled by characteristic scale L_0 in Eq. (2.11), and time is scaled by L_0/u_0 . The fluid and magnetic diffusivities, $\bar{\nu}$ and $\bar{\eta}$, are defined as $\bar{\nu} = \nu/(u_0L_0)$, $\bar{\eta} = \eta/(u_0L_0)$, where ν and η are the kinematic viscosity and resistivity of the plasma. Since most parameters in our problem are of order one, $\bar{\nu}$ and $\bar{\eta}$ are approximately the inverses of the fluid and magnetic Reynolds numbers respectively. Because Eq. (2.11) is incompressible and lacks radial density stratification, the model is better suited for study of liquid metal laboratory experiments than a real accretion disk.

For all global calculations, I consider a simplified version of the equilibrium in cylindrical coordinates proposed by Kersalé *et al.* (2004). This model includes a very small radial inflow

velocity,

$$U_r = \alpha/r, \quad (2.12)$$

driven by the viscosity acting on the azimuthal component of the velocity,

$$U_\theta = U_0 r^{1+\alpha/\bar{\nu}}. \quad (2.13)$$

I take α to be $-3/2\bar{\nu}$ to give a Keplerian rotation profile and set $U_0 = 1$ in keeping with our normalization. For simplicity, I use the magnetic field

$$\mathbf{B}_0 = (0, rB_{0\theta}, B_{0z}), \quad (2.14)$$

with $B_{0\theta}$, B_{0z} constant. The pressure is determined through the equilibrium equation, and $\Phi = -1/r$. Note that the equilibrium is determined by only four free parameters $B_{0\theta}$, B_{0z} , $\bar{\nu}$ and $\bar{\eta}$. For all calculations presented here, I use the domain $(0.25, 2.25)$ in r . While details are not given here, I have also carried out calculations with more general profiles; the results seem to be quite similar.

The global linear equations are obtained by linearizing Eqs. (2.11) about the background profile; i.e., substituting

$$\begin{aligned} \mathbf{u} &= \mathbf{u}_0 + \mathbf{u}', & \mathbf{B} &= \mathbf{B}_0 + \mathbf{B}', \\ p &= p_0 + p', \end{aligned} \quad (2.15)$$

and inserting the ansatz

$$f(r, \theta, z, t) = f(r, t) e^{im\theta + ik_z z}, \quad (2.16)$$

for each of the variables \mathbf{u}' , \mathbf{B}' , p' . Finally, one rewrites the equations in terms of the Orr-Sommerfeld like variables,

$$\begin{aligned} u_r &= u'_r, & B_r &= B'_r, \\ \zeta &= ik_z u'_\theta - i\frac{m}{r} u'_z, & \eta &= ik_z B'_\theta - i\frac{m}{r} B'_z, \end{aligned} \quad (2.17)$$

and rearranges the equations to eliminate as many derivatives as possible. This choice of variables eliminates the pressure and reduces the eight equations to four, at the cost of causing fourth-order derivatives of u_r to appear in the equations. Because of the length of the equations resulting from this variable choice, I present them in Appendix A.1.

2.3.2 Local model

I utilize the incompressible shearing-box (SB) equations [Eq. (1.14)] for the local studies presented here, as discussed in Sec. 1.1.3. Again, since most parameters in the problem are of order one, $\bar{\nu}$ and $\bar{\eta}$ are approximately the inverses of the fluid and magnetic Reynolds numbers respectively. The background velocity is azimuthal with linear shear in the radial direction, $\mathbf{U}_0 = -q\Omega x$ and the background magnetic field is taken to be constant, $\mathbf{B}_0 = (0, B_{0y}, B_{0z})$. As for the global case one linearizes the equations about the background, $\mathbf{u} = \mathbf{u}_0 + \mathbf{u}'$, $\mathbf{B} = \mathbf{B}_0 + \mathbf{B}'$, $p = p_0 + p'$, and Fourier analyzes in y and z through insertion of

$$f(x, y, z, t) = f(x, t) e^{ik_y y + ik_z z} \quad (2.18)$$

for each dependent variable. Changing into the variables,

$$\begin{aligned} u &= u'_x, \quad B = B'_x, \\ \zeta &= ik_z u'_y - ik_y u'_z, \quad \eta = ik_z B'_y - ik_y B'_z, \end{aligned} \quad (2.19)$$

which have the advantage of eliminating the pressure, and simplifying, one obtains the four linear partial differential equations in x and t ,

$$\begin{aligned} \frac{\partial}{\partial t} \begin{pmatrix} \nabla^2 u \\ \zeta \\ B \\ \eta \end{pmatrix} \\ = \begin{pmatrix} \bar{\nu} \nabla^4 + iqxk_y \nabla^2 & 2ik_z & iF \nabla^2 & 0 \\ i(q-2)k_z & \bar{\nu} \nabla^2 + iqxk_y & 0 & iF \\ iF & 0 & \bar{\eta} \nabla^2 + iqxk_y & 0 \\ 0 & iF & ik_z & \bar{\eta} \nabla^2 + iqxk_y \end{pmatrix} \cdot \begin{pmatrix} u \\ \zeta \\ B \\ \eta \end{pmatrix}, \end{aligned} \quad (2.20)$$

where $F \equiv k_y B_{0y} + k_z B_{0z}$ and $\nabla^2 \equiv -k_y^2 - k_z^2 + \partial^2/\partial x^2$. Since these equations have no time dependence they can be Fourier analyzed in time using $\partial/\partial t \rightarrow -i\omega$ to obtain a set of linear eigenvalue ODEs; however, since much of this work focuses on nonmodal stability methods, I prefer to keep the time dependence general even though they have been solved computationally from the eigenvalue standpoint (see Sec. 2.2).

Shearing wave equations A common way to study the local non-axisymmetric linear MRI has been using a decomposition in terms of *shearing waves*. Shearing waves are simply sinusoidal waves that are static in the frame of the background flow (they have also been termed spatial

Fourier harmonics or Kelvin waves by various authors). As part of this work, I shall compare the solutions obtained from assuming such a decomposition with global nonmodal stability calculations, showing excellent agreement.

The shearing wave equations are straightforwardly derived by inserting the ansatz

$$f(x, t) = f(t)e^{iqk_y(t-t_{SW})x}, \quad (2.21)$$

for each dependent variable in Eqs. (2.20), where the initial orientation of the wave is determined by the parameter t_{SW} through $k_x(0) = -qk_y(0 - t_{SW})$. This yields the set of ordinary differential equations in time,

$$\frac{\partial}{\partial t}U(t) = \begin{pmatrix} -\bar{\nu}k^2 - 2qk_xk_y/k^2 & -2ik_z/k^2 & iF & 0 \\ i(q-2)k_z & -\bar{\nu}k^2 & 0 & iF \\ iF & 0 & -\bar{\eta}k^2 & 0 \\ 0 & iF & -iqk_z & -\bar{\eta}k^2 \end{pmatrix} \cdot U(t), \quad (2.22)$$

with $U(t) = (u, \zeta, B, \eta)$ and $k^2 = (k_x^2 + k_y^2 + k_z^2)^{1/2}$. Due to the time dependence of k_x and k , Eqs. (2.22) cannot be usefully Fourier analyzed in time and must be solved numerically in general, although various analytic results have been obtained in previous works (Balbus and Hawley, 1992; Terquem and Papaloizou, 1996; Johnson, 2007; Mamatsashvili *et al.*, 2013). It so happens that Eqs. (2.22) are nonlinearly valid due to rather fortuitous cancellations of nonlinear terms, if the initial conditions include only one Fourier mode (Goodman and Xu, 1994; Balbus and Hawley, 2006). As such, they can be derived by simply inserting the shearing wave ansatz directly into the nonlinear equations [Eqs. (1.14)] and changing variables [Eqs. (2.19)], skipping the linearization step entirely.

2.3.3 Energy

The local energy norm, as required for application of nonmodal stability theory, is

$$E = \frac{2\pi^2}{k_y^2 + k_z^2} \int dx \left[|\zeta|^2 + |\eta|^2 + (k_y^2 + k_z^2) (|u|^2 + |B|^2) + |\partial_x u|^2 + |\partial_x B|^2 \right] \quad (2.23)$$

in the local Orr-Sommerfeld variables [Eq. (2.19)] choosing the y and z domains to stretch from 0 to 2π . Similarly, in the global variables [Eq. (2.17)]

$$E = 2\pi^2 \int dr \left[|u_r|^2 + |B_r|^2 + \frac{1}{m^2 + k_z^2 r^2} (|\partial_r (r u_r)|^2 + |\partial_r (r B_r)|^2 + |r \zeta|^2 + |r \eta|^2) \right]. \quad (2.24)$$

Note that for the shearing wave equations [Eq. (2.22)], the inner product is time dependent due to $\partial_x u$ and $\partial_x B$.

2.4 General properties

In this section I outline some basic properties of MRI pseudo-modes through examples, in both the local and global cases. We see that non-axisymmetric modes invariably resemble shearing waves and in general look very different from the most unstable eigenmodes. For the global case in particular, the pseudo-modes are often localized in a completely different region of space than the most unstable eigenmodes. In the final subsection I give an example of initializing using random initial conditions, illustrating the much greater relevance of pseudo-mode growth compared to that of the unstable eigenmodes.

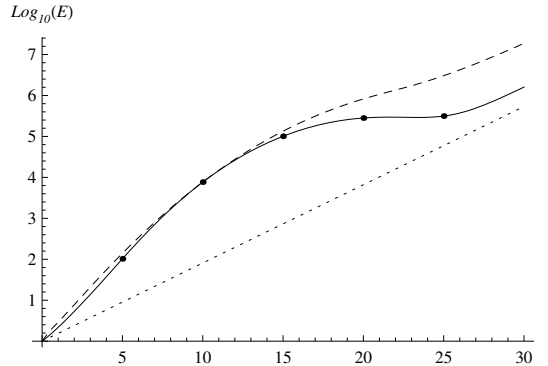


Figure 2.2: $G_T(t, 10)$ (solid), $G(t)$ (dashed) and the most unstable eigenmode growth (dotted) for the local model with hard wall boundary conditions and $k_y = 1$, $k_z = 4$, $B_{0z} = 1/10$, $B_{0y} = 0$, $\bar{\nu} = \bar{\eta} = 10^{-4}$. The dots on the solid curve correspond to the spatial structures illustrated in Figure 2.3.

2.4.1 Local computations

Let us start by considering a non-axisymmetric mode in the simplest possible background field configuration in the local box, a constant magnetic field in the z direction. However, in contrast to standard local stability approaches, the full local differential equations [Eqs. (2.20)] are solved with hard wall (perfectly conducting) boundary conditions. The reason for this choice is to illustrate the general irrelevance of the eigenmode at intermediate times; shearing wave structures are strongly apparent in the pseudo-mode, despite their incompatibility with the boundary conditions.

The transient and eigenmode growths for a weakly non-axisymmetric ($k_y = 1$) mode⁴ are illustrated in Fig. 2.2 at $B_{0z} = 1/10$. To demonstrate the importance of the shearing wave, I also illustrate the time evolution of the pseudo-mode spatial structure (for $t_0 = 10$) in Fig. 2.3. There are several important insights that can be gained from Figs. 2.2 and 2.3:

⁴In this domain at the chosen magnetic field ($B_{0z} = 1/10$, $B_{0y} = 0$), the fastest growing eigenmode in the ideal limit with (shearing) periodic boundary conditions is a channel mode ($k_x = k_y = 0$), with vertical wavenumber $k_z = \sqrt{15/16}/B_{0z}$ and growth rate $q/2 = 0.75$. The hard wall boundary conditions and dissipation change this growth rate very little (the growth rate of the mode that fills the box radially is numerically calculated as 0.730479). Since we have specified that the solutions be non-axisymmetric ($k_y = 1$, $k_z = 4$), this channel mode grows substantially faster than the both the eigenmode and the pseudo-mode presented in Figs. 2.2 and 2.3, as is to be expected.

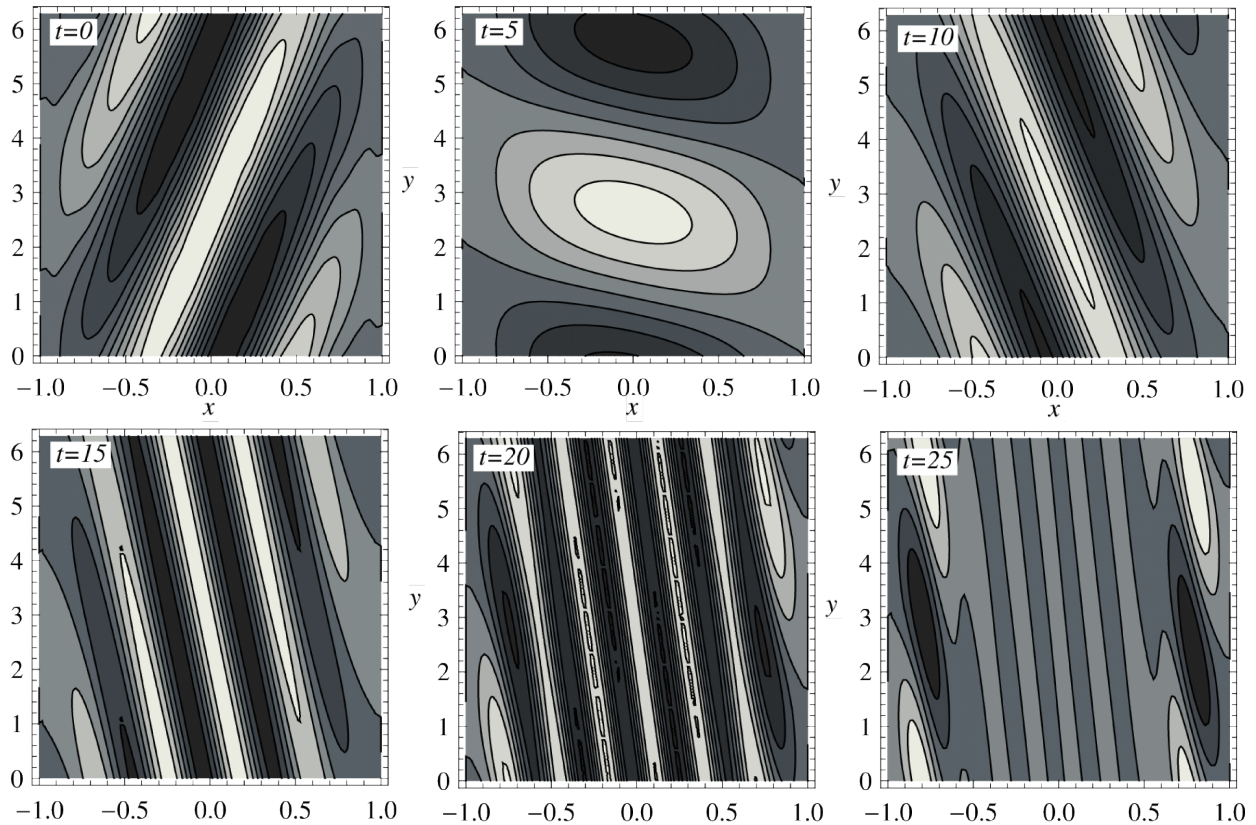


Figure 2.3: Time evolution of the spatial structure of the magnetic field component B_x of pseudo-mode $\Gamma(t, 10)$ for the same parameters as Figure 2.2. White and black shaded regions show positive and negative values respectively.

1. The maximum linear growth rate achievable [$G(t)$ and $G_\Gamma(t, 10)$ in Fig. 2.2] is approximately twice as large as that of the eigenmode. In addition, this fast growth rate continues until the perturbation has been amplified by a factor of nearly 10^5 . In a system with relatively strong initial perturbations, this amplification is presumably sufficient for various nonlinear effects or secondary instabilities to become significant, while in the case of small initial perturbations the most unstable channel mode would be many orders of magnitude larger than non-axisymmetric modes by the time such nonlinear effects took over (e.g., by $t = 30$ the energy of most unstable channel mode would be 10^{13} times larger than that of the eigenmode in Fig. 2.2). Thus, one can surmise that the non-axisymmetric eigenvalue growth rate is *largely irrelevant* at these parameters. This important conclusion carries over to the global case (Fig. 2.4).
2. The pseudo-mode is a shearing wave, despite the presence of the hard wall boundary conditions. Considering that the most unstable eigenmodes are localized near the boundaries of the domain, it is perhaps initially surprising that the pseudo-mode is localized in the middle of the domain, at least until the transient growth subsides (around $t = 20$). Note that a very similar effect is seen in the hydrodynamic case; see, for example, Mukhopadhyay *et al.* (2005). The general dominance of the shearing wave is nicely justified by the proof in Sec. 2.5 that shearing wave growth rates are always larger over short timescales than those of static structures.
3. Unlike the (spectrally stable) hydrodynamic case, the time at which $k_x \approx 0$ (i.e., the shearing wave is horizontal) does not correspond to any obvious change in the growth (in the hydrodynamic case $k_x \approx 0$ when $G(t)$ is maximum; see Mukhopadhyay *et al.* 2005). In addition, there is little change in the initial shearing wave orientation [$k_x(0)$] with changes in dissipation, $\bar{\nu}$ and $\bar{\eta}$, in stark contrast to the hydrodynamic case. In fact, in all pseudo-mode calculations I have carried out for non-axisymmetric modes, the initial conditions

satisfy $k_x(0) \approx k_y$. This is partially explained by the calculations in Sec. 2.5, where it is seen that the strongest growth over very short timescales ($t = 0^+$) is for a shear wave with $k_x(0) = \pm k_y$.

4. At intermediate timescales the boundaries of the domain seem largely irrelevant. Indeed, it is a general feature of nonmodal stability that the transient growth is much less sensitive to modifications of the system than the eigenmode growth (Trefethen *et al.*, 1993; Trefethen and Embree, 2005). In this case, the modification is the change of boundary conditions from those that naturally accept shearing waves (e.g., shearing-box boundary conditions) to those that do not (hard-wall conditions).
5. At late times the pseudo-mode starts to more closely resemble the most unstable eigenmodes (as might be expected) becoming more localized near the wall. As an interesting corollary of this, note that the eventual decay of shearing waves due to the increasing k_x (Balbus and Hawley, 1992; Brandenburg and Dintrans, 2006) is not necessarily physically important, even discounting nonlinear effects. The reason is that the eigenmode growth can "take over" at large times, with the shearing structure transitioning into a non-shearing structure. I conjecture that this could also be true when shearing-box boundary conditions are utilized, with the very late time structure starting to resemble some type of time-periodic Floquet eigenmode, an idea which is discussed in more detail in App. A.3. Of course, such a (time-periodic) eigenmode could be stable and decay, although perhaps more slowly than a shearing wave.
6. As the dissipation parameters ($\bar{\nu}$ and $\bar{\eta}$) are decreased, the period over which the pseudo-mode resembles the shearing wave increases in time, thus leading to a larger total amplification of the disturbance. This is in spite of the fact that the non-axisymmetric spectral instability can disappear as the dissipation is decreased (Kitchatinov and Rüdiger, 2010). This is essentially implying that nonmodal effects become more important as $\bar{\nu}, \bar{\eta} \rightarrow 0$.

Note that the shearing wave growth will not continue forever even if $\bar{v} = \bar{\eta} = 0$, as can be seen by solving the shearing wave equations [Eqs. (2.22)] in the dissipation-less limit (e.g., Brandenburg and Dintrans 2006).

The structure of the pseudo-mode in time does depend on the choice of when to maximize the growth, t_0 . For instance, for large t_0 the structure is more localized near the boundaries at all times, but is still strongly shearing with the background flow. Note that the other variables (u, ζ, η) have very similar time evolution (not shown). The illustrated transient growth is not simple stretching of the initial perturbation by the background flow (as in Sec. 2.1.1), which can be confirmed by noting that all three components of \mathbf{B}' grow at similar rates (not shown). I have also run calculations with different boundary conditions in x , including standard periodic conditions and the local equivalent of those advocated in Kersalé *et al.* (2004). These show that the structures observed in the pseudo-modes are always shearing waves in support of Item 4 above, so long as there are no strongly unphysical energy sources or sinks in the chosen boundary conditions.

Finally, note that transient growth is not limited to non-axisymmetric modes, but can also be significant for the axisymmetric channel mode ($k_y = k_x = 0$) in the chosen energy norm. To be precise, some transient growth is possible even with periodic boundary conditions, whenever the vertical wavenumber is different from the wavenumber that gives maximum eigenmode growth, $k_z = 1/B_{0z}\sqrt{15/16}$. In the local case, there is no substantial difference in spatial structure between the eigenmodes and pseudo-modes with hard-wall boundary conditions, but the ratios of components (u, ζ, B, η) is different. Note that one can straightforwardly choose a simple energy-like norm that removes the transient growth of axisymmetric modes, at least in the 2-D hydrodynamic case⁵ (Zhuravlev and Razdoburdin, 2014). However, as illustrated by the introductory

⁵Note that one can choose a norm for which there is no transient growth for *any* chosen mode (k_y, k_z) in the time-independent system, simply by choosing the norm matrix F to be the inverse of the matrix of eigenvectors. Of course, such a norm will be physically meaningless in the majority of cases, and the notion of using a norm with physical significance is central to nonmodal stability theory.

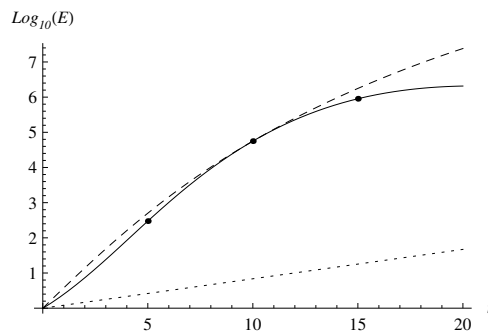


Figure 2.4: $G_{\Gamma}(t, 10)$ (solid), $G(t)$ (dashed) and the most unstable eigenmode growth (dotted) for the global model with hard wall boundary conditions and $m = 2$, $k_z = 15$, $B_{0z} = 1/30$, $B_{0\theta} = 0$, $\bar{\nu} = \bar{\eta} = 10^{-4}$. The dots on the solid curve correspond to the spatial structures illustrated in Figure 2.5.

example (Sec. 2.1.1), transient growth of the axisymmetric instability is a very real physical effect.

I give an example of global axisymmetric pseudo-mode growth in Sec. 2.6.

2.4.2 Global computations

To illustrate that the prevalence of shearing wave structures is by no means unique to the local model, in Figures 2.4 and 2.5 I display the pseudo-mode growth and structure for a weakly non-axisymmetric mode in a weak purely vertical field. Note that the chosen k_z is around the lower limit of what might be physically relevant in a thin accretion disk (Kersalé *et al.*, 2004). We see that all of the same conclusions that held in the local computation carry over to the global case. In fact, generally one observes a *greater* prominence of transient effects in the global equations than the local equations, probably due to a greater propensity for pseudo-modes and eigenmodes to be localized in very different regions. This is certainly the case here, as evidenced by comparison of Figs. 2.5 and 2.6 (the most unstable eigenmode) – while the eigenmode is strongly localized near the outer boundary, the pseudo-mode is far removed from this. Of course, at very large times (not shown) the pseudo-mode moves out in radius and starts to more closely resemble the eigenmode. Terquem and Papaloizou (1996) noted a similar difference between the localization

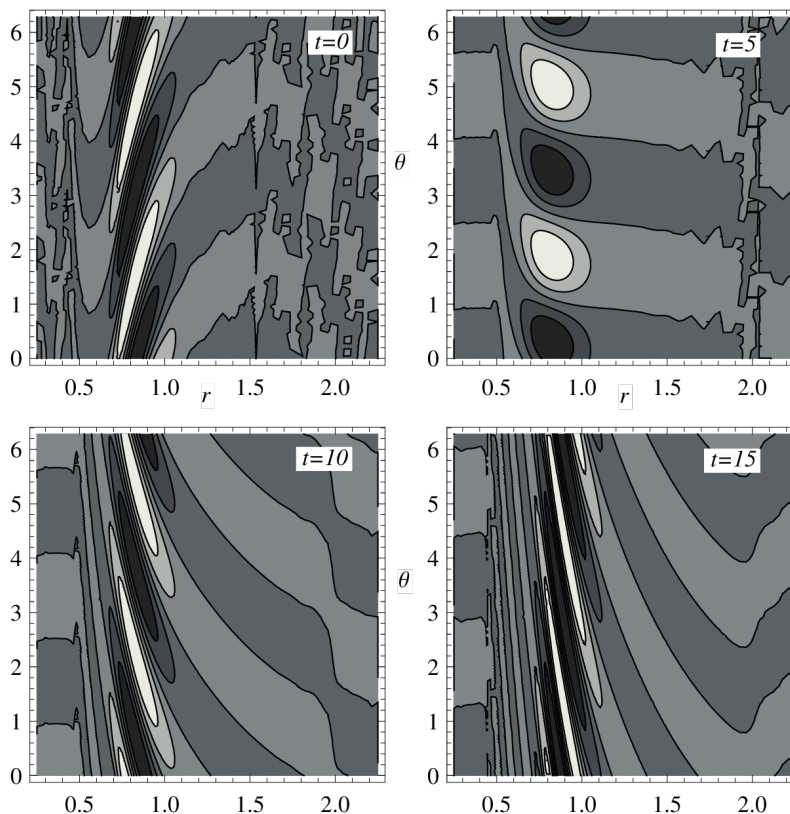


Figure 2.5: Time evolution of the spatial structure of the magnetic field component of the global pseudo-mode $\Gamma(t, 10)$ for the same parameters as Figure 2.4. White and black shaded regions show positive and negative values respectively. The small-scale oscillations in the outer regions at small times is caused by numerical errors in the Chebyshev method of calculating eigenmodes (these are then added to create the pseudo-mode), but these only affect regions of low amplitude.

of eigenmodes and that of structures emerging from random noise (in a toroidal field with no nonlinear effects). They explain these findings in terms of the local growth rates, a connection that is made in Sec. 2.6. Finally, note the extreme difference in growth rate between the nonmodal structures and eigenmodes (Fig. 2.4). The pseudo-mode grows approximately six times faster than the least stable eigenmodes and reaches an amplification of 10^5 before this fast growth shows any sign of slowing.

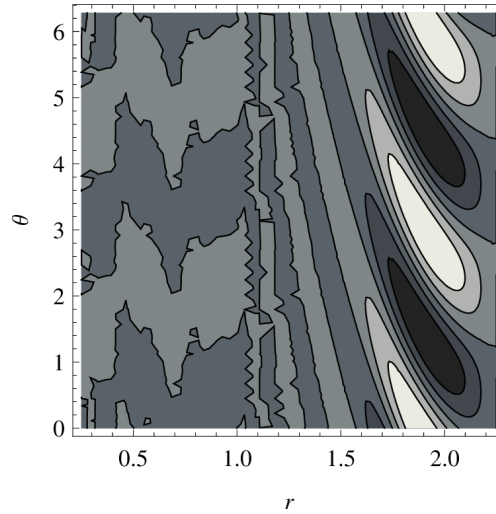


Figure 2.6: The structure of the most unstable eigenmode for the same parameters as Figure 2.4. Comparison with the structures in Figure 2.5 demonstrates the completely different spatial localization of the pseudo-mode.

2.4.3 Evolution from random initial conditions

As a final example to illustrate the greater relevance of pseudo-modes over eigenmodes, I initialize with random realizations of Gaussian noise and examine growth rates and prominent structures. This calculation can mitigate fears that the pseudo-mode structures might be less likely to be excited for some reason, and that total growth may not always be a good indicator of dynamical importance in a physical situation. I present an example of this calculation in Fig. 2.7, for local parameters very similar to those of Fig. 2.2. After an initial dip due to damped modes in the initial conditions,⁶ the growth curve follows that of $G(t)$ very closely. In fact, for these parameters, even the *minimum* growth seen out of 100 realizations has overtaken that of the most unstable eigenmode by late times; i.e., the most unstable eigenmode is statistically an exceptionally bad choice of initial condition for the total amplification of the disturbance. Observing the structure of random realizations (not shown) one sees a strong dominance of shearing waves at later times.

⁶Note that this dip and subsequent offset of the mean from the maximum growth curve (in Fig. 2.6 a factor of approximately 10) is also seen in normal systems and is unrelated to the transient nature of the growth.

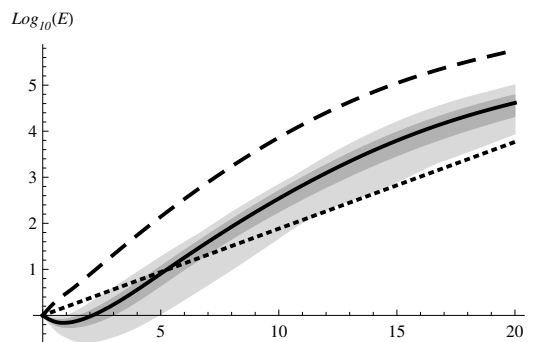


Figure 2.7: Linear evolution of the energy from 100 random initial conditions for $k_y = 1$, $k_z = 4$, $B_{0z} = 1/10$, $B_{0y} = 0$, $\bar{\nu} = \bar{\eta} = 2 \times 10^{-4}$. The solid line is the the mean of 100 random (Gaussian noise) initial conditions, the darker and lighter shaded regions show the standard deviation and total range of all data respectively. The dashed line shows $G(t)$ and the dotted line the most unstable eigenmode growth.

2.5 The dynamical importance of shearing waves

Noting the ubiquitous occurrence of shearing waves in simulations and the nonmodal calculations in the previous section, we were motivated to compare the growth of shearing structures with eigenmodes. In this section, I prove that shearing wave structures (I include the axisymmetric mode as a special case of this) always grow faster over short timescales than static (eigenmode-like) structures so long as dissipation is not too large. Interestingly, the local ideal short-time energy growth rate has the *same* maximum value, $-d\Omega/d \ln r$, regardless of the vertical and azimuthal wavenumbers. I also show how such calculations can be extended to more general situations with a weakly spatially dependent shearing wave expansion.

I shall compare growth of shearing waves and eigenmodes in the $t = 0^+$ limit, at a chosen x using a WKB approximation. Noting that the defining characteristic of an eigenmode is that its wavenumber is constant in time, I term the local approximation of eigenmodes *static waves* to distinguish from the shearing counterpart. While caution is advised in attempting to predict stability using such methods (Knobloch, 1992), here I simply compare static and shearing growth at a *given* k_x . Thus, subtle issues regarding the choice of k_x relevant to an eigenmode are alleviated

and I make no claim that these approximations are a substitute for the solution of the x -dependent problem (but see Blokland *et al.* 2005). Note that in both cases, static and shearing, the growth calculation is nonmodal; I insert an ansatz for the spatial form of the disturbance to better understand the structures that will appear in an x dependent nonmodal solution, such as those presented in Sec. 2.4.

The static equations can be derived straightforwardly to lowest order by inserting the WKB ansatz $f(x, t) \sim f(t) e^{ik_x x}$, and substituting $\partial/\partial t \rightarrow \partial/\partial t - iU_0 k_y = \partial/\partial t + iqxk_y$ (this simply shifts the spectrum without changing growth rates). The shearing wave equations were derived in sec. 2.3.2. The static and shearing wave equations are

$$\frac{\partial}{\partial t} U(t) = \begin{pmatrix} -\bar{\nu}k^2 - 2\Xi qk_x k_y/k^2 & -2ik_z/k^2 & iF & 0 \\ i(q-2)k_z & -k^2\bar{\nu} & 0 & iF \\ iF & 0 & -k^2\bar{\eta} & 0 \\ 0 & iF & -iqk_z & -k^2\bar{\eta} \end{pmatrix} \cdot U(t). \quad (2.25)$$

where $\Xi = 0$ or 1 for static and shearing waves respectively. Recall that for the shearing waves, the equations are time dependent since $k_x = qk_y(t - t_0)$. Solving for the eigenvalues of Eqs. (2.25) with $k_x = k_y = 0$ leads to the standard MRI dispersion relation (Balbus and Hawley, 1991).

The local energy norm [Eq. (2.23)] leads to

$$F = \left[2\pi^2 (k_y^2 + k_z^2)^{-1} \right]^{1/2} \begin{pmatrix} k & 0 & 0 & 0 \\ 0 & 1 & 0 & 0 \\ 0 & 0 & k & 0 \\ 0 & 0 & 0 & 1 \end{pmatrix} \quad (2.26)$$

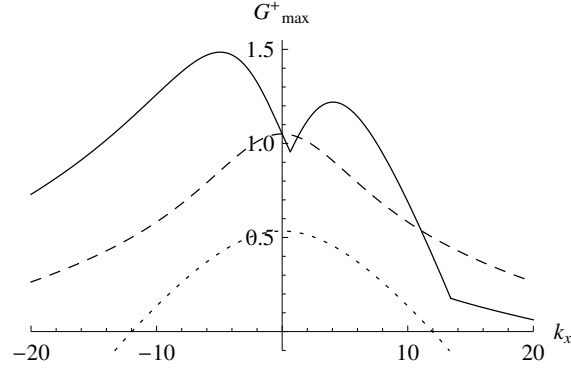


Figure 2.8: G_{\max}^+ as a function of $k_x(0)$ for shearing waves (solid) and static solutions (dashed). The parameters are $q = 3/2$, $k_z = 5$, $k_y = 5$, $\bar{\nu} = 10^{-4}$, $\bar{\eta} = 2 \times 10^{-3}$, with the large value of $\bar{\eta}$ chosen to illustrate the dominance of static structures in for large $k_x(0)$. Also shown is twice the imaginary part of most unstable eigenvalue (dotted) for a vertical field $B_{0z} = 1/20$. In the ideal limit, the eigenvalue will match G_{\max}^+ for wavenumbers $k_y = k_x = 0$, $k_z = 20\sqrt{15/16}$.

for the Cholesky decomposition of the energy norm, for both shearing and static waves. Then, using Eq. (2.8) one obtains the remarkably simple results:

$$G_{\max}^+ = \max \left\{ q \frac{k_z}{k} - 2\bar{\nu}k^2, q \frac{k_z}{k} - 2\bar{\eta}k^2 \right\} \quad (2.27)$$

for the static waves (with $\max\{\cdot\}$ denoting the maximum of the two functions), and

$$G_{\max}^+ = \max \left\{ q \left[\frac{1}{k} \left(k_z^2 + \frac{k_x^2 k_y^2}{k^2} \right)^{1/2} - \frac{k_x k_y}{k^2} \right] - 2\bar{\nu}k^2, \right. \\ \left. q \left[\frac{1}{k} \left(k_z^2 + \frac{k_x^2 k_y^2}{k^2} \right)^{1/2} + \frac{k_x k_y}{k^2} \right] - 2\bar{\eta}k^2 \right\} \quad (2.28)$$

for the shearing wave solutions, with k , k_x evaluated at $t = 0$.

Consider first the ideal limit of Eqs. (2.27) and (2.28), $\bar{\nu} = \bar{\eta} = 0$. We see that at all wavenumbers the shearing wave can grow faster than a static structure (or as fast at $k_x = 0$ where they are identical). In addition, the shearing wave growth rate has maxima at $k_x(0) = \pm k_y$, at which the growth is $q\Omega$, i.e., the maximum eigenvalue of the MRI, reached when $k_y = k_x = 0$, $k_z =$

$1/B_{0z}\sqrt{15/16}$. Thus, in the ideal limit, the MRI can have the same growth rate, $q\Omega$, for any choice of k_y, k_z , so long as the shearing wave initial condition satisfies $k_x(0) = \pm k_y$. Note that *all* channel mode perturbations ($k_x = k_y = 0$) grow at the same rate $q\Omega$, showing that even this most basic of MRI modes can grow transiently when $k_z \neq 1/B_{0z}\sqrt{15/16}$. This transient growth is a real physical effect; as discussed in Sec. 2.1.1, in the ideal limit any axisymmetric perturbation involving B_x can grow arbitrarily large through simple advection. At all wavenumbers, the initial conditions to obtain G_{\max}^+ are either purely hydrodynamic or purely magnetic. Of course, these pure modes will quickly become mixed under time evolution due to coupling terms in Eqs. (2.25). Unsurprisingly, adding dissipation alters this result. In particular, static waves can grow *faster* than shearing waves at sufficiently high wavenumbers when $\text{Pm} = \bar{\nu}/\bar{\eta} \neq 1$, with $\text{Pm} > 1$ ($\text{Pm} < 1$) causing static structures to dominate for $k_x(0) < 0$ ($k_x(0) > 0$). In essence, this behavior is seen in our spatially dependent pseudocode calculations (e.g, Fig. 2.3, $t = 25$) – at late times, the dissipation becomes more important and the shearing structure transitions into a static (eigenmode) structure. A graphical illustration of the previous discussion is given in Fig. 2.8, which shows the functions Eqs. (2.27) and (2.28), as well as the eigenmode growth rates.

Inclusion of global effects. As presented in Sec. 2.3.2, the shearing wave equations are derived through first applying a local expansion about the global equilibrium (App. A.2, also Umurhan and Regev 2004), then inserting the shearing wave ansatz. However, a more general way to obtain such equations is by directly inserting a shearing wave ansatz into the global equations, and only then applying the local expansion. For axisymmetric modes, the first step (insertion of a shear wave ansatz) is essentially a standard WKB expansion and has been used in many previous works. For example, in Blokland *et al.* (2005) the full WKB expansion (without a local approximation) is compared directly to r -dependent eigenmode solutions, showing excellent agreement.

One can extend the results in Eqs. (2.27) and (2.28) to situations in which aspects of the local approximation may not hold (see, for example, Pessah and Psaltis 2005; Kirillov and Stefani 2013)

by starting the analysis from the standard MHD equations in cylindrical coordinates (Bondeson *et al.*, 1987) and considering shearing and static waves with weak dependence on the radial coordinate. Motivated by liquid metal experiments (Rüdiger *et al.*, 2013; Kirillov and Stefani, 2013), here I consider the incompressible MHD equations at constant density with the velocity profile $\mathbf{U}_0 = U_{0\theta} r^{-q+1} \hat{\boldsymbol{\theta}}$ and the magnetic field profile $\mathbf{B}_0 = B_{0\theta} r^{2\text{Rb}+1} \hat{\boldsymbol{\theta}} + B_{0z} \hat{\mathbf{z}}$. This is essentially the global model described earlier (Sec. 2.3.1), with the addition of a spatially dependent magnetic field for illustrative purposes. The extension of the technique to more complex stratifications and compressibility (Pessah and Psaltis, 2005; Salhi *et al.*, 2012) is straightforward.

The static wave equations are obtained in much the same way as for the local case, by inserting the ansatz $f(r, t) \sim f(t) e^{ik_r r}$ and assuming $(k_r r, k_z r, m) \sim 1/\epsilon$, $(\bar{\nu}, \bar{\eta}) \sim \epsilon^2$ to obtain a set of ODEs in time.⁷ Similarly, the shearing wave equations are obtained by assuming a shearing wave envelope that varies slowly in the r direction. To lowest order, they can be straightforwardly derived by inserting the ansatz $f(r, t) \sim f(t) \exp(-im/r U_0 r^{-q+1}(t - t_0))$ and making the same ordering assumptions as for the static case. After non-dimensionalizing variables using the length-scale r and the timescale $1/\Omega(r)$, one obtains

$$\partial_t U = \begin{pmatrix} -k^2 \bar{\nu} - 2q \Xi m k_r / k^2 & -2i k_z / k^2 & iF(r) & 2i k_z B_{az} / k^2 \\ i(q-2)k_z & -k^2 \bar{\nu} & 2i(\text{Rb}+1)k_z B_{az} & iF(r) \\ iF(r) & 0 & -k^2 \bar{\eta} & 0 \\ -2i \text{Rb} k_z B_{az} & iF(r) & -i q k_z & -k^2 \bar{\eta} \end{pmatrix} \cdot U. \quad (2.29)$$

Here $U = (u, \zeta, B, \eta)$, $\Xi = 1$ or 0 for shearing waves and static waves respectively, $B_{az} \equiv B_{0\theta} r^{2\text{Rb}+1}$, $F(r) \equiv k_z B_{0z} + m B_{az}$, wavenumbers (k_r, k_z) have been scaled by r and $(\bar{\nu}, \bar{\eta})$ have

⁷These ordering assumptions arise from assuming the solution varies faster than the background equilibrium. If either $\bar{\nu}$ or $\bar{\eta}$ are very large one may wish to alter these, which is straightforward and leads to slightly different shearing wave equations.

been scaled by $r^2\Omega(r)$. For the static equations, I have substituted $\partial/\partial t \rightarrow \partial/\partial t - i\mathbf{u}_0 m/r$ (as in the local calculation) and for the shearing waves, $k_r \equiv qU_0 m r^{-q}(t - t_0)$. While all variables in Eqs. (2.29) technically depend on both r and t , the dependence on r is parametric. The static version ($\Xi = 0$) of Eqs. (2.29) is very similar to the dispersion relation given in Kirillov and Stefani (2013), aside from slight differences in how the azimuthal wavenumber m appears in the dissipation terms. Note that Eqs. (2.29) reduce to Eqs. (2.25) in the "local" limit (Umurhan and Regev, 2004).

Applying the same procedure as earlier to calculate the $t = 0^+$ growth rates leads to

$$G_{\max}^+ = \pm \left[\left(k^2 (\bar{\eta} - \bar{\nu}) - \Xi q \frac{k_r m}{k^2} \right)^2 + 4B_{az} (1 + \text{Rb})^2 \frac{k_z^2}{k^2} \right]^{\frac{1}{2}} + \frac{q}{k} \sqrt{k_z^2 + \Xi \frac{m^2 k_r^2}{k^2}} - k^2 (\bar{\eta} + \bar{\nu}), \quad (2.30)$$

with the \pm chosen to obtain the maximum value of G_{\max}^+ . Note that $|r \partial_r f|^2 \approx r^2 |\partial_r f|^2$ has been applied in the energy norm used to calculate Eq. (2.30), in keeping with approximations used earlier. Eq. (2.30) demonstrates that the fundamental results presented earlier are essentially unchanged by the addition of field curvature effects, as well as illustrating the importance of shearing waves in flows with more complex shear profiles. The extra terms in the global equations change the maximum of G_{\max}^+ with respect to $k_x(0)$, and the MRI can grow faster than $q\Omega$ for strong $B_{0\theta}$. It is interesting that for the very large $\bar{\eta}$ characteristic of liquid metal experiments there is a large regime (for $k_x(0) > 0$) where static structures grow faster than shearing waves (see Fig. 2.8).

This more global way of considering the problem may have several advantages. Firstly, it is straightforward to extend the shearing wave equations to much more complicated domains and physical models. For example, strong magnetic fields, compressibility, stratification, or more complex diffusion operators (see, for example, Pessah and Psaltis 2005; Heinemann and Papaloizou 2009; Salhi *et al.* 2012; Rosin and Mestel 2012) could easily be accounted for in the shearing

wave equations.⁸ Secondly, the approach elucidates the connection between previous results that illustrate the quality of WKB methods for axisymmetric modes, and results (presented in Sec. 2.6 below) that show the accuracy of the shearing wave equations over moderate timescales. We have primarily explored global models in which the local approximation (App. A.2) is accurate. In future work it would be interesting to study global models that include more complex physical effects, comparing global pseudo-modes to nonmodal solutions of the extended shearing wave equations derived directly from the chosen global equations. It seems likely that a general condition for the validity of extended shearing wave equations will be related to the existence of an intermediate scale between the dissipation and global curvature scales. Such scale separation will allow terms associated with the velocity shear to dominate, leading to the growth of shearing structures over intermediate time scales.

Finally, it is worth clarifying that shearing wave equations can only ever give a good approximation to the global pseudo-mode behavior over moderate timescales. The reason is that eventually the eigenmode will take over, since the structures in a shearing wave necessarily move to smaller scales in time. This causes dissipative effects to dominate and the shearing wave to damp, even when the global system has one or more unstable eigenmodes. This effect is clearly seen in the last pane of Fig. 2.3, where the pseudo-mode eventually starts to resemble the least stable eigenmodes. From a practical standpoint, the shearing wave equations accurately represent the global pseudo-mode up until their solution starts to decrease in time.

In the next section, much of the above discussion is explored from a computational standpoint, directly comparing the local and global shearing wave evolutions.

⁸Of course, such effects can also be accounted for in local equations using other methods, a potential advantage of the shearing wave method is its conceptual simplicity.

2.6 The relationship between the shearing wave equations and global structures

The appearance of shearing structures in the global pseudo-modes, as well as the discussions in the previous section, lead naturally to the question: How well do the shearing wave equations approximate global linear behavior? As far as I know, this question has not been previously explored for general non-axisymmetric modes, with most authors focusing on eigenmodes in global studies and shearing waves in local studies. In this section, I directly compare the global pseudo-mode evolution with the shearing wave equations [Eq. (2.22)] finding excellent agreement in a variety of parameter regimes. This seems to be the first explicit demonstration of the connection between global eigenmodes (through their connection to the pseudo-modes) and local shearing wave approximations for both axisymmetric and non-axisymmetric modes.

Our method to compare global pseudo-modes with the local equations uses the following sequence of steps:

1. Calculate the global pseudo-mode that maximizes the energy amplification at t_0 , $\Gamma(t, t_0)$, for some chosen global parameters.
2. Choose a radial point in the global domain, r_0 , at which to compare the global and local solutions. This should be chosen where the global pseudo-mode is relatively large to mitigate numerical errors in the pseudo-mode.
3. Calculate the local parameters that correspond to the global parameters at r_0 . This procedure is outlined in App. A.2.
4. From the pseudo-mode structure at r_0 , determine the initial k_x value for the shearing wave. This is most easily carried out by observing when $k_x \approx 0$ in the pseudo-mode evolution to obtain t_{SW} [Eq. (2.21)].

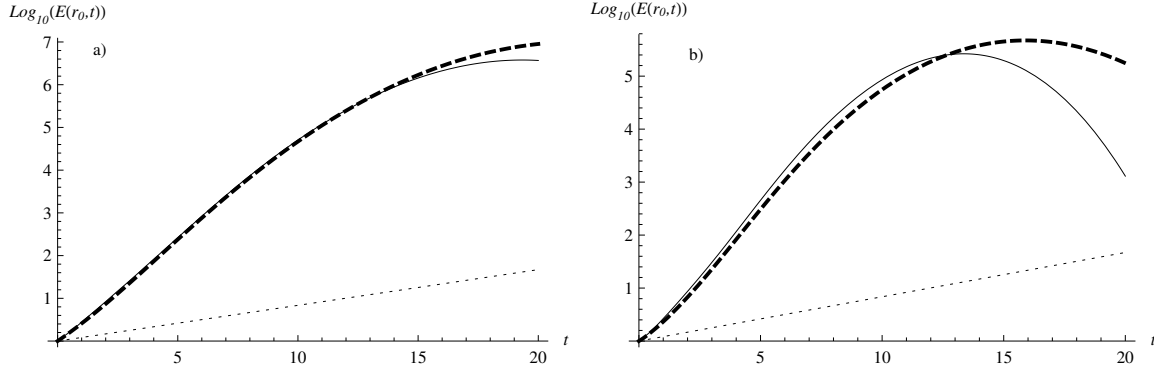


Figure 2.9: Comparison of the energy growth of the global pseudo-mode (thick, dashed) and local shearing wave (solid) at a) $r_0 = 1$, $t_{SW} = 4.7$ and b) $r_0 = 0.75$, $t_{SW} = 4.5$. The dotted line illustrates the most unstable eigenmode growth for comparison. The parameters are $m = 2$, $k_z = 15$, $B_{0z} = 1/30$, $B_{0\theta} = 0$, $\bar{\nu} = \bar{\eta} = 10^{-4}$, the same as Fig. 2.5. Both the global and shearing wave amplification are maximized at $t_0 = 10$ as in Fig. 2.5.

5. Determine the shearing wave initial conditions $(u(0), \zeta(0), B(0), \eta(0))$ that maximize the energy amplification at the chosen t_0 using the nonmodal stability method, Eq. 2.6. Stated in another way, one compares the global pseudo-mode with the shearing wave pseudo-mode.
6. Solve the shearing wave equations in time.
7. Calculate the shearing wave energy growth and compare this to the energy growth of the global solution at r_0 .

Once the global parameters and r_0 have been chosen, the only free parameter is the initial shearing wave orientation $k_x(0)$. Since this is set by the global structure, I wish to emphasize that I am not adjusting any free parameters to improve the energy growth agreement. In the axisymmetric case (Fig. 2.10) there are no free parameters.

2.6.1 Non-axisymmetric modes

In Figure 2.9 I illustrate the comparison of shearing waves with global pseudo-mode energy growth using the procedure outlined above. The parameters chosen are those for a weakly non-

axisymmetric mode in a vertical field (the same as Fig. 2.5), with two values of r_0 chosen for comparison. We see excellent agreement, although unsurprisingly the growth is most similar where it is strongest, around the maximum of the pseudo-mode ($r_0 = 1$). Moving very far from the maximum (e.g., $r_0 = 2$, not shown), one sees rather poor agreement, presumably due to noise and errors in the numerical result. Many other similar computations have been run, with excellent agreement seen across a wide range of parameters.

As an interesting corollary of such results, one can approximately *predict* the structure of the global pseudo-mode using the shearing wave equations. The basic idea is to solve the shearing wave equations at each point in the global domain, maximizing the growth at a chosen t_0 using the nonmodal technique. Examining the amplification as a function of radius gives an approximation of the structure of the global pseudo-mode. While an exact comparison is tricky due to the choice of t_0 in the shearing wave equations, I have considered a range of parameters (not shown here) and the agreement generally appears rather good. In particular, the prediction of the spatial location of the pseudo-mode maximum is quite accurate. Such computations present further evidence that the local shear wave approximation is accurate in many cases (Papaloizou and Terquem, 1997), and will be more meaningful than global eigenmodes over moderate timescales.

2.6.2 Axisymmetric modes

Figure 2.10 presents a similar comparison for the case of an axisymmetric mode in a purely azimuthal field (the behavior is very similar to the case with no magnetic field). While such a case could be argued to be somewhat pathological due to the importance of even a wisp of vertical field (at least without dissipation, I discuss this point more in Sec. 2.7.1; see also Balbus and Hawley 1998), it provides an interesting example. Despite the eigenmode being stable, there is rather strong growth, with the pseudo-mode amplified by $\sim 10^3$ by $t = 7$. The agreement with the shearing wave – in this case a simple channel mode with $k_y = k_x = 0$ – is remarkably good. Of

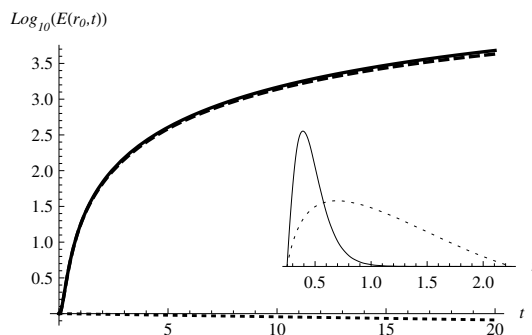


Figure 2.10: Comparison of the energy growth of the global pseudo-mode (thick, dashed) and local shearing wave (solid) for a $k_z = 10$ axisymmetric mode in a purely azimuthal field ($B_{0y} = 0.2$, $B_{0z} = 0$, $\bar{v} = \bar{\eta} = 10^{-4}$). The dotted line illustrates the eigenmode least stable growth for comparison. The growth of the global and local pseudo-modes are maximized at $t_0 = 10$ and the local shearing wave parameters are taken from $r_0 = 0.5$. Inset: radial structure of the radial magnetic field component of the pseudo-mode (solid) at $t = 5$ (the structure is nearly time-independent) and the least stable eigenmode (dotted). (Values are normalized for illustrative purposes.)

course, as discussed in Sec. 2.1.1, we are seeing simple advection of an initial field by the flow; nonetheless, it is comforting to see that the global pseudo-mode is locally behaving in the same way with very similar optimal initial conditions. For comparison, the inset to Fig. 2.10 illustrates the radial structure of the pseudo-mode and least-stable eigenmode for the radial magnetic field. In this case the two are rather different; however, in the case of axisymmetric modes in a pure vertical field (not shown) the pseudo-mode generally closely resembles the eigenmode and the nonmodal growth is less significant due to the strong exponential growth of the standard MRI.

2.7 Nonmodal growth of the shearing wave equations

As discussed in the previous sections, since the shearing wave equations themselves are motivated by nonmodal ideas, it is most natural to consider their solutions from the nonmodal standpoint, solving for those initial conditions that give the maximum amplification for some chosen time. An important notion here is that the non-modality does not arise purely from the time dependence of

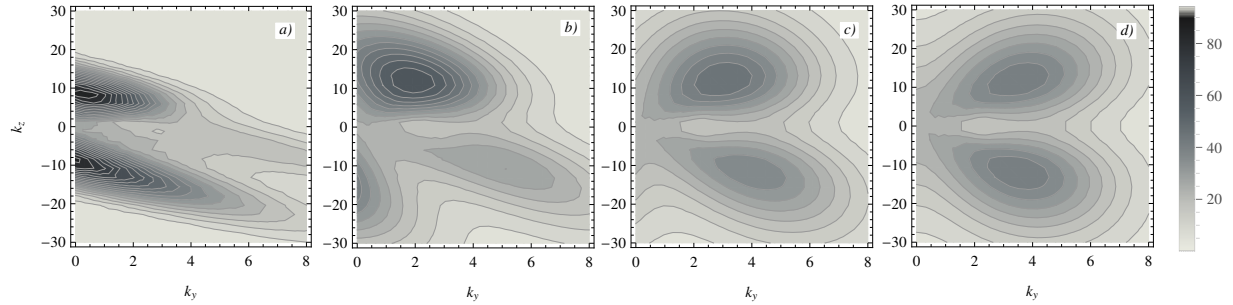


Figure 2.11: Maximum amplification by $t = \pi$ as a function of k_y, k_z for $B_{0y} = 1/5, \bar{\nu} = \bar{\eta} = 1/3000$ and (a) $B_{0z} = 1/10$, (b) $B_{0z} = 1/30$, (c) $B_{0z} = 1/100$, (d) $B_{0z} = 0$. At each (k_y, k_z) the data shows the maximum growth obtained over all choices of initial conditions and initial shearing wave orientation (i.e., each point is maximized over $k_x(0)$). All plots use the color scale shown on the right-hand side. For reference, the maximum possible growth of the ideal MRI corresponds to an amplification of $\exp(q\Omega \times \pi) \approx 111$ in these units.

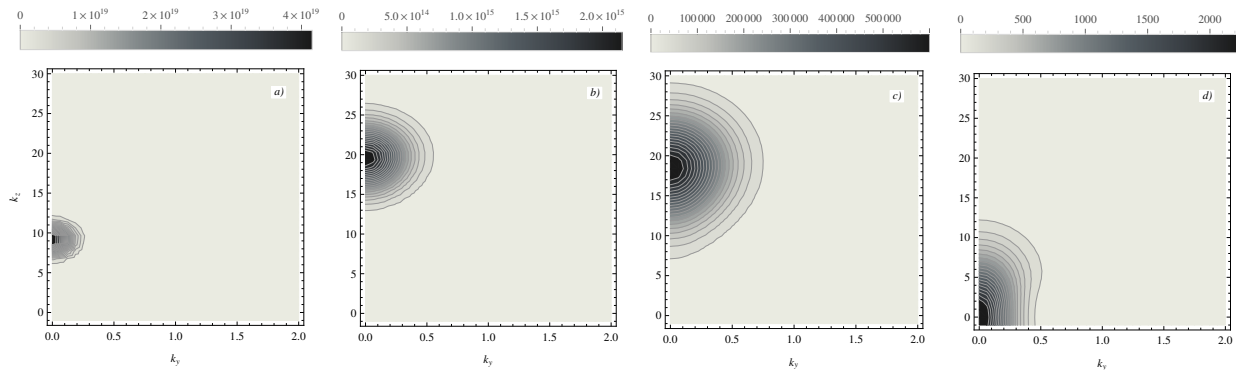


Figure 2.12: Same as Fig. 2.11 but showing maximum amplification by $t = 10\pi$. Due to the large time and relatively high dissipation, these plots are much closer to the eigenmode structure and thus are entirely dominated by axisymmetric modes. A separate color scale is used for each plot since the amplification changes substantially as B_{0z} is altered. For reference, the maximum possible growth of the ideal MRI corresponds to an amplification of $\exp(q\Omega \times 10\pi) \approx 2.9 \times 10^{20}$ in these units.

the equations (i.e., the original ansatz for the spatial form of the solution), but is a consequence of the original time-independent system. Indeed, nonmodal effects can be important even in the axisymmetric case, when the shear wave equations are time-independent.

In this section I focus on how nonmodal techniques can be useful in studying the local MRI, in particular the relative importance of different mode numbers as external parameters are changed. In addition, I consider a rather unconventional view of the MRI as a general nonmodal instability brought about by the addition of MHD effects, but rather separate from the presence of a background magnetic field.

2.7.1 The dependence of the MRI on azimuthal field

As a useful example, here I present a simple study of how the local MRI changes with imposed vertical field while in a strong background azimuthal field. There are two primary motivations behind this choice of problem:

1. Using analyses based on eigenmodes (or similar ideas for time-dependent shear waves e.g., Balbus and Hawley 1992; Johnson 2007) the MRI behaves a little unusually in an azimuthal field in the limit $B_{0z} \rightarrow 0$ (Balbus and Hawley, 1998). In particular, the growth rate is very sensitive to even a minute vertical field and enormous changes in the mode structure are seen for tiny changes in vertical field. Here I show that this problem is, unsurprisingly, very strongly dependent on the timescale considered: over shorter timescales the behavior is quite smooth as $B_{0z} \rightarrow 0$.
2. This system is the simplest choice of problem with some relevance to unstratified shearing-box turbulence simulations. In particular, the strong azimuthal field could be generated by an MRI dynamo (see, for example, Käpylä and Korpi 2011; Lesur and Ogilvie 2008a), while the vertical field comes from a net flux threading the domain.⁹ Of particular relevance may be the

⁹Note that the character, or even existence, of the unstratified MRI dynamo is not particularly well understood. In zero-net-flux shearing boxes there is good evidence that a strong, self-generated azimuthal magnetic field plays an

work of Longaretti and Lesur (2010), where the authors study how various characteristics shearing-box turbulence with net magnetic flux (i.e., mean B_{0z}) change with parameters. Here I illustrate that trends in their turbulent simulations seem to be well matched by the linear physics, so long as one studies the growth of finite timescales.

I illustrate these ideas in Figs. 2.11 (short time growth) and 2.12 (long time growth). These each show the maximum amplification of a disturbance as a function of (k_y, k_z) , at fixed azimuthal magnetic field, as the vertical field is decreased from left to right. At each point (k_y, k_z) the amplification is also maximized over the initial orientation of the shearing wave, $k_x(0)$; thus, the contours represent the maximum growth possible at the chosen (k_y, k_z) . This is really for ease of presentation and there could certainly be interesting information in the $k_x(0)$ structure that could be studied in future work. (Such plots are similar in spirit to hydrodynamic results given in Yecko 2004 and Mukhopadhyay *et al.* 2005.) I use a rather large dissipation ($\bar{\nu} = \bar{\eta} = 1/3000$) to have some relevance to nonlinear simulations. Of course, in a shearing box the $(k_x(0), k_y, k_z)$ is necessarily discretized based on the box size; nonetheless, the continuous k results presented here can either be considered as pertaining to a continuous range of box sizes or, more usefully, to different dissipation values and magnetic fields through a rescaling of the shearing-box equations as outlined in App. A.2.

The enormous difference between Figs. 2.11 and 2.12 is a stark illustration of the importance of correctly choosing the relevant timescale for a given situation. Over the long timescales illustrated in Fig. 2.12 we are essentially observing eigenmode behavior, with very little contribution from non-axisymmetric modes (this is more severe than it would be at lower dissipation). In addition, the change in behavior with B_{0z} is extreme; a change in amplification by 14 orders of magnitude with a 1 order of magnitude change in B_{0z} . In contrast, over moderate timescales $t = 0 \rightarrow \pi$ (Fig. 2.11) the change with B_{0z} is rather smooth, even as it vanishes completely [Fig. 2.11(d)]. The

important role in the turbulence (see Lesur and Ogilvie 2008b); however, I know of no work that explores this dynamo explicitly for the case with net vertical flux.

growth in the case of $B_{0z} = 0$ is still substantial, with non-axisymmetric modes being amplified by a factor of 40, around a third of the amplification of the fastest growing channel mode. Note that the general trend of increasing non-axisymmetry with decreasing vertical field¹⁰ matches the characteristics of nonlinear turbulence (e.g., Fig. 9 from Longaretti and Lesur 2010) rather well. I have also considered the change in the mode structure with dissipation parameters (not shown) and do not see the contradictions between linear and nonlinear results that are discussed in Longaretti and Lesur (2010). Also of interest are the results of Lesur and Longaretti (2011), where it is shown numerically that the energy injection spectrum in net-flux MRI turbulence is broadly distributed across a wide range of wavenumbers. With these results in mind, it seems likely that nonmodal analyses could be useful in studying aspects of MRI turbulence from a linear standpoint, since growth over short timescales is almost certainly more relevant to turbulent situations than the $t \rightarrow \infty$ limit explored by eigenmode analyses (Friedman and Carter, 2014). Note that, as shown in Sec. 2.5, for $t \rightarrow 0$ amplification plots such as Figs. 2.11 and 2.12 become completely homogenous (aside from the effects of dissipation), with no preference for one wavenumber over any other.

2.7.2 The MRI with zero background field

Another interesting case that is simple to analyze using nonmodal techniques is the MRI with no background magnetic field at all. In this case the system is spectrally stable; nevertheless, there can be significant growth over a wide range of wavenumbers, which can be sufficient to cause a transition to turbulence given large enough initial conditions (Rempel *et al.*, 2010; Riols *et al.*, 2013). Figure 2.13 illustrates the maximum amplification of perturbations with no background field in (a) the magnetohydrodynamic case and, (b) the well-studied hydrodynamic (HD) case with Keplerian shear. It is interesting to note the enormous change afforded by adding in magnetic perturbations, not in the magnitude of the maximum amplification, but in the range of wavenumbers

¹⁰This trend has of course been discussed previously by other authors (Terquem and Papaloizou, 1996; Ogilvie and Pringle, 1996), especially for the ideal MRI at zero resistivity

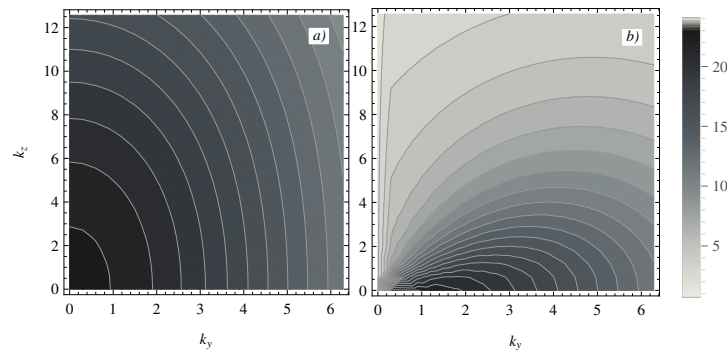


Figure 2.13: (a) Maximum amplification by $t = \pi$ as a function of k_y, k_z at $\nu = \eta = 1/3000$ but with no background magnetic field, $B_{0y} = B_{0z} = 0$. (b) Same as (a) but without allowing magnetic perturbations, i.e., for the hydrodynamic shearing box. The addition of magnetic perturbations allows reasonable growth over a much larger range of wavenumbers.

that can be strongly amplified. In particular, while vertical perturbations (non-zero k_z) are strongly suppressed in the HD case, these can grow rather strongly in the MHD system. The MHD growth mechanism is simple advection of the initial perturbation, as in the introductory example Sec. 2.1.1 (with some added dissipation for non-axisymmetric modes due to shearing). Because of this, the time dependence of the perturbation growth strongly resembles Fig. 2.1.

Of course, one can never hope to understand the transition to turbulence with purely linear physics, and the addition of nonlinear interactions increases the complexity of the problem enormously (see, for example, Shen *et al.* 2006; Lithwick 2007). Nonetheless, knowing *a priori* that the zero-net-flux MHD system readily transitions to turbulence, while the hydrodynamic system appears to stay laminar even at high Reynolds numbers (Lesur and Longaretti, 2005; Balbus and Hawley, 2006), it is interesting to note their differences from the purely linear perspective.

2.8 Summary and discussion

In this chapter, I have explored aspects of the magnetorotational instability using nonmodal stability techniques. In fluids, these techniques have primarily been applied to systems that are spectrally

stable, presumably due to the dramatic failure of eigenmode predictions when a subcritical transition to turbulence is possible. However, despite the fact many configurations of the axisymmetric and non-axisymmetric MRI have unstable eigenmodes, nonmodal methods have proven to be very fruitful. In particular, nonmodal structures will be more physically meaningful than eigenmodes in many cases, leading to an intuitive connection between global results and the local shearing wave picture, as well as being far more robust with respect to slight changes to the system (e.g., boundary conditions).

I consider the main conclusions of this work, which have been used to motivate the examples and discussions throughout the chapter, to be as follows:

- For non-axisymmetric modes at low dissipation, eigenmodes will often be *irrelevant* to the linear dynamics of the system in both local and global domains. We have seen that the fastest growing structures (pseudo-modes) invariably resemble shearing waves, even when the boundary conditions of the model are incompatible with the shear wave's time-dependent structure. Similar behavior is seen for the hydrodynamic case (see for example, Ioannou and Kakouris 2001; Yecko 2004). In addition, the growth of the pseudo-mode is generally much faster than that of the eigenmode and this fast growth can persist until the disturbance has grown by many orders of magnitude (see Figs. 2.2 and 2.4).
- In global domains, the fact that the pseudo-mode structure resembles shearing waves provides a very natural connection between the global (radially stratified) MRI and the local shearing-box picture, which (to my knowledge) has not been previously discussed. A direct comparison of global pseudo-mode growth to the local shearing wave equations [Eqs. (2.22)] in Sec. 2.6 shows very good agreement, for both axisymmetric and non-axisymmetric modes.
- The possibility of algebraic (transient) growth of the MRI has often been framed as being a consequence of the time dependence of the shearing wave ansatz (e.g., Johnson 2007; Tevzadze *et al.* 2008). In fact, the shearing wave ansatz and resulting equations are use-

ful for predicting MRI growth *because* shear wave disturbances are strongly amplified by the underlying spatially dependent equations; the time dependence of the equations is of subsidiary importance. Thus, it is most natural to analyze the local shearing wave system [Eq. (2.22)] using nonmodal techniques also. In addition, the axisymmetric case, though time-independent, can be analyzed using exactly the same framework and transient growth is also important for such modes. This growth is simply advection of the initial perturbation by the flow, which continues indefinitely in the dissipationless limit even when no unstable eigenmodes are present.

- Nonmodal ideas are particularly important if one wishes to consider linear or quasi-linear explanations for MRI turbulence and dynamo. The reason for this is straightforward; any perturbation that grows in a turbulent system will be quickly destroyed by the underlying randomness. Thus, short-time growth rates will be much more relevant and correspondingly, nonmodal analysis techniques must be utilized (Farrell and Ioannou, 2003; Friedman and Carter, 2014). As an example, a quick comparison of Figs. 2.11 and 2.12 illustrates the enormous difference in mode structure that arises from considering the instability over a longer timescale. Evidently, one must be very careful in applying eigenmode ideas to an analysis of MRI turbulence.

Given the large number of works studying hydrodynamic nonmodal growth, as well as previous studies of transient growth in the MRI shearing wave equations, it is curious that these ideas have not been formally explored previously. Nevertheless, like its hydrodynamic cousin, the MRI system is strongly non-normal and an over-reliance on eigenmode analyses can lead to seemingly contradictory and confusing results.

My presentation here has been rather perfunctory due to the desire to include a variety of non-modal MRI analyses, from both global and local perspectives. Of course, there is much room for future work. For simplicity, I have entirely neglected the effects of compressibility and density

stratification in the global model, which certainly limits its relevance to a real accretion disk. Examination of the effects of vertical stratification in a fully 2-D model could also be interesting, although the non-modality would almost certainly not be nearly so extreme as that arising from radial stratification and the physics of the linear MRI has generally been seen to be relatively insensitive to the addition of more complex physical effects (see, for example, Latter *et al.* 2010; Mamatsashvili *et al.* 2013). Along these lines, it would also be prudent to consider in more detail the general shearing wave expansions discussed in Sec. 2.5, examining the agreement between global pseudo-modes and various local approximations.

Of course, there are situations where the nonmodality brought about by the shear may not be so important. Most obviously, the most unstable MRI mode with eigenvalue $q/2$ is not self-adjoint in the energy norm [see Eq. (2.22) with $k_z = \sqrt{q(1 - q/4)}/B_{0z}$, $k_y = 0$], yet there is no transient growth.¹¹ Another possible example is the Rossby wave instability (Papaloizou and Pringle, 1985) – essentially the Kelvin-Helmholtz instability in a rotating disk – where the normal mode picture seems to work well in comparison to nonlinear simulation (Meheut *et al.*, 2010). Of course, the nonmodal approach subsumes the modal approach; nevertheless, the added complexity involved in the nonmodal analysis means the application of modal results is desirable where possible. Some advances have been made in understanding the physical origins of modal instabilities in this regard (Bakas and Ioannou, 2009; Guha and Lawrence, 2014), and similar methods may prove useful for gaining physical insight into when MRI-like instabilities can be treated using modal techniques.

Finally, what conclusions can we draw about the character of MRI turbulence using nonmodal ideas? As an example, the existence of strong linear growth at all scales seems to support the notion that MRI turbulence does not exhibit a well-defined inertial range (Fromang and Papaloizou, 2007; Bratanov *et al.*, 2013), at least at larger scales (Schumacher, 2004). Methods such as that used to create Fig. 2.11 may assist in quantifying such ideas; for instance, an examination of mode

¹¹This particular situation is rather specific, occurs only at the k_z required for the fastest MRI growth rate, and is related to the magnetic part of the MRI eigenfunctions being orthogonal.

structure as a function of dissipation parameters (in particular magnetic Prandtl number) could be helpful in understanding aspects of shearing-box turbulence.

Extending such general ideas into a more formal setting, in the next chapter I study the self-consistent interaction of the linear MRI with space- and time-dependent mean fields in a driven quasi-linear system. Nonmodal linear growth is inherently built into this method, and the concept of shearing waves has been fundamental in gaining a conceptual understanding of some of the important processes. Of course, linear ideas alone can never hope to fully explain the enormous complexity of a self-sustaining turbulent system and I do not wish to make such a claim. Nonetheless, it seems imprudent to discount the importance of linear physics without using a method of analysis that appropriately handles the relevant timescales of the problem.

Chapter 3

Statistical simulation of the MRI dynamo

This chapter, some of which was published in Squire and Bhattacharjee (2015a), serves as a lead-in to the more systematic study of the MRI dynamo in the later parts of the thesis. Having seen the likely importance of linear modes in MRI turbulence (see Chapter 2), we were motivated to apply such ideas in a more systematic fashion towards the study of the turbulent state. This led to the idea of studying MRI turbulence and dynamo in the zero-net-flux unstratified shearing box using quasi-linear statistical simulation methods [from hereon I shall use the term second-order cumulant expansion (CE2; Marston *et al.* 2008), although the term stochastic structural stability theory (S3T; Farrell and Ioannou 2003) is also common and pertains to similar ideas]. This involves considering an ensemble of linear fluctuations evolving in mean fields that depend only on the vertical co-ordinate (z). The nonlinear stresses of these fluctuations self-consistently drive evolution of the mean fields. The motivation for this method is two-fold. Firstly, despite being a rather recent subject, direct statistical simulation – the method of simulating flow *statistics* rather than an individual realization – has proven to be a useful computational technique in understanding large-scale structure generation across a variety of applications in geophysics, fluid dynamics and

plasma physics.¹ An equilibrium of the system is in general a *turbulent* state, and analysis of its stability properties and bifurcations can be very rewarding. This idea of studying the stability of turbulence to large-scale perturbations is very similar to those developed in mean-field dynamo theory, a connection that will be explored further in later chapters. Secondly, fully developed MRI turbulence is incredibly complex and there may be much useful insight to be gained by selectively removing important physical effects in the hope of discovering underlying principles. Based on the idea that nonmodal linear growth can be an important turbulence driver at all scales, the quasi-linear model involves neglecting almost all of the nonlinear interactions in the system and can easily be systematically reduced further for the study of specific effects.

Remarkably, despite the strongly reduced nonlinearity, the qualitative dependence of saturated CE2 states on magnetic Prandtl number (P_m) is the same as nonlinear MRI turbulence. In particular, at fixed magnetic Reynolds number (R_m), an increase in P_m causes an increase in the intensity of the turbulence (as measured by the angular momentum transport), despite the fact that the system is becoming more dissipative. This illustrates that the strong P_m dependence of MRI turbulence (Fromang *et al.*, 2007) is (at least partially) due to increased large-scale dynamo action at higher P_m ; this is the only physical effect retained in the CE2 model beyond simple excitation of linear waves (which show the opposite trend). As discussed, CE2 is well suited to the study of bifurcations between turbulent states of the system. We shall see two important bifurcations – the first marking the onset of a dynamo instability of homogenous turbulence, the second a transition to a time-dependent state – and the P_m dependence of several aspects of these transitions is strongly suggestive. The hope is that gaining insight into the cause of such behavior will allow extrapolation to the most astrophysically relevant low/high P_m regimes. The basic idea of the model is similar to the inhomogenous shearing waves studied in Lesur and Ogilvie (2008a) and Lesur and Ogilvie (2008b), extended to include self-consistent nonlinear saturation and the effects of B_x and

¹See, for example, Farrell and Ioannou (2003), Srinivasan and Young (2012), and Tobias and Marston (2013) for geophysical applications; Farrell and Ioannou (2012) for application to shear flows; Farrell and Ioannou (2009) and Parker and Krommes (2013) for application to plasma physics; Tobias *et al.* (2011) for other astrophysical applications.

the large-scale velocity fields. Note that the approach is quite distinct from, and complementary to, other nonlinear dynamics work on MRI dynamo (Rincon *et al.*, 2007; Riols *et al.*, 2013), which has focused on searching for cycles in the full nonlinear system at low R_m . Strong similarities can be drawn between the nonlinear cycles identified in these works and magnetic field generation in our CE2 model (Farrell and Ioannou, 2012).

The chapter proceeds as follows. I shall first outline the model, giving a very basic overview of the CE2 method, before describing our computational implementation and the CE2 MRI equations in more detail. I then discuss the MRI dynamo instability as seen in self-consistent statistical simulations of MRI turbulence (published in Squire and Bhattacharjee 2015a). Finally, I shall briefly explore the saturation mechanism of the instability through calculation of the electromotive force (EMF) as a function of mean fields in the nonlinear regime. This discussion, while incomplete, can serve as a basic extension to the model of Lesur and Ogilvie (2008a) and Lesur and Ogilvie (2008b).

3.1 The CE2 method and numerical implementation

The starting point of our study is the local incompressible MHD equations in a shearing background in the rotating frame, repeated here for convenience,

$$\frac{\partial \mathbf{u}}{\partial t} - Sx \frac{\partial \mathbf{u}}{\partial y} + (\mathbf{u} \cdot \nabla) \mathbf{u} + 2\Omega \hat{\mathbf{z}} \times \mathbf{u} = -\nabla p + \mathbf{B} \cdot \nabla \mathbf{B} + Su_x \hat{\mathbf{y}} + \bar{\nu} \nabla^2 \mathbf{u} + \boldsymbol{\sigma}_u, \quad (3.1a)$$

$$\frac{\partial \mathbf{B}}{\partial t} - Sx \frac{\partial \mathbf{B}}{\partial y} = -SB_x \hat{\mathbf{y}} + \nabla \times (\mathbf{u} \times \mathbf{B}) + \bar{\eta} \nabla^2 \mathbf{B} + \boldsymbol{\sigma}_B, \quad (3.1b)$$

$$\nabla \cdot \mathbf{u} = 0, \quad \nabla \cdot \mathbf{B} = 0, \quad (3.1c)$$

where $\boldsymbol{\sigma}_u$ and $\boldsymbol{\sigma}_b$ describe a driving noise, which is needed in CE2 but would not be included in a self-sustaining nonlinear simulation. A description of the derivation of Eq. (3.1) can be found in Sec. 1.1.3. Equation (3.1) has been written explicitly in terms of Ω and S , with $S/\Omega = q$, for

compatibility with studies of rotation in the following chapters²; however, in this chapter I focus exclusively on Keplerian rotation with $\Omega = 1$, $S = 1.5$. Throughout this chapter I consider a homogenous background (no vertical stratification), with zero net magnetic flux, and use an aspect ratio $(L_x, L_y, L_z) = (1, \pi, 1)$. Despite its linear stability, this system can undergo subcritical transition to a turbulent state and seems to be the simplest system with application to turbulence in disks (Hawley *et al.*, 1995; Balbus and Hawley, 1998).

The cornerstone of our application of CE2 to MRI turbulence is a splitting of Eq. (3.1) into its mean and fluctuating parts, defined by the horizontal average, $\overline{f(\mathbf{x})}(z) \equiv (L_x L_y)^{-1} \int dx dy f(\mathbf{x})$. This averaging is chosen because it is the simplest possible that allows for the strong z -dependent B_y observed in nonlinear simulations (Brandenburg *et al.*, 1995; Hawley *et al.*, 1996; Lesur and Ogilvie, 2008b). Before giving details of MRI CE2 and the computational implementation, it is useful to describe the CE2 system schematically. Let us represent the state of the system $(\mathbf{u}, \mathbf{B}, P)$ as U , and decompose of Eq. (3.1) into equations for \bar{U} and $u' = U - \bar{U}$, in a similar way to mean-field theory (see Sec. 1.2). This gives

$$\partial_t \bar{U} = \mathcal{A}_{\text{mean}} \cdot \bar{U} + \overline{\mathcal{R}(u', u')}, \quad (3.2a)$$

$$\partial_t u' = \mathcal{A}_{\text{fluct}}(\bar{U}) \cdot u' + \left\{ \mathcal{R}(u', u') - \overline{\mathcal{R}(u', u')} \right\} + \xi_t, \quad (3.2b)$$

where $\mathcal{A}_{\text{mean}}$ and $\mathcal{A}_{\text{fluct}}(\bar{U})$ are the linear operators for the mean and fluctuating parts, $\mathcal{R}(u', u')$ represents the nonlinear stresses, and ξ_t is an additional white-in-time driving noise term. Note that there is no nonlinear term in the mean equation [Eq. (3.2a)] because of the chosen averaging operation, which kills terms of the form $\bar{U} \cdot \nabla \bar{U}$. The principle approximation, which is key to CE2 and leads to the *quasi-linear* system, is to neglect the eddy-eddy nonlinearity $\left\{ \mathcal{R}(u', u') - \overline{\mathcal{R}(u', u')} \right\}$ in Eq. (3.2b), causing the only nonlinearity to arise from the coupling to Eq. (3.2a).

²As defined here (to comply with astrophysical conventions), S is the *negative* of the large-scale vorticity, $S = -(\nabla \times \mathbf{U}_0)_z$.

As a side note, it is worth briefly discussing the role of the driving noise ξ_t in the quasi-linear system Eq. (3.2). Two different philosophies exist in the literature. The first – which is followed in the work of Marston, Tobias, and coworkers – is that the noise arises from some physical source, which would also be present in the nonlinear system. This could be some linear instability not included in a simplified model, mechanical stirring, or another more complex physical effect that is more easily modeled using a white-noise source. The second – which is followed in works by Farrell, Ioannou, and coworkers – is that the noise acts as a simple closure term, representing (in a very crude way) the effects of the neglected nonlinear terms $\{\mathcal{R}(u', u') - \overline{\mathcal{R}(u', u')}\}$. This idea is based on the hypothesis that the exact form of the nonlinear interactions should not be vitally important, but rather their effect in populating the full range of scales. The most obvious problem with this is that the noise cannot be chosen to retain energy conservation in the model. In particular, in real turbulence, some modes must act as sources of energy for others, which cannot be taken into account by such a simple closure. In this work, the two philosophies are mixed, with this chapter primarily following the second, while the dynamo studies in chapter 4 are more aligned with the first. In particular, throughout this chapter, the noise will be kept at a fixed level and extend across all scales, to create a bath of turbulent fluctuations. Of course, there is no fundamental difference in practical implementation between the two philosophies, except perhaps in the chosen spatial correlation of the driving noise.

Rather than evolving the non-deterministic Eq. (3.2b), the idea of CE2 is to consider the single-time correlation matrix of an ensemble of fluctuations $\mathcal{C}_{ij}(\mathbf{x}_1, \mathbf{x}_2, t) = \langle u'_i(\mathbf{x}_1, t) u'_j(\mathbf{x}_2, t) \rangle$, where $\langle \cdot \rangle$ denotes the average over realizations of ξ_t . Multiplying Eq. (3.2b) by $\partial_t u(\mathbf{x}_2)$ followed by an ensemble average leads to (see App. B),

$$\partial_t \mathcal{C} = \mathcal{A}_{\text{fluct}}(\bar{U}) \cdot \mathcal{C} + \mathcal{C} \cdot \mathcal{A}_{\text{fluct}}(\bar{U})^\dagger + \mathcal{Q}, \quad (3.3)$$

where $\langle \xi_t(\mathbf{x}_1, t) \xi_t(\mathbf{x}_2, t) \rangle = \mathcal{Q}(\mathbf{x}_1 - \mathbf{x}_2) \delta(t - t')$ specifies the spatial correlation of the noise.³ As written Eq. (3.3) is six-dimensional, but by using homogeneity in x and y it can be reduced to four dimensions with the change of variables $x = x_1 - x_2$, $y = y_1 - y_2$. In addition, by assuming ergodicity – the equivalence of the horizontal and ensemble averages – the nonlinear stresses $\overline{\mathcal{R}(u', u')}$ in the mean-field equations [Eq. (3.2a)] can be calculated directly from \mathcal{C} . We thus arrive at

$$\partial_t \bar{U} = \mathcal{A}_{\text{mean}} \cdot \bar{U} + \overline{\mathcal{R}(\mathcal{C})}, \quad (3.4a)$$

$$\partial_t \mathcal{C}(x, y, z_1, z_2; t) = \mathcal{A}_{\text{fluct}}(\bar{U}) \cdot \mathcal{C} + \mathcal{C} \cdot \mathcal{A}_{\text{fluct}}(\bar{U})^\dagger + \mathcal{Q}, \quad (3.4b)$$

which is a schematic representation of the CE2 system solved throughout this work. The complexity of the system is hidden in the linear operator $\mathcal{A}_{\text{fluct}}$, which contains all details of the evolution of a shearing wave in inhomogenous U and B fields. Aside from the noise, conservation laws are inherited from the nonlinear system (e.g., energy, magnetic helicity).

Before continuing, let me note an important, but somewhat subtle, point regarding the differences between the CE2 and quasi-linear system. This difference arises when we equate the horizontal and ergodic averages to enable the insertion of nonlinear stresses into the mean-field equations. This is not the same as taking an ensemble average of individual realizations of the quasi-linear system [Eqs. (3.2a) and (3.2b)], since such an average also includes realizations of the mean field itself. In fact, there does not seem to be any exact correspondence between the dynamics of the two except in certain cases, for instance, when the mean field is zero. For this reason, one should be careful with equating CE2 dynamics to the dynamics of the quasi-linear system, particularly when a CE2 calculation does not reach a time-independent steady state. The

³ Equation (3.3), the basis for the CE2 system, can also be derived as a truncation of the cumulant expansion (in an inhomogenous background) at second order (Tobias *et al.*, 2011). This can be generalized to yield higher-order statistical equations that are often similar to inhomogenous versions of well known closure models, e.g., the eddy-damped quasi-normal Markovian approximation (Marston, 2012).

quasi-periodic oscillations seen in the saturated state of MRI will thus be considered an indication that the time-independent saturated state is unstable, or that no simple turbulent equilibrium exists (Farrell and Ioannou, 2012). Alternatively, if similar dynamics are observed in the quasi-linear and CE2 evolution, this is an indication that fluctuations in the nonlinear stress $\mathcal{R}(u', u')$ about its mean are not of fundamental importance for the dynamics of the system. More information and discussion can be found in Farrell and Ioannou (2014), as well as in Bouchet *et al.* (2013), where the authors consider more explicitly how fluctuations in $\mathcal{R}(u', u')$ can be added into the dynamics of U . In chapter 4 I shall give examples in which there is a marked difference between the quasi-linear and CE2 evolutions. This arises because the large-scale dynamo is primarily driven by fluctuations in the nonlinear stresses.

3.1.1 Details and computational implementation

In this section I describe details of the CE2 scheme for the unstratified shearing box, including the computational implementation. In addition, looking forward to the studies in chapters 4-6, I will describe the direct quasi-linear simulation (DQLS) code, since the implementation is similar to CE2 and it is sensible to describe both together. I shall start by giving the basic mean-field and fluctuation equations, then describe the reduced variable set and the implementation in Fourier space using Fast Fourier Transforms (FFTs). Finally I shall give details of the C++ class structure, parallelization, and use of *Mathematica* for automatic code generation.

For the MRI problem of interest here, the mean-field equations become

$$\begin{aligned}
 (\partial_t - Sx\partial_y) \mathbf{U} &= -2\Omega\hat{\mathbf{z}} \times \mathbf{U} + SU_x\hat{\mathbf{y}} \\
 &\quad + \bar{\nu}\partial_z^2\mathbf{U} - \langle \mathbf{u} \cdot \nabla \mathbf{u} \rangle + \langle \mathbf{b} \cdot \nabla \mathbf{b} \rangle,
 \end{aligned} \tag{3.5a}$$

$$(\partial_t - Sx\partial_y) \mathbf{B} = -SB_x\hat{\mathbf{y}} + \bar{\eta}\partial_z^2\mathbf{B} + \nabla \times \langle \mathbf{u} \times \mathbf{b} \rangle, \tag{3.5b}$$

$$\partial_z B_z = \partial_z U_z = 0, \tag{3.5c}$$

and the fluctuating equations are

$$(\partial_t - Sx\partial_y) \mathbf{u} = -2\Omega\hat{\mathbf{z}} \times \mathbf{u} + Su_x\hat{\mathbf{y}} + \bar{\nu}\nabla^2\mathbf{u} - \nabla p \\ - (\mathbf{u} \cdot \nabla\mathbf{U} + \mathbf{U} \cdot \nabla\mathbf{u}) + (\mathbf{B} \cdot \nabla\mathbf{b} + \mathbf{b} \cdot \nabla\mathbf{B}) + \boldsymbol{\sigma}_u, \quad (3.6a)$$

$$(\partial_t - Sx\partial_y) \mathbf{b} = Sb_x\hat{\mathbf{y}} + \bar{\eta}\nabla^2\mathbf{b} + \nabla \times (\mathbf{u} \times \mathbf{B}) + \nabla \times (\mathbf{U} \times \mathbf{b}) + \boldsymbol{\sigma}_b, \quad (3.6b)$$

$$\nabla \cdot \mathbf{u} = 0, \quad \nabla \cdot \mathbf{b} = 0. \quad (3.6c)$$

Note that from hereon, for simplicity of notation, I shall use bare capital letters for the mean field (i.e., dispense with the overbar), and lower-case letters for the fluctuating fields.

The CE2 equations will not be written out explicitly due to their complexity. They can be straightforwardly (if tediously) derived by multiplying Eq. (3.6) by $\mathbf{u}(t)$ and $\mathbf{b}(t)$ before taking the ensemble average. Following the reduction in dimensionality due to the homogeneity, and removal of the pressure using the divergence constraint in x and y , this leads to an equation for

$$\frac{\partial}{\partial t} \mathcal{C}(x, y, z_1, z_2) = \frac{\partial}{\partial t} \begin{pmatrix} \langle u_i u_j \rangle & \langle u_i b_j \rangle \\ \langle b_i u_j \rangle & \langle b_i b_j \rangle \end{pmatrix}, \quad (3.7)$$

for $i, j = 1 \rightarrow 3$. In general, it has been more convenient to consider the operator form of the equations for \mathcal{C} [see Eq. (3.3), as well as Eq. (3.11) below] and utilize the reduced variable set (described below).

I shall work exclusively in the shearing frame for both CE2 and DQLS, in which the x dependence of Eqs. (3.5) and (3.6) disappears and the shearing periodic boundary conditions become periodic boundary conditions. The sheared variables (X, Y, Z, T) are defined by

$$X = x, \quad Y = y + Stx, \quad Z = z, \quad T = t \\ \implies \partial_x \rightarrow \partial_X + ST\partial_Y, \quad \partial_y \rightarrow \partial_Y, \quad \partial_z \rightarrow \partial_Z, \quad \partial_t \rightarrow \partial_T + SX\partial_Y, \quad (3.8)$$

which, when substituted into the sheared MHD equations [Eq. (3.1)] or the quasi-linear equations [Eqs. (3.5) and (3.6)], lead to the cancelation of the x dependence. The price of this simplification is an explicit wavevector, which is introduced through $\partial_x \rightarrow \partial_X + ST\partial_Y$. While this is easily handled by defining the operator $\bar{\partial}_x = \partial_X + ST\partial_Y$, which in Fourier space becomes $\bar{k}_x = k_x + STk_y$, a *remapping* procedure (described below) is necessary to keep the radial wavenumbers near the range $\pi/L_x(-N_x, N_x)$. If this is not done, dissipation will quickly overwhelm the simulation as k^2 increases in time.

Reduced variables

Since it is necessary to solve for correlations between all variables, any CE2 algorithm will necessarily scale with m^2 , where m is the number of variables. Because of this, and due to the convenience of eliminating the pressure, the equations for \mathcal{C} are cast in terms of the variables⁴ $u \equiv u_X$, $b \equiv b_X$, $\zeta \equiv \partial_Z u_Y - \partial_Y u_Z$, $\eta \equiv \partial_Z b_Y - \partial_Y b_Z$. These variables were also utilized in various forms in the linear studies in chapter 2 and have become standard in hydrodynamic shear flow simulation (Kim *et al.*, 1987; Lee *et al.*, 2013), although they are not commonly used in the astrophysics community.

The primary downside of the reduced variable set is that the equations become significantly more complex, particularly in real space. Their derivation proceeds by noting the relationship

$$\begin{aligned} \Delta_2 u_Y &= -\bar{\partial}_x \partial_Y u + \partial_Z \zeta, & \Delta_2 u_Z &= -\bar{\partial}_x \partial_Z u - \partial_Y \zeta, \\ \Delta_2 b_Y &= -\bar{\partial}_x \partial_Y b + \partial_Z \eta, & \Delta_2 b_Z &= -\bar{\partial}_x \partial_Z b - \partial_Y \eta, \end{aligned} \quad (3.9)$$

where $\Delta_2 \equiv \partial_Y^2 + \partial_Z^2$. Inverting Δ_2 , one inserts these definitions into Eq. (3.6) and forms $\partial_Z \partial_T u_y - \partial_Y \partial_T u_z$ (and $\partial_Z \partial_T b_y - \partial_Y \partial_T b_z$), before applying the operator $\nabla^2 - \nabla \nabla \cdot ()$ to the u equation to

⁴ Note that η is used as a variable here, distinguished from the resistivity by the lack of an overbar.

where $\mathcal{C} = \phi \phi^\dagger$ is now a 4×4 matrix in the reduced variable set.

Equation (3.12) is already formidable in length, and the inclusion of other mean-field variables in addition to B_y renders $\mathcal{A}_{\text{fluct}}$ significantly more complex. Thus to save work and mitigate human error, automatic code generation is used in the CE2 implementation, which will be described below. For DQLS it is simpler to first calculate $(u_x, u_y, u_z, b_x, b_y, b_z)$ using Eq. (3.9), and then form the products $\mathbf{U} \cdot \nabla \mathbf{u}$, $\mathbf{u} \cdot \nabla \mathbf{U}$, $\mathbf{B} \cdot \nabla \mathbf{u}$, \dots directly, converting back to (u, ζ, b, η) before advancing in time. The reduced variable set still has significant advantages in reducing memory usage and interprocessor communication.

Using Eq. (3.9) it is straightforward to calculate the fluctuation energy as

$$E = \frac{1}{2} \int d\mathbf{x} (\mathbf{u}^2 + \mathbf{b}^2) = \frac{1}{2} \int d\mathbf{x} [\bar{\Delta} \Delta_2^{-1} (u^2 + b^2) + \Delta_2^{-1} (\zeta^2 + \eta^2)]. \quad (3.13)$$

The angular momentum transport and energy dissipation can easily be calculated from similar expressions. For CE2, these are calculated by applying appropriate operators to the \mathcal{C} matrix (described below).

Fourier space implementation

As with nonlinear fluid equations, the CE2 and DQLS equations are particularly convenient to solve in Fourier space, since derivatives involve simple multiplication and FFT algorithms can be used. Further, noting the linear operator $\mathcal{A}_{\text{fluct}}$ has no x or y dependence, one can split Eq. (3.10) into $N_x \times N_y$ separate equations for each Fourier mode, with the replacements $\partial_Y \rightarrow ik_y$, $\bar{\partial}_x \rightarrow i\bar{k}_x = ik_x + iSTk_y$. This is particularly convenient both conceptually and computationally, since it renders the system very easily parallelizable. It is then necessary to calculate the operator matrices $\mathcal{A}_{\text{fluct}}(k_x, k_y, U)$ (where U represents all mean fields), which can be achieved with $\mathcal{O}(4N_z)$ one-dimensional Fourier transforms, each of length $\mathcal{O}(4N_z)$, for each (k_x, k_y) pair.⁶ Thus the equation

⁶Note that as described, this is the *spectral* method, rather than the pseudo-spectral method.

for \mathcal{C} becomes

$$\partial_t \mathcal{C}_{k_x, k_y} = \mathcal{A}_{\text{fluct}}(k_x, k_y, U) \cdot \mathcal{C}_{k_x, k_y} + \mathcal{C}_{k_x, k_y} \cdot \mathcal{A}_{\text{fluct}}(k_x, k_y, U)^\dagger + \mathcal{Q}_{k_x, k_y}, \quad (3.14)$$

where \mathcal{C}_{k_x, k_y} is now a $4N_z \times 4N_z$ matrix in Fourier space. The matrix $\mathcal{A}_{\text{fluct}}(k_x, k_y, U)$ must be recalculated at every time step due to its dependence on the mean fields.

Throughout this thesis, the noise is chosen such that each mode with wavenumber $k = |\mathbf{k}|$ in some chosen range, $k_{c, \text{lower}} < k < k_{c, \text{upper}}$, is driven equally in energy. More precisely (Farrell and Ioannou, 2012), I choose \mathcal{Q}_{k_x, k_y} such that in equilibrium all modes are in equipartition if the linear operator is chosen to cause constant damping across all wavenumbers, $\mathcal{A}_{\text{fluct}} = I/(2r)$. Noting that the derivative operators in the fluctuation energy [Eq. 3.13] become diagonal in the Fourier basis, which implies

$$E = \frac{1}{N_x^2 N_y^2 N_z^2} \sum_{k_x, k_y} \text{Tr}(M_{k_x k_y} \mathcal{C}_{k_x k_y}) \quad (3.15)$$

for

$$M_{k_x k_y} = \begin{pmatrix} \bar{\Delta} \Delta_2^{-1} & 0 & 0 & 0 \\ 0 & \Delta_2^{-1} & 0 & 0 \\ 0 & 0 & \bar{\Delta} \Delta_2^{-1} & 0 \\ 0 & 0 & 0 & \Delta_2^{-1} \end{pmatrix}, \quad (3.16)$$

we see that the diagonal matrix $\mathcal{Q}_{k_x k_y} = f_\xi^2 M_{k_x k_y}^{-1}$ is the required driving “noise.” Here f_ξ is simply a constant to control the driving strength, and it is easy to enforce $k_{c, \text{lower}} < k < k_{c, \text{upper}}$ by simply zeroing out elements of $\mathcal{Q}_{k_x k_y}$. The noise in DQLS is generated using a random number generator with the relative strengths of various wavenumbers controlled by $\mathcal{Q}_{k_x k_y}$. Since the noise is generated in Fourier space, it is important to ensure its inverse transform is real by enforcing appropriate symmetries.

The final remaining step in solving the CE2 or DQLS equations involves the mean-field equations, which should be solved simultaneously with the fluctuation equations. Solving these in 1-D Fourier space, the only step of any difficulty is the calculation of the nonlinear stresses arising from the fluctuations, $-\langle \mathbf{u} \cdot \nabla \mathbf{u} \rangle + \langle \mathbf{b} \cdot \nabla \mathbf{b} \rangle$ and $\nabla \times \langle \mathbf{u} \times \mathbf{b} \rangle$. In the case of DQLS these can be easily calculated by forming \mathbf{u} and \mathbf{b} to give $-\overline{\mathbf{u} \cdot \nabla \mathbf{u}} + \overline{\mathbf{b} \cdot \nabla \mathbf{b}}$ and $\nabla \times \overline{\mathbf{u} \times \mathbf{b}}$. Despite appearances, these products do not require Fourier transforms in the x and y directions, since the $k_x = k_y = 0$ component of the Fourier transform of the product (i.e., the Fourier transform in the z direction of the mean over x and y) can be simply related to the sum of the products calculated for each Fourier mode separately. This is very important for reducing communication between processes and also removes the necessity of dealiasing operations in the k_x and k_y dimensions (since no transforms are ever performed along these directions).

For CE2, calculation of the nonlinear stresses is less intuitive, but can be achieved through application of matrix operators to the \mathcal{C} matrix. For example, to compute $\langle b_x \bar{\partial}_x u_x \rangle$, one forms the operators

$$L_{k_x k_y}^{b_x} = (0, 0, I_{N_z}, 0)^T, \quad L_{k_x k_y}^{\bar{\partial}_x u_x} = (i \bar{k}_x I_{N_z}, 0, 0, 0)^T, \quad (3.17)$$

(where I_{N_z} is the $N_z \times N_z$ identity matrix) and uses

$$\begin{aligned} \langle b_x \bar{\partial}_x u_x \rangle_{k_x k_y} &= \frac{1}{2} \text{diag} \left\{ (b_x)_{k_x k_y} (\bar{\partial}_x u_x)_{k_x k_y}^\dagger \right\} = \frac{1}{2} \text{diag} \left\{ \langle (L_{k_x k_y}^{b_x} \phi_{k_x k_y}) (L_{k_x k_y}^{\bar{\partial}_x u_x} \phi_{k_x k_y})^\dagger \rangle \right\} \\ &= \frac{1}{2} \text{diag} \left\{ L_{k_x k_y}^{b_x} \langle \phi_{k_x k_y} (\phi_{k_x k_y})^\dagger \rangle (L_{k_x k_y}^{\bar{\partial}_x u_x})^\dagger \right\} = \frac{1}{2} \text{diag} \left\{ L_{k_x k_y}^{b_x} \mathcal{C}_{k_x k_y} (L_{k_x k_y}^{\bar{\partial}_x u_x})^\dagger \right\}. \end{aligned} \quad (3.18)$$

Here $\text{diag} \{ \cdot \}$ represents the diagonal components of the matrix. Only diagonal components needed because the nonlinear stresses involve correlations between variables at the same points in space [i.e., $\mathbf{u}(\mathbf{x}) \cdot \nabla \mathbf{u}(\mathbf{x})$ rather than $\mathbf{u}(\mathbf{x}) \cdot \nabla \mathbf{u}(\mathbf{x}')$]. To form the full set of nonlinear stresses, one first converts all quadratic products (e.g., $\mathbf{u} \cdot \nabla \mathbf{b}$) into equivalent forms in the (u, ζ, b, η) vari-

ables, then converts this into the sum of operators on \mathcal{C} . Again, it is possible to calculate each k_x , k_y separately and sum the result, avoiding global Fourier transforms.

I have so far neglected to discuss the consequences of the shearing frame, simply replacing any mention of k_x with $\bar{k}_x = k_x + STk_y$. In practice, little more than this replacement is required except for a *remapping* procedure, which is necessary to keep radial wavenumbers from continuously growing in time (as would be the case if $\bar{k}_x = k_x + STk_y$ were naively applied with no modification). I use a very simple method, similar to that proposed in Lithwick (2007), which relies on the idea that in a finite domain (of length L_x , discretized by N_x Fourier modes), the wavenumbers k_x and $k_x + pN_x(2\pi/L_x)$, $p \in \mathbb{Z}$ describe the same mode due to aliasing. Thus, when a $\bar{k}_x(t)$ grows sufficiently that it falls outside the range $2\pi/L_x(-N_x/2, N_x/2)$, one simply subtracts $N_x(2\pi/L_x)$ to remap it back into the correct range, then sets the amplitude of the mode to zero.⁷ This procedure is done at every time step and does not require moving data in any way, but simply a relabeling of the wavenumber attached to a given mode. The ability to carry out the remapping in such a simple manner relies on not having to take Fourier transforms in the x direction (otherwise it would be necessary to move modes in memory). In addition, the method requires an odd number of Fourier modes to be used in the x direction, since there can be no Nyquist mode. This requirement makes no difference for the quasi-linear system (in fact it is better to exclude the Nyquist mode), but is inconvenient for a fully nonlinear code where transforms must be taken in three directions.

Numerical implementation

In this section I will briefly describe aspects of the numerical implementation for the DQLS and CE2 codes. The codes are written in C++ and based on the *Eigen* (Guennebaud *et al.*, 2010) and FFTW (Frigo and Johnson, 2005) libraries. Rather than storing the data as a large contiguous 3-D array (or some distributed generalization of this) as would be standard in a nonlinear code, it is more convenient to store fluctuation data as an $N_x \times N_y$ array of $(4N_z)^2$ matrices (for CE2), or

⁷Without setting the mode to zero, trailing waves would be unphysically converted into leading waves.

$4N_z$ vectors (for DQLS). The wavenumber pairs (k_x, k_y) are then stored in separate arrays for each element. Both codes are organized into class structures that make it very easy to change the time integrators or solve different systems of equations. In both the CE2 and DQLS codes, the standard time integrator is a third-order Runge-Kutta scheme (Lundbladh *et al.*, 1992) with a variable time step calculated from the Courant condition. Dissipation terms are treated implicitly so as to reduce the time-step restriction that arises through terms with k^2 dependence.

It is worth briefly explaining some optimizations that together have led to relatively significant gains in computational speed. Firstly, as noted previously, dealiasing is unnecessary in the x and y directions, which leads to gains of $(3/2)^2$ in storage and computation for CE2. Similarly, since the real-space equations have no imaginary part, only half of the Fourier modes must be considered. In practice, this is most easily achieved by only considering modes for which $k_y > 0$, ensuring that this is correctly accounted for in reductions (e.g., nonlinear stresses) by counting modes twice if $k_y \neq 0$. Although I described the Fourier space implementation in the discussion above in terms of the spectral method (explicit calculation of the operators $\mathcal{A}_{\text{fluct}}$), in practice it is somewhat faster to use the pseudo-spectral method. Here, Fourier transforms are used directly on the \mathcal{C} matrix, rather than forming $\mathcal{A}_{\text{fluct}}$ and using matrix multiplication.⁸

One disadvantage of the pseudo-spectral method is that the code for the CE2 time advance becomes more complex, and this motivated the use of *Mathematica* to automatically generate C++ code. This allowed the very complex CE2 equations⁹ to be easily input into a “Model” class structure in C++, greatly reducing the possibility of human error. In addition, through enabling the use of a more direct calculation of \mathcal{C} evolution (the pseudo-spectral rather than spectral method), automatic code generation resulted in substantial speed improvements. Finally, an obvious ben-

⁸ As is well known, the gain of the pseudo-spectral method over the spectral method is enormous for direct numerical simulation, and it is an obvious choice for DQLS. However, the difference is much less substantial in CE2, the reason being that fewer Fourier transforms are required to form $\mathcal{A}_{\text{fluct}}$ than to calculate directly its operation on \mathcal{C} (only 1-D transforms are required to form $\mathcal{A}_{\text{fluct}}$, while 2-D transforms are required for pseudo-spectral evolution). In practice, use of the pseudo-spectral method reduced computation time by approximately a factor of 2.

⁹Consider Eq. (3.11), with the addition of three other mean fields and z derivatives up to third order!

efit is the ease with which new models may be studied, by simply generating a new equation set and copying this directly to the existing class structure. The method, coded as a *Mathematica* notebook, starts from the nonlinear MHD equations in standard variables [Eq. (3.1)], calculates the quasi-linear equations, converts to the reduced variable set, and then explicitly forms the matrix operator $\mathcal{A}_{\text{fluct}}$. It then calculates the operator product $\mathcal{A}_{\text{fluct}}\mathcal{C} + \mathcal{C}\mathcal{A}_{\text{fluct}}^\dagger$, determining which operations must be performed using Fourier transforms (i.e., products of fluctuations with mean fields) and automatically creating sets of temporary variables for necessary intermediate calculations. A `C++` pseudo-code is then generated, which involves only operations that are able to be performed numerically. Finally, this is converted into a string of text using replacement rules, and this can be copied directly into the `C++` file. As a measure of the labor saved through this procedure, $\mathcal{A}_{\text{fluct}}\mathcal{C} + \mathcal{C}\mathcal{A}_{\text{fluct}}^\dagger$ amounts to over 600 lines of `C++` code when the effect of all mean fields is included.

The parallelization of both the CE2 and DQLS codes, which is achieved using the Message Passing Interface (MPI), is straightforward. At each time step, a single sum across processors is needed to form the nonlinear stresses required for mean-field evolution. These stresses contain $m_{\text{MF}}N_z$ real elements (where m_{MF} is the number of mean fields), so the amount of data movement is almost always minimal in comparison to the total stored on each process (particularly for CE2). This reduction is achieved using a single call to the MPI function `MPI_Allreduce`, which passes the result of the summation across processes to all processes (this is necessary since the mean fields must be stored on all processes). Similarly, global quantities such as energy, angular momentum, and dissipation, can be calculated through single scalar reduction after calculating quantities separately on each process. In fact, the trickiest aspect of parallelization was the generation of DQLS noise, which is complex but must have the correct symmetries in Fourier space.¹⁰ This is carried out by having modes store a “partner’s” location using `C++` iterators and only generating a random number once for each pair. Global input/output operations (e.g., dumping of the

¹⁰Generating noise in real space and converting back would be very harmful to the parallelization.

full solution) are carried out in parallel, using the HDF5 library (The HDF Group, 2010) for the DQLS code, and through the creation of separate files for each process for the CE2 code. In the work presented in this thesis, I have run the CE2 code on up to 256 processors with no obvious degradation from linear scaling with processor number. This has allowed calculations with resolutions up to $80 \times 160 \times (4 \times 128)^2$ ($\sim 3.4 \times 10^9$ elements) to be completed without excessively long computations.

Throughout the writing of the quasi-linear codes, I have verified their correctness, to the extent possible. Most straightforwardly, I have tested energy conservation in both codes through calculation of

$$\partial_t E_T = S \langle U_{Tx} U_{Ty} \rangle - S \langle B_{Tx} B_{Ty} \rangle - \bar{v} \langle (\nabla \times \mathbf{U}_T)^2 \rangle - \bar{\eta} \langle (\nabla \times \mathbf{B}_T)^2 \rangle, \quad (3.19)$$

for evolution in the absence of driving. In addition, the comparison between DQLS and CE2 evolution provides a relatively thorough check of the codes correctness, since each implements the equations quite differently. The most stringent check comes from initializing $\mathcal{C}_{k_x k_y}$ as a product state

$$\mathcal{C}_{k_x k_y} = \phi_{k_x k_y} (\phi_{k_x k_y})^\dagger, \quad (3.20)$$

in which case its evolution under CE2 is the same as that of $\phi_{k_x k_y} (\phi_{k_x k_y})^\dagger$, with $\phi_{k_x k_y}$ calculated from the quasi-linear equations. The correctness of the driving noise has been checked by taking long time averages (with fixed mean fields) of the DQLS equations and comparing to the statistics obtained from the equivalent CE2 run, as well as through extensive calculation of EMFs in fixed mean fields (see chapter 4). Finally, I have also compared results to those of Lesur and Ogilvie (2008a) and Lesur and Ogilvie (2008b), although this comparison was necessarily of a somewhat qualitative nature.

3.2 The MRI dynamo instability

In contrast to the original MHD equations [Eq. (3.1)], a general stable equilibrium of the CE2 system [Eq. (3.4)] corresponds to a statistically stationary *turbulent* state (within the quasi-linear approximation). If such an equilibrium is rendered unstable by a change in system parameters, this turbulent state is no longer possible and a rearrangement of the mean fields and flow statistics will occur. This type of instability has no counterpart in standard MHD stability theory; it pertains to the idea that the collective effect of the ensemble of fluctuating fields is to re-enforce perturbations to the mean fields through the nonlinear stresses, causing instability. Of course, such ideas are familiar in mean-field electrodynamics (Moffatt, 1978), and the method is very helpful for the more formal dynamo studies presented later in the thesis. When the mean fields are sufficiently small to be a linear perturbation to the fluctuations, our CE2 approximation is similar to the quasi-linear kinematic theory of Sridhar and Subramanian (2009) and Sridhar and Singh (2010), as well as the second-order correlation approximation of dynamo theory (see chapter 6 and Brandenburg and Subramanian 2005).

All calculations presented here are initialized with $\mathcal{C} = 0$, with the noise chosen to drive all modes equally in energy ($k_{c,\text{lower}} = 0$, $k_{c,\text{upper}} = \infty$), multiplied by the amplitude factor f_ξ . While I have explored the dependence on f_ξ , for simplicity all calculations in this chapter use the same value ($f_\xi = 4$ in the normalization used for the code) and the physical parameters Rm and Pm are varied to illustrate bifurcations of the system. For reference, this noise level drives homogenous turbulence at $\text{Rm} = 12000$, $\text{Pm} = 1$ to a mean total energy of ~ 0.05 . $\text{Rm} = 12000$ computations use the resolution¹¹ $40 \times 80 \times (4 \times 64)^2$. To ensure convergence, I have verified that doubling the resolution (to $80 \times 160 \times (4 \times 128)^2$) does not change results, for the $\text{Pm} = 1$ and $\text{Pm} = 4$ calculations.

¹¹Recall that dealiasing is not required in the x and y directions, so 40 grid points is equivalent to 60 with dealiasing.

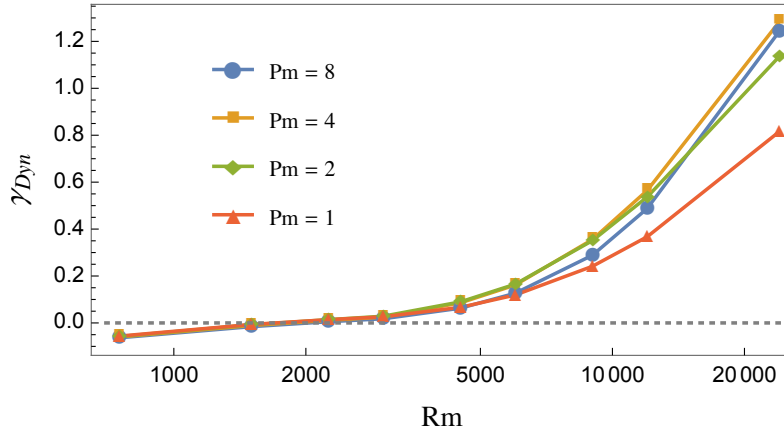


Figure 3.1: Growth rate γ_{Dyn} of the mean field, $\bar{B}_y = \bar{B}_{y0}(z) e^{\gamma_{\text{Dyn}} t}$, as a function of magnetic Reynolds number at $\text{Pm} = 1, 2, 4$ and 8 .

Homogenous turbulence, with $(\mathbf{U}, \mathbf{B}) = 0$, is the simplest nontrivial equilibrium of the CE2 MRI system, with all nonlinear stresses vanishing identically. However, at fixed noise, as Re and Rm are increased from zero this equilibrium becomes unstable around $\text{Rm} \approx 1500$ (this value depends on f_ξ). Such behavior is illustrated in Fig. 3.1, which shows the growth rate γ_{Dyn} of the dynamo instability (γ_{Dyn} is real for all cases studied here). This is calculated by first evolving Eq. (3.3) to the homogenous equilibrium by artificially removing the nonlinear feedback, then introducing a very small ($\sim 10^{-15}$) random mean field (with the amplitudes of \mathbf{U} and B_x 1/10 that of B_y). (While theoretically possible to solve for the Floquet eigenspectrum directly,¹² this is challenging due to the grid size.) Following the introduction of mean-field feedback there is a sustained period of exponential growth in $\bar{\mathbf{B}}$ for $\text{Rm} \gtrsim 1500$. The observed eigenmodes are sinusoidal in z (as is necessary due to spatial homogeneity) although not generally the largest mode in the box, satisfy $B_x \ll B_y$, and appear to have no mean velocity component,¹³ (i.e., $\mathbf{U} = 0$). While it is certainly expected that γ_{Dyn} increase strongly with Rm – fluctuations grow

¹² It would be necessary to calculate the Floquet spectrum because the system is not time independent due to the shearing boundary conditions, increasing the computational difficulty substantially.

¹³ This may not be the case at the highest Rm studied, since \mathbf{U} grows slowly but does not ever get small enough relative to \mathbf{B} to say for sure whether the eigenmode satisfies $\mathbf{U} = 0$ or just $\mathbf{U} \ll \mathbf{B}$. In either case, it is far too small to be of dynamical importance in the linear growth phase.

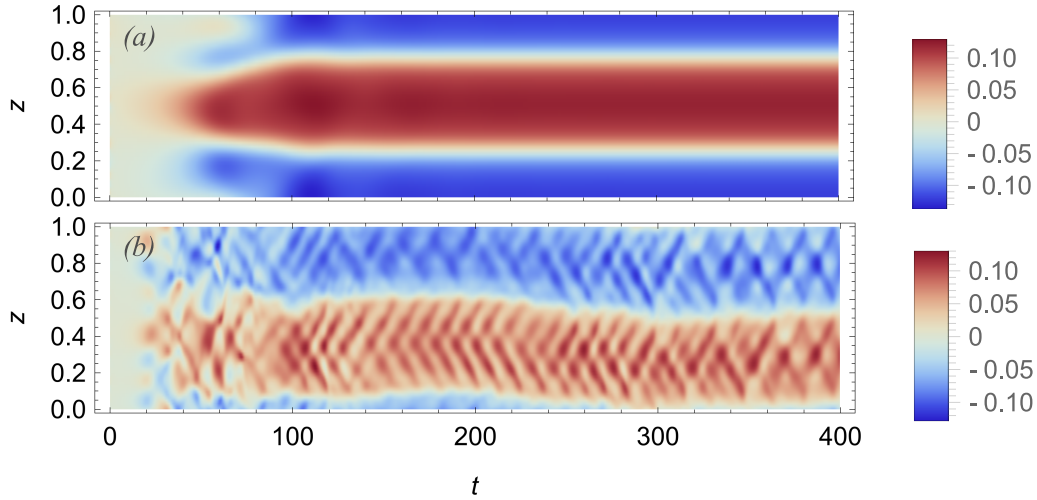


Figure 3.2: Evolution of B_y as a function of (z, t) at $P_m = 4$ for (a) $R_m = 4500$, time-independent saturated state, and (b) $R_m = 12000$, time-dependent saturated state.

to a higher amplitude and there is less \mathbf{B} dissipation – its dependence on P_m is more interesting and suggestive. An increase in P_m implies more dissipation (through increasing $\bar{\nu}$), yet Fig. 3.1 shows that γ_{Dyn} can increase, particularly at higher R_m . In addition, $\partial\gamma_{\text{Dyn}}/\partial R_m$ increases with P_m , with potentially interesting consequences for the very high R_m limit. The instability is driven by the radial stress $(\nabla \times \langle \mathbf{u} \times \mathbf{b} \rangle)_x$ causing an increase in B_x , which in turn drives B_y through the Ω effect, $-qB_y$ [see Eq. (3.5)]. The effect of the azimuthal stress $(\nabla \times \langle \mathbf{u} \times \mathbf{b} \rangle)_y$ is to damp the dynamo. This is the "shear-current effect" (Rogachevskii and Kleeorin, 2003; Brandenburg *et al.*, 2008a), which has been analyzed previously in the context of dynamo cycles in nonlinear MRI turbulence (Lesur and Ogilvie, 2008a,b), and has similarities to exact nonlinear dynamo solutions at low R_m (Rincon *et al.*, 2007; Riols *et al.*, 2013). An in-depth analysis of the shear-current effect from the standpoint of dynamo theory is the subject of chapters 4-6.

Of more relevance to fully developed turbulence are the saturation characteristics of the dynamo instability. For computational convenience, moderately strong random¹⁴ mean fields are used to initialize simulations (amplitude of $\bar{B}_y \approx 0.01$, B_x and \mathbf{U} initialized at 1/10 that of B_y).

¹⁴ The largest mode of the box has also been used for initialization, leading to similar results.

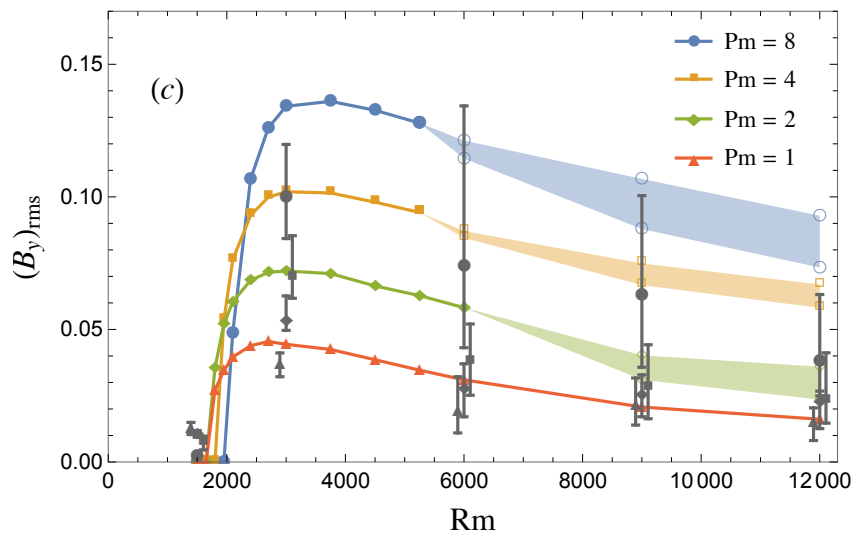


Figure 3.3: Magnitude of B_y as measured by $(B_y)_{\text{rms}} = (L_z^{-1} \int dz |B_y|^2)^{1/2}$ at saturation, as a function of Rm and Pm . The shaded regions illustrate the approximate maxima and minima of the time-dependent B_y when the system did not reach a time-independent statistical equilibrium. Gray points (point styles as for CE2 results) illustrate the mean values of equivalent driven nonlinear simulations, with error bars illustrating the approximate maxima and minima. The slight horizontal offset of $Pm = 1, 4$ points is for clarity and the same Rm is used for all Pm .

As Rm is increased and the homogenous equilibrium is rendered unstable, the system saturates to a new CE2 equilibrium with a strong background B_y that varies on the largest scale in the box, as illustrated by the example in Fig. 3.2(a). As one increases Rm further, a second bifurcation occurs, at which the inhomogenous equilibrium appears to become unstable and the system transitions to a quasi-periodic time-dependent state. An example of this state, which occurs more readily at higher Pm , is shown in Fig. 3.2(b). These two bifurcations – first to an inhomogenous state dominated by mean fields, then the loss of equilibrium of this state – bear a strong resemblance to the transitions seen in hydrodynamic plane Couette flow (Farrell and Ioannou, 2012), in which the second transition is associated with self-sustaining behavior. Such a self-sustaining process is not possible within our model due to the choice of 1-D mean fields (as opposed to 2-D in Farrell and Ioannou 2012), but the similarity as well as its Pm dependence is striking. Understanding physical mecha-

nisms behind the loss of equilibrium may give useful insights into the self-sustaining dynamo that is so fundamental to zero-net-flux turbulence.

This information is presented more compactly in Fig. 3.3, which illustrates the saturated B_y amplitude over a range of R_m , P_m . The dependence of the saturated amplitude on P_m is enormous [contrary to previous results on the large-scale dynamo (Brandenburg, 2009)], and can be well understood at low R_m using the linear properties of inhomogeneous shearing waves (see Sec. 3.3 below). Also shown is the mean azimuthal field $\overline{B_y(\mathbf{x})}(z) \equiv (L_x L_y)^{-1} \int dx dy B_y(\mathbf{x})$ (where B_y here is the full turbulent field) in driven nonlinear simulations (using noise that is statistically equivalent to that for the CE2 calculations), which shows the same trends although amplitudes are somewhat smaller. These simulations are run at a resolution $64 \times 128 \times 64$ ($R_m \leq 9000$) and $128 \times 256 \times 128$ ($R_m = 12000$) using the SNOOPY code (Lesur and Longaretti, 2007), and mean values are obtained through time averages from $t = 200 \rightarrow 400$. The large error bars on these results illustrate how statistical simulation can be very profitable for observing such trends in data. Note that in contrast to most nonlinear simulation, the driving noise extends to the smallest scales available. Interestingly, there is a marked *decrease* in the saturated amplitudes at all P_m as R_m is increased. This depends critically on the interaction of the fluctuating fields with \bar{B}_x , and seems to have a relationship to radial MRI modes contributing to the azimuthal EMF (see Sec. 3.3 below). This illustrates that some important physical effects are absent from the dynamo saturation mechanism proposed in Lesur and Ogilvie (2008b) and Lesur and Ogilvie (2008a), which only includes the effect of B_y fields on saturation.

In Fig. 3.4 I show the angular momentum transport as a function of time for the highest R_m calculations presented in Fig. 3.3. The increase in transport with P_m despite the increased dissipation is evident, suggesting a relationship between the enormous dependence of MRI turbulence on P_m (Fromang *et al.*, 2007; Fromang, 2010) and the large-scale dynamo (since this is the only physical effect included in the CE2 model beyond linear waves). While the scaling is not so pronounced as self-sustained nonlinear turbulence [see for example, Fromang *et al.* (2007) figure 7], this is to

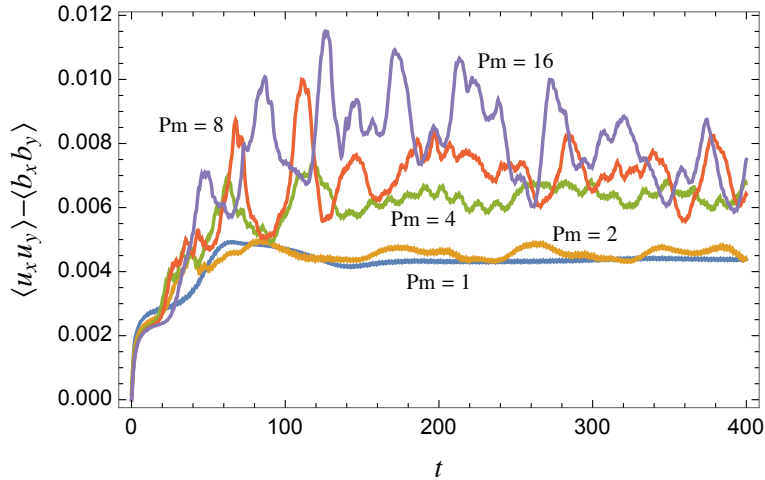


Figure 3.4: Angular momentum transport $\langle u_x u_y \rangle - \langle b_x b_y \rangle$ (including mean and fluctuating variables) as a function of time for $Rm = 12000$, $Pm = 1 \rightarrow 16$.

be expected since the CE2 calculations are driven. The scaling in our driven nonlinear simulations (see Fig. 3.3, not shown in Fig. 3.4) is similar, although the overall transport level is a factor of ~ 1.5 smaller. Note that the increase in transport is not primarily from the mean fields directly (that is, through $\langle \bar{B}_x \bar{B}_y \rangle$), but rather due to the fluctuations becoming more intense as a consequence of the stronger mean fields, despite the higher dissipation.

3.3 The saturation mechanism of the dynamo instability

In this section I give a basic explanation for the saturation of the dynamo, including aspects of its dependence on Pm . The fundamental saturation mechanism involves a nonlinear change to the dependence of the azimuthal EMF on the magnetic field, such that it damps rather than drives the dynamo. This is similar to the mechanism proposed by Lesur and Ogilvie (2008a) and Lesur and Ogilvie (2008b), but we shall see that the radial magnetic field is critical. While far from complete, this discussion serves two purposes. The first is to show that the basic saturation mechanism (including its Pm dependence) can be roughly understood through study of the EMFs calculated

from time-independent B fields.¹⁵ While not unexpected, this knowledge is important for further study, in particular from analytic or semi-analytic standpoints. The second purpose is to illustrate the fundamental importance of the radial magnetic field and the radial MRI, which was neglected in Lesur and Ogilvie (2008a) and Lesur and Ogilvie (2008b). Again, this is not wholly surprising (indeed, this is essentially a turbulent resistivity); however, its effect, especially at low P_m , is dramatic. In fact, if the CE2 system is modified to include only the effects of the B_y field on the fluctuations, the system fails to saturate above $R_m \sim 4000$, a property that is more severe at lower P_m . Instead, B_x grows to unphysically large values, causing either wild oscillations in the mean fields or a complete crash of the code. The discussion in this section addresses the interesting transition to the time-dependent equilibrium (see Fig. 3.3) only from a very qualitative standpoint. We have been unable to find a simple physical explanation for the cause of the transition, but it is likely associated with a saddle-node bifurcation (Farrell and Ioannou, 2012), implying there may be no equilibrium state above this second bifurcation.

3.3.1 Method

The method involves specifying CE2 mean fields and calculating \mathcal{C} (from $\mathcal{C} = 0$), thus finding a set of fluctuation statistics associated with the chosen mean fields. These statistics are then used to calculate the resulting EMF. Such a process is akin to calculation of the transport coefficients in standard mean-field dynamo theory, but in the nonlinear regime where the ansatz $\mathcal{E} = \alpha B + \beta \nabla B + \dots$ is far from valid. Ideally, one would be able to evolve \mathcal{C} until it was time independent, thus solving

$$\mathcal{A}_{\text{fluct}}(U) \mathcal{C} + \mathcal{C} \mathcal{A}_{\text{fluct}}(U)^\dagger + \mathcal{Q} = 0. \quad (3.21)$$

¹⁵ The amplitude of U is substantially less than that of B_y in the growth phase and saturated state. Because of this, and since it does not influence B_y directly (like B_x), U seems to be playing a subsidiary role, and I have not observed substantial qualitative changes when its effect is removed from CE2 simulation altogether.

However, there is a fundamental problem with this approach; the chosen mean fields can support spectral instability when a radial magnetic field is included, in particular a generalization of the radial MRI. This implies that Eq. (3.21) can never be solved, since \mathcal{C} grows continuously in time. As a particularly simple way to get around this, I instead evolve \mathcal{C} until $t = 20$, and take the statistics at this time. The reported results do not depend significantly on this choice of time over a reasonable range of values (approximately $t \sim 5$ to $t \sim 30$). A better method, which I leave to future work due to its increased complexity, would be to specify a harmonic time dependence in the mean fields, thus allowing the time response of the EMFs to be measured in a systematic way.

Following Lesur and Ogilvie (2008b), let us consider the action of \mathcal{E} on the mean fields through

$$\partial_t B_x = -\partial_z \mathcal{E}_y + \bar{\eta} \Delta B_x, \quad (3.22a)$$

$$\partial_t B_y = -S B_x + \partial_z \mathcal{E}_x + \bar{\eta} \Delta B_y, \quad (3.22b)$$

and study the behavior using the correlation integrals,

$$\Gamma_x = \frac{1}{\langle B_y \rangle} \langle B_y \partial_z \mathcal{E}_y \rangle \quad \text{and} \quad \Gamma_y = \frac{1}{\langle B_y \rangle} \langle B_y \partial_z \mathcal{E}_x \rangle, \quad (3.23)$$

where $\langle f(z) \rangle \equiv L_z^{-1} \int dz f(z)$. From Eq. (3.22) it is straightforward to see that Γ_y measures the capacity of \mathcal{E}_x to amplify or damp B_y directly (with a positive value for amplification), while Γ_x measures the effect of \mathcal{E}_y on B_y , acting through the shear term $-S B_x$ (again, a positive value indicates \mathcal{E}_y amplifies B_y). Since I shall include a small B_x in some calculations, which always has the same spatial form as B_y , Γ_x can contain similar magnitude contributions from B_x (the turbulent resistivity), B_y (an off-diagonal turbulent resistivity), and possibly some nonlinear function of both. (For Γ_y , the B_x contribution will be much smaller than the B_y contribution, see chapters 4–6 for more information.) As discussed in the previous section, the dynamo instability is driven by $\Gamma_x > 0$

(i.e., through B_x), while $\Gamma_y < 0$, due to the turbulent resistivity from B_y . For small \mathbf{B} (and \mathbf{U}), the spatial form of \mathcal{E} must be the same as that of \mathbf{B} , shifted by $\pi/2$ in phase, since the mean fields are a small perturbation to the turbulence. However, this is not true for large mean fields and in general \mathcal{E} can have a somewhat complicated structure even for sinusoidal mean fields (one requirement is $\langle \mathcal{E} \mathbf{B} \rangle = 0$, since there can be no α effect, see chapter 6).

Calculations are run with sinusoidal mean fields, $B_y = B_{y0} \cos(k_1 z)$, $B_x = -B_{x0} \cos(k_1 z)$, where $k_1 = 2\pi/L_z$. I consider both $B_{x0} = 0$ and $B_{x0} = B_{y0}/10$ to ascertain the importance of the radial field on the saturation characteristics (note that B_{y0} does not evolve in time for nonzero B_{x0}). This form of the mean fields is chosen to approximate the saturated state of the dynamo [see Fig. 3.3(a)], although the ratio of B_{x0} to B_{y0} is itself set by the saturation dynamics (and could be time dependent) and 1/10 is chosen as an order-of-magnitude value for what is seen in the self-consistent CE2 simulations. Note that this approach, calculating the EMF with both nonzero B_x and B_y , is somewhat nonstandard in dynamo literature. However, for this problem in which we are explicitly studying the nonlinear saturation behavior, it is more natural to specify \mathbf{B} in a form that might be found in the saturated state of a CE2 simulation. The driving noise is identical to that discussed in Sec. 3.2, with resolution $(N_x, N_y, N_z) = (32, 32, 48)$ at an aspect ratio $(L_x, L_y, L_z) = (1, 2, 1)$. In plotting results, Γ is normalized by the energy E_{fluct} such that results become independent of the driving noise level.¹⁶

A note on the spectral instability As mentioned, the chosen mean fields can be spectrally unstable for the higher values of \mathbf{B} and Rm studied. The instability acts on $k_y = 0$, $k_x \neq 0$ modes (as must be the case, since $k_y \neq 0$ modes shear in time) and is essentially a generalization of the radial MRI to a spatially dependent B_x . This can be seen by examining the spectrum of modes after longer evolution times, and verifying that the scaling $k_x B_x \sim \text{constant}$ is approximately sat-

¹⁶ This normalization also implies that a steady-state value can be obtained, even when the system is spectrally unstable. However, since this takes some time to reach, and such a steady state includes *only* the most unstable mode, it seems more physically meaningful to consider the $t = 20$ values in any case.

ified for the most unstable mode at relatively large B_x (such that the dissipation is unimportant). Note that these modes would not be a true spectral instability in reality, since with nonzero B_x , B_y is necessarily time dependent and would eventually become important (see Balbus and Hawley 1991 for further discussion). These modes contribute most significantly to the turbulent diagonal resistivity; thus, through B_x their influence significantly decreases Γ_x , enhancing the saturation of the dynamo. This means that in a self-consistent simulation, as B_x grows such that the mean fields are nearly unstable, the resulting EMFs will act to reduce B_x thus removing the spectral instability. Such a process could feasibly lead to the time-dependent saturated state seen in Fig. 3.2(b), with the change in the prevalence of the state with Pm having some relation to the steepness of the $\mathcal{E}_y = 0$ crossing or a time delay in the response of the fluctuations (although this is entirely speculation).

3.3.2 Results

Results in the range $B_{y0} = 0.02 \rightarrow 0.2$ ($B_{x0} = 0.002 \rightarrow 0.02$) for $\text{Pm} = 1$ and $\text{Pm} = 8$ are illustrated in Figs. 3.5 and 3.6 respectively. Let us first discuss the behavior of Γ_y , the direct contribution of the EMF to the generation of B_y . As expected, this is always negative, indicating a standard turbulent resistivity. Γ_y is approximately linear in B_y , at least below $B_y \approx 0.1$, which implies the turbulent resistivity (β_0 , see Sec. 1.2) is constant. The difference between the case with and without radial field is minor at low fields, but significant at high fields where the radial MRI causes a sharp increase in the turbulent resistivity due to strong growth of $k_y = 0$, $k_x \neq 0$ modes.

The behavior of Γ_x is more interesting. As expected, at very low field strengths, $\Gamma_x > 0$ both with and without the inclusion of B_x , at all Pm and Rm . This shows (as is already known) that dynamo instability is possible. We are most interested in the B_y at which Γ_x becomes negative. This gives some indication of the level of saturation, since $\Gamma_x < 0$ implies the dynamo is damped

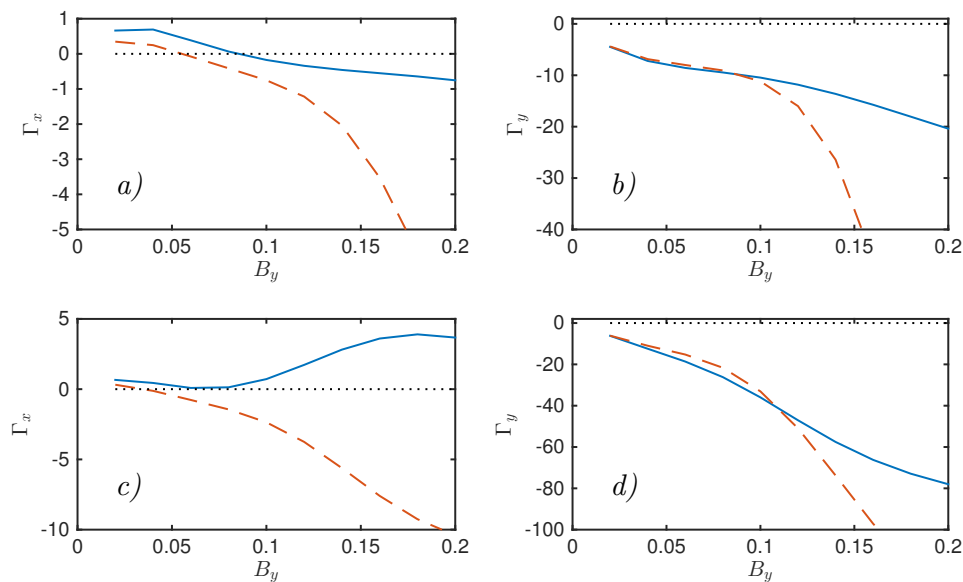


Figure 3.5: $\Gamma_x/E_{\text{fluct}}$ (left) and $\Gamma_y/E_{\text{fluct}}$ (right) as a function of B_{y0} for $\text{Pm} = 1$ and (a-b) $\text{Rm} = 3000$, (c-d) $\text{Rm} = 7500$. In each plot, the blue (solid) line shows Γ with only B_y influencing the fluctuations (i.e., mean fields $B_y = B_{y0} \cos(k_1 z)$, $B_x = 0$), while the red (dashed) line shows Γ with both B_y and B_x (i.e., mean fields $B_y = B_{y0} \cos(k_1 z)$, $B_x = -B_{y0}/10 \cos(k_1 z)$). The dotted (black) line simply indicates the zero crossing.

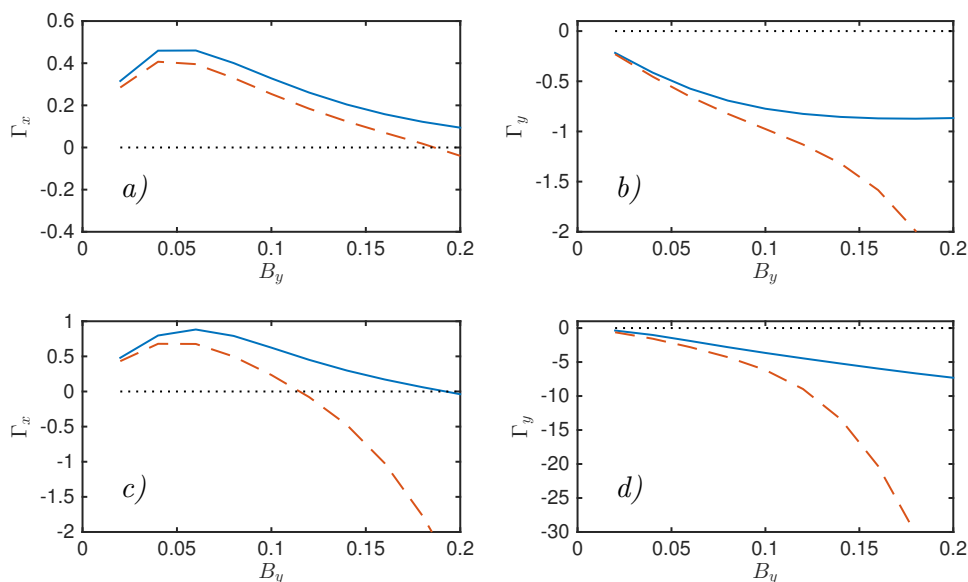


Figure 3.6: Same as Fig. 3.5 but for $\text{Pm} = 8$.

by the EMFs.¹⁷ Considering for the moment those results obtained with B_x (i.e., dashed curves in Figs. 3.5 and 3.6), the most obvious feature is the very strong dependence of this zero crossing on P_m ; while relatively small for $P_m = 1$ ($B_{y0} \approx 0.04$) much larger values are seen for $P_m = 8$ ($B_{y0} \approx 0.15$). In addition, there is a decrease in the saturation point with R_m . These trends nicely match the self-consistent saturation behavior shown in Fig. 3.3, and the inferred values of B_y are similar. Nonetheless, caution is advised in assuming we have predictive power here: firstly because the ratio of B_x to B_y is not *a-priori* known, and secondly because I have somewhat arbitrarily chosen $t = 20$ for evaluation of \mathcal{C} .

Turning to the behavior with $B_x = 0$, we see immediately why the effect of B_x on \mathcal{C} is so important for obtaining a saturated state in self-consistent CE2 calculations – Γ_x does not become negative sufficiently fast with B_y if $B_x = 0$. Its behavior at $P_m = 1$, $R_m = 7500$ is particularly interesting, staying positive for the entire range of B_{y0} tested (it does eventually become negative at $B_x \approx 0.3$). This peculiar drop in Γ_x followed by a rise, seems to become more prominent at higher R_m , and I currently lack physical intuition for what is causing such behavior. The effect of B_x is more straightforward to understand, essentially as a turbulent resistivity of a similar form as the B_y contribution to Γ_y . At lower B_{y0} this is nearly linear in B_x , while at higher values, the radial MRI becomes important causing a large negative contribution to Γ_x [e.g., this effect counteracts the rise in Γ_x in Fig. 3.5(c)].

Finally, it is worth comparing this discussion to the model proposed in Lesur and Ogilvie (2008a) and Lesur and Ogilvie (2008b). These works suggest a dynamo cycle can arise through the nonlinear change in sign of Γ_x through the action of B_y alone, and find the dissipation coefficients and P_m to be of subsidiary importance unless the dissipation is quite large. What is this sign change and how does it relate to Figs. 3.5 and 3.6? For the higher dissipation cases presented here, one can see the sign change [e.g., Fig. 3.5(a) at $B_{y0} \approx 0.1$]; however for the $P_m = 1$, $R_m = 7500$

¹⁷Although, the dynamo does not necessarily grow if $\Gamma_x > 0$, the positive effect must overwhelm the negative effect due to Γ_y .

case, this occurs at higher B_{y0} (approximately $B_{y0} = 0.3$). It seems likely that this *second* drop in Γ_x will become independent of dissipation when for sufficiently high R_m , Re , and that this is the transition studied analytically in Lesur and Ogilvie (2008a). I would thus propose the addition of B_x to their model as a vital component of dynamo saturation. Recently, Donnelly (2013) has presented an extension of the analytic work in Lesur and Ogilvie (2008a) to include dissipation explicitly, some effects from B_x , and stratification. While they conclude that the model cannot explain the P_m dependence of shearing box simulations, extensions to capture the effects seen in Figs. 3.5 and 3.6 may be feasible, and this would be worth pursuing in future work.

Overall, we see that this basic exploration of the nonlinear stresses for fixed mean fields explains aspects the saturation behavior seen in Fig. 3.3, so long as one includes the effect of a mean B_x on the fluctuations. Nonetheless, the above discussion could hardly be considered complete, leaving entirely open the question of *why* the EMFs (in particular \mathcal{E}_y) show such strong P_m dependence. The answer appears to be related in some way to a stronger turbulent resistivity in comparison to off-diagonal terms at lower P_m , which is perhaps related to the radial MRI, since this causes a more significant decrease in Γ_x for a given B_x . It seems worth noting that $k_y = 0$ modes can be completely excluded from self-consistent CE2 simulations, and one obtains similar results. This is not surprising in light of the nonmodal analysis from chapter 2 – other modes that are “near” the unstable ones can probably grow transiently to significant amplitudes, thus having a similar effect to modes that are truly unstable.

3.4 Discussion

The primary motivation for this work has been to disentangle the important processes involved in MRI turbulence and the associated dynamo. With this aim, we have enormously reduced the nonlinearity of the unstratified shearing box system, keeping only those interactions that involve the $k_x = k_y = 0$ modes (the mean fields). This removes the usual turbulent cascade, although

fluctuations are still swept to the smallest scales by the mean shear. The primary result is that despite this huge simplification – the only nonlinearity is due to the mean-field dynamo – the CE2 system displays qualitatively similar trends to fully developed MRI turbulence. In particular, a decrease in Re at fixed Rm (i.e., an increase in Pm), causes an increase in angular momentum transport – the reverse of the linear behavior. This illustrates the relationship of this trend to the large-scale dynamo and facilitates future analytic studies to understand the primary causes for such behavior. The hope is that such understanding would allow extrapolation into the high and low Pm regimes that are so computationally challenging. In addition, statistical simulation (i.e., CE2, Farrell and Ioannou 2003; Marston *et al.* 2008) provides very clear information on the bifurcations between turbulent states of the system. We see two important bifurcations as Rm is increased: the first is the transition from stable homogenous turbulence to a stable inhomogenous equilibrium with strong mean fields (the dynamo instability), the second a loss of stability of the inhomogenous equilibrium and transition to a near-periodic time-dependent state. Given the strong dependence of both the saturated states and the second bifurcation on Pm , as well as the marked similarity to studies of plane Couette flow (Farrell and Ioannou, 2012), it seems likely that further study of this dynamo instability will yield important insights into the fundamental nature of the MRI system.

In the next three chapters, I shall analyze the linear behavior of observed dynamo instability, arriving at the interesting conclusion that it is driven primarily by the magnetic fluctuations. The novel nature of this dynamo makes it appealing for other applications outside of the context of the MRI. Of course, for the sake of understanding MRI turbulence, the dynamo’s nonlinear behavior is more significant. The examination of this saturation through direct calculation of EMFs in Sec. 3.3 was unsatisfyingly cursory, and may be seen as a starting point for more complete studies. (It is at least comforting to see such strong Pm dependence in the EMFs, given that this is absent in the model of Lesur and Ogilvie 2008b.) In particular, while the basic idea that the radial MRI causes an increased turbulent dissipation of B_x seems reasonable, more work is needed to assess exactly why this shows such strong Pm dependence, and what the fate of such a mechanism would

be at high Reynolds numbers. In addition, helicity conservation and transport have historically been of particular importance in dynamo saturation (Bhattacharjee and Hameiri, 1986; Blackman and Field, 2002), and understanding how these effects interact with the nonlinear changes to the transport coefficients discussed above may be crucial in obtaining a complete theory of the dynamo saturation. Given the strong helicity fluxes observed in global unstratified disk simulations (Ebrahimi and Bhattacharjee, 2014), there is reason to expect these effects will be significant. While such studies may prove be very fruitful, due to time constraints, these interesting subjects are not explored further in this thesis.

Chapter 4

Nonhelical shear dynamos: the effect of rotation and small-scale magnetic fluctuations

4.1 Introduction to the magnetic shear-current effect

We have seen in the previous chapter that a large-scale dynamo is excited in CE2 computations of MRI turbulence in the unstratified shearing box. The saturated state of this dynamo bears a strong resemblance to aspects of self-sustaining zero-net-flux turbulence, in particular the increase in turbulence intensity with a decrease in Re (increase in Pm). Far from being obvious, the mere existence of this dynamo is rather surprising when one compares with previous dynamo literature. As discussed in the introduction (Sec. 1.2), most dynamo studies focus on the α effect, which is impossible in the unstratified shearing box due to the mirror symmetry and homogeneity. How, then, is the dynamo excited? The large-scale shear is certainly fundamental to the mechanism, most obviously strengthening the dynamo through simple stretching of the mean field (the Ω effect), although a variety of other more subtle effects may also enhance growth (see, for example, Vishniac

and Cho 2001; Brandenburg 2008; Tobias and Cattaneo 2014). While large-scale homogenous nonhelical dynamos have been studied previously in shear flows (Brandenburg *et al.*, 2008a; Yousef *et al.*, 2008b; Singh and Jingade, 2015), we shall see in this chapter that the dynamo observed in our CE2 calculations is of a fundamentally different character from the mechanism studied in most previous literature (e.g., Brandenburg *et al.* 2008a; Heinemann *et al.* 2011). In particular, it is a coherent dynamo in which the crucial transport coefficient is primarily determined by the small-scale *magnetic* fluctuations. The work presented in this chapter is currently under review for publication in *The Astrophysical Journal* (Squire and Bhattacharjee, 2015c).

Nonhelical shear dynamos have been an object of fascination in the dynamo literature for some years. Two fundamentally different explanations have been proposed for how large-scale fields can be generated without any symmetry-breaking process. The first – the so-called “shear-current effect” – is in essence an off-diagonal turbulent resistivity (Rogachevskii and Kleeorin, 2003, 2004). When coupled with the shear, even rather small values of this transport coefficient can overcome the standard (diagonal) turbulent resistivity and cause growth of a mean-field dynamo. The second explanation – the stochastic- α effect – relies on the idea that even if the mean α coefficients vanish, sufficiently strong fluctuations can lead to large-scale field growth (Vishniac and Brandenburg, 1997; Silant’ev, 2000; Heinemann *et al.*, 2011). This dynamo is not mean-field in the usual sense since it relies on the finite size of the system to cause mean-field growth; nonetheless, given that the universe is sampling a single realization of turbulence, *not* the ensemble average, such effects could be entirely physical. At the present time, much of the community appears to have converged on the idea that nonhelical shear dynamos are incoherent in nature; i.e., the stochastic- α effect is more important than the shear-current effect. The primary reasoning is that the crucial transport coefficient required for the shear-current effect appears to have the incorrect sign, at least at moderate Reynolds numbers (Rädler and Stepanov, 2006; Rüdiger and Kitchatinov, 2006; Brandenburg *et al.*, 2008a). At the same time, given the variety of different, but related, incoherent dynamo mechanisms that have been suggested (Silant’ev, 2000; Heinemann *et al.*, 2011; Mitra and Bran-

denburg, 2012; Richardson and Proctor, 2012; Sridhar and Singh, 2014), one is led to the idea that such effects should be relatively generic and operate across a wide range of parameters.

Here, and in Chapters 5 and 6, I re-examine the possibility of large-scale coherent nonhelical shear dynamos. Motivated primarily by understanding the MRI dynamo observed in the previous chapter, we propose a fundamentally different mechanism to those discussed above – that a coherent large-scale magnetic field can be excited by small-scale magnetic fluctuations. In addition to the MRI dynamo, such a mechanism may prove important in a wide variety of other astrophysical scenarios. In particular, any MHD system above low magnetic Reynolds numbers is unstable to the small-scale (or fluctuation) dynamo (Schekochihin *et al.*, 2007), and the magnetic field at the smallest scales of the turbulent spectrum will grow very rapidly. Such growth is sufficiently fast that it always eclipses large-scale field growth, and thus a mean-field dynamo must be able to grow on top of both velocity and magnetic fluctuations (Kulsrud and Anderson, 1992; Boldyrev *et al.*, 2005; Cattaneo and Hughes, 2009). This idea is fundamentally related to α -quenching, in which the small-scale magnetic fluctuations quench the growth of the large-scale field before it has a chance to reach significant amplitude. As discussed in Sec. 1.2, such considerations have caused many in the field to question whether the α effect really can explain observed large-scale fields. Our proposal is in some sense the opposite to quenching: for nonhelical shear-dynamos, the back-reaction from the small-scale dynamo may be a *positive* effect, enhancing the large-scale dynamo growth rate.

In this chapter, I focus on understanding such a magnetic dynamo in the regime of low Reynolds numbers. In this regime the problem becomes substantially simpler, due to the greater applicability of quasi-linear approximations and the lack of a small-scale dynamo (Yousef *et al.*, 2008a). This enables the effects of velocity and magnetic fluctuations to be studied separately (e.g., through driving the induction equation) even in nonlinear direct numerical simulation (DNS), as well as allowing simple calculation of transport coefficients and fluctuation statistics. We shall see that with sufficiently strong small-scale magnetic fluctuations, the character of the observed large-scale

dynamo changes, becoming more coherent in time and saturating at higher field strengths. That this is a coherent dynamo effect is confirmed through numerical evaluation of the relevant transport coefficients. In Chapter 5, I consider the more interesting and relevant case where the magnetic fluctuations are self-consistently excited by the small-scale dynamo at higher Reynolds numbers, driving a large-scale dynamo once they reach saturation.

In addition to studying the magnetic dynamo, I re-examine the kinematic dynamos presented in Yousef *et al.* (2008a) and Yousef *et al.* (2008b), since it is necessary to understand the intricacies of the kinematic dynamo before moving on to the magnetically driven case. It is found that in their non-rotating examples, the dynamo seen by Yousef *et al.* (2008a) is indeed a stochastic- α effect, of the type suggested by Heinemann *et al.* (2011). However, anti-cyclonic (e.g., Keplerian) rotation can substantially alter the picture, causing a coherent dynamo to become possible by changing the sign of the off-diagonal resistivity. This behavior is well explained by the $\boldsymbol{\Omega} \times \mathbf{J}$, or Rädler, effect (Krause and Rädler, 1980; Moffatt and Proctor, 1982). Although not commented on by Yousef *et al.* (2008a), these conclusions are entirely compatible with their results, nicely explaining observed trends in growth rates.

In chapter 6, I confirm the main conclusions of this chapter analytically using the second-order correlation approximation (SOCA). In particular, I show that magnetic fluctuations cause an off-diagonal resistivity (of the required sign) that is of substantially larger magnitude than the kinematic effect. Importantly, this agrees with previous calculations using the τ -approximation (Rogachevskii and Kleeorin, 2004), as well as calculations using shear quasi-linear theory with magnetic fluctuations (this is simply CE2 but is very similar to Sridhar and Subramanian 2009; Singh and Sridhar 2011), and perturbative calculations of inhomogenous MRI shearing waves (Lesur and Ogilvie, 2008a). Such agreement is in contrast to the originally proposed kinematic shear-current effect, in which sign of the off-diagonal resistivity disagrees between the τ -approximation (Rogachevskii and Kleeorin, 2003), SOCA (Rädler and Stepanov, 2006; Rüdiger and Kitchatinov, 2006) and shear quasi-linear theory (Singh and Sridhar, 2011). In addition, all three closure

methods agree that the magnetic effect is substantially larger than the kinematic effect (for similar fluctuation levels $b_{\text{rms}} \sim u_{\text{rms}}$). Our hope is that this agreement speaks to the robustness of the effect at both high and low Reynolds numbers. Regarding the kinematic dynamo, the analytic SOCA results also confirm the qualitative change to the dynamo that results from the addition of Keplerian rotation.

Since self-sustaining MRI turbulence is highly nonlinear and linear dynamo results will be generally inapplicable, what does this theoretical dynamo study add to the discussion? Rather than expecting quantitative application for dynamo growth rates, one can consider the presence of a large-scale dynamo instability to be an indication that the turbulence will always be accompanied by large-scale structures. Specifically, since the primary results of this chapter are that both anti-cyclonic rotation and magnetic fluctuations have a positive influence on the coherent dynamo, it seems reasonable to surmise that this mechanism should play an important role in MRI turbulence. It is also worth noting that the conclusion that the MRI dynamo arises through an off-diagonal resistivity has been reached computationally from basic measurements of \mathcal{E} in unstratified MRI simulations (Lesur and Ogilvie, 2008b). Of course, for the purposes of understanding MRI turbulence, the nonlinear behavior of the dynamo will be important, but aside from the brief discussions in chapter 3, I leave this complex topic to future work (Rogachevskii and Kleeorin, 2004; Rogachevskii *et al.*, 2006; Lesur and Ogilvie, 2008a).

4.1.1 Outline

Since results on both the magnetically driven and kinematic dynamo are presented, I feel it helpful to provide a “roadmap” for chapter’s structure. This is intended to outline how central results relate to each other, and provide motivation for the structure of the chapter.

As discussed, the most important results of this chapter are those regarding the “magnetic shear-current effect,” which act as a prelude to chapter 5, but in the simpler low- R_m regime. However,

to be able to convincingly interpret results – in particular, observations of the magnetic dynamo in nonlinear simulation – it is necessary to first explore the kinematic dynamo, its primary driving mechanisms, and its dependence on physical parameters. Thus, I first present results (Sec. 4.4) on the dynamo mechanism in the simulations of Yousef *et al.* (2008a) and Yousef *et al.* (2008b), which show that this kinematic dynamo is primarily incoherent (although coherent effects become important with rotation) and provides a comparison point for later results on the magnetic dynamo. This section also acts to illustrate the effectiveness of the quasi-linear and statistical simulation methods in disentangling incoherent and coherent dynamo mechanisms, and demonstrates that the direct measurement of transport coefficients yields results in agreement with other methods.

The magnetic shear-current effect dynamo is then studied in Sec. 4.5. To argue for its existence, I use the same tools as for the kinematic dynamo: qualitative examination of the dynamo from direct numerical simulation, statistical simulations at the same physical parameters as in the kinematic case, and direct measurement of transport coefficients. I hope that together these methods provide a strong argument for the existence of the effect and its potential importance in dynamo theory.

These sections on the kinematic and magnetic shear dynamos are preceded by a theoretical discussion of the different dynamo mechanisms that are possible in this geometry (Sec. 4.2), and an explanation of the numerical methods (Sec. 4.3). The primary purpose of the theoretical discussion is to explain the differences between incoherent and coherent dynamos, and what properties might be used to distinguish these. A different stochastic dynamo mechanism (Silant'ev, 2000; Sridhar and Singh, 2014), based on the work of Kraichnan (1976), is discussed in App. C.1, where I come to the conclusion that this dynamo is unlikely to be causing observed field generation due to the effects of off-diagonal α fluctuations. I finish the chapter in Sec. 4.6 with conclusions, including a detailed comparison with previous works.

Throughout this chapter, nonlinear simulations will utilize a similar numerical setup to that of Yousef *et al.* (2008a), with tall boxes ($L_z \gg L_x = L_y$) to enhance scale separation, and relatively small Reynolds numbers ($\text{Re} = \text{Rm} = 100$) to avoid the complications of the small-scale dynamo.

4.2 Shear dynamos

In this section I conceptually examine the possibilities of incoherent (stochastic- α), and coherent (shear-current) dynamos, arising from nonhelical turbulence in a Cartesian shearing box. Specifically, I consider an imposed linear velocity shear, $\mathbf{U}_0 = -Sx\hat{\mathbf{y}}$, and mean fields are defined by simple averaging over the horizontal (x and y) directions. (Note that S is defined in the same way as the rest of the thesis using the conventions of astrophysical literature, and that this is the reverse of that used in most previous shear dynamo works). A more comprehensive exploration of possible dynamo mechanisms in this geometry can be found in Mitra and Brandenburg (2012).

In the conventional way, I start by defining mean and fluctuating fields through the relation $\mathbf{B}_T = \overline{\mathbf{B}_T} + \mathbf{b} = \mathbf{B} + \mathbf{b}$, where \mathbf{B}_T is the full turbulent magnetic field and an overbar denotes the mean-field average (simply a spatial average over x and y). I shall also make use of the ensemble mean, denoted $\langle \cdot \rangle$, which is the average over an ensemble of realizations at the same physical parameters (see the discussion in Sec. 3.1). Averaging the induction equation leads to the standard mean-field dynamo equations for the mean magnetic field \mathbf{B} (Moffatt, 1978; Krause and Rädler, 1980)

$$\partial_t \mathbf{B} = \nabla \times (\mathbf{U}_0 \times \mathbf{B}) + \nabla \times \mathcal{E} + \frac{1}{\text{Rm}} \Delta \mathbf{B}. \quad (4.1)$$

Here $\mathcal{E} = \overline{\mathbf{u} \times \mathbf{b}}$ is the electromotive force, assumed to be of the form $\mathcal{E}_i = \alpha_{ij} B_j + \beta_{ijk} B_{j,k} + \dots$ due to scale separation (more discussion is given in Sec. 1.2). Due to the simplicity of the average \mathbf{B} is a function only of z , implying $B_z = 0$, and there are only 4 nonzero components of the β_{ijk} tensor¹ (see Brandenburg and Sokoloff 2002; Rädler and Stepanov 2006). Expanding Eq. (4.1)

¹Specifically $\beta_{i3k} = 0$ since $B_z = 0$, and $\beta_{ijk} = 0$ if $k \neq 3$ since $\partial_x \mathbf{B} = \partial_y \mathbf{B} = \mathbf{0}$.

one obtains

$$\partial_t B_x = -\alpha_{yx} \partial_z B_x - \alpha_{yy} \partial_z B_y - \eta_{yx} \partial_z^2 B_y + (\eta_{yy} + \bar{\eta}) \partial_z^2 B_x \quad (4.2a)$$

$$\partial_t B_y = -S B_x + \alpha_{xx} \partial_z B_x + \alpha_{xy} \partial_z B_y - \eta_{xy} \partial_z^2 B_x + (\eta_{xx} + \bar{\eta}) \partial_z^2 B_y, \quad (4.2b)$$

where the η_{ij} are defined nonzero components of β_{ijk} ; $\eta_{xx} = \beta_{xyz}$, $\eta_{xy} = -\beta_{xxz}$, $\eta_{yy} = -\beta_{yxx}$, $\eta_{yx} = \beta_{yyz}$ (these definitions are more natural when the current is used in \mathcal{E} instead of $B_{i,j}$; i.e., $\mathcal{E}_i = \alpha_{ij} B_j - \eta_{ij} J_j$). At this stage, the α and η coefficients are not assumed constant in time, space, or over realizations (i.e., $\alpha_{ij} \neq \langle \alpha_{ij} \rangle$) – indeed with the mean-field average taken over a finite sized domain, they can fluctuate strongly. General symmetry arguments (Rädler and Stepanov, 2006; Brandenburg *et al.*, 2008a) show that $\langle \alpha_{ij} \rangle = 0$, while there are no such constraints on the form of η_{ij} when effects are present that break the isotropy of the turbulence (e.g., shear, rotation). I shall assume that the diagonal components of the resistivity, η_{yy} and η_{xx} , are positive, since the scale separation assumptions of mean-field theory will presumably become invalid if this is not the case.

In the following sections I discuss the two fundamental dynamo mechanisms that are examined in this work.

Coherent shear dynamo

This dynamo arises primarily from the coupling between the off-diagonal resistivity η_{yx} and the shear term $-S B_x$. Specifically, for Eq. (4.2) with $\alpha_{ij} = 0$ and $\eta_{yy} = \eta_{xx} = \eta_t$ for simplicity,² it is straightforward to show that an eigenmode with the spatial structure $B_i = B_{i0} e^{ikz}$ has the growth rate

$$\gamma_\eta = k \sqrt{\eta_{yx} (-S + k^2 \eta_{xy})} - k^2 \eta_t. \quad (4.3)$$

²A relaxation of this assumption does not qualitatively change the dynamo mechanism.

Neglecting η_{xy} by assuming $|k^2\eta_{xy}| \ll S$ for all k for which scale separation holds, positive dynamo growth is possible if $-S\eta_{yx} > 0$ and $k\sqrt{-\eta_{yx}S} > k^2\eta_t$. The maximum growth rate is $\gamma_\eta = |S\eta_{yx}|/4\eta_t$, obtained at $k = \sqrt{|S\eta_{yx}|}/2\eta_t$ (if this wavenumber fits in the box). For a single mode of this dynamo, B_x and B_y are π out of phase, $B_x = -k\sqrt{|\eta_{yx}/S|}B_y$, and their phases are constant in time, meaning $Re \langle B_x B_y^* \rangle = -(\langle B_x B_x^* \rangle \langle B_y B_y^* \rangle)^{1/2}$. A nonzero η_{yx} can arise from the effect of shear through the shear-current effect (Rogachevskii and Kleeorin, 2003), from rotation through the $\boldsymbol{\Omega} \times \boldsymbol{J}$ (or Rädler) effect (Krause and Rädler, 1980; Rädler *et al.*, 2003), or from a combination of both. Since $\eta_{yx} \propto S$ if η_{yx} arises through the shear-current effect, the maximum growth rate of the coherent dynamo should scale as $\gamma \sim S^2$ (this also holds with rotation if Ω/S is held fixed).

Stochastic- α effect

This dynamo arises from the combination of zero-mean α_{yy} fluctuations and the mean shear S . Consider Eq. (4.2) with $\eta_{xy} = \eta_{yx} = 0$, $\langle \alpha_{ij} \rangle = 0$, and again take $\eta_{yy} = \eta_{xx} = \eta_t$. For simplicity,³ I set $\alpha_{xy}(t) = \alpha_{yx}(t) = \alpha_{xx}(t) = 0$, assume white noise fluctuations in α_{yy} ,

$$\langle \alpha_{yy}(t) \alpha_{yy}(t') \rangle = D_{yy} \delta(t - t'), \quad (4.4)$$

and again take $B_i = B_{i0} e^{ikz}$. One can show using standard techniques of stochastic calculus (Gardiner, 2004) that while $\langle B_i(t) \rangle$ decays due to turbulent resistivity, it is possible for $\langle B_i B_j^* \rangle$ to grow at the rate

$$\gamma_\alpha = \left(\frac{k^2 S^2 D_{yy}}{2} \right)^{1/3} - k^2 \eta_t. \quad (4.5)$$

Thus, positive dynamo growth is possible if fluctuations in α are sufficiently large. The maximum growth rate of this dynamo is $\gamma = 0.074 S \sqrt{D_{yy}/\eta_t}$, obtained at $k = \sqrt{S} (D_{yy}/54\eta_t^3)^{1/4}$. Note

³When the shear is larger than fluctuations in α , $\{\alpha_{xy}, \alpha_{yx}, \alpha_{xx}\}$ are each subdominant to α_{yy} in their effect on the growth rate; see Mitra and Brandenburg (2012).

that in any single realization of this dynamo, as observed in simulation, B_x and B_y will grow approximately exponentially; the fact that $\langle B_i \rangle = 0$ would only become apparent if a large ensemble of simulations were carried out at the same physical parameters (with the same initial conditions for the mean field). Importantly, initial conditions must be forgotten over the timescale associated with the turbulent resistivity, $t \sim (k^2 \eta_t)^{-1}$ (since $\langle B_i(t) \rangle$ simply decays exponentially), which implies that the dynamo cannot have a constant phase as it grows in time. For a single mode of the dynamo, B_x and B_y are on average $\pi/4$ out of phase (as for the coherent α shear dynamo), $Re \langle B_x B_y^* \rangle = -2^{-1/2} (\langle B_x B_x^* \rangle \langle B_y B_y^* \rangle)^{1/2}$. The stochastic- α dynamo will also have a dependence on the horizontal domain size, since averaging over a larger domain will decrease the size of the fluctuations in α , thus decreasing the magnitude of the growth rate. More information, including the effects of other nonzero α coefficients and correlations between different α_{ij} , can be found in Mitra and Brandenburg (2012). This type of stochastic- α dynamo has also been derived from the MHD equations directly by quasi-linearly considering a collection of forced shearing waves (Heinemann *et al.*, 2011; McWilliams, 2012).

It is interesting to note that the growth rate of a stochastic- α dynamo can be arbitrarily increased or decreased by changing the volume of the mean-field average. In particular, an increase in the volume of the average by a factor a must lead to a reduction in the magnitude of $\langle \alpha^2 \rangle$ by a also, assuming the turbulence in each sub-volume is statistically independent. With smaller $\langle \alpha^2 \rangle$, a reduction in the dynamo growth rate would result. In fact, we see this effect explicitly in the simulations presented in Sec. 4.4 by simply doubling the horizontal dimensions of our domain, keeping all other parameters fixed.

A fundamentally different type of stochastic- α shear dynamo has also been proposed and studied in Silant'ev (2000) and Sridhar and Singh (2014). This dynamo is essentially the same as that proposed by Kraichnan (1976), arising from sufficiently strong fluctuations in α with a correlation between diagonal components $\langle \alpha_{xx}(t) \alpha_{yy}(t) \rangle \neq 0$. Importantly, there is also an opposing contribution to this effect that arises from fluctuations in the off-diagonal components of α , the potential

significance of which has not been discussed in previous literature (of which I am aware). For this reason, this effect is unlikely to be the mechanism driving the large-scale dynamos studied in this thesis. Further details are given in App. C.1.

Of course, in a real turbulent situation, the coherent and incoherent dynamo mechanisms can be mixed, and distinguishing the two may be rather difficult. In particular, the η_{ij} coefficients discussed for the coherent shear dynamo will also fluctuate in time and the mean fields will generally be noisy, even if the stochastic- α effect is not the dominant dynamo driver. In this work I use a variety of methods to compare the two in different physical situations, from directly calculating transport coefficients, to simply observing mean-field temporal evolution. In the case of magnetic fluctuations, one might also include an additive noise into Eq. (4.2) which arises from $\partial_z \overline{(\mathbf{u} \times \mathbf{b})}$ of the background (spatially homogenous) fluctuations.

4.3 Equations and numerical method

In this section I outline the equations solved and discuss the numerical methods, including the nonlinear MHD code SNOOPY (Lesur and Longaretti, 2007) and my implementation of the test-field method within this framework. The fundamental equations are the nonlinear magnetohydrodynamic equations with a background shear flow $U_0 = -Sx\hat{y}$ as outlined in chapter 3 [Eq. 3.1]. Throughout this chapter, the driving noise (σ_u and σ_b) is nonhelical and white in time, localized in wavenumber around $k = 6\pi$ (in the dimensions of the box) with width $6\pi/5$ (i.e., $k_{c,\text{lower}} = 6\pi - 6\pi/5$, $k_{c,\text{upper}} = 6\pi + 6\pi/5$) and is used to generate an homogenous bath of small-scale velocity and/or magnetic fluctuations.⁴ Note that unlike in the previous chapter, I shall study the case of pure shear without rotation, $\Omega = 0$, as well as those with rotation. Throughout this work I consider initially homogenous turbulence with zero average helicity. I use a Cartesian box

⁴This forcing is of the same form as Yousef *et al.* (2008a).

of dimensions (L_x, L_y, L_z) with periodic boundary conditions in z and y , and shearing periodic boundary conditions in x .

As the primary tool for solving the shearing box MHD equations [Eq. (3.1)], I will utilize the SNOOPY code (Lesur and Longaretti, 2007). SNOOPY uses a standard Fourier pseudo-spectral method in the shearing frame, with a third-order variable time step Runge-Kutta integrator and 3/2 dealiasing. It is written in the `c` programming language and is primarily based on the standard FFTW library (Frigo and Johnson, 2005), parallelized with MPI and OpenMP. The remapping procedure in SNOOPY, necessary to ensure k_x values do not constantly grow during the simulation, differs from that used in the quasi-linear and CE2 codes (see Sec. 3.1). In particular, rather than remapping a radial wavenumber $k_x(t) = k_x(0) + Stk_y$ as soon as its value is outside the specified range $2\pi N_x/L_x(-1/2, 1/2)$, remapping is carried out on all wavenumbers simultaneously every $T_{\text{SB}} = L_y/SL_x$ (this period, T_{SB} , is the period with which the lowest k_y wavenumbers are remapped in the CE2 method). While this method, which has historically been the standard approach, leads to high wavenumbers reaching larger values and thus a more “choppy” simulation, it has the advantage of allowing an even sized grid, which is highly beneficial for speed if Fourier transforms are taken across all three dimensions. Recently, a method that utilizes a slight modification to the Fourier transform has been proposed (Brucker *et al.*, 2007), dispensing with remapping entirely. This seems to have a number of advantages and would probably be the ideal choice for a future Fourier shearing box code.

4.3.1 Measurement of the transport coefficients

At a variety of points throughout this work it has been invaluable to measure the transport coefficients directly. This has been done both in nonlinear simulation, using the test-field method as well as other approaches (see chapter 5), and within the quasi-linear approximation (primarily with CE2). The latter (quasi-linear measurement) is quite straightforward, since the equations are

already defined in terms of the mean and fluctuating fields. In particular, as outlined in chapter 3, it is simply necessary to solve the fluctuation equations [Eq. (3.6)] alone, with some chosen (fixed in time) \mathbf{U} and \mathbf{B} . One then simply calculates \mathcal{E}_i from the fluctuations. Of course, this process is rendered particularly convenient within CE2, since the statistics are solved for directly, and thus \mathcal{E}_i is calculated exactly. I have thoroughly checked the consistency between these CE2 calculations and the values obtained by taking very long time averages in direct quasi-linear simulation with fixed mean fields. Within the quasi-linear model, kinetic and magnetic fluctuations are treated in the same way, and the transport coefficients arising from each can be calculated separately and summed to obtain the coefficients arising from a turbulent bath with both \mathbf{u}_0 and \mathbf{b}_0 .

The test-field method⁵ allows the calculation of transport coefficients without the quasi-linear approximation and has become a common tool in dynamo studies over the past decade (Brandenburg *et al.*, 2008a). The method involves solving for a set of “test fields” in addition to the standard “base” MHD equations. The test fields \mathbf{b}^q are simply additional sets of magnetic fluctuations, which satisfy the equation

$$\partial_t \mathbf{b}^q = \nabla \times (\mathbf{u} \times \mathbf{B}^q) + \nabla \times (\mathbf{U} \times \mathbf{b}^q) + \nabla \times (\mathbf{u} \times \mathbf{b}^q - \overline{\mathbf{u} \times \mathbf{b}^q}) + \bar{\eta} \nabla^2 \mathbf{b}^q. \quad (4.6)$$

Here \mathbf{u} and \mathbf{U} are the fluctuating and mean velocity fields taken from the base MHD simulation. The mean magnetic fields \mathbf{B}^q are fixed (specified at the start of a simulation), with one \mathbf{B}^q for each \mathbf{b}^q . By computing the EMF that results from \mathbf{b}^q in the mean field \mathbf{B}^q , one can calculate the transport coefficients. Note that Eq. (4.6) is almost the same as the fluctuating quasi-linear induction equation [Eq. (3.6b)], except for the inclusion of the fluctuating EMF $\mathcal{E}' = \mathbf{u} \times \mathbf{b}^q - \overline{\mathbf{u} \times \mathbf{b}^q}$. This term can render the test fields unstable to the small-scale dynamo above moderate Reynolds numbers, and for this reason it can be necessary to reset test fields to zero periodically, where the period T_{reset} is chosen such that $\mathbf{b}^{(q)}$ does not grow larger than the small-scale velocity

⁵Note that there is a similarly named, but unrelated, method due to Kraichnan in statistical turbulence literature; see, for example, Kraichnan (1971).

field.⁶ The implementation of the method in SNOOPY involved adding test fields into the basic framework of the code. Any number of extra test fields (specified through the preprocessor macro `NUM_TEST_FIELDS`), with arbitrary specified mean fields can be used for a given run with either the hydrodynamic or MHD equations (see below). The resulting spatiotemporal EMFs, $\mathcal{E}^q = \langle \mathbf{u} \times \mathbf{b}^q \rangle$, are saved to file for post-processing.

The test-field method can be used in different ways, depending on the needs for a given simulation. In each case, one usually specifies harmonic functions for \mathbf{B}^q , with sufficiently small amplitudes such that \mathcal{E} is linear in \mathbf{B}^q , ideally defining one test field for each two transport coefficients.⁷ Its simplest – and most obviously meaningful – use, is to run a hydrodynamic simulation for \mathbf{u} , thus calculating kinematic transport coefficients. Most of the studies presented in this thesis have utilized the test-field method in this fashion. A simple extension is the “quasi-kinematic” method (Brandenburg *et al.*, 2008b; Hubbard *et al.*, 2009), for which one runs an MHD simulation in which \mathbf{u} is influenced by self-consistent magnetic fields, and extracts the \mathbf{u} to insert into the test-field equations. This can most obviously be used to understand how the kinematic coefficients are modified by a mean field \mathbf{B} , or the small-scale dynamo field, but transport coefficients that arise directly through \mathbf{b} are not included. A variety of subtleties exist, however, and care must be used in interpreting results, see Hubbard *et al.* (2009). The method has been used to study the accretion disk dynamo in Gressel (2010), with nice, although somewhat inconclusive, results.

Note that unlike with quasi-linear simulation, the extension of the test-field method to explicitly include background \mathbf{b}_0 fluctuations is nontrivial (here “background” specifically refers to those fluctuations that exist independently of a mean field). In particular, without linearization (as in

⁶ This process possibly introduces systematic errors in the transport coefficients, especially at higher Reynolds numbers where the small-scale dynamo growth is faster, requiring a smaller T_{reset} . In higher Rm calculations I have checked that results are independent of T_{reset} over a moderate range; however, this empirical approach does not seem entirely satisfactory and it would be interesting to study this issue more thoroughly.

⁷ If the system is homogenous, one test field is sufficient to calculate four transport coefficients (for our horizontal mean-field average); e.g., $\mathbf{B}^q = (0, B_{y0} \cos(k_1 z), 0)$ can be used to calculate η_{yx} , η_{xx} , α_{yy} , and α_{xy} . The use of more test fields allows calculation of the spatial variation of coefficients, for instance if stratification is used or a strong \mathbf{U} is seen to develop.

the quasi-linear method), it is difficult to ensure that the test fields b^q and u^q are linear in the test mean fields. In addition, it is no longer the case that transport coefficients in MHD turbulence (i.e., with both u_0 and b_0) are the sum of the kinetic and magnetic contributions. A method has been proposed and explored in Rheinhardt and Brandenburg (2010), but it is rather complex and, in certain cases, it can involve four different versions that may give different results. Of course, with our interest in magnetic fluctuations in this thesis, the use of such a method would in principle be highly rewarding. Nonetheless, given that the experimental nature of the method would have necessitated a thorough exploration of a variety of dynamos to have confidence in results, due to time constraints I have opted to employ other methods to measure transport coefficients in the presence of the small-scale dynamo. These are described in chapter 5.

In all test-field method calculations, error in the transport coefficients is estimated by dividing the time-series into N segments and calculating the standard deviation of the mean. I shall generally take $N = 100$, but results are quite insensitive to this choice, so long as the segments are statistically independent and sufficiently many are used (in practice $N \gtrsim 20$).

A note on the utility of quasi-linear approximation for the studies in this chapter The quasi-linear model involves a rather drastic approximation to the full nonlinear equations: what has been gained by utilizing the quasi-linear system for these dynamo studies? Most simply, the methods provide a straightforward way to calculate transport coefficients by fixing mean fields in both the magnetically driven and kinematic cases, followed by a clear check of whether a mean-field dynamo is observed at the same physical parameters. Given the importance of incoherent dynamo mechanisms, this connection between transport coefficients and mean-field growth is not always so obvious as it might seem. Related to this, one of the most important benefits of these methods is afforded by the comparison between CE2 and direct quasi-linear simulation (DQLS). This provides an unambiguous test of whether the dynamo is coherent or incoherent, since statistical averages are inserted directly into the CE2 mean-field equations and an incoherent dynamo is not possible.

Thus, if similar results are observed between CE2 and DQLS, we can be sure that the dynamo arises through η_{ij} transport coefficients. Another beneficial aspect of CE2 is that long periods of exponential mean-field growth can be observed, even when strong small-scale magnetic fluctuations are present (e.g., due to magnetic driving). Contrast this to DNS or DQLS, for which it is nearly impossible to observe exponential dynamo growth in the presence of strong magnetic fluctuations, since the finite size of the domain causes the mean field to come into near equipartition with the fluctuations almost instantaneously, and nonlinear saturation effects become important relatively early on.

Finally, I note that CE2 calculations in fixed mean fields are in essence the same calculation as the semi-analytic results presented in Sridhar and Singh (2010); Singh and Sridhar (2011). The only substantial difference is the forcing – a singular forcing $\sigma_u \sim \delta(\mathbf{k} - \mathbf{k}_f)$ is used in Singh and Sridhar (2011), while I use the same forcing as detailed above for the self-consistent simulations. Our results agree with their findings in the zero-rotation case with only momentum equation forcing, but are much more easily extendable to arbitrary rotation⁸ and strong magnetic fluctuations.

4.3.2 Simulation setup

The standard simulation setup is to seed from random Gaussian initial conditions in \mathbf{u} and \mathbf{B} at a very small amplitude and reasonably large scales (wavelengths greater than ~ 0.2). The forcing, σ_u (and sometimes σ_b), causes a small-scale turbulent bath of fluctuations, and growth of the dynamo is studied on scales larger than the forcing (i.e., $k < 15$). As in Yousef *et al.* (2008a), the separation of scales between mean fields and fluctuations is aided by choosing a box that is very elongated in the z direction, $L_z > L_x, L_y$. The development of the dynamo is studied by numerically averaging \mathbf{B}_T over x and y to obtain the mean magnetic fields, \mathbf{B} (see Sec. 4.2). Overall, the numerical setup

⁸Rotation complicates the analytic problem substantially, although perturbative methods may be feasible; see Leprovost and Kim (2008).

of our nonlinear runs is nearly identical to that of Yousef *et al.* (2008a), aside from the addition of forcing in the induction equations in some simulations. As defined (see chapter 3), the Reynolds numbers as defined are with respect to the large-scale shear. It is also useful to keep in mind a more standard definitions of these using the small-scale velocity, denoted Rm_f and Re_f . Since I use the same forcing spectrum throughout this work, these are related to Rm and Re through

$$\text{Rm}_f = \frac{u_{\text{rms}}}{k_f} \text{Rm} = 0.053 u_{\text{rms}} \text{Rm} \quad (4.7)$$

with the similar definition for Re_f . Most of the calculations presented in this chapter have $\text{Re}_f = \text{Rm}_f \sim 5$.

4.4 Kinematic dynamo

Before exploring the dynamo with magnetic fluctuations it is important to fully understand the kinematic dynamos presented in Yousef *et al.* (2008a). With this aim, I have reproduced many of their simulations across a variety of S , Ω and L_z , to better understand the fundamental dynamo mechanisms. I present the most relevant of these results here.

For the kinematic dynamo, only the momentum equation is driven (i.e., $\sigma_b = 0$), and at these Reynolds numbers the small-scale field arises purely from tangling of the mean field by velocity, $\nabla \times (\mathbf{u} \times \mathbf{B})$, an effect that is quite distinct from the small-scale dynamo (Schekochihin *et al.*, 2007). In both the rotating and non-rotating cases, there is a mean-field dynamo above some threshold in L_z and $\langle \sigma_u^2 \rangle$ i.e., the dynamo is only excited in a sufficiently tall box if driven hard enough. Given the scaling of the growth rates in Eqs. 4.3 and 4.5 and the fact that η_t is the sum of a turbulent and physical resistivity, this behavior is expected for both incoherent and coherent

dynamos.⁹ The main finding is that the non-rotating case is a stochastic- α dynamo (essentially that explored analytically in Heinemann *et al.* 2011, but including nonzero k_z) but that rotation qualitatively changes the mechanism, decreasing η_{yx} to negative values and causing the dynamo to be more coherent.

In both the non-rotating and rotating cases, I present DNS, DQLS, and CE2 calculations at identical parameters. The primary purpose of this comparison is to illustrate the difference between CE2 and DQLS, which arises due to the incoherent mean-field dynamo, while also showing that DNS and DQLS exhibit a qualitatively similar dynamo. Although the spatiotemporal evolution of the mean field is similar in each case, we shall see that the DNS and DQLS runs exhibit slightly different growth rates. This can be attributed to inaccuracies in the quasi-linear approximation at these Reynolds numbers.

Non-rotating dynamo Fig. 4.1 illustrates the growth of the nonrotating dynamo using DNS, DQLS and CE2, at $S = 2$ and $L_z = 16$, $L_x = L_y = 1$. As in Yousef *et al.* (2008a), I use a resolution $(32, 32, 512)$ for DNS and DQLS, but use $(32, 32, 256)$ for the CE2 run due to its computational scaling with N_z^2 (see Sec. 3.1.1). I have verified that identical results are obtained at half this resolution and are confident that $N_z = 256$ is sufficient to resolve all important scales.

Firstly, it is worth noting that the mean field, as plotted in Fig. 4.1(a-b), is truly a “large-scale” dynamo. One can estimate the wavenumber of B_y as approximately $3 \times 2\pi/L_z \approx 1.2$, far smaller than the forcing scale, $k_f = 6\pi$. Next, let us compare the CE2 with the the nonlinear and quasi-linear DNS. It is evident that the dynamo in this case is purely incoherent – while slow mean-field growth is observed in DNS and DQLS, the magnetic field simply decays in the CE2 simulation in exactly the way that would be expected due to a positive η_{yx} coefficient. It is also worth noting the qualitative appearance of the mean fields in DQLS and DNS, which appear to wander randomly,

⁹One might expect the dynamo to disappear again if $\langle \sigma_u^2 \rangle$ is increased further, due to the increase in η_t causing the dynamo to become stable. This behavior is seen in the quasi-linear case, but it seems that at these parameters in the nonlinear runs, a small-scale dynamo is excited before this occurs.

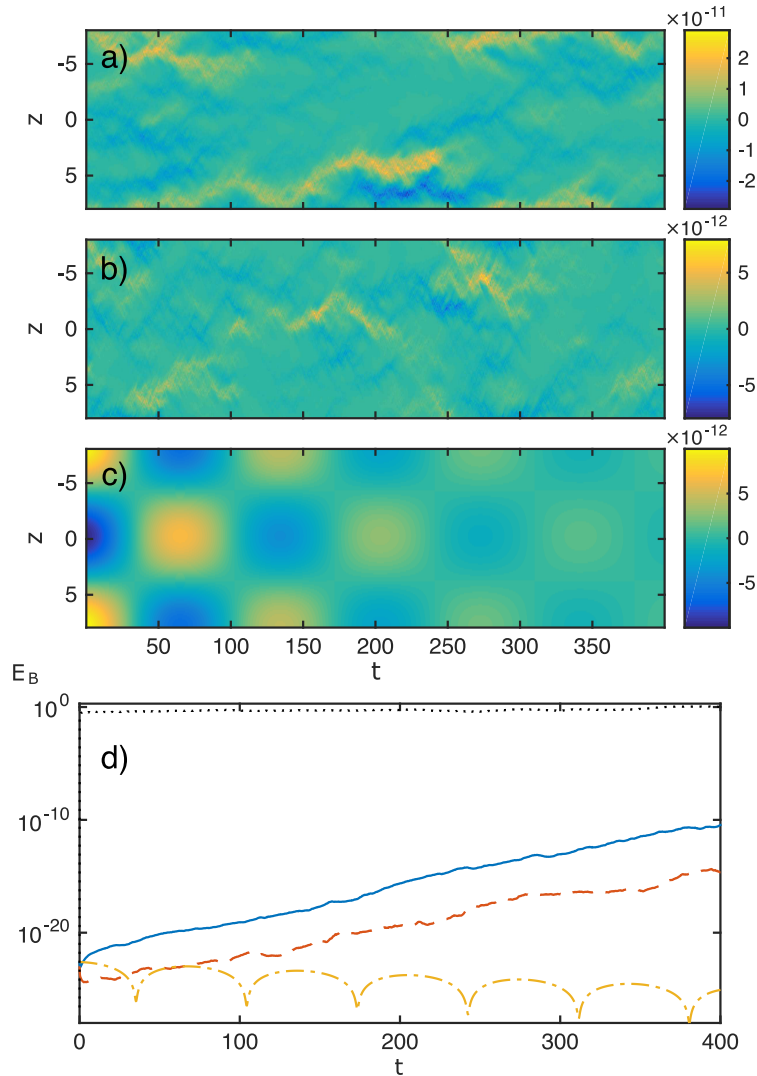


Figure 4.1: (a-c) Illustration of $B_y(z, t)$ from non-rotating turbulence with $S = 2$, $L_z = 16$, $u_{\text{rms}} = 0.8$, for DNS, DQLS, and CE2 from (a)-(c). In the two direct runs (a) and (b), I remove the exponential growth [i.e., plot $e^{-\gamma t} B_y(z, t)$ where γ is the measured growth rate] so that the full time evolution can be observed. (d) Growth in time of the mean field for (solid, blue) the nonlinear equations; (dashed, red) quasi-linear DNS; and (dash-dot, yellow) CE2, each at the same physical parameters as in (a-c). While both nonlinear and quasi-linear DNS exhibit a positive mean-field dynamo, the CE2 calculation does not, illustrating the dynamo must be incoherent. The dotted black line shows the energy of u fluctuations.

as expected due to a stochastic- α effect. A final piece of evidence for the incoherency of this non-rotating dynamo comes from doubling the box size in the x and y dimensions, keeping all other parameters fixed¹⁰ (not shown). This causes the growth rate of the mean-field dynamo to change from $\gamma = 0.062$ [for the dynamo in Fig. 4.1(a)] to being almost stable, $\gamma = 0.0096$, and since a coherent dynamo should be mostly unaffected by such a change (unless the added wavenumbers significantly affect the transport coefficients), this constitutes a simple check of the dynamo's incoherency without using the quasi-linear approximation.

Rotating dynamo Figure 4.2 illustrates the same calculations as Fig. 4.1, but with a Keplerian Coriolis force added [$\Omega = 2/3S$ in Eq. (3.1)]. While the dynamo in the quasi-linear and nonlinear direct simulations are similar to the non-rotating case (with a slightly higher growth rate), the CE2 dynamo is markedly different, exhibiting mean-field growth. This illustrates that in adding net rotation to the system one enables a coherent dynamo, which can be understood as arising from a change in sign of η_{yx} (see also Figs. 4.5-4.6 below). The cause of this change is simply the well-known Rädler, or $\Omega \times \mathbf{J}$, effect (Krause and Rädler, 1980; Moffatt and Proctor, 1982). This idea seems to have been missed in Yousef *et al.* (2008a), who state “There does not appear to be much difference, qualitative or quantitative, between the rotating and nonrotating cases.” As shown in chapter 6, the contributions to the η_{yx} transport coefficient from rotation and the shear have identical forms, and together give $\eta_{yx} \propto S - 2\Omega$. For Keplerian rotation this is slightly negative, leading to the possibility of coherent dynamo growth if η_{yx} overwhelms the diagonal turbulent resistivity. Finally, I have again doubled the horizontal dimensions of the box for this rotating case (not shown), which causes the dynamo growth rate to drop from $\gamma = 0.067$ [in Fig. 4.2(a)] to $\gamma = 0.041$. A comparison with the results in the previous paragraph ($\gamma = 0.062$ and $\gamma = 0.0096$ in the narrow and wide boxes respectively) shows that while in the narrow box ($L_x = L_y = 1$) rotation causes only a minor difference to the growth rate (because the stochastic- α

¹⁰I would like to thank A. Schekochichin for suggesting this numerical experiment.

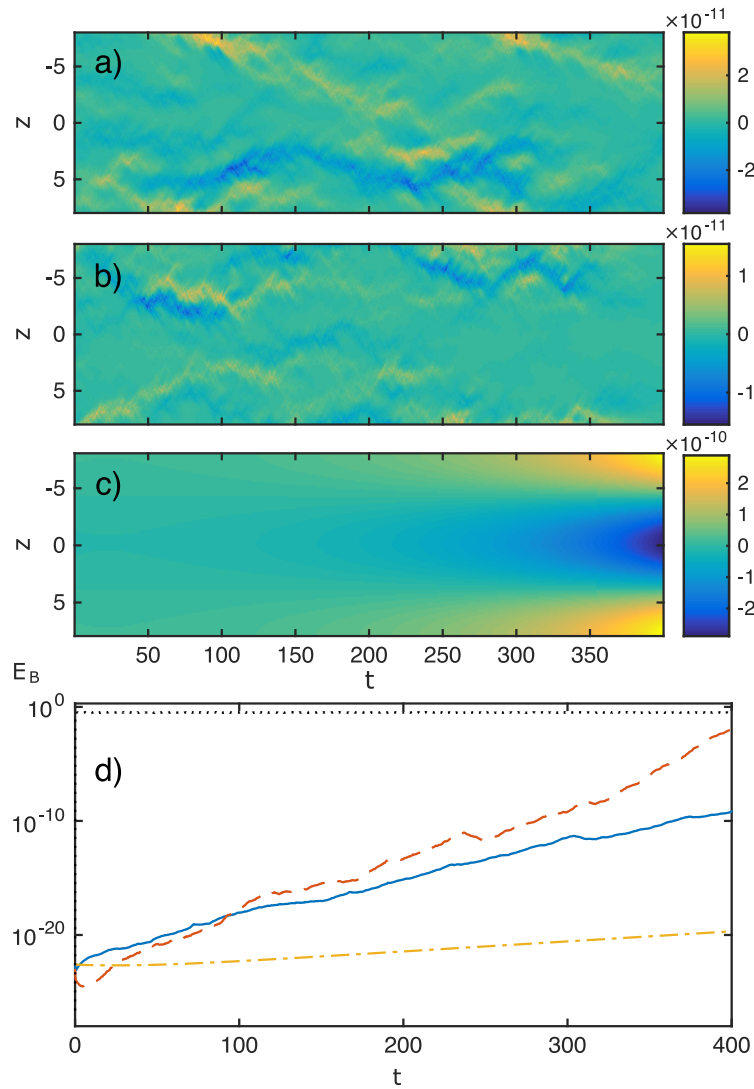


Figure 4.2: Same as Fig. 4.1 but for Keplerian rotating turbulence, $u_{\text{rms}} = 0.75$ (velocity fluctuations are suppressed slightly by the rotation). In contrast to Fig. 4.1, the CE2 calculation also shows a growing dynamo, albeit at a much smaller growth rate, illustrating that the dynamo is partially coherent.

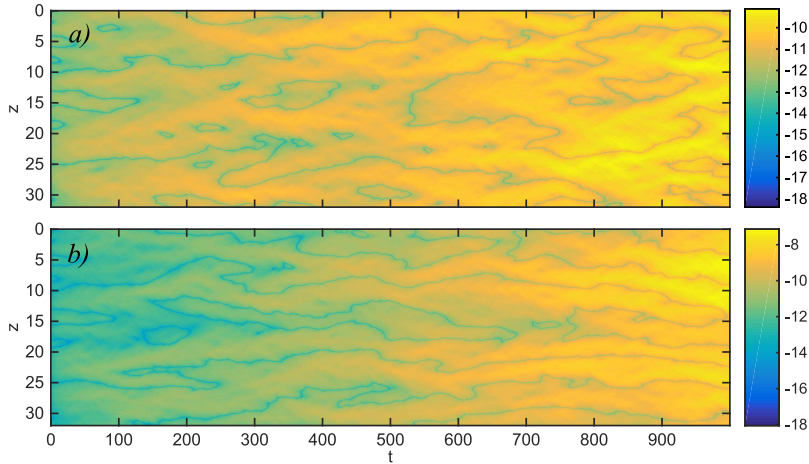


Figure 4.3: Spatiotemporal evolution of $\log_{10}(|B_y(z,t)|)$ at $S = 1$, $L = 32$, for (a) nonrotating case ($u_{\text{rms}} \approx 0.47$), (b) Keplerian rotation ($u_{\text{rms}} \approx 0.43$; again velocity fluctuations are slightly suppressed by rotation). The log color scale is chosen so as to easily see the mean-field phase evolution. The difference in the two dynamos is evident from the evolution of the phase of B_y as the dynamo grows. While in the non-rotating case the phase wanders somewhat randomly, as is characteristic of an incoherent dynamo mechanism (see Sec. 4.2), we see a relatively constant phase of B_y in the case with rotation. Note also the faster growth rate of the rotating dynamo.

effect significantly overwhelms the coherent dynamo), in the wider box (where fluctuations in α have been significantly reduced), the difference in growth rates is much more substantial. This behavior is consistent with the rotating dynamo being driven through a combination of stochastic- α and coherent effects [see Eq. 4.8 below], with the coherent effect being mostly unmodified by the change in box dimensions.

While the $B_y(z,t)$ evolution pictured in Figs. 4.1(a) and 4.2(a) looks qualitatively rather similar between the rotating and non-rotating runs (although perhaps structures are slightly longer lived in Fig. 4.2), this is not always the case. In Fig. 4.3 I compare spatiotemporal evolutions of $B_y(z,t)$, in a longer box ($L_z = 32$) with less driving noise, which causes a lower growth rate and a decrease in the relative importance of the stochastic- α effect compared to the coherent dynamo. As is evident, the two dynamos are qualitatively different, with the phase of B_y wandering quasi-randomly in the non-rotating case, while in the rotating case it is approximately constant in time. This constant phase is not consistent with a dynamo driven purely by the stochastic- α effect (see Sec. 4.2)

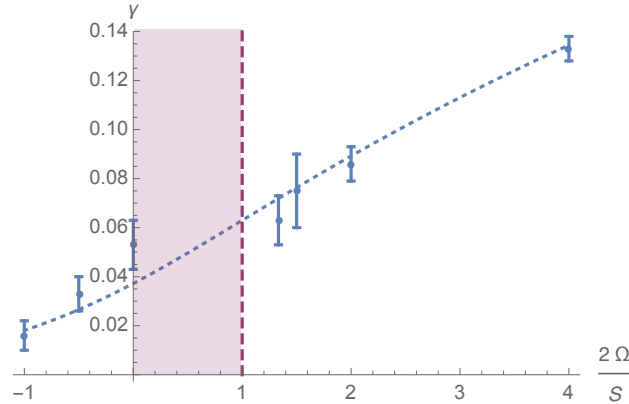


Figure 4.4: Growth rate of B_{rms} as a function of $2\Omega/S$, for fixed shear $S = 2$, and velocity driving $u_{\text{rms}}^2 \approx 1$ (except for the point $\Omega = 0$, for which $u_{\text{rms}}^2 \approx 1.5$). The shaded region shows where the flow is hydrodynamically unstable (neglecting dissipation), and the dashed vertical line shows the SOCA prediction for where the coherent dynamo growth rate vanishes. Of course, due to the strong stochastic- α effect, the dynamo can still grow even when the predicted coherent growth rate is zero or negative. The dotted line is an approximate fit of predicted growth rate, Eq. (4.8), to the data, using $\eta_t = u_{\text{rms}}/3k_f = 0.018$, $\eta_{yx} = 0.0007 \times (2\Omega - S)$, and $\langle \alpha_{yy}^2 \rangle = 6.2 \times 10^{-5}$. Error bars are estimated by fitting the growth rate to half of the time-series data for each run.

From Figs. 4.2 and 4.3, we can interpret the Keplerian rotating shear dynamo around these parameters as being driven by both incoherent and coherent mechanisms. This interpretation is entirely consistent with all numerical results given in Yousef *et al.* (2008b) and Yousef *et al.* (2008a). In particular, their Fig. 5 illustrates that the addition of rotation enhances the growth of the dynamo in all cases. Furthermore, while $\gamma \sim S$ for the non-rotating dynamo, with rotation it is evident that the growth of γ is somewhat faster than linear in S . Since one expects $\gamma \sim S^2$ for a coherent dynamo (since η_{yx} itself must scale linearly with S for small S), their observed trends are consistent with the dynamo being driven through a mix of incoherent and coherent mechanisms.

Varying the rotation As one final test of the importance of net rotation in this system, I have run a series of simulations, increasing the rotation from $\Omega = -1$ (cyclonic rotation) to $\Omega = 4$ (anticyclonic rotation). Results from this series of simulations are illustrated in Fig. 4.4. As expected, we see a substantial increase in dynamo growth rate as the rotation becomes anticyclonic,

in broad agreement with the SOCA prediction $\eta_{yx} \propto S - 2\Omega$. Due to the presence of the stochastic- α effect, one would not expect a linear scaling of γ with Ω . Instead, the growth rate (including an η_{yx} and fluctuating α_{yy}) is the most positive root of¹¹

$$-4D_{yy}k^2S^2 - 4\eta_{yx}k^2S\xi + \xi^3 = 0, \quad (4.8)$$

where $\xi = 2\eta_t k^2 + \gamma$ (Mitra and Brandenburg, 2012). I plot a fit of Eq. (4.8) to the data in Fig. 4.4 [with $\eta_t = u_{\text{rms}}/3k_f$, $\eta_{yx} = \eta_{yx0}(2\Omega - S)$], illustrating good agreement away from the instability boundaries ($\Omega = 0$ and $\Omega = S/2$). Close to the boundary, it seems that some other nonlinear effect may be important, increasing the growth rate on the cyclonic side and decreasing it on the anticyclonic side.¹²

4.4.1 Direct calculation of transport coefficients

To validate and quantify the conclusions discussed above, in this section I directly calculate the transport coefficients, comparing results from CE2¹³ and the test-field method (Brandenburg and Subramanian, 2005). There is no small-scale dynamo at these parameters, which simplifies the test-field calculations since b^q arises purely due to the presence of B^q (see Sec. 4.3.1 for more information). Test-field calculations are run from $t = 0 \rightarrow 1000$ to obtain accurate results. For future reference, it is worth noting that at low Rm, a very small time step must be utilized in any direct calculation of the transport coefficients (i.e., with the test-field method or DQLS). The reason is that the convergence of stochastic portion of the time integrator is of quite low order ($t^{1/2}$), and at low Rm the statistical equilibrium is primarily a balance between the driving noise and the dissipation term, $\bar{\nu}k^2\mathbf{u}$.

¹¹In reality, one will also see a change in growth rate due to η_{xy} and fluctuations in the other α coefficients, but these effects seem minor and are ignored here.

¹²This should not be entirely unexpected. Of course, inside the instability boundaries, SOCA predictions fail spectacularly.

¹³DQLS gives identical results to CE2, albeit with errors due to the random noise.

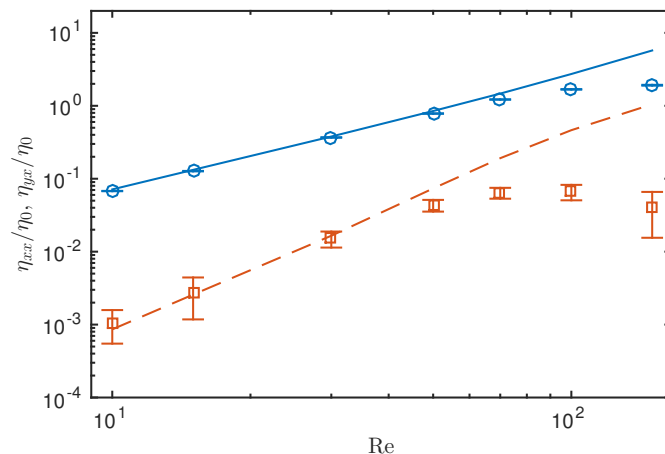


Figure 4.5: Transport coefficients for the kinematic non-rotating dynamo as a function of Re (at $Pm=1$), for $S = 2$; solid line and circle markers (blue), η_{xx} ; dashed line and square markers (red), η_{yx} . The curves show the quasi-linear results, calculated using CE2, while the markers show the nonlinear test-field calculations with error bars (see text). As is common, coefficients are normalized by the “high-conductivity” SOCA turbulent resistivity $\eta_0 = u_{\text{rms}}/(3k_f)$. Across all simulations, the absolute level of the forcing (i.e., σ_u) is kept constant at the same level as Fig. 4.1, which means that the lower- Re simulations have somewhat lower u_{rms} .

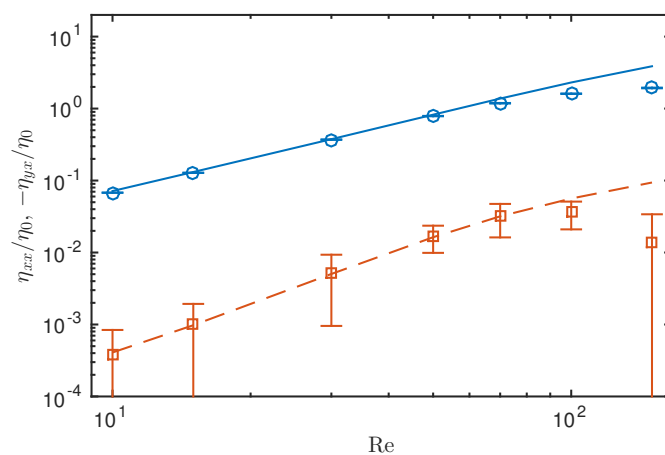


Figure 4.6: Same as for Fig. 4.6 but with Keplerian rotation. Note that $\eta_{yx} < 0$ in this case, so I plot $-\eta_{yx}$ so as to utilize a log scale.

Results are illustrated in Figs. 4.5 and 4.6. We see that in both cases the quasi-linear and nonlinear coefficients agree at lower Rm as expected, diverging somewhat past $Rm \gtrsim 70$. In agreement with the conclusions from simulations earlier in the section, $\eta_{yx} > 0$ in the non-rotating case, while $\eta_{yx} < 0$ with rotation, showing that a coherent dynamo is possible at sufficiently small k_z . It is also worth noting that the magnitude of η_{yx} is less in the rotating case, as known from SOCA calculations (see chapter 6, also Rädler and Stepanov 2006). For $Rm = 100$, as used in Figs. 4.1 to 4.4, there are some differences between quasi-linear and nonlinear results due to inaccuracies in the quasi-linear approximation, which explains the discrepancy in dynamo growth rates¹⁴ observed in Fig. 4.2. Interestingly, given the controversies surrounding the kinematic “shear-current” effect (Rogachevskii and Kleeorin, 2003), nonlinear corrections appear to be particularly important for η_{yx} without rotation (this coefficient shows the largest discrepancy between the nonlinear and quasi-linear calculations).

In addition to the results for η_{yx} and η_{xx} shown, I have also calculated η_{xy} and η_{yy} by setting $B_x = B_{x0} \cos(k_1 z)$, $B_y = 0$. It is found that $\eta_{xx} = \eta_{yy}$ to a high degree of accuracy, while η_{xy} , which is positive, is mostly unaffected by rotation. Its magnitude (compared to the other η) depends strongly on the shear and Reynolds number. Due to the dominance of the shear, such an η_{xy} has little effect on the growth rate, even though its magnitude is larger than that of η_{yx} . In addition to the results illustrated and discussed above, I have also verified the expected linear dependence of η_{yx} on S at low Rm and confirmed that the transport coefficients change very little with L_z over the range $L_z = 1 \rightarrow 8$.

¹⁴ It seems that for Fig. 4.1, the lower values of η_{xx} and η_{yx} in comparison to the quasi-linear runs cancel each other, leading to the same growth rate.

4.5 Magnetically driven dynamo

Having now broadly understood the shear dynamos of Yousef *et al.* (2008a) and Yousef *et al.* (2008b), I examine the effect of small-scale magnetic fluctuations. Before presenting numerical results, I shall explain in more detail exactly what is meant by a magnetically driven linear dynamo. Similar ideas have been considered before (see, for example, Rädler *et al.* 2003; Park and Blackman 2012, and Rheinhardt and Brandenburg 2010 for a particularly thorough analysis).

As is obvious from Eq. (4.1), an unstable dynamo requires inhomogeneity in the fluctuations \mathbf{u} and \mathbf{b} , such that $\nabla \times \mathcal{E} \neq 0$. Since fluctuations (termed \mathbf{u}_0 and \mathbf{b}_0) are assumed to be initially homogenous, this inhomogeneity must be introduced by \mathbf{B} , which is assumed small. Considering the linearized fluctuation equations for simplicity (this is just the quasi-linear dynamo, which we know works in any case),¹⁵ it is evident that the kinematic dynamo arises from inhomogeneity induced in \mathbf{b} fluctuations through the term $\nabla \times (\mathbf{u}_0 \times \mathbf{B})$ in the fluctuation induction equation [Eq. (3.6b)]. This leads to an inhomogenous contribution to \mathcal{E} through $\mathbf{u}_0 \times \mathbf{b}_{\text{inhom}}$. In contrast, in the presence of \mathbf{b}_0 , an inhomogenous part of \mathbf{u} will arise from the Lorentz force $\mathbf{b}_0 \cdot \nabla \mathbf{B} + \mathbf{B} \cdot \nabla \mathbf{b}_0$ [see Eq. (3.6a)], giving a contribution to \mathcal{E} through $\mathbf{u}_{\text{inhom}} \times \mathbf{b}_0$. Without a mean-field flow, such a contribution is not possible from the induction equation alone. In calculating the transport coefficients (Secs. 4.4.1 and 4.5.2) I have verified that artificial removal of the Lorentz force causes the transport coefficients to return to their kinematic values. It may be interesting in future work to examine in the vorticity dynamo (i.e., generation of \mathbf{U}) in more detail, in particular its interaction with the magnetic dynamo. These effects are almost certainly much more important in the non-rotating case.

Before proceeding it is worth commenting on an important difference between the magnetic shear-current effect discussed below and the standard magnetic α effect. This difference stems from the fact that the magnetic α effect can have either sign, since it is related to the small-scale

¹⁵Inclusion of nonlinear terms introduces several additional complexities, see Rheinhardt and Brandenburg (2010).

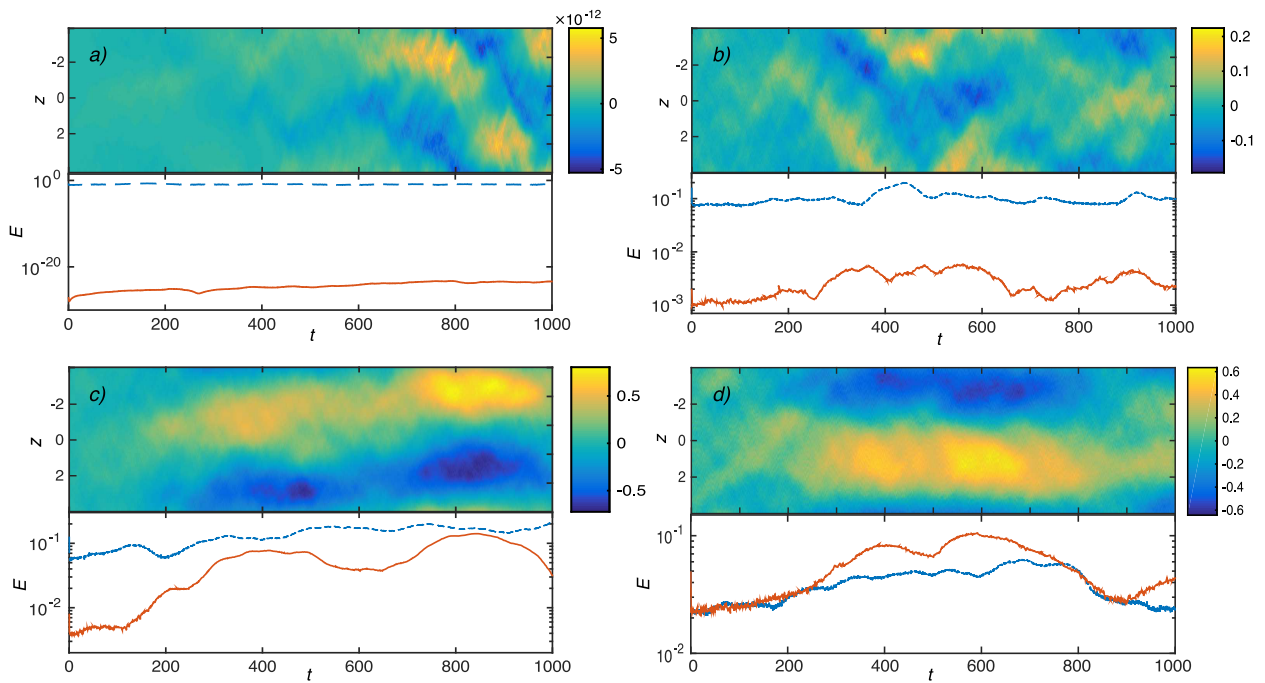


Figure 4.7: Low-Rm driven DNS at $S = 1$, $L_z = 8$, and no rotation, with $\sigma_u + \sigma_b = \sigma$ chosen to be constant in each simulation (the level is such that $u_{\text{rms}} \approx 0.2$ when only velocity forcing is used). The proportion of magnetic forcing is (a) $\sigma_b = 0$, (b) $\sigma_b = 0.1\sigma$, (c) $\sigma_b = 0.2\sigma$ (d) $\sigma_b = 0.5\sigma$. The top row of each subfigure illustrates the time development of $B_y(z, t)$, the bottom row illustrates the kinetic energy (dashed, blue) and magnetic energy (solid, red).

current helicity, $\alpha_M \sim \langle \mathbf{b} \cdot \nabla \times \mathbf{b} \rangle$. In practice, as the small-scale dynamo grows in the presence of helical velocity fluctuations, α_M grows with the *opposite sign* to the kinematic α effect¹⁶ – the origin of catastrophic quenching (Blackman and Field, 2002; Brandenburg and Subramanian, 2005). In contrast, since the magnetic shear-current effect drives the dynamo through a resistivity, $\eta \sim \langle \mathbf{b}^2 \rangle$, its sign is fixed. This implies that the the source of magnetic fluctuations can be the small-scale dynamo, in some sense the inverse of quenching. In chapter 5, we shall see a marked decrease in η_{yx} after saturation of the small-scale dynamo, which can in turn drive a coherent large-scale dynamo.

4.5.1 Numerical experiments on the magnetic dynamo

Here, I argue for the existence of the magnetic dynamo through numerical experiments. I shall first consider nonlinear DNS, forcing the induction equation to excite \mathbf{b}_0 , then illustrate the quasi-linear dynamo with CE2 calculations including magnetic forcing. CE2 is convenient for examining the magnetic dynamo since a sustained period of exponential mean-field growth is observable, while in direct simulations the mean field quickly reaches equipartition with velocity fluctuations.

Nonlinear DNS

Since there is no small-scale dynamo due to the low R_m , homogenous magnetic fluctuations (\mathbf{b}_0) are excited in DNS through forcing the induction equation with σ_b (the statistical properties of which are chosen to be the same as σ_u). As a simple numerical experiment to test the effects of small-scale magnetic noise, I start from pure velocity forcing and increase the forcing in the induction equation, while keeping the total forcing $\sigma_u + \sigma_b = \sigma$ fixed. (While I have carried out these experiments both with and without Keplerian rotation, I present only the non-rotating cases

¹⁶ One possible exception to this that may be very important could occur in the presence of magnetic instabilities, for instance the MRI. In this case it seems more likely that the magnetic α effect might overwhelm the kinematic effect, since \mathbf{b} fluctuations do not arise purely as a consequence of small-scale dynamo action (Gressel, 2010; Park and Blackman, 2012).

here as the rotating results are similar but with a somewhat stronger coherent dynamo. This is expected since a kinematic coherent dynamo is possible with Keplerian rotation.)

Results in the range $\sigma_b = 0 \rightarrow 0.5\sigma$ are illustrated in Fig. 4.7. At $\sigma_b = 0$, one sees a dynamo of a similar type to that in Fig. 4.1, although it is a little weaker due to the lower u_{rms} and choice $S = 1$. This is a stochastic- α effect, as seen by the slowly growing mean fields that wander significantly in phase. Let us now consider the more interesting behavior of the other cases, $\sigma_b = 0.1\sigma$, $\sigma_b = 0.2\sigma$ and $\sigma_b = 0.5\sigma$. Firstly, it is worth noting that the stronger mean-field in the presence of magnetic fluctuations is unsurprising; this simply results from the approximate equipartition of \mathbf{B} with \mathbf{b} due to the finite size of the domain. The main result is instead the substantial qualitative difference in the appearance of the mean-field evolution between $\sigma_b = 0.1\sigma$ and the cases with higher magnetic forcing. Specifically, at $\sigma_b = 0.1\sigma$ we see some wandering of the field as well as possibly a slow growth, behavior I interpret as a stochastic- α effect near its saturated state. In contrast, at $\sigma_b = 0.2\sigma$ and $\sigma_b = 0.5\sigma$, a relatively fast growth of \mathbf{B} is observed until saturation at substantially larger values than seen at $\sigma_b = 0.1\sigma$. In addition, the profile of $B_y(z, t)$ for $\sigma_b \gtrsim 0.2\sigma$ is relatively constant in phase, suggesting that the dynamo is coherent.

This behavior suggests that a coherent dynamo can be driven by small-scale magnetic fluctuations – the magnetic analogue of the shear-current effect. This magnetic dynamo saturates at larger field strengths than the stochastic- α dynamo, with the saturation amplitude being roughly independent of the level of magnetic fluctuations [as seen by comparison of Figs. 4.7(c) and (d)]. Note also that this dynamo field appears to show quasi-cyclic behavior of some sort in its nonlinear regime (in Fig. 4.7(d) the large-scale field reappears again at later times). The reason for this interesting behavior and its relevance to the cycles seen in MRI turbulence (Lesur and Ogilvie, 2008b) remains unclear.

To ensure the observed behavior is robust, I have rerun each of the simulations in Fig. 4.7 several times, varying the initial conditions and random number seed. These (not shown) have

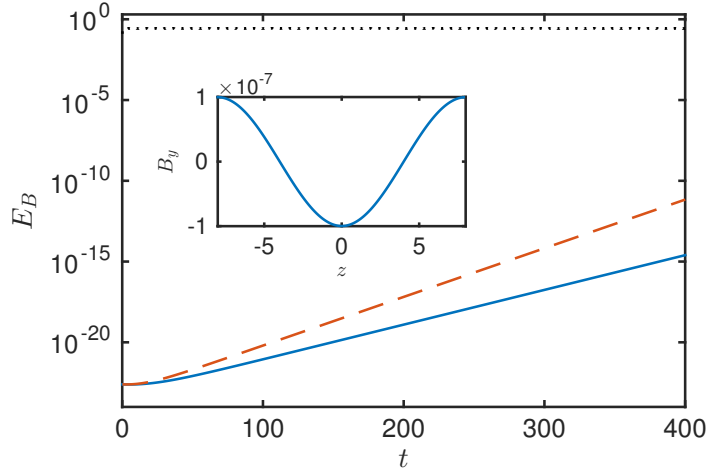


Figure 4.8: Mean-field energy evolution in CE2 calculations at the same parameters ($\text{Re} = 100$, $S = 2$, $L_z = 16$) as Figs. 4.1 and 4.2, but with magnetic fluctuations driven at the same level as velocity fluctuations (such that the total forcing is the same as Figs. 4.1-4.2). Solid (blue), non-rotating $\Omega = 0$; dashed (red), Keplerian rotation $\Omega = 4/3$; the dotted (black) curve gives the sum of velocity and magnetic fluctuation energies (this is similar for the two cases). The inset illustrates the spatial form of $B_y(z, t = 400)$ for $\Omega = 0$, which is exactly sinusoidal as expected.

illustrated that the $\sigma_b = 0.1\sigma$ simulations occasionally excite the coherent dynamo similar to that in Fig. 4.7(c-d), and will eventually do so if evolved for a sufficiently long time. In addition, the $\sigma_b = 0.2\sigma$ occasionally *fails* to excite the coherent dynamo as quickly as observed in Fig. 4.7(c). This brings us to the conclusion that the coherent dynamo can be excited for $\sigma_b \gtrsim 0.1 \rightarrow 0.2$ and the simulation outcome depends on properties of an individual realization around this boundary. I have failed to find coherent dynamo excitation at $\sigma_b = 0.05\sigma$, having tested a number of realizations over very long time periods. This dependence on realization is very similar to the behavior observed in shear-dynamos at higher Rm , where the small-scale dynamo acts as the source of \mathbf{b}_0 fluctuations (see chapter 5).

CE2 dynamo

The magnetically driven dynamo is also seen ubiquitously in quasi-linear and CE2 simulations. Conveniently, in CE2 calculations, it is possible to observe exponential dynamo growth over long

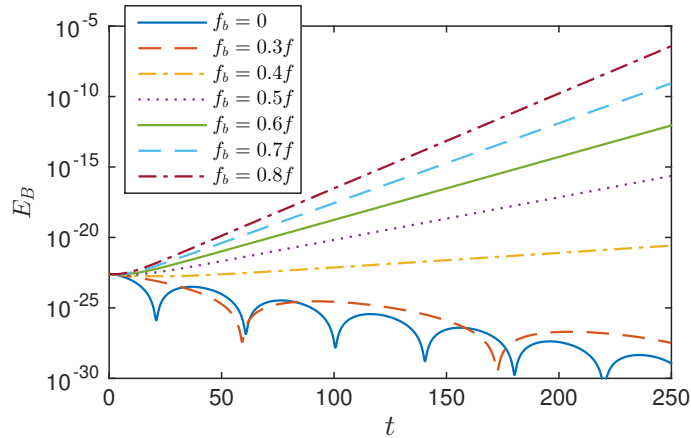


Figure 4.9: Mean-field energy in CE2 at $Rm = 500$, $Pm = 1$, $u_{\text{rms}} \approx 0.2$ (at $\sigma_b = 0$) $S = 2$, $\Omega = 0$ and box dimensions $(L_x, L_y, L_z) = (1, 1, 4)$ with resolution $(28, 28, 128)$. Total forcing is kept constant in each simulation, but the proportion of magnetic forcing is increased from 0 to 0.8. As this is done, the growth rate of the mean field increases enormously due to the magnetically driven dynamo.

time periods, in contrast to direct simulations [e.g., Fig. 4.7(b)-(d)]. For example, in Fig. 4.8 I illustrate the the magnetically driven coherent dynamo, using statistical simulation at the same parameters as Figs. 4.1 and 4.2. Specifically, I keep the same forcing $(\sigma_u + \sigma_b)$ as Figs. 4.1-4.2, but set $\sigma_b = \sigma_u$. As is evident (c.f. Figs. 4.1 and 4.2), magnetic fluctuations enormously enhance the growth rate of the dynamo. In addition, there is now fast coherent growth both with and without rotation, which demonstrates that the magnetic effect significantly overwhelms the kinematic effect. To illustrate the continuous change as magnetic forcing is increased, another example is given in Fig. 4.9. Here, I keep the total forcing constant, changing the proportion driving the induction equation from 0 to 0.8 of the total. The presence of the magnetically driven dynamo is evident, becoming slightly unstable when magnetic forcing accounts for 0.4 of the total and increasing the growth rate thereafter. Since only coherent dynamos are possible within the CE2 formalism, we again arrive at the conclusion that small-scale magnetic fluctuations drive a strong coherent shear dynamo.

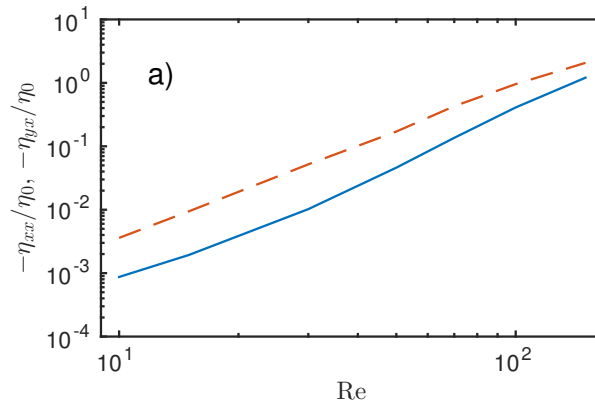


Figure 4.10: Transport coefficients for the magnetic dynamo as a function of Re (at $P_m = 1$), for $S = 2$ and $\Omega = 0$; solid (blue), $-\eta_{xx}$; dashed (red) $-\eta_{yx}$. (Note that both η_{xx} and η_{yx} are negative.) The calculations are carried out at $L_z = 4$ using CE2 (as for the kinematic case, there is very little dependence of L_z). Coefficients are normalized by the u_{rms} values from Figs. 4.5 and 4.6, such that the values of the u and b transport coefficients can be directly compared.

4.5.2 Direct calculation of transport coefficients

As in Sec. 4.4.1, one can directly calculate the transport coefficients of the magnetic dynamo by fixing the mean fields and driving magnetic fluctuations. Within quasi-linear theory, this is a straightforward generalization of kinematic calculations, and the transport coefficients in the presence of both magnetic and velocity fluctuations will be the sum of those calculated with one or the other, $\eta = \eta_u + \eta_b$. However, because of the complexity of including magnetic fluctuations in the test-field method (Rheinhardt and Brandenburg 2010, see Sec. 4.3.1) I leave magnetic test-field method studies to future work.

Figure 4.10 illustrates η_{yx} and η_{xx} when only magnetic fluctuations are present, as calculated by setting $\sigma_u = 0$ and fixing B_y in CE2, with the same technique as detailed in Sec. 4.4.1. Most notably, we see both that η_{yx} and η_{xx} are negative, both with and without rotation, and are of similar magnitudes. Importantly, a comparison of Fig. 4.10 with Figs. 4.5 and 4.6 shows that η_{yx} is substantially larger in magnitude than the kinematic value, which implies that when $b_{\text{rms}} \sim u_{\text{rms}}$ the magnetic contribution should dominate. For example, without rotation, the quasi-linear

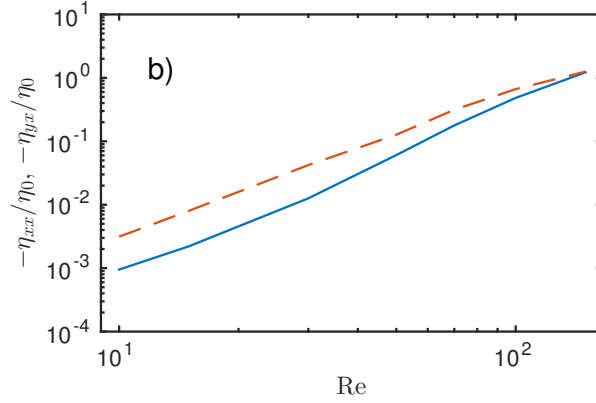


Figure 4.11: As for Fig. 4.10 but with Keplerian rotation $\Omega = 4/3$. (Note that both η_{xx} and η_{yx} are negative.)

magnetically driven η_{yx} is larger than the kinematic η_{yx} by approximately a factor of 2 at $\text{Rm} = 100$, implying the presence of magnetic fluctuations could change the sign of η_{yx} and excite a coherent large-scale dynamo once $b_{\text{rms}} \gtrsim u_{\text{rms}}/2$. This prediction is not far off the observed transition at $\sigma_b \approx 0.2\sigma$ in Fig. 4.7, with the discrepancy presumably arising due to inaccuracies in the quasi-linear approximation, as well as the additional presence of an incoherent dynamo mechanism. Note that η_{xx} in the magnetic case is much smaller than the kinematic value and will cause only a very small (probably unnoticeable) change to η_{xx} unless $u_{\text{rms}} \ll b_{\text{rms}}$. This is basically in agreement with the well-known result that magnetic fluctuations do not significantly quench the turbulent resistivity. (In our analytic SOCA calculations in chapter 6, for which the shear is added perturbatively, the contribution of b_{rms} to η_{xx} is exactly zero.)

Overall, we see that results of Figs. 4.10 and 4.11 agree well with conclusions from earlier in the section. Magnetic fluctuations in the presence of shear cause a non-negligible negative contribution to η_{yx} , which can overwhelm (or enhance in the presence of anticyclonic rotation) the kinematic coefficient. Thus, with sufficiently strong magnetic fluctuations, a nonhelical coherent large-scale dynamo is possible through the magnetic shear-current effect.

4.6 Discussion and conclusions

The main purpose of this chapter has been to propose and explore numerically a novel possibility for large-scale magnetic field generation in turbulent plasmas – the magnetic shear-current effect. The basic idea is that in the presence of large-scale velocity shear, small-scale magnetic fluctuations produce an off-diagonal turbulent resistivity (η_{yx}) with the correct sign to cause mean-field dynamo instability when coupled with the shear. This is the magnetic analogue of the controversial shear-current effect (Rogachevskii and Kleeorin, 2003, 2004) and the $\boldsymbol{\Omega} \times \boldsymbol{J}$ (or Rädler) effect (in the presence of shear). Importantly, this effect opens the possibility of the saturated small-scale dynamo *driving* the large-scale dynamo, in stark contrast to standard α quenching ideas where the small-scale dynamo is harmful to mean-field growth. Contrary to the kinematic shear-current effect, the sign of the magnetic effect agrees between analytic SOCA calculations (chapter 6), the τ approximation (Rogachevskii and Kleeorin, 2004), and shear quasi-linear theory (Singh and Sridhar 2011; magnetic results presented here) improving our confidence in its robustness.

In addition to the magnetic dynamo, I have presented results concerning the kinematic shear dynamo, as studied previously by a number of authors (e.g., Rogachevskii and Kleeorin 2003; Yousef *et al.* 2008a; Brandenburg *et al.* 2008a; Singh and Jingade 2015). The primary result is the qualitative (and quantitative) change in the mean-field dynamo that occurs due to the addition of rotation. This is caused by the well-known $\boldsymbol{\Omega} \times \boldsymbol{J}$ (or Rädler) effect (Krause and Rädler, 1980), which for anticyclonic rotation will cause the off-diagonal resistivity η_{yx} to have the required sign for a mean-field dynamo (Moffatt and Proctor, 1982). We have seen in a variety of examples how this can cause a change in the mean-field dynamo from being completely driven by fluctuations in α (the stochastic- α effect), to being driven (at least partially) by the off-diagonal turbulent resistivity. The change is observable both qualitatively, in the spatiotemporal evolution of B_y , and quantitatively, through an increase in the dynamo growth rate.

This chapter has focused on the dynamo at low Reynolds numbers, similar to that studied by Yousef *et al.* (2008a) and Yousef *et al.* (2008b). This choice has the advantage of both removing the complications of small-scale dynamo from the problem, and enabling the use of the quasi-linear approximation (chapter 3, also Sridhar and Subramanian 2009) with some degree of accuracy. The former advantage allows clean and straightforward separation of kinematic and magnetic effects, while the latter enables the use of statistical simulation techniques (CE2) that make the differences between incoherent and coherent dynamos particularly transparent. Nonetheless, precisely by enabling these simplifications, the low Reynolds number case is also less interesting. In particular, the magnetic fluctuations cannot arise self-consistently through the small-scale dynamo, which is far more natural than a direct forcing of the induction equation (except perhaps in the presence of magnetic instabilities such as the MRI). To rectify this, in the following chapter I give numerical results that illustrate that the magnetic fluctuations arising from the small-scale dynamo can indeed cause a coherent large-scale dynamo through η_{yx} .

Given the historical controversy surrounding some aspects of the shear dynamo, I feel it helpful to give a brief survey of the relationship to several previous works. As mentioned throughout the chapter, results here on the kinematic dynamo agree very nicely with numerical results in Yousef *et al.* (2008a) and Yousef *et al.* (2008b). In particular, the conclusion that rotation fundamentally changes the shear dynamo is nicely supported by Yousef *et al.* (2008a) Fig. 5 (although they state the opposite conclusion early on in the manuscript), and can even be observed in the spatiotemporal plots of their Fig. 4. I also find basic agreement with the quantitative results of Brandenburg *et al.* (2008a) – for instance, the transport coefficient calculations showing $\eta_{yx} > 0$ – since these are carried out kinematically (neglecting the Lorentz force). However, I tentatively propose a different interpretation of their Fig. 8 (and possibly Fig. 7), whereby the *magnetic* shear-current effect is acting to drive the observed mean-field dynamo coherently (note the high Pm, which should lead to strong magnetic fluctuations). In support of this I note the very coherent appearance of the dynamo, as well as the near cyclic behavior in the saturation phase (cf. Fig. 4.7). Of course, more work is

needed to assess this possibility more thoroughly. Similarly, the $R_m > 1$ simulations of Singh and Jingade (2015) (Figs. 6-8) may permit a similar explanation, although it is unclear whether there is truly a small-scale dynamo at their parameters. Finally, I mention again the analytic work of Rogachevskii and Kleeorin (2004), where the magnetic shear-current effect is derived within the τ approximation, although the authors do not comment on the result extensively. Specifically, it is clear from their Fig. 3 that the magnetic effect is far stronger than the kinematic effect (when the mean field is zero), in broad agreement with our results here and in chapter 6.

Of course, since this work has explored only regimes of low Reynolds numbers, a variety of future studies will be important. Of particular interest will be the interaction of the effect with magnetic helicity conservation arguments. This has been explored analytically and using quenching models in Rogachevskii *et al.* (2006) (see also the appendix of Brandenburg *et al.* 2008a), but more numerical studies would be needed before any definite conclusions can be drawn. It would also be interesting to explore the relevance of the magnetic shear-current effect in flows with helicity and a deterministic α effect. Is it possible that the effect could be present, perhaps after saturation of the $\alpha\Omega$ dynamo? This may also be complicated by recent results showing that shear may help to enhance helical dynamos by reducing the small-scale field generation (Cattaneo and Tobias, 2014; Tobias and Cattaneo, 2014).

Chapter 5

Generation of large-scale magnetic fields by the small-scale dynamo in shear flows – the magnetic shear-current effect

In this chapter, which contains what I consider to be the most important results of this thesis, I illustrate that a large-scale dynamo can be excited by the saturated state of the small-scale dynamo. The mechanism is the “magnetic shear-current effect,” introduced in the previous chapter. As discussed previously, above even moderate R_m numbers, the small-scale dynamo will always be unstable (Schekochihin *et al.*, 2007), growing and saturating much faster than any large-scale mechanism (Boldyrev *et al.*, 2005; Cattaneo and Hughes, 2009). In the case of dynamos driven by the α effect, because of the opposite signs of the kinematic and magnetic α effects, this small-scale field significantly hinders large-scale growth in a way that most likely scales very unfavorably to astronomically relevant Reynolds numbers (Gruzinov and Diamond, 1994; Bhattacharjee and Yuan, 1995; Blackman and Field, 2002; Hotta *et al.*, 2015). Here, I show using direct numerical simulation that it is possible and realizable to have the small-scale dynamo *enhance* the growth of the large-scale dynamo instead. So far as we are aware, this is the first demonstration of this

interesting behavior. Although the primary motivation for these studies has been the MRI dynamo, the necessary ingredients for the mechanism – velocity shear and magnetic fluctuations – are ubiquitous in astrophysical objects. We thus hope that the magnetic shear-current dynamo mechanism may find application outside of accretion disks, although more study is needed to thoroughly assess such possibilities. The main results in this chapter, reformatted as a letter, are currently under review for *Physical Review Letters* (Squire and Bhattacharjee, 2015b).

As discussed more thoroughly in Sec. 4.2, for the horizontal mean-field average, the mean magnetic fields evolve according to

$$\partial_t B_x = -\alpha_{yx} \partial_z B_x - \alpha_{yy} \partial_z B_y - \eta_{yx} \partial_z^2 B_y + (\eta_{yy} + \bar{\eta}) \partial_z^2 B_x, \quad (5.1a)$$

$$\partial_t B_y = -S B_x + \alpha_{xx} \partial_z B_x + \alpha_{xy} \partial_z B_y - \eta_{xy} \partial_z^2 B_x + (\eta_{xx} + \bar{\eta}) \partial_z^2 B_y, \quad (5.1b)$$

using velocity shear $\mathbf{U}_0 = -Sx\hat{\mathbf{y}}$ but neglecting other mean velocities. Due to homogeneity and reflectional symmetry (vanishing net helicity), α_{ij} must vanish when averaged over a suitably large time or number of realizations (Brandenburg and Subramanian, 2005). There is no such constraint on η_{ij} , and a negative value for the crucial η_{yx} coefficient can lead to the “shear-current” effect, with growth rate

$$\gamma = k \sqrt{\eta_{yx} (-S + k^2 \eta_{xy})} - k^2 \eta_t. \quad (5.2)$$

(Here, I have neglected temporal fluctuations in α and set $\eta_{yy} + \bar{\eta} = \eta_{xx} + \bar{\eta} = \eta_t$.) Subsequent to early analytic work (Rogachevskii and Kleeorin, 2003), it was found that kinematically $\eta_{yx} > 0$ (at least at low Rm), and several authors have concluded that this coherent shear dynamo cannot explain observed field generation (Rädler and Stepanov, 2006; Brandenburg *et al.*, 2008a; Singh and Sridhar, 2011). Instead, a popular theory is that temporal fluctuations in α_{ij} cause an incoherent mean-field dynamo. While such incoherent dynamos are certainly possible in a variety of situations, following on from chapter 4 I argue for a different situation – magnetic fluctuations ex-

cited by the small-scale dynamo act to substantially decrease η_{yx} , causing the onset of a coherent large-scale dynamo that overwhelms the incoherent dynamo in some situations.

The methods used to illustrate this effect in numerical simulation are somewhat nonstandard in the dynamo literature. In particular, at each set of physical parameters I carry out an ensemble of simulations, each with different noise realizations. Measurement of the transport coefficients in each of these, followed by an ensemble average, shows a statistically significant decrease in η_{yx} after saturation of the small-scale dynamo. That this can drive a coherent dynamo is illustrated by qualitative observation of the mean-field pattern, as well as solution of the mean-field equations [Eq. (5.1)] using the measured transport coefficients. The reason we require an ensemble of simulations is that only a relatively short period of large-scale dynamo growth can be observed before nonlinear saturation. This is because the large-scale magnetic field starts its growth (when the small-scale dynamo saturates) at relatively large amplitudes, being in approximate equipartition with the small-scale fluctuations due to the finite size of the mean-field average. We shall see that in many cases, the growth of the mean field lasts little more than $20 \rightarrow 30$ shearing times before saturating in some way, and that its behavior can vary substantially between realizations. Because of this, the ensemble average over simulations is highly advantageous for accurate determination of the transport coefficients.

The method for measuring the transport coefficients from simulation data after small-scale dynamo saturation is also nonstandard, and will be explained in some detail. As discussed in Sec. 4.3.1, test-field methods that explicitly include the magnetic fluctuations are rather complex and in the earlier stages of development (Rheinhardt and Brandenburg, 2010), and I instead choose to measure transport coefficients directly from mean-field and EMF data taken from simulations. The method, which is a modified version of that proposed in Brandenburg and Sokoloff (2002), involves approximately solving $\mathcal{E}_i = \alpha_{ij}B_j - \eta_{ij}J_j$ at each time-step and taking spatiotemporal averages to obtain transport coefficients. To ensure that one obtains correct results, it is applied to compute transport coefficients for the low-Rm kinematic shear dynamos discussed in chapter 4,

comparing directly to the test-field method. In addition, mean-field evolution will be compared to that expected from the measured transport coefficients, illustrating nice agreement.

Similar to the studies presented in the previous chapter, calculations are carried out using the nonlinear MHD equations within the shearing box formalism [Eq. (3.1)], with homogenous Cartesian geometry and periodic boundary conditions in the shearing frame. Using the SNOOPY code (Lesur and Longaretti, 2007), I utilize nonhelical forcing of the momentum equation at small scales and study the generation of larger scale magnetic fields (Yousef *et al.* 2008a; Brandenburg *et al.* 2008a; see also chapter 4). As in chapters 3 and 4, system rotation is included through a mean Coriolis force.

I shall first discuss the method for measurement of transport coefficients, including its application to low- R_m kinematic dynamos and direct comparison to the test-field method. I then present the main set of results, which include two sets of 100 simulations at $R_m = 2000$, with and without rotation. After a qualitative discussion of the observed large-scale dynamo, I give detailed measurements of the resistive transport coefficients before and after small-scale dynamo saturation. Finally, as a second confirmation that the measurement method is returning useful results, I solve the mean-field equations using the measured transport coefficients. As well as acting as a consistency check on the transport coefficients, this illustrates that the dynamo is indeed being driven through the coherent mechanism in most realizations.

5.1 Measuring the transport coefficients

In this section I describe the method, based on that in Brandenburg and Sokoloff (2002), for obtaining the transport coefficients from simulation data. In addition, I verify its accuracy through direct comparison to test-field method calculations at low R_m . While the test-field method gives unambiguous answers for kinematic transport coefficients (before the small-scale dynamo saturation), results can become more difficult to interpret in the presence of magnetic fluctuations (Cattaneo

and Hughes, 2009; Hubbard *et al.*, 2009; Rheinhardt and Brandenburg, 2010). In contrast, the method detailed here does not rely on any assumptions regarding the importance of small-scale magnetic fields, operating purely from the mean-field data from a given simulation. In addition to this method, I have also applied a weighted least-squares method, fitting simulation data for a single mode (Kowal *et al.*, 2005). This has led to almost identical results for both the simulations presented in Sec. 5.2 the manuscript and the low-Rm example here. However, the least-squares method was generally found to be somewhat less reliable and rather delicate, and I do not discuss the details.

The starting point of the method is the standard Taylor expansion of \mathcal{E} in terms of \mathbf{B} . In coordinates this is [cf. Eq. (5.1)]

$$\mathcal{E}_x = \alpha_{xx}B_x + \alpha_{xy}B_y - \eta_{xy}\partial_z B_x + \eta_{xx}\partial_z B_y, \quad (5.3a)$$

$$\mathcal{E}_y = \alpha_{yx}B_x + \alpha_{yy}B_y - \eta_{yy}\partial_z B_x + \eta_{yx}\partial_z B_y. \quad (5.3b)$$

Note that I have not necessarily assumed linearity in \mathbf{B} , since α_{ij} and η_{ij} are not assumed constant. The basic idea of the fitting method, proposed in Brandenburg and Sokoloff (2002), is to extract time-series data for \mathcal{E}_i and B_i from nonlinear simulation, solving for the transport coefficients in Eq. (5.3) at each time point. In principle, all coefficients can be solved for directly, given mean-field and \mathcal{E} data that consists of at least 2 Fourier modes. One calculates

$$\mathbf{E}^{(i)} = (\langle B_x \mathcal{E}_i \rangle, \langle B_y \mathcal{E}_i \rangle, \langle \partial_z B_x \mathcal{E}_i \rangle, \langle \partial_z B_y \mathcal{E}_i \rangle)^T \quad (5.4)$$

and the matrix

$$M = \begin{pmatrix} \langle B_x B_x \rangle & \langle B_x B_y \rangle & \langle B_x \partial_z B_x \rangle & \langle B_x \partial_z B_y \rangle \\ \langle B_y B_x \rangle & \langle B_y B_y \rangle & \langle B_y \partial_z B_x \rangle & \langle B_y \partial_z B_y \rangle \\ \langle \partial_z B_x B_x \rangle & \langle \partial_z B_x B_y \rangle & \langle \partial_z B_x \partial_z B_x \rangle & \langle \partial_z B_x \partial_z B_y \rangle \\ \langle \partial_z B_y B_x \rangle & \langle \partial_z B_y B_y \rangle & \langle \partial_z B_y \partial_z B_x \rangle & \langle \partial_z B_y \partial_z B_y \rangle \end{pmatrix}, \quad (5.5)$$

where $\langle \cdot \rangle$ here denotes an average over z and possibly time (the studied systems are all homogenous in z). Then, solving

$$\mathbf{E}^{(i)} = M \mathbf{C}^{(i)}, \quad (5.6)$$

for $C^{(1)} = (\alpha_{xx}, \alpha_{xy}, -\eta_{xy}, \eta_{xx})$, $C^{(2)} = (\alpha_{yx}, \alpha_{yy}, -\eta_{yy}, \eta_{yx})$, one obtains the full set of transport coefficients.

The data for \mathcal{E} and \mathbf{B} are generally quite noisy and care is required to avoid spurious effects that lead to incorrect results. In particular, while pure white noise in each variable might be expected to average out over time, there are correlations between components that can significantly pollute the data. These correlations arise from the fact that Eq. (5.3) is not the only expected relationship between components of \mathbf{B} and \mathcal{E} ; \mathbf{B} is also directly driven by \mathcal{E} and itself through

$$\partial_t \mathbf{B} = -S B_x \hat{\mathbf{y}} + \nabla \times \mathcal{E} + \bar{\eta} \Delta \mathbf{B}. \quad (5.7)$$

From Eq. (5.7) and by examining data, it is found that the most harmful of the correlations are a correlation between B_x and B_y [as expected due to $-S B_x$ in Eq. (5.7)] and a correlation between fluctuations in \mathcal{E}_y and B_x (B_x is directly driven by $\partial_z \mathcal{E}_y$). Note that this correlation of \mathcal{E}_y and B_x is not the same as a nonzero α_{yx} or η_{yy} coefficient.¹ (The correlation between B_y and \mathcal{E}_x is not

¹For example, a change in the imaginary part of \mathcal{E}_y by ϵ will cause a change in B_x of $\sim k\epsilon\Delta t$ after some time Δt , related to the correlation time of the fluctuations. If the fluctuations are of similar or larger magnitude than the range of (B_x, \mathcal{E}_y) explored in the course of the entire simulation, this correlation can cause a negative value for the fit parameter η_{yy} , since the data *scatter* has a preferred slope.

so damaging due to the $-SB_x$ term in the B_y equation and larger range of B_y values explored throughout a simulation.) The most prominent spurious effect that results from these correlations is a consistently negative value for η_{yy} , which was also noted in Brandenburg and Sokoloff (2002). That this is unphysical can be seen by comparison to test-field calculations (see below). Importantly, the value of η_{yy} is coupled to that of α_{iy} and η_{yx} , implying one cannot simply ignore this effect since the average values of other coefficients will become polluted.

The basic approach to overcoming these issues is to minimize the influence of B_x on the calculation, to the extent possible. This is motivated by the fact that B_x is very noisy in comparison to B_y and is involved in both of the aforementioned damaging correlations. The approach works very well for shear dynamos because B_x is much smaller than B_y (e.g., in the simulations presented in the Sec. 5.2, B_x is usually between 25 and 150 times smaller than B_y depending on the realization). In addition, those transport coefficients that require B_x for their calculation (e.g., η_{xy}) are substantially less interesting, since they do not significantly effect the dynamo growth rate. To enable this reduction in the influence of B_x two approximations are made to Eq. (5.3). The first and most important is to assume that diagonal transport coefficients are equal, $\eta_{yy} = \eta_{xx}$ and $\alpha_{yy} = \alpha_{xx}$. This is not strictly required by the symmetries of the turbulence with shear (Rädler and Stepanov, 2006), but a variety of test-field calculations, including those after saturation of the small-scale dynamo (i.e., quasi-kinematic calculations, Hubbard *et al.* 2009; Gressel 2010), have shown this to be the case to a high degree of accuracy. The second approximation is to neglect η_{xy} and α_{yx} . This is justified by the fact that $B_x \ll B_y$ and $\eta_{xy} < \eta_{xx}$ on average, thus its effect on the mean value of η_{xx} should be very small.²

It is useful to briefly consider the proportional error in η_{xx} and η_{yx} that might arise from these approximations. First, in considering the neglect of η_{xy} , one starts with the conservative estimate $25B_x \approx B_y$. Noting that test-field calculations give $\eta_{xy} \sim 0.25\eta_{xx}$ for the simulations given in the

² η_{xy} and α_{yx} coefficients can actually be included and similar results obtained; however they fluctuate wildly in time, far more than η_{xx} for example, and cause increased fluctuations in the values of the other transport coefficients.

manuscript (see also Brandenburg *et al.* 2008a), we see that this approximation should cause less than a 1% systematic error in η_{xx} . Second, since we are primarily interested in determining η_{yx} , let us consider the error in η_{yx} that results from an error in η_{yy} (caused by either the neglect of η_{xy} or the assumption $\eta_{xx} = \eta_{yy}$). Noting that $B_x \sim -k\sqrt{\eta_{yx}/S}B_y$ for a coherent shear dynamo, we can estimate that $ik\eta_{yx}B_y \gtrsim ik\eta_{yy}B_x$ when $k\eta_{yy} \lesssim \sqrt{|S\eta_{yx}|}$. This inequality is satisfied if the coherent dynamo has a positive growth rate; thus, very approximately, at marginality one would expect the proportional errors in η_{yx} and η_{yy} to be similar. Combining these two conclusions, one should expect the two approximations to cause very little systematic error in the determination of η_{yx} , despite the coefficient's small values.

Summarizing the previous paragraphs, I shall fit

$$\mathcal{E}_x = \alpha_{yy}B_x + \alpha_{xy}B_y + \eta_{xx}\partial_z B_y, \quad (5.8a)$$

$$\mathcal{E}_y = \alpha_{yy}B_y - \eta_{xx}\partial_z B_x + \eta_{yx}\partial_z B_y, \quad (5.8b)$$

to simulation data at each time point. Since there are now fewer coefficients than rows of $\mathbf{E}^{(i)}$, the matrix equations are solved in the least-squares sense. One final difference from the method as utilized in Brandenburg and Sokoloff (2002) is a filtering of the data to include only the first two Fourier modes. This is done to improve scale separation, since the small scales of the mean field will be dominated by fluctuations due to the finite size of the horizontal average, and cannot be expected to conform to the ansatz in Eq. (5.3).

Finally, note that α coefficients can be excluded from these calculations altogether, and since their average over long times vanishes, this does not affect the results for η_{ij} . I have chosen to permit nonzero α in all calculations presented below and in Sec. 5.2, both as a consistency check and because over shorter time-windows α may not average to exactly zero. Nonetheless, repeating all calculations presented here and in Sec. 5.2 with $\alpha_{ij} = 0$ imposed artificially, one obtains the same results (to within the margin of error). This illustrates that in the neglect of

transport coefficients considered above (e.g., α_{yx}), it is only necessary to consider the errors arising from neglect of η coefficients, since those due to neglect of α coefficients average to zero.

5.1.1 Verification: low-Rm shear dynamo

Here, I verify that the method recovers the correct transport coefficients for low-Rm shear dynamos, similar to those studied in the previous chapter (Sec. 4.4) and Yousef *et al.* (2008a,b). The primary advantage of testing the method in this parameter regime is that there is no small-scale dynamo and simulations exhibit a very long kinematic growth period over which the small-scale velocity field is unaffected by the magnetic field. It is thus straightforward to compare results obtained with the fitting method to those using the test-field method, where the only the fluctuating part of the induction equation is solved.

The simulations are carried out in the same numerical setup as that used in chapter 4, at $\text{Re} = \text{Rm} = 100$ in shearing boxes of dimension $(L_x, L_y, L_z) = (1, 1, 8)$. The velocity field is forced at $k = 6\pi$ to a level $u_{rms} \approx 0.8$. Keeping $S = 2$, I present cases that are non-rotating, $\Omega = 0$, as well as $\Omega = 4/3$ (Keplerian) and $\Omega = 4$, with the rotation added through the mean Coriolis force. As discussed in chapter 4, this change in Ω causes η_{yx} to change sign due to the $\Omega \times J$ (or Rädler) effect. I have run 10 simulations at each parameter set from $t = 0$ to $t = 1000$, although the rotating cases saturate earlier ($\Omega = 4/3$ at $t \approx 900$, $\Omega = 4$ at $t \approx 500$) due to faster dynamo growth. Note that the ratio of B_y to B_x in these simulations ($\sim 10 \rightarrow 30$ during growth) is somewhat higher than that for the magnetically driven dynamos studied later (Sec. 5.2); thus, if anything, one might expect larger errors in these simulations than the estimate given above.

Test-field calculations are conducted as discussed in Sec. 4.3.1. Due to the lack of a small-scale dynamo, the \mathbf{b} fluctuations quickly reach a steady state, and an average of \mathcal{E} is taken over $t = 0 \rightarrow 1600$ to obtain η_{xx} and η_{yx} . Errors are obtained through the standard deviation of the mean after dividing the data set into 100 chunks (\pm values indicate the 95% confidence interval). Results

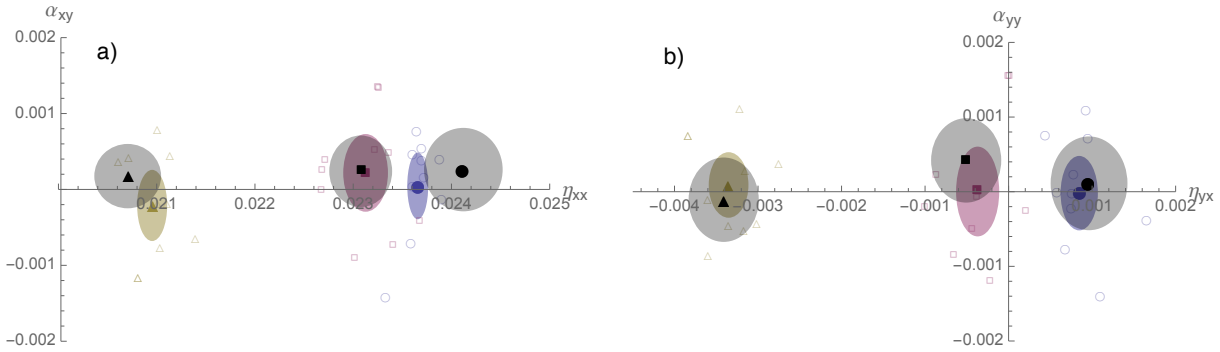


Figure 5.1: Measured transport coefficients for $\text{Re} = \text{Rm} = 100$ shearing-box simulations (as described in the text). (a) η_{xx} , (b) η_{yx} . Squares, circles and triangles show $\Omega = 0$, $\Omega = 4/3$ and $\Omega = 4$ respectively, with the hollow markers illustrating those measured from each simulation. The mean of these measurements is shown by the solid colored marker, with its error shown with the shaded circle (calculated from the standard deviation). Test-field method results, against which least-squares results should be compared, are illustrated by black markers, with the shaded area showing the error in these measurements. (I have also included the measured α values here, although in all cases these are zero to within error.)

from the test-field method, which I consider as the reference values against which to compare coefficients obtained using the fitting method, are illustrated in Fig. 5.1 in black. These values are comparable (in the ratio of η_{xx} to η_{yx}) to those obtained in previous work for the non-rotating case (Brandenburg *et al.*, 2008a), as well as exhibiting trends expected from chapter 4. In all cases the test-field measured α_{ij} are zero to within error as expected (see Fig. 5.1).

Results obtained by fitting the self-consistent dynamo simulations are also illustrated in Fig. 5.1. The transport coefficients (α_{xy} , α_{yy} , η_{xx} , η_{yx}) are measured as described in the previous section for the duration of each simulation, excluding times after which the dynamo has saturated. Because of the long averaging time in comparison to the measurements presented in Sec. 5.2, the spread of values between different simulations is quite small. It is seen that the measured coefficients agree with the test-field calculations to within error margins in all cases. The largest discrepancy is in η_{xx} at $\Omega = 0$, which may be related to the vorticity dynamo that develops without rotation (the difference is still only of the order of 1%). Note that a growing dynamo is observed in all of the self-consistent simulations, and at $\Omega = 0$ this is purely due to a stochastic- α effect, as

discussed in chapter 4. We can thus be sure that the fitting method is not somehow measuring a property of the dynamo growth rate rather than coherent transport coefficients.

5.2 Results – the magnetically driven dynamo

In this section I show that small-scale fields arising self-consistently through the small-scale dynamo can drive a coherent large-scale dynamo. To this end, I directly calculate transport coefficients from nonlinear simulations before (using the test-field method) and after (using the method outlined in Sec. 5.1) the saturation of the small-scale dynamo. The simulations in this section use moderate Reynolds numbers, $R_m = 2000$, $P_m = 8$ (similar to the final examples in Yousef *et al.* 2008a), small enough such that there is no transition to self-sustaining turbulence when the noise is removed. Ensembles of 100 simulations are run, both with and without Keplerian rotation.

As shown in Fig. 5.2, at these parameters, the prevalence of a coherent large-scale dynamo after saturation of the small-scale dynamo (at $t \sim 45$) depends on the realization. Specifically, it appears that the coherent effect cannot always overcome fluctuations in \mathcal{E} immediately after small-scale saturation, although the dynamo always develops after a sufficiently long time [e.g., Fig. 5.2(d) near $t = 150$]. This behavior seems generic when the coherent dynamo is close to its threshold for excitation – similar structures were observed in chapter 4 at lower R_m with induction equation driving (when the proportion of magnetic noise was in the range $0.1 \rightarrow 0.2$; see discussion in Sec. 4.5). Notwithstanding this variability in the dynamo’s qualitative behavior, measurement of the transport coefficients illustrates that the η_{yx} coefficient decreases after the magnetic fluctuations reach approximate equipartition with velocity fluctuations at small scales.

At low times, the kinematic α and η are measured using the test-field method, fixing the mean field and calculating \mathcal{E} , with no Lorentz force (Brandenburg and Subramanian, 2005; Brandenburg *et al.*, 2008a). Calculations are run from $t = 0 \rightarrow 2000$ with the errors estimated as described in Sec. 4.3.1. Since the small-scale dynamo grows quickly, test fields are reset every $t = 5$. After

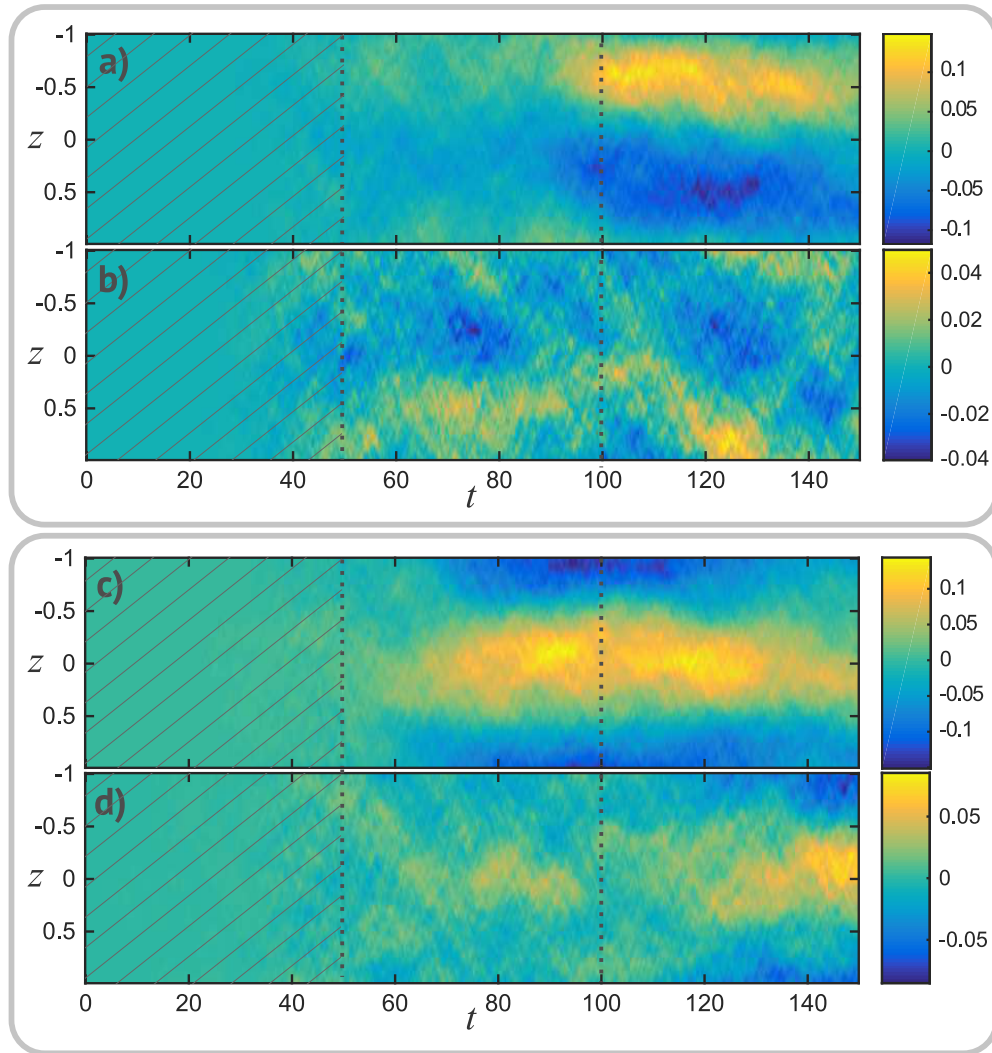


Figure 5.2: Example spatiotemporal B_y evolutions for (a-b) non-rotating, and (c-d) Keplerian rotating turbulence, at $k_f = 6\pi$, $\text{Rm} = 1/\bar{\eta} = 2000$, $\text{Pm} = 8$, $S = 1$, in a box of dimension $(1, 4, 2)$ with resolution $(64, 128, 128)$. The first examples in each case [(a) and (c)] show B_y when a coherent dynamo develops, while the second examples [(b) and (d)] illustrate the case when it is more incoherent. The main factors in distinguishing these are the coherency in phase of B_y over some time period and the amplitude at saturation, which is larger in the coherent cases. In general the rotating simulations are substantially more coherent. The hatched area illustrates the region of small-scale dynamo growth. The fitting method used to compute transport coefficients (see Fig. 5.3) is applied between the dashed lines ($t = 50 \rightarrow 100$).

small-scale saturation, I utilize the method described in Sec. 5.1 to measure coefficients directly from the observed mean-field and EMF evolution.³ The time window of these measurements has been limited to $t = 50 \rightarrow 100$, since in some realizations the large-scale field is seen to saturate around $t = 100$ [e.g., Figs. 5.2(a) and (c)]. Since this saturation presumably occurs due to a change of sign of η_{yx} as \mathbf{B} increases (see chapter 3), it is important to not include this saturation phase in the measurement of η_{yx} . As should be expected from Fig. 5.2 and due to the short time window, measurements of the transport coefficients after small-scale saturation vary significantly between realization. Nonetheless, an average over the ensemble illustrates a statistically significant change in η_{yx} that is consistent with observed behavior, in both the rotating and non-rotating simulation ensembles.

Figure 5.3 illustrates the results. In the kinematic phase without rotation, we see $\eta_{yx} = (4.1 \pm 1.6) \times 10^{-4}$, in qualitative agreement with previous studies (Brandenburg *et al.*, 2008a). With rotation, we find $\eta_{yx} = (0.6 \pm 1.2) \times 10^{-4}$, consistent with a reduction in η_{yx} due to the $\boldsymbol{\Omega} \times \mathbf{J}$ effect (Krause and Rädler 1980, but note the deviation from the lower-Rm case and SOCA result, which predicts negative η_{yx}). After saturation of the small-scale dynamo, $\eta_{yx} = (-0.1 \pm 1.0) \times 10^{-4}$ for the non-rotating case, while $\eta_{yx} \approx -(2.0 \pm 0.8) \times 10^{-4}$ in the rotating case – the same reduction in each to within error. Values for the diagonal resistivity are smaller after saturation, as expected since the velocity fluctuation energy decreases (by a factor ~ 1.4).

The numerical values of (η_{xx}, η_{yx}) show that the coherent dynamo is slightly stable on average in the non-rotating case and marginal in the rotating case. However, the coefficients vary significantly between realizations, sometimes yielding larger growth rates, and it is important to check that the observed mean-field evolution has some relation to this variation. This serves two

³ While it would be ideal to measure coefficients before and after saturation using the same technique for consistency, this is difficult. As discussed previously the magnetic test-field method (Rheinhardt and Brandenburg, 2010) is rather complex, while the measurement of kinematic coefficients using the fitting method (Sec. 5.1) is hindered by the small-scale dynamo causing the mean-field evolution to be completely overwhelmed by small-scale noise. While I have experimented with seeding the initial conditions with large-scale fields to obtain a short period of kinematic evolution, results were inconclusive due to very high levels of noise in the measurements.

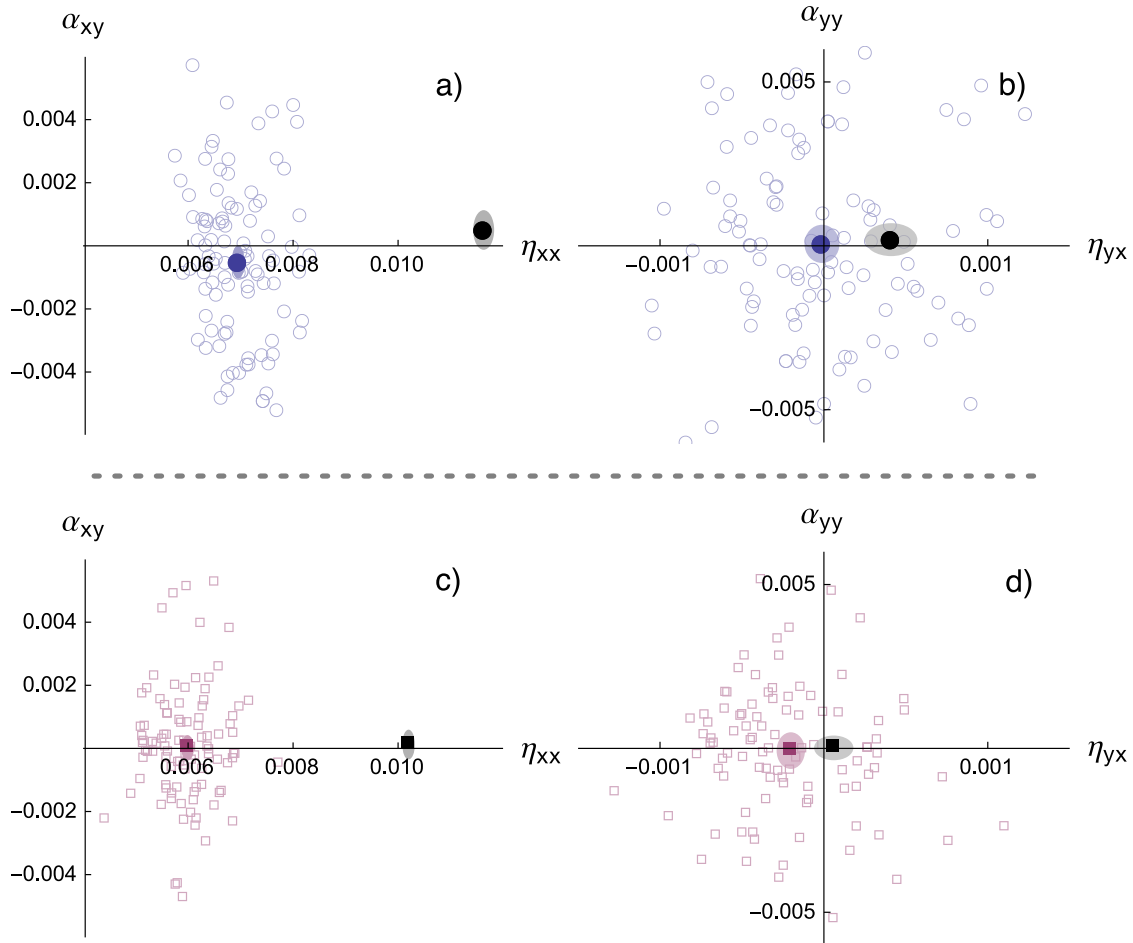


Figure 5.3: Measurements of the turbulent transport coefficients for 100 realizations of the simulations at the same parameters as those in Fig. 5.2; (a) η_{xx} coefficients, no rotation, (b) η_{yx} coefficients, no rotation, (c) η_{xx} coefficients, rotating, (d) η_{yx} coefficients, rotating. Unfilled markers in each plot (circles and squares for non-rotating and rotating runs respectively) show coefficients measured from each of the individual realizations, with mean values displayed by solid markers and the shaded regions indicating error in the mean (2 standard deviations). Black markers illustrate the kinematic transport coefficients, with grey shaded regions indicating the error. After saturation of the small-scale dynamo, η_{ij} is calculated using the method detailed in Sec. 5.1, taking the mean from $t = 50$ to $t = 100$. This limited time window is chosen to avoid capturing the saturation phase of the large-scale dynamo, since η_{ij} is presumably modified in this phase. In both methods used to compute transport coefficients, the corresponding α coefficients are also calculated. In all cases these are zero to within error as expected, and the scatter between simulations is of a similar magnitude to that of η_{ij} if their different units are accounted for (it is necessary to divide α by a characteristic k value).

purposes. First, it acts as a check that the transport coefficients are being measured correctly. Second, it illustrates that those realizations exhibiting the strongest growth are indeed being driven by the shear-current mechanism; that is, they are driven by η_{yx} rather than residual variation of α about mean zero. This corroborates the earlier conclusion that the approximately constant phase of $B_y(z, t)$ in the development of the dynamo (Fig. 5.2) is inconsistent with an α effect.

The method for checking this consistency is to use the *measured* transport coefficients to solve for the expected evolution of the largest Fourier mode of B_i [using Eq. (5.1)], comparing this to the observed evolution from the full simulation. This is carried out for each realization separately, initializing using the mean-field data and filtering the transport coefficients in time with a Gaussian filter of width 5 to remove the rapid fluctuations. Results from the first 12 realizations for rotating and non-rotating runs are shown in Figs. 5.4 and 5.5 respectively. The agreement is good, with qualitatively similar features between calculated and measured evolution in all realizations, and many cases showing quantitative agreement. It seems that in most instances for which there is a substantial divergence between the predicted and observed mean-field evolution, it is due to a slight error building up in B_x that subsequently gets amplified enormously due to the $-SB_x$ term in the B_y equation.

In addition to solving for expected evolution using both η_{ij} and α_{ij} measurements, I present calculations obtained in an identical way, but with α_{ij} coefficients artificially set to zero. The purpose of this numerical experiment is to examine the degree to which the dynamo is driven by η_{yx} , rather than variation in α about its mean of zero. Through a comparison of the curves with and without α_{ij} it is clear that in many realizations of the rotating simulation set, the dynamo is primarily driven by η_{yx} , as shown by the agreement between dashed and dotted curves. Furthermore, the mean of η_{yx} over the time interval (printed on each subfigure; these are taken from Fig. 5.3) agrees nicely with the observed behavior. That is, large negative values for η_{yx} correspond to those realizations with both strong dynamo growth and good agreement between evolution with and without α . In contrast, higher values of η_{yx} (for which the dynamo is stable) either grow very little or diverge

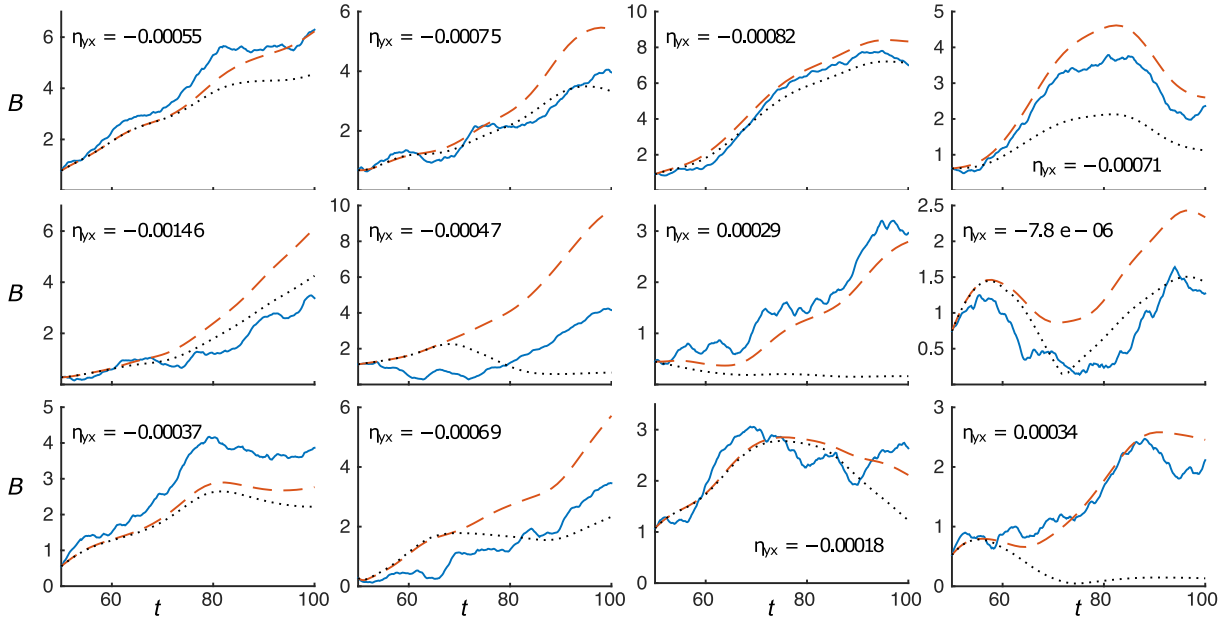


Figure 5.4: Evolution of the mean-field magnitude for the first 12 of the ensemble of rotating simulations discussed in the manuscript. Here B , the mean-field magnitude, is $(|\hat{B}_x^1|^2 + |\hat{B}_y^1|^2)^{1/2}$ where \hat{B}_i^1 is the largest scale Fourier mode of B_i . In each plot the solid blue curve shows data taken from the simulation. The dashed red curve shows the corresponding expected evolution, using the smoothed calculated values of the transport coefficients (see text). Finally, the dotted black curve illustrates the expected evolution, artificially setting all α coefficients to zero. I list the measured mean of η_{yx} in each plot to show that lower values do generally lead to substantially more growth of the mean field as expected for a coherent dynamo. For reference, at the measured $\eta_{xx} \approx 0.006$, the coherent dynamo is unstable below $\eta_{yx} = -0.00036$.

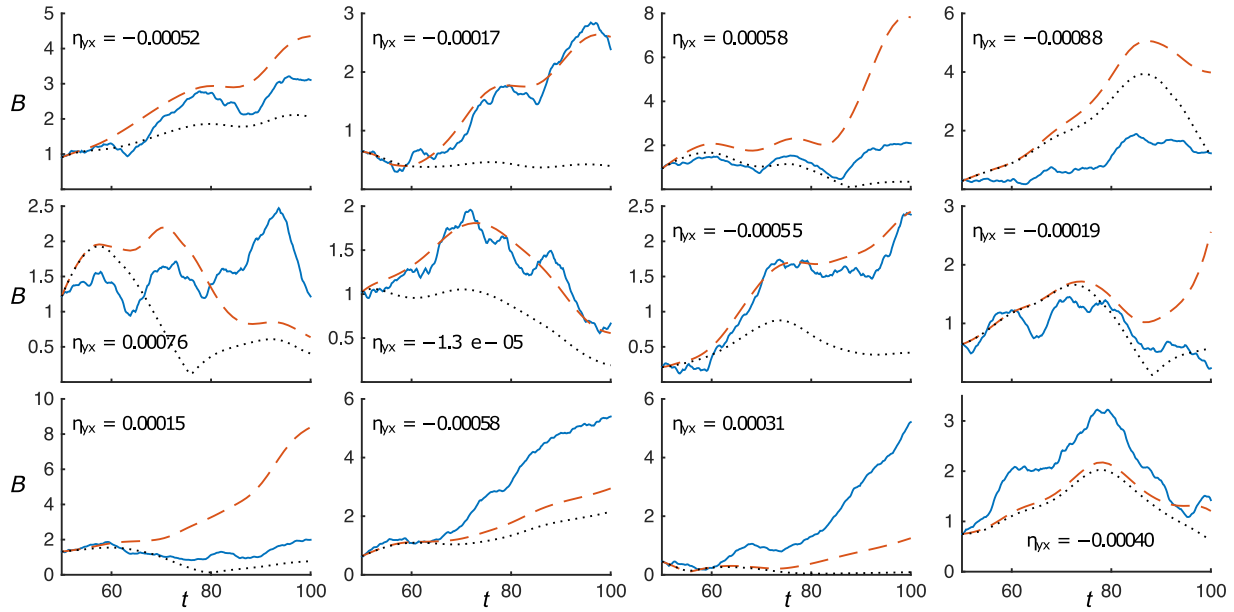


Figure 5.5: Same as figure 5.4, but for the non-rotating simulations. As expected, the mean-field growth is not so substantial in this case. For reference, at the measured $\eta_{xx} \approx 0.007$, the coherent dynamo is unstable below $\eta_{yx} = -0.00049$, showing that in most cases illustrated here the coherent dynamo is stable.

substantially between evolution with and without α . This shows that sometimes, for realizations in which the magnetic shear-current effect is weaker, a stochastic α effect is the primary driver. As expected, in the non-rotating case, coherent dynamo growth is much less prevalent. Since in most realizations η_{yx} is larger than the threshold at which the dynamo becomes unstable, this is not surprising.

We thus conclude that small-scale magnetic fluctuations act to *decrease* η_{yx} , and that in some realizations (or after a sufficiently long time period) a coherent large-scale dynamo develops as a result. This demonstrates that small-scale magnetic fluctuations, excited by small-scale dynamo action, can drive large-scale magnetic field generation. The mechanism is a magnetic analogue of the “shear-current” effect Rogachevskii and Kleeorin (2004, 2003), arising through the off-diagonal turbulent resistivity in the presence of large-scale shear flow.

The simulations presented in this chapter have been chosen to show that a magnetically forced large-scale dynamo is *possible*, not necessarily that such effects should be important in all situations. More work is certainly needed to precisely assess regimes in which the magnetically driven dynamo might dominate, in particular its behavior at higher Reynolds numbers. There are two important effects that require study to assess this: the first is the behavior of the shear-current transport coefficients with R_m for a given \mathbf{b}_0 ; the second, the behavior of small-scale dynamo saturation at high Re and R_m . Each of these could play an important role in determining the viability of the magnetic shear-current effect for generating large-scale fields, and both will be very challenging to answer definitively. There are also questions regarding the dynamo's behavior in regimes where self-sustained turbulence is possible, as for MRI turbulence (Lesur and Ogilvie, 2008b), and whether differences arise due to a lack of scale separation. Given the results of chapter 3, this seems unlikely to be especially important. Another interesting line of research regards whether a magnetic dynamo can remain influential in the presence of net helicity and an α effect, particularly as small-scale dynamo may be suppressed by shear (Tobias and Cattaneo, 2014). While such questions may be difficult to answer definitively, the generic presence of magnetic fluctuations in plasma turbulence gives us some confidence that the proposed mechanism could cause large-scale dynamo growth in the wide variety of astrophysical systems with velocity shear.

Chapter 6

Analytic studies of the magnetic shear-current effect and stratified disk dynamamos

In this chapter – much of which is currently under review for publication in *Physical Review E* (Squire and Bhattacharjee, 2015d) – I present a very general examination of different mean-field dynamo effects, within the theoretical framework of the second-order correlation approximation (SOCA). In particular, I include the effects of specified large-scale velocity gradients, rotation, density and turbulence stratification, helicity, and a bath of strong small-scale magnetic fluctuations (treated in the same way as the velocity fluctuations). For the accretion-disk dynamo – our primary inspiration in this thesis – each of these effects can be important in some way, and this will also be the case in a wide variety of other astrophysical scenarios. Of particular note is the presence of homogenous magnetic fluctuations, which have not been included in most previous theoretical mean-field dynamo investigations (but see, for example, Vainshtein and Kichatinov 1983; Rogachevskii and Kleeorin 2004; Rädler *et al.* 2003; Pipin 2008). These are expected to be generically present, at a level similar to velocity fluctuations, in magnetohydrodynamic (MHD)

turbulence above moderate Reynolds numbers due to small-scale dynamo action. While SOCA itself cannot capture the small-scale dynamo, by assuming the presence of the magnetic fluctuations one can compute expected changes to the EMF, in particular whether a small-scale magnetic field might suppress, or enhance, kinematic dynamo effects.

The most important result presented here is an analytic confirmation of the numerical work related to the “magnetic shear-current effect,” studied in chapters 4 and 5. Generically, this type of dynamo is nonhelical, driven by the interaction of an off-diagonal turbulent resistivity with a mean shear flow (Moffatt and Proctor, 1982; Urpin, 1999, 2002; Rogachevskii and Kleeorin, 2003). Some controversy has surrounded the kinematic version of this effect, since after early work (Urpin, 1999; Rogachevskii and Kleeorin, 2003), others found that the crucial transport coefficient η_{yx} had the incorrect sign to promote dynamo action (Rüdiger and Kitchatinov, 2006; Rädler and Stepanov, 2006; Brandenburg *et al.*, 2008a; Singh and Sridhar, 2011). Here, I show with SOCA that the magnetic version of this effect is much more robust and of the correct sign. Not only is its magnitude substantially larger than the kinematic effect, but a variety of calculation methods agree on this: SOCA (presented here), the τ approximation (Rogachevskii and Kleeorin, 2004), shear quasi-linear theory (chapter 4 and Singh and Sridhar 2011) and perturbative shearing wave calculations (Lesur and Ogilvie, 2008a).

Turbulence and density stratification is invariably significant in astrophysical scenarios, including in accretion disks away from the central plane of the disk. With this application in mind, I also apply results to the case of stratified rotating turbulence with strong velocity shear, considering the resulting α effects. This shows that for a Keplerian (or more generally, anticyclonic) rotation profile, the contributions from shear and rotation, and those from kinetic and magnetic fluctuations, are each of opposite signs. The dominant contribution will depend strongly on the magnetic Prandtl number as well as the relative intensities of magnetic and kinetic turbulence. This is confusing in light of the beautifully coherent “butterfly diagrams” that are often seen in stratified accretion disk simulations (Brandenburg and Sokoloff, 2002; Brandenburg *et al.*, 1995; Gressel, 2010; Simon

et al., 2012), which would suggest a robust negative value for α_{yy} . I note that the contributions to these α effects from velocity shear are at least as strong as those from rotation and should not generally be neglected.

The structure of the calculation almost identically follows that of Rädler and Stepanov (2006), with the additional effects of magnetic fluctuations, density stratification (within an anelastic approximation) and net helicity. The inclusion of such a variety of physical effects leads to a rather prodigious number of terms, and I have used the *VEST* package (Squire *et al.* 2014; described briefly appendix E) in *Mathematica* to carry out the bulk of the calculations. I shall start, in Sec. 6.1, by outlining the setup of the calculation, including the most general form of \mathcal{E} allowed by the symmetries of the problem, as well as the relation of the transport coefficients in Cartesian domains with velocity shear (i.e., the shearing box) to this general form. I also give the perturbation expansion used, which is a generalization of that in Rädler and Stepanov (2006) to include magnetic turbulence at lowest order. Note that stratification, velocity gradients, rotation, and the mean magnetic field are kept to linear order only.¹ In Sec. 6.2, I outline the procedure used in the calculation itself, skipping many details for the sake of brevity. Particular focus is placed on the unstratified shear dynamo – especially the magnetic shear-current effect – in Sec. 6.3, while the stratified α effect is examined in the same geometry in Sec. 6.4. Readers interested primarily in the application of calculated coefficients to disk dynamos may wish to skip directly to these sections. Due to the length of algebraic expressions, the full set of transport coefficients is given in App. D.2.

¹Previous calculations that include nonlinear contributions from some of these effects include Rüdiger (1990); Kichatinov and Rüdiger (1992); Rüdiger and Kichatinov (1993); Rädler *et al.* (2003); Rogachevskii and Kleeorin (2004). In a very general calculation, Pipin (2008) includes nonlinearity due to all of these effects; however, the calculation method, the “minimal τ approximation,” has a rather unknown range of validity.

6.1 Fundamentals of mean-field electrodynamics

To enable the inclusion of density stratification, the starting point for work in this chapter is the compressible MHD equations

$$\frac{\partial \rho}{\partial t} + \nabla \cdot (\rho \mathbf{U}_T) = 0, \quad (6.1a)$$

$$\begin{aligned} \rho \frac{\partial \mathbf{U}_T}{\partial t} + \rho (\mathbf{U}_T \cdot \nabla) \mathbf{U}_T + 2\rho \boldsymbol{\Omega} \times \mathbf{U}_T + \nabla p = \mathbf{B}_T \cdot \nabla \mathbf{B}_T \\ + \nabla \cdot [\rho \bar{\nu} (\nabla \mathbf{U}_T + (\nabla \mathbf{U}_T)^T) + \rho \bar{\zeta} \delta_{ij} \nabla \cdot \mathbf{U}_T] + \boldsymbol{\sigma}_u, \end{aligned} \quad (6.1b)$$

$$\frac{\partial \mathbf{B}_T}{\partial t} = \nabla \times (\mathbf{U}_T \times \mathbf{B}_t) + \bar{\eta} \nabla^2 \mathbf{B}_t + \boldsymbol{\sigma}_b, \quad (6.1c)$$

$$\nabla \cdot \mathbf{U}_T = 0, \quad \nabla \cdot \mathbf{B}_t = 0. \quad (6.1d)$$

Here \mathbf{U}_T and \mathbf{B}_T are the full velocity and magnetic fields, $\bar{\nu}$ is the kinematic viscosity, $\bar{\zeta}$ is the bulk viscosity (this will not contribute), $\bar{\eta}$ is the resistivity, and $\boldsymbol{\Omega}$ is the rotation. Before calculating transport coefficients from Eq. (6.1) the anelastic approximation will be utilized (Kichatinov and Rüdiger, 1992; Rüdiger and Kichatinov, 1993), assuming nearly incompressible fluctuations with $\nabla \cdot (\rho \mathbf{u}) = 0$ [see Eq. (6.2)]. This allows low-order effects due to a mean density gradient to be retained, while still preserving most of the simplicity of an incompressible calculation.

As in earlier chapters, I split fields into a mean and fluctuating part;

$$\mathbf{U}_T = \mathbf{U} + \mathbf{u}, \quad \mathbf{B}_T = \mathbf{B} + \mathbf{b}, \quad (6.2)$$

with $\mathbf{U} = \langle \mathbf{U}_T \rangle$, $\mathbf{B} = \langle \mathbf{B}_T \rangle$. The averaging operation $\langle \cdot \rangle$ should filter out small scales and satisfy the Reynolds averaging rules.² Applying $\langle \cdot \rangle$ to the induction equation leads to the mean-field

²Note that I have chosen the different notation for the average here to clarify that for the majority of this chapter, the mean-field average is kept entirely general (only in Secs. 6.3 and 6.4 is the horizontal average specified).

induction equation (see Sec. 1.2)

$$\partial_t \mathbf{B} = \nabla \times (\mathbf{U} \times \mathbf{B}) + \nabla \times \mathcal{E} + \bar{\eta} \Delta \mathbf{B}. \quad (6.3)$$

The goal of analytical mean-field theory is to calculate \mathcal{E} as a function of \mathbf{B} and other parameters in the problem (i.e., \mathbf{U} , Ω , $\nabla \ln \rho$, and the small-scale turbulence statistics), thereby closing Eq. (6.3). If $\mathcal{E}(\mathbf{B})$ is such that a small magnetic field will be reinforced by the small-scale turbulence, one has a dynamo instability.

Before commencing with a full calculation of \mathcal{E} , it is worth examining the symmetries of the problem. Assuming scale separation between the mean and fluctuating fields, one can Taylor expand the EMF as

$$\mathcal{E}_i = a_{ij} B_j + b_{ijk} B_{j,k} + \dots \quad (6.4)$$

(I shall use the Einstein summation convention throughout this chapter.) The tensors a_{ij} and b_{ijk} are the transport coefficients determined by the turbulence. Note that in contrast to the Taylor expansion of \mathcal{E} given in Sec. 1.2, the velocity field U_i is not included. Instead, the dependence on U is contained within a_{ij} and b_{ijk} , and U is considered fixed. In the astrophysically relevant case where U arises through large-scale external forces (e.g., gravity), this seems to be a more natural approach to the problem. In keeping with the separation of scales assumption, I consider linear \mathbf{B} fields $(\mathbf{B})_i = B_i + B_{ij} x_j$, velocity fields $(\mathbf{U})_i = U_{ij} x_j$ and density $\rho = \rho_0 + \rho_0 \mathbf{x} \cdot \nabla \ln \rho$ (the constant velocity part can be removed by Galilean transformation). As in Rädler and Stepanov (2006) (hereafter RS06), to cleanly separate different dynamo effects it is helpful to split $\nabla \mathbf{U}$ and $\nabla \mathbf{B}$ into symmetric and antisymmetric parts,

$$U_{ij} = D_{ij} - A_{ij}^U = D_{ij} - \frac{1}{2} \varepsilon_{ijk} W_k, \quad (6.5a)$$

$$B_{ij} = (\nabla \mathbf{B})_{ij}^{(s)} - A_{ij}^B = (\nabla \mathbf{B})_{ij}^{(s)} - \frac{1}{2} \varepsilon_{ijk} J_k, \quad (6.5b)$$

where D_{ij} and $(\nabla \mathbf{B})_{ij}^{(s)}$ are the symmetric and antisymmetric parts of U_{ij} and B_{ij} , $\mathbf{W} = \nabla \times \mathbf{U}$ is the background vorticity and $\mathbf{J} = \nabla \times \mathbf{B}$ is the mean current. Due to the assumption $\nabla \cdot \mathbf{U} = 0$ in Eq. (6.5), I have implicitly assumed $\mathbf{U} \cdot \nabla \rho = 0$, a requirement that could easily be relaxed if desired.

I shall allow for general inhomogenous background turbulence in both \mathbf{u} and \mathbf{b} , modified by mean velocity gradients, rotation, and density stratification. The density stratification is assumed to be aligned with the turbulence stratification in the direction $\hat{\mathbf{g}}$, but their magnitudes and signs are allowed to differ; that is, defining

$$\nabla \ln \rho = \chi_\rho \hat{\mathbf{g}}, \quad \nabla \ln \bar{u} = \chi_{\bar{u}} \hat{\mathbf{g}}, \quad \nabla \ln \bar{b} = \chi_{\bar{b}} \hat{\mathbf{g}}, \quad (6.6)$$

I allow $\chi_\rho \neq \chi_{\bar{u}} \neq \chi_{\bar{b}}$ (where $\bar{u} = \langle u_0^2 \rangle^{1/2}$, $\bar{b} = \langle b_0^2 \rangle^{1/2}$). For completeness, I include both nonhelical and helical contributions to the turbulence³ but neglect the effects of inhomogeneity on the helical part.⁴ It is assumed that the EMF due to the background turbulence vanishes, $\langle \mathbf{u} \times \mathbf{b} \rangle_0 = 0$. Such a \mathbf{B} -independent contribution could be important in some situations (see, for example, Yoshizawa and Yokoi 1993) and the method applied here can be used to calculate well-known effects of this type if desired, for instance the cross-helicity effect (Yokoi, 2013). In addition, I do not calculate the components of the Reynolds stress, which would force a mean-field velocity \mathbf{U} . This is not justified for any particular reason other than our primary interest in the magnetic field dynamics. While it is possible that there are important interactions between \mathbf{U} and \mathbf{B} that lead to other instabilities (Courvoisier *et al.*, 2010), their systematic study is left to future work.

³The primary reasoning for including the helical part of the correlation here has been to check that standard results are obtained using this method; for example, $\alpha^{(0)} \sim \langle \mathbf{u} \cdot \nabla \times \mathbf{u} \rangle - \langle \mathbf{b} \cdot \nabla \times \mathbf{b} \rangle$ (Pouquet *et al.*, 1976).

⁴Stratification of helical turbulence would presumably provide a host of contributions to the resistivity tensor that would likely be much smaller than contributions from the nonhelical fluctuations. Given the rather immense size of the calculation without such effects, it seemed prudent to ignore these.

A careful consideration of the symmetry properties of the system leads to the general representation of \mathcal{E} in terms of a set of scalar transport transport coefficients,⁵

$$\begin{aligned}
\mathcal{E} = & -\alpha_H^{(0)} \mathbf{B} - \alpha_H^{(D)} D_{ij} B_j - \gamma_H^{(\Omega)} \boldsymbol{\Omega} \times \mathbf{B} - \gamma_H^{(W)} \mathbf{W} \times \mathbf{B} \\
& -\alpha_1^{(\Omega)} (\hat{\mathbf{g}} \cdot \boldsymbol{\Omega}) \mathbf{B} - \alpha_2^{(\Omega)} [(\hat{\mathbf{g}} \cdot \mathbf{B}) \boldsymbol{\Omega} + (\mathbf{B} \cdot \boldsymbol{\Omega}) \hat{\mathbf{g}}] \\
& -\alpha_1^{(W)} (\hat{\mathbf{g}} \cdot \mathbf{W}) \mathbf{B} - \alpha_2^{(W)} [(\hat{\mathbf{g}} \cdot \mathbf{B}) \mathbf{W} + (\mathbf{B} \cdot \mathbf{W}) \hat{\mathbf{g}}] \\
& -\alpha^{(D)} (\varepsilon_{ilm} D_{lj} \hat{g}_m + \varepsilon_{jlm} D_{li} \hat{g}_m) B_j \\
& -(\gamma^{(0)} + \gamma^{(\Omega)} \hat{\mathbf{g}} \times \boldsymbol{\Omega} + \gamma^{(W)} \hat{\mathbf{g}} \times \mathbf{W} + \gamma^{(D)} D_{ij} \hat{g}_j) \times \mathbf{B} \\
& -\beta^{(0)} \mathbf{J} - \beta^{(D)} D_{ij} J_j - (\delta^{(W)} \mathbf{W} + \delta^{(\Omega)} \boldsymbol{\Omega}) \times \mathbf{J} \\
& -(\kappa^{(W)} \mathbf{W} + \kappa^{(\Omega)} \boldsymbol{\Omega})_j (\nabla \mathbf{B})_{ji}^{(s)} - 2\kappa^{(D)} \varepsilon_{ijk} D_{kr} (\nabla \mathbf{B})_{jr}^{(s)}
\end{aligned} \tag{6.7}$$

Here I have conformed to the sign conventions in RS06. The subscript \cdot_H denotes a coefficient that is only allowed by the helical part of the turbulence, while all other coefficients arise only through the nonhelical part. In addition, since I assume small-scale fluctuations in both \mathbf{u} and \mathbf{b} , I shall further split each transport coefficient into these contributions; e.g., $\kappa^{(W)} = (\kappa^{(W)})_u + (\kappa^{(W)})_b$. Since SOCA is utilized in the linear regime (where \mathbf{B} is small), these are always additive and transport coefficients in an MHD turbulent bath can be calculated separately from the \mathbf{u} and \mathbf{b} turbulent contributions.

Cartesian geometry

In Sec. 6.3 I shall give specific results for the numerically convenient Cartesian shear dynamo with nonhelical, unstratified background turbulence. This is essentially a generalization of the

⁵The derivation of Eq. (6.7) involves consideration of the elements from which \mathcal{E} can be constructed. Some of these are pseudo-tensors and change sign with a coordinate system reflection (e.g., \mathbf{B} , ε_{ijk} , and α_H coefficients) and some are true tensors, which do not (e.g., $\hat{\mathbf{g}}$, D_{ij} , and β coefficients). Since \mathcal{E} is a true vector, it must not change sign under reflection, and with the assumption of linearity in each of $\hat{\mathbf{g}}$ (really χ_ρ), $\boldsymbol{\Omega}$, \mathbf{U} and \mathbf{B} , Eq. (6.7) is the most general form possible. See RS06 for a full explanation.

unstratified shearing box. In this case, mean fields depend only on z , $\mathbf{U} = -Sx\hat{\mathbf{y}}$ (giving $\mathbf{W} = -S\hat{\mathbf{z}}$), $\Omega = \Omega\hat{\mathbf{z}}$, and the mean-field average is a horizontal average, $\langle \cdot \rangle = (L_x L_y)^{-1} \int \cdot dx dy$. The mean-field equations simplify to

$$\partial_t B_x = -\eta_{yx} \partial_z^2 B_y + \eta_{yy} \partial_z^2 B_x, \quad (6.8a)$$

$$\partial_t B_y = -SB_x - \eta_{xy} \partial_z^2 B_x + \eta_{xx} \partial_z^2 B_y, \quad (6.8b)$$

where the η_{ij} are defined to be the relevant components of b_{ijk} that are nonzero for the chosen average and mean field (see chapter 4). For $B_i = B_{i0} e^{ikz} e^{\Gamma t}$ a coherent dynamo is possible if

$$\Gamma = k \left\{ -S\eta_{yx} + k^2 \left[\eta_{xy}\eta_{yx} + \frac{1}{2}(\eta_{xx} - \eta_{yy})^2 \right] \right\}^{1/2} - k^2(\eta_{xx} + \eta_{yy}) \quad (6.9)$$

has a real part greater than 0. One can neglect the term multiplying k^2 in the square root of Eq. (6.9) since S is presumed to be large compared to all transport coefficients. This gives $\eta_{yx}S < 0$ as a necessary condition for instability. Computing the relationship between Eq. (6.7) and Eq. (6.8), one can show

$$\eta_{yx} = -S \left[\delta^{(W)} - \frac{1}{2} (\kappa^{(W)} - \beta^{(D)} + \kappa^{(D)}) \right] + \Omega \left(\delta^{(\Omega)} - \frac{1}{2} \kappa^{(\Omega)} \right), \quad (6.10a)$$

$$\eta_{xy} = S \left[\delta^{(W)} - \frac{1}{2} (\kappa^{(W)} + \beta^{(D)} - \kappa^{(D)}) \right] - \Omega \left(\delta^{(\Omega)} - \frac{1}{2} \kappa^{(\Omega)} \right), \quad (6.10b)$$

and $\eta_{xx} = \eta_{yy} = \beta^{(0)}$. Note that Eq. (6.9) only describes the growth due to a coherent dynamo process; fluctuations in α or η that arise in any finite system can cause a dynamo in and of themselves (see chapter 4, also Heinemann *et al.* 2011; Mitra and Brandenburg 2012). I shall specialize to the Cartesian case in Secs. 6.3 and 6.4, and keep \mathbf{U} general for the calculation of the scalar transport coefficients listed in Eq. (6.7).

In Sec. 6.4 I give results specific to the case of stratified sheared rotating turbulence. This is motivated by consideration of the upper (or lower) portions of an accretion disk. Again, mean fields depend only on z , $\mathbf{U} = -Sx\hat{\mathbf{y}}$, $\mathbf{\Omega} = \Omega\hat{\mathbf{z}}$, and $\hat{\mathbf{g}} = \hat{\mathbf{z}}$. I neglect off-diagonal resistivity contributions and use $\eta_{xx} = \eta_{yy} = \beta^{(0)}$. The mean-field equations simplify to

$$\partial_t B_x = -a_{yx}\partial_z B_x - a_{yy}\partial_z B_y + \beta^{(0)}\partial_z^2 B_x, \quad (6.11a)$$

$$\partial_t B_y = -SB_x + a_{xy}\partial_z B_x + a_{xx}\partial_z B_y + \beta^{(0)}\partial_z^2 B_y. \quad (6.11b)$$

With $a_{xy} = -a_{yx}$ and considering $B_i = B_{i0}e^{ikz}e^{\Gamma t}$, one obtains the growth rate

$$\Gamma = \left(ikSa_{yy}/2 + k^2a_{yy}a_{xx} \right)^{1/2} + ik a_{xy} - k^2\beta^{(0)}. \quad (6.12)$$

Again, S is presumed large in comparison to all transport coefficients, so we see that any nonzero a_{yy} can lead to instability at sufficiently long wavelength. Of course, in practice there will be a minimum k possible in the system, particularly since the turbulence is stratified, so a finite a_{yy} will be necessary to overcome the turbulent resistivity. The coefficients in Eq. (6.11) are related to those in Eq. (6.7) through $a_{xy} = -a_{yx} = \gamma^{(0)}$ and

$$a_{yy} = S \left(\alpha_1^{(W)} - \alpha^{(D)} \right) - \Omega \alpha_1^{(\Omega)}, \quad (6.13a)$$

$$a_{xx} = S \left(\alpha_1^{(W)} + \alpha^{(D)} \right) - \Omega \alpha_1^{(\Omega)}. \quad (6.13b)$$

6.1.1 Perturbation expansion to describe the fluctuations

The second-order correlation approximation (SOCA), which involves solving linear equations for the fluctuations by neglecting third-order and higher correlations, is rigorously valid only at low

Reynolds numbers where dissipation dominates over nonlinearities for the fluctuations.⁶ In addition, the shear, rotation, and density stratification are included perturbatively in the calculation (Rogachevskii and Kleeorin, 2003; Rädler and Stepanov, 2006); that is, I consider only the linear response of transport coefficients to these effects. An analytic calculation with shear included at zeroth order can be found in Singh and Sridhar (2011), while the computation of magnetic dynamo transport coefficients with non-perturbative shear and rotation was presented in chapter 4.

Following Rüdiger (1990), Kichatinov and Rüdiger (1992), and Rüdiger and Kichatinov (1993), I start by making an anelastic approximation to the full compressible equations, $\nabla \cdot (\rho \mathbf{u}) = 0$. This should be valid for weakly compressible turbulence and allows the inclusion of a weak density stratification into the problem, which is important in a wide variety of mean-field dynamos. I shall assume that the large-scale flow is incompressible, since our primary application is to shear flows. It is then more convenient to work in terms of the small-scale momentum (Rüdiger and Kichatinov, 1993; Kichatinov and Rüdiger, 1992), $\mathbf{m} \equiv \rho \mathbf{u}$, since the calculation for \mathbf{m} proceeds in a manner similar to the incompressible case.

In retaining both strong homogenous velocity and magnetic fluctuations, denoted \mathbf{u}_0 (or \mathbf{m}_0) and \mathbf{b}_0 respectively, the momentum and induction equations must be treated on the same theoretical footing. One starts from Eq. (6.1) by splitting into mean-field and fluctuation equations, applying the anelastic approximation followed by the change of variables $\mathbf{u}_0 = \mathbf{m}_0/\rho$. One then linearizes the small-scale equations and expand $\mathbf{m} = \mathbf{m}_0 + \mathbf{m}^{(0)} + \mathbf{m}^{(1)} + \dots$, $\mathbf{b} = \mathbf{b}_0 + \mathbf{b}^{(0)} + \mathbf{b}^{(1)} + \dots$, to perturbatively find the change to the background turbulence caused by the shear, rotation and stratification. This leads the SOCA equations that will be used to calculate all transport coefficients:

⁶SOCA can also be valid in the small Strouhal number limit [Eq. (6.32)]. See Brandenburg and Subramanian (2005) for a more thorough discussion.

$$\begin{aligned}
(\partial_t - \bar{\nu}\Delta) \mathbf{m}^{(0)} &= -(\mathbf{m}_0 \cdot \nabla \mathbf{U} + \mathbf{U} \cdot \nabla \mathbf{m}_0 - (\mathbf{g}_\rho \cdot \mathbf{U}) \mathbf{m}_0) \\
&\quad - \nabla p^{(0)} - 2\boldsymbol{\Omega} \times \mathbf{m}_0 + (\mathbf{b}_0 \cdot \nabla \mathbf{B} + \mathbf{B} \cdot \nabla \mathbf{b}^{(0)}) - \bar{\nu} \mathbf{g}_\rho \cdot \nabla \mathbf{m}_0,
\end{aligned} \tag{6.14a}$$

$$\begin{aligned}
(\partial_t - \bar{\nu}\Delta) \mathbf{m}^{(1)} &= -(\mathbf{m}^{(0)} \cdot \nabla \mathbf{U} + \mathbf{U} \cdot \nabla \mathbf{m}^{(0)} - (\mathbf{g}_\rho \cdot \mathbf{U}) \mathbf{m}^{(0)}) \\
&\quad - \nabla p^{(1)} - 2\boldsymbol{\Omega} \times \mathbf{m}^{(0)} + (\mathbf{b}^{(0)} \cdot \nabla \mathbf{B} + \mathbf{B} \cdot \nabla \mathbf{b}^{(0)}) - \bar{\nu} \mathbf{g}_\rho \cdot \nabla \mathbf{m}^{(0)},
\end{aligned} \tag{6.14b}$$

$$\begin{aligned}
(\partial_t - \bar{\eta}\Delta) \mathbf{b}^{(0)} &= \rho^{-1} [(\mathbf{g}_\rho \cdot \mathbf{m}_0) \mathbf{B} - \mathbf{m}_0 \cdot \nabla \mathbf{B} + \mathbf{B} \cdot \nabla \mathbf{m}_0 \\
&\quad - (\mathbf{g}_\rho \cdot \mathbf{B}) \mathbf{m}_0] + \mathbf{b}_0 \cdot \nabla \mathbf{U} - \mathbf{U} \cdot \nabla \mathbf{b}_0,
\end{aligned} \tag{6.14c}$$

$$\begin{aligned}
(\partial_t - \bar{\eta}\Delta) \mathbf{b}^{(1)} &= \rho^{-1} [(\mathbf{g}_\rho \cdot \mathbf{m}^{(0)}) \mathbf{B} - \mathbf{m}^{(0)} \cdot \nabla \mathbf{B} + \mathbf{B} \cdot \nabla \mathbf{m}^{(0)} \\
&\quad - (\mathbf{g}_\rho \cdot \mathbf{B}) \mathbf{m}^{(0)}] + \mathbf{b}^{(0)} \cdot \nabla \mathbf{U} - \mathbf{U} \cdot \nabla \mathbf{b}^{(0)},
\end{aligned} \tag{6.14d}$$

along with divergence constraints for each $\mathbf{m}^{(0)}$, $\mathbf{b}^{(0)}$, $\mathbf{m}^{(1)}$, $\mathbf{b}^{(1)}$. Here $\mathbf{g}_\rho \equiv \chi_\rho \hat{\mathbf{g}}$ and I have neglected second derivatives of \mathbf{U} and ρ , as well as products of $\nabla \mathbf{B}$ with χ_ρ [these contributions should vanish in the transport coefficients, since Eq. (6.7) illustrates that there is no contribution to the resistivity from $\hat{\mathbf{g}}$ at linear order]. In addition, I neglect any terms that involve quadratic products of \mathbf{U} , $\boldsymbol{\Omega}$, and χ_ρ [e.g., $(\mathbf{g}_\rho \cdot \mathbf{U}) \mathbf{m}_0$], and assume terms are linear in space to take the Fourier transport of Eq. (6.14) (see App. D.1).

While it may seem surprising that one requires terms two orders higher than \mathbf{m}_0 and \mathbf{b}_0 , it is straightforward to see that only considering $\mathbf{m}^{(0)}$ and $\mathbf{b}^{(0)}$ will not lead to contributions to \mathcal{E} that depend on products of \mathbf{B} with \mathbf{U} or $\boldsymbol{\Omega}$ (these are the interesting terms in the dynamo, describing the effect of rotation or velocity). With this in mind, the EMF is calculated as

$$\begin{aligned}
\mathcal{E}_{ij} = \langle u_i b_j \rangle &= \langle \rho^{-1} m_{0i} b_{0j} \rangle + \langle \rho^{-1} m_{0i} b_j^{(0)} \rangle + \langle \rho^{-1} m_{0i} b_j^{(1)} \rangle \\
&\quad + \langle \rho^{-1} m_i^{(0)} b_{0j} \rangle + \langle \rho^{-1} m_i^{(1)} b_{0j} \rangle + \langle \rho^{-1} m_i^{(0)} b_j^{(0)} \rangle.
\end{aligned} \tag{6.15}$$

Despite the fact that all the terms in Eq. (6.15) give some contribution, there are also a large number of terms that contain quadratic products of U_{ij} , Ω_i , χ_ρ , or \mathbf{B} , which are neglected. As is evident, with background turbulence in both \mathbf{u} and \mathbf{b} there will be contributions to \mathcal{E} from the Maxwell stress ($\mathbf{B} \cdot \nabla \mathbf{b} + \mathbf{b} \cdot \nabla \mathbf{B}$) that one would expect to be of a magnitude similar to the standard kinematic dynamo arising from the Lorentz force [$\nabla \times (\mathbf{u} \times \mathbf{B})$]. Note that this choice of perturbation expansion is the natural generalization of RS06 to the case with \mathbf{b}_0 fluctuations (although note that $\mathbf{u}^{(1)}$ in RS06 has become $\mathbf{u}^{(0)}$ in our notation such that \mathbf{u} and \mathbf{b} are treated on equal footings). Results for the kinematic dynamo ($\mathbf{b}_0 = 0$) without density stratification agree with RS06 aside from a single numerical coefficient (see Appendix D.2).

6.2 Outline of the calculation of \mathcal{E}

The calculation follows the methods and notation in RS06, and a full explanation is given in that work. Here I give a very brief outline, in particular the choices involved, with final results given in Appendix D.2. The entire calculation was carried out in *Mathematica* using the *VEST* package to handle abstract tensor manipulations (see App. E).

The two-point correlation of two fields \mathbf{v} and \mathbf{w} is defined as

$$\phi_{ij}^{(vw)}(\mathbf{x}_1, t_1; \mathbf{x}_2, t_2) = \langle v_i(\mathbf{x}_1, t_1) w_j(\mathbf{x}_2, t_2) \rangle. \quad (6.16)$$

It is convenient to write such quantities in the variables

$$\mathbf{R} = (\mathbf{x}_1 + \mathbf{x}_2)/2, \quad \mathbf{r} = \mathbf{x}_1 - \mathbf{x}_2, \quad (6.17a)$$

$$T = (t_1 + t_2)/2, \quad t = t_1 - t_2, \quad (6.17b)$$

giving

$$\phi_{ij}^{(vw)}(\mathbf{R}, T; \mathbf{r}, t) = \left\langle v_i \left(\mathbf{R} + \frac{\mathbf{r}}{2}, T + \frac{t}{2} \right) w_j \left(\mathbf{R} - \frac{\mathbf{r}}{2}, T - \frac{t}{2} \right) \right\rangle. \quad (6.18)$$

One then Fourier transforms in the small-scale variable \mathbf{r} to obtain

$$\phi_{ij}^{(vw)}(\mathbf{R}, T; \mathbf{r}, t) = \int d\mathbf{k} d\omega \tilde{\phi}_{ij}^{(vw)}(\mathbf{R}, T; \mathbf{k}, \omega) e^{i(\mathbf{k} \cdot \mathbf{r} - \omega t)}, \quad (6.19)$$

with

$$\tilde{\phi}_{ij}^{(vw)}(\mathbf{R}, T; \mathbf{k}, \omega) = \int d\mathbf{K} d\Omega \langle [\hat{v}(\mathbf{k}, \omega)]_+ [\hat{w}(\mathbf{k}, \omega)]_- \rangle e^{i(\mathbf{K} \cdot \mathbf{R} - \Omega T)}, \quad (6.20)$$

where $\hat{v}(\mathbf{k}, \omega)$ and $\hat{w}(\mathbf{k}, \omega)$ denote the Fourier transforms of v and w , and I use the $[\cdot]_{\pm}$ notation of RS06,

$$[\hat{f}(\mathbf{k}, \omega)]_{\pm} = \hat{f}(\pm\mathbf{k} + \mathbf{K}/2, \pm\omega + \Omega/2). \quad (6.21)$$

As in RS06, I calculate

$$\begin{aligned} \mathcal{E}_{ij}(\mathbf{R}, T; 0, 0) &= \int d\mathbf{k} d\omega \tilde{\mathcal{E}}_{ij}(\mathbf{R}, T; \mathbf{k}, \omega) \\ &= \int d\mathbf{K} d\Omega d\mathbf{k} d\omega \langle [\rho^{-1} \hat{m}_i]_+ [\hat{b}_i]_- \rangle e^{i\mathbf{K} \cdot \mathbf{R} - i\Omega T} \\ &= \int d\mathbf{K} d\Omega d\mathbf{k} d\omega \rho_0^{-1} \langle [\hat{m}_i - ig_{\rho j} \partial_{k_j} \hat{m}_i]_+ [\hat{b}_i]_- \rangle e^{i\mathbf{K} \cdot \mathbf{R} - i\Omega T}, \end{aligned} \quad (6.22)$$

setting $\mathbf{R}, T \rightarrow 0$ only after extracting the coefficients of B_i and B_{ij} (i.e., the transport coefficients a_{ij}, b_{ijk}).

With these notations defined, the starting point of the calculation is the substitution of the linear forms for \mathbf{U} , ρ and \mathbf{B} and into Eq. (6.14), followed by a Fourier transform. This leads to Eqs. (D.2)-(D.5). One then substitutes $\hat{m}_i^{(0)}, \hat{b}_i^{(0)}$ into $\hat{m}_i^{(1)}, \hat{b}_i^{(1)}$ to form explicit expressions for \hat{u}_i ,

\hat{b}_i in terms of \hat{u}_{0i} , \hat{b}_{i0} . Defining

$$\tilde{m}_{ij} = \langle [\hat{m}_{0i}]_+ [\hat{m}_{0j}]_- \rangle, \quad (6.23a)$$

$$\tilde{b}_{ij} = \langle [\hat{b}_{0i}]_+ [\hat{b}_{0j}]_- \rangle, \quad (6.23b)$$

to specify the statistics of \mathbf{u}_0 and \mathbf{b}_0 , one can form Eq. (6.15) in terms of \tilde{m}_{ij} and \tilde{b}_{ij} , neglecting all terms that contain $U_{ij}U_{rs}$, $U_{ij}\Omega_j$, $\Omega_i\Omega_r$, $U_{ij}\chi_\rho$, $\Omega_i\chi_\rho$, $(\nabla \ln \rho)^2$, or any products of B_i and B_{ij} . Recall that $\langle \mathbf{u}_0 \mathbf{b}_0 \rangle = 0$ is assumed, implying that all terms in the expansion of \mathcal{E}_{ij} contain B_i or B_{ij} . In keeping with the expansion to linear order in background quantities, it is necessary to expand $[f(\mathbf{k})]_\pm$ to first order in \mathbf{K} in those terms that contain B_i (i.e., α coefficients). These lead to terms involving the gradient of the turbulence intensity. Note that $[f(\mathbf{k})]_\pm \rightarrow f(\pm \mathbf{k})$ for resistive terms (coefficients of B_{ij}) since these already contain a derivative of \mathbf{B} , implying the expansion should be carried out to zeroth order. Some useful identities in the above procedure are given in RS06 Eqs. (33)-(35), which are needed to remove $\partial/\partial k_i$ derivatives from u_{0i} and b_{0i} . Similarly, I apply the identities

$$k_i \tilde{m}_{ij} = -\frac{K_i}{2} \tilde{m}_{ij}, \quad k_i \tilde{m}_{ji} = \frac{K_i}{2} \tilde{m}_{ji} \quad (6.24)$$

(and similarly for \tilde{b}_{ji}), which arise from the divergence constraints on \hat{m}_i and \hat{b}_i .

Extracting the coefficients of B_i and B_{ij} in the expression for $\mathcal{E}_i = \varepsilon_{ijk} \mathcal{E}_{jk}(\mathbf{0}, 0)$, at this stage one has large integral expressions for a_{ij} and b_{ijk} in terms of \tilde{m}_{ij} and \tilde{b}_{ij} and their spatial derivatives [for example, RS06 Eqs. (39)-(40)]. Without further interpretation, such expressions are nearly useless, and it is helpful to insert explicit forms for \tilde{m}_{ij} and \tilde{b}_{ij} . Assuming isotropy in the limit of vanishing mean flow and rotation, I use

$$\tilde{m}_{ij} = \frac{1}{2} \left[\delta_{ij} - \frac{k_i k_j}{k^2} - \frac{1}{2k^2} (k_i K_j - k_j K_i) \right] W_m(\mathbf{K}; k, \omega) - i \varepsilon_{ijl} \frac{k_l}{k^2} H_u(k, \omega), \quad (6.25a)$$

$$\tilde{b}_{ij} = \frac{1}{2} \left[\delta_{ij} - \frac{k_i k_j}{k^2} - \frac{1}{2k^2} (k_i K_j - k_j K_i) \right] W_b(\mathbf{K}; k, \omega) - i \varepsilon_{ijl} \frac{k_l}{k^2} H_b(k, \omega), \quad (6.25b)$$

where $k = |k_i|$. Here $W_{m,b}$ represents a nonhelical part and $H_{m,b}$ a helical part of the background turbulence (Rüdiger and Kichatinov, 1993; Kichatinov and Rüdiger, 1992). This form for W_m is particularly convenient since to first order in the scale of density variation

$$W_m(\mathbf{x}; k, \omega) = \rho^2(\mathbf{x}) W_u(\mathbf{x}; k, \omega), \quad (6.26)$$

where $W_u(\mathbf{x}; k, \omega)$ is a similar function specifying the statistics of \mathbf{u} and $W_m(\mathbf{x}; k, \omega) = \int d\mathbf{K} e^{i\mathbf{K}\cdot\mathbf{x}} W_m(\mathbf{K}; k, \omega)$ (Kichatinov and Rüdiger, 1992). In this way,

$$\nabla W_m(\mathbf{x}; k, \omega) = \hat{\mathbf{g}}(2\chi_\rho + 2\chi_{\bar{u}}) W_m(\mathbf{x}; k, \omega), \quad (6.27)$$

separating effects arising from density and turbulence stratification. Similarly, for the magnetic fluctuations

$$\nabla W_b(\mathbf{x}; k, \omega) = 2\hat{\mathbf{g}}\chi_{\bar{b}} W_b(\mathbf{x}; k, \omega). \quad (6.28)$$

It transpires that all terms now depend on \mathbf{k} only through k , and all of the integrals can be substantially simplified using

$$\int d\mathbf{k} k_i k_j f(k) = \frac{1}{3} \delta_{ij} \int dk k^2 f(k), \quad (6.29a)$$

$$\int d\mathbf{k} k_i k_j k_k k_l f(k) = \frac{1}{15} (\delta_{ij} \delta_{kl} + \delta_{ik} \delta_{jl} + \delta_{il} \delta_{jk}) \int dk k^4 f(k), \quad (6.29b)$$

where the integrals over k on the right-hand side of Eq. (6.29) are taken from $k = 0 \rightarrow \infty$. One then splits U_{ij} and B_{ij} using Eq. (6.5), putting \mathcal{E}_i in the form given by Eq. (6.7). Following this, transport coefficients, $\alpha_H^{(0)}, \dots, \alpha^{(\Omega)}, \dots, \beta^{(0)}, \dots$, can be straightforwardly read off the expression

as integrals of the form

$$\left(\alpha_H^{(\cdot)}\right)_{u,b} = 4\pi \int dk d\omega k^2 \tilde{\alpha}_H^{(\cdot)}(k, \omega) H_{u,b}(k, \omega), \quad (6.30a)$$

$$\left(\alpha^{(\cdot)}\right)_{u,b} = 4\pi \int dk d\omega k^2 \tilde{\alpha}^{(\cdot)}(k, \omega) W_{u,b}(k, \omega), \quad (6.30b)$$

$$\left(\beta^{(\cdot)}\right)_{u,b} = 4\pi \int dk d\omega k^2 \tilde{\beta}^{(\cdot)}(k, \omega) W_{u,b}(k, \omega). \quad (6.30c)$$

The full list of coefficients $\tilde{\alpha}_H^{(0)}, \dots, \tilde{\alpha}^{(\Omega)}, \dots, \tilde{\beta}^{(0)}, \dots$ is given in App. D.2.

Finally, it is possible to carry out the integrals of the form in Eq. (6.30) for a specific form of W and H , leading to explicit expressions for the transport coefficients in terms of the physical parameters. For examining expressions and plotting, a convenient form is the Gaussian W used in RS06,

$$W_u = \bar{u}^2 \frac{2\lambda_c^3 \tau_c}{3(2\pi)^{5/2}} \frac{(k\lambda_c)^2 e^{-(k\lambda_c)^2/2}}{1 + (\omega\tau_c)^2}, \quad (6.31)$$

with a similar definition of W_b . With this choice, all integrals can be carried out explicitly without further approximation. As in RS06, I shall put such expressions in terms of the non-dimensional variables (and ρ_0)

$$\begin{aligned} \epsilon &= \bar{b}/\bar{u}, \quad p = \lambda_c^2/\bar{\nu}\tau_c, \quad q = \lambda_c^2/\bar{\eta}\tau_c, \quad \text{Pm} = \bar{\nu}/\bar{\eta}, \\ \text{Re} &= \bar{u}\lambda_c/\bar{\nu}, \quad \text{Rm} = \bar{u}\lambda_c/\bar{\eta}, \quad \text{St} = \bar{u}\tau_c/\lambda_c. \end{aligned} \quad (6.32)$$

Here Pm, Re, Rm, and St are respectively the magnetic Prandtl number, the fluid Reynolds number, the magnetic Reynolds number and the Strouhal number. p and q are the ratio of diffusion times, $\lambda_c^2/\bar{\nu}$ and $\lambda_c^2/\bar{\eta}$, to the correlation time τ_c . Thus $q \rightarrow 0$ denotes the low conductivity limit, while $q \rightarrow \infty$ denotes a high-conductivity limit (with a similar result for p and fluid diffusivity). A sufficient condition for the validity of the first-order smoothing approximation⁷ (i.e., neglect of

⁷These conditions are only true in the absence of rotation and velocity shear. We also require U_{ij} and Ω_i be a small perturbation to the background turbulence.

nonlinear terms in the correlation equations) is $\text{Rm} \ll 1$ in the limit $q \rightarrow 0$, and $\text{St} \ll 1$ in the limit $q \rightarrow \infty$; see Brandenburg and Subramanian (2005) and Rädler and Stepanov (2006) for more discussion of these validity regimes. The substitutions (6.32) allow all transport coefficients to be written in terms of only q and Pm (equivalently q and p), multiplied by some prefactor involving Rm and dimensional quantities (the coefficients have different units). This property makes the form very convenient for exploration of the functional dependence of coefficients, and I shall use these forms for plotting transport coefficients over a range of q at various Pm .

In practice, I have carried out the full sequence of steps detailed above in *Mathematica* using the *VEST* package (Squire *et al.* 2014; App. E) to enable straightforward manipulation of tensors in index notation. This has the obvious advantage of handling the very long expressions with ease and making the calculation straightforward to generalize or modify. The sequence of steps is essentially the same as that detailed above. I first define $\mathbf{m}^{(0)}$, $\mathbf{m}^{(1)}$, $\mathbf{b}^{(0)}$, and $\mathbf{b}^{(1)}$, insert $\mathbf{m}^{(0)}$ and $\mathbf{b}^{(0)}$ into $\mathbf{m}^{(1)}$ and $\mathbf{b}^{(1)}$, then only later remove products that are quadratic in U_{ij} , Ω , or χ_ρ . It is then straightforward to define $[\cdot]_{\pm}$ operators, their associated product rules, and methods to in expand in \mathbf{K} . This allows the construction of the entirety of \mathcal{E} in one step. Insertion of the explicit forms for \tilde{v}_{ij} and \tilde{b}_{ij} [Eq. (6.25)] and the partial integration using isotropy [Eq. (6.29)] is easily carried out using replacement rules. Finally, replacement rules allow straightforward decomposition of products of B_{ij} with U_{ij} , Ω , and \hat{g} into the form given in Eq. (6.7), enabling the coefficients listed in App. D.2 to be simply extracted from the total expression. Finally, if so desired, these can be directly integrated with the specific form of W [Eq. (6.31)] by carefully substituting the dimensionless variables [Eq. (6.32)] and using *Mathematica*'s native `Integrate` function.

6.2.1 Agreement with previous works

The results agree with related works of other authors, including those utilizing different calculation methods. As discussed throughout the work, all results of RS06 are recovered in the limit

$\nabla \ln \rho = 0$ (aside from one discrepancy, in $(\beta^{(D)})_u$). This agrees with Rüdiger and Kitchatinov (2006), many results of Pipin (2008) (see his App. B), as well as the shear quasi-linear methods in Sridhar and Subramanian (2009) and Singh and Sridhar (2011). As is well known, there is a discrepancy between these kinematic quasi-linear results and those obtained using the τ approximation (Rogachevskii and Kleeorin, 2003, 2004), possibly due to a change in sign of η_{yx} with R_m (Brandenburg *et al.*, 2008a). The results also compare favorably to previous works without velocity gradients but including magnetic fluctuations. As expected, the helical magnetic α effect has the sign opposite to the kinematic effect, and there is no change to $\beta^{(0)}$ due to the addition of magnetic fluctuations. In addition, the signs of $\delta_u^{(\Omega)}$ and $\delta_b^{(\Omega)}$ agree with the τ approximation calculation of Rädler *et al.* (2003) ($\delta_u^{(\Omega)} < 0$, $\delta_b^{(\Omega)} > 0$), although there is not an exact cancellation at $\bar{u} = \bar{b}$ as in Rädler *et al.* 2003).

The α effects arising through stratification and inhomogeneity also show broad agreement with previous works. Because of the linearity of the expansion in $\nabla \ln \rho$, U , and Ω , the density stratification contributes very little to the coefficients, aside from directly through ∇W_m [Eq. (6.27)]. This means χ_ρ generally appears together with the turbulent gradient $\chi_{\bar{u}}$. The one exception to this is the “turbulent diamagnetism” term, $\gamma^{(0)}$, which interestingly depends only on the turbulence gradient, not the density gradient, due to a cancellation (this is in agreement with Kichatinov and Rüdiger 1992). Again results without mean velocity broadly agree with the spectral τ approximation magnetic turbulence results given in Rädler *et al.* (2003); for instance, the fact that $(\gamma^0)_b = -(\gamma^0)_u$ and the opposing signs of the rotational kinematic and magnetic diagonal α effects $(\alpha_1^\Omega)_{u,b}$, with $|(\alpha_1^\Omega)_u| > |(\alpha_1^\Omega)_b|$ (although one sees a strong dependence of these parameters on Pm ; see Sec. 6.4).

6.3 Specific results for unstratified shear dynamos

In this section I discuss the results pertinent to our primary motivation for this work, the shear dynamo in a Cartesian box. As shown in Eq. (6.8), in this geometry with a horizontal mean-field average, the number of transport coefficients is significantly lower than the general case. As in previous chapters, the sign of the η_{yx} coefficient is particularly interesting because of its importance for dynamo growth due to its coupling with the shear [Eq. (6.9)]. Here I outline the contribution to η_{yx} from velocity and magnetic fluctuations in the presence of shear, both with and without rotation. This geometry is particularly relevant for the unstratified MRI, in which there is strong flow shear, stratification may be subdominant, and there is no source of net helicity in either velocity or magnetic fluctuations.

Utilizing Eq. (6.10) and the results in listed in App. D.2, one obtains, after some impressive cancellations,

$$(\eta_{yx})_u^S = \int d\omega dk \frac{32\pi k^2 W_u(k, \omega) \omega^2 \tilde{\eta}^2}{15 (\tilde{\eta}^2 + \omega^2)^2 (\tilde{\nu}^2 + \omega^2)}, \quad (6.33a)$$

$$\begin{aligned} (\eta_{yx})_b^S = \int d\omega dk 8\pi k^2 \rho^{-1} W_b(k, \omega) & \left(\frac{4\omega^4}{15 (\tilde{\nu}^2 + \omega^2)^3} \right. \\ & - \frac{2\tilde{\eta}\tilde{\nu}^3 + \tilde{\eta}^2\tilde{\nu}^2 + 2\omega^2\tilde{\eta}^2 + 3\omega^4}{15 (\tilde{\eta}^2 + \omega^2) (\tilde{\nu}^2 + \omega^2)^2} \\ & \left. + \frac{4\omega^2\tilde{\eta}\tilde{\nu}}{15 (\tilde{\eta}^2 + \omega^2)^2 (\tilde{\nu}^2 + \omega^2)} \right), \end{aligned} \quad (6.33b)$$

$$(\eta_{yx})_u^\Omega = - \int d\omega dk \frac{64\pi k^2 W_u(k, \omega) \omega^2 \tilde{\eta}^2}{15 (\tilde{\eta}^2 + \omega^2)^2 (\tilde{\nu}^2 + \omega^2)}, \quad (6.33c)$$

$$(\eta_{yx})_b^\Omega = - \int d\omega dk \frac{8\pi k^2 \rho^{-1} W_b(k, \omega) (\tilde{\nu}^4 - 12\omega^2\tilde{\nu}^2 + 3\omega^4)}{15 (\tilde{\nu}^2 + \omega^2)^3}. \quad (6.33d)$$

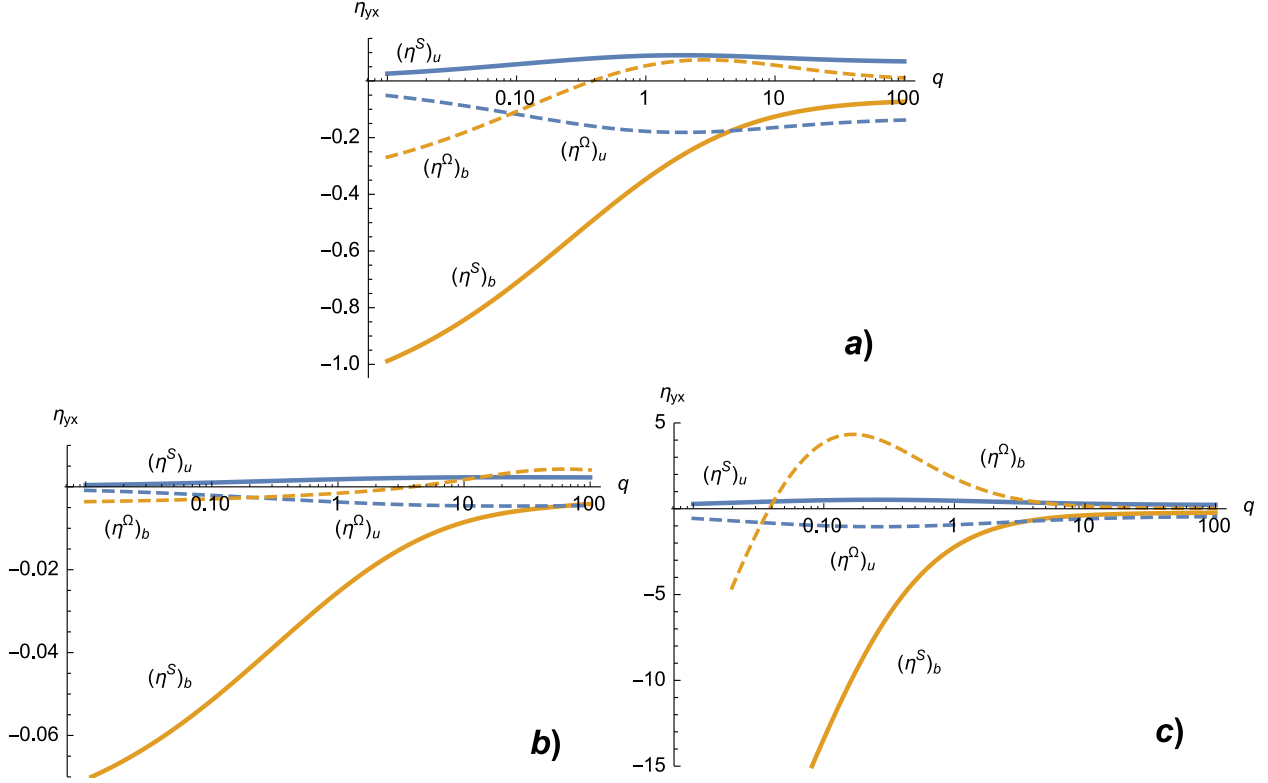


Figure 6.1: Transport coefficients $(\eta_{yx})_u^S$ (solid, blue), $(\eta_{yx})_u^\Omega$ (dashed, blue), $(\eta_{yx})_b^S$ (solid, orange) and $(\eta_{yx})_b^\Omega$ (dashed, orange) as a function of q for (a) $\text{Pm} = 1$, (b) $\text{Pm} = 10$, and (c) $\text{Pm} = 1/10$. Each coefficient has been calculated using the form given in Eq. 6.31 for W , and normalized by $(\beta^{(0)})_u$ with the magnetic diffusion time, $\lambda_c^2/\bar{\eta}$, held constant (equivalently $\tau_c = 1/q$). (Note that this choice is necessary because the coefficients have different units, and is chosen purely for plotting purposes, since it reduces the variation of coefficients with q .)

Here $\tilde{\nu} = \bar{\nu}k^2$, $\tilde{\eta} = \bar{\eta}k^2$, integration over ω is from $-\infty$ to ∞ , and integration over k is from 0 to ∞ . I have defined each coefficient such that

$$\eta_{yx} = S [(\eta_{yx})_u^S + (\eta_{yx})_b^S] + \Omega [(\eta_{yx})_u^\Omega + (\eta_{yx})_b^\Omega], \quad (6.34)$$

to keep all signs consistent. Recall from Eq. (6.9) that with my definition of S , $\eta_{yx}S < 0$ is required for a growing dynamo (note that this is the reverse of RS06). Since vorticity and rotation are opposite (i.e., anticyclonic) when S and Ω have the same sign, for Keplerian rotation $\Omega = 2S/3$.

Let us first examine the coefficients for a kinematic dynamo, i.e., one with strong homogenous velocity fluctuations [the coefficients $(\eta_{yx})_u$, Eqs. (6.33a) and (6.33c)]. Firstly, note that the contributions from S and Ω have identical forms, and that the integrands are positive definite,⁸ see Fig. 6.1. Thus, as is well known, one sees that $(\eta_{yx})_u^S$, the “shear-current effect,” has the incorrect sign for dynamo action within this quasi-linear approximation. Although the basic $\Omega \times \mathbf{J}$ effect (also known as the Rädler effect) is well known, the explicit calculation of transport coefficients including shear and rotation seems to have been mostly ignored, although there is discussion in early literature on the subject (see, for example, Krause and Rädler 1980 and Moffatt and Proctor 1982). Given the identical forms of Eqs. (6.33a) and (6.33c), one can immediately write down the result

$$(\eta_{yx})_u = (S - 2\Omega) \Xi, \quad (6.35)$$

where Ξ is the (positive) integral in Eq. (6.33a). Thus, one finds that the addition of Keplerian rotation ($\Omega = 2S/3$) (as relevant to turbulence in disks), will change the sign of η_{yx} to slightly negative and a coherent dynamo instability should be possible. Indeed, this is seen in the work in chapter 4 (in particular Fig. 4.4).

Turning to the coefficients for magnetic fluctuations I analytically confirm the conclusions of chapters 4 and 5 that a magnetically driven dynamo is possible. In particular, as shown in App. D.3 and Fig. 6.1, the coefficient $(\eta_{yx})_b$ is consistently negative and generally larger than the other contributions, in particular $(\eta_{yx})_u^S$. This implies that a dynamo can be excited by magnetic fluctuations, themselves presumably arising from a small-scale dynamo process, or perhaps an MHD instability of some sort. The addition of rotation renders the effect of magnetic fluctuations more complex, and no simple result seems possible. In particular, the sign of the $(\eta_{yx})_b^\Omega$ coefficient depends on the

⁸The result for $(\eta_{yx})_u^S$ is different to RS06, in particular only containing the first part of their Eq. (D5), and I am currently unsure from where this discrepancy arises (it is not related to the addition of magnetic fluctuations). There is one difference in the full transport coefficients (in the $\beta^{(D)}$ term; see App. D.2), but this difference alone does not fix the discrepancy. In any case, the main conclusion – that $(\eta_{yx})_u^S$ has the incorrect sign for dynamo action – is unchanged. Our expressions for $(\eta_{yx})_u^\Omega$ are identical.

parameters, and is generally negative for large $\bar{\nu}$ and $\bar{\eta}$ and positive at lower dissipation, although smaller in magnitude than $(\eta_{yx})_b^S$. However, given that the quasi-linear approximation becomes less valid in this limit, it would be unwise to draw any conclusions about the high-Rm limit from this behavior.

6.4 Specific results for stratified accretion disks

In this section I briefly outline how the general results apply to stratified sheared rotating turbulence. The primary motivation is the upper and lower regions of accretion disks, where the turbulence is stratified in density and intensity by the vertical gravity, perpendicular to the velocity shear. Self-sustaining turbulence simulations in this geometry (for instance with shear-periodic boundary conditions in the radial direction) exhibit a very coherent dynamo, with quasi-time-periodic behavior in B_y and B_x creating a “butterfly diagram” (Brandenburg *et al.* 1995; Gressel 2010; see also chapter 1). Large-scale magnetic structures are seen to emanate from the central portion of the disk, migrating upwards into the lower-density regions and becoming more intense as they do so (Simon *et al.*, 2012). This migration behavior would be characteristic of a dynamo driven by α_{yy} above and below the mid-plane; as shown in Eq. (6.12), growth of this type of “ $\alpha\omega$ ” dynamo is always accompanied by dynamo waves since Γ is complex. Note that a negative imaginary part of Γ is required for upwards migration of mean-field structures with $\hat{\mathbf{g}} = \hat{\mathbf{z}}$. This occurs for $a_{yy} < 0$ and $a_{xy} < 0$, ($a_{yx} > 0$) (Rüdiger and Pipin, 2000).

Utilizing Eq. (6.13) with the results listed in App. D.2, and setting Pm = 1 here for simplicity, one obtains

$$(a_{yy})_u^S = 8\pi\chi_{\rho\bar{u}} \int d\omega dk \frac{k^2 W_u(k, u) \tilde{\nu}^2 (5\tilde{\nu}^2 + \omega^2)}{15 (\tilde{\nu}^2 + \omega^2)^3}, \quad (6.36a)$$

$$(a_{yy})_b^S = -4\pi\chi_{\bar{b}} \int d\omega dk \rho^{-1} W_b(k, u) k^2 \frac{7\tilde{\nu}^4 - 4\omega^2 \tilde{\nu}^2 - 3\omega^4}{15 (\tilde{\nu}^2 + \omega^2)^3}, \quad (6.36b)$$

$$(a_{yy})_u^\Omega = -64\pi\chi_{\rho\bar{u}} \int d\omega dk \frac{k^2 W_u(k, u) \tilde{\nu}^2 (\tilde{\nu}^2 + 5\omega^2)}{15 (\tilde{\nu}^2 + \omega^2)^3}, \quad (6.36c)$$

$$(a_{yy})_b^\Omega = -64\pi\chi_{\bar{b}} \int d\omega dk \frac{\rho^{-1} W_b(k, u) k^2 \omega^2 (\omega^2 - 3\tilde{\nu}^2)}{15 (\tilde{\nu}^2 + \omega^2)^3}. \quad (6.36d)$$

Finally, for the off-diagonal component, $\gamma^{(0)} = a_{xy} = -a_{yx}$, one has

$$(\gamma^{(0)})_u = 4\pi\chi_{\bar{u}} \int d\omega dk \frac{k^2 W_u(k, u) \tilde{\eta}}{3 (\tilde{\eta}^2 + \omega^2)}, \quad (6.37a)$$

$$(\gamma^{(0)})_b = -4\pi\chi_{\bar{b}} \int d\omega dk \frac{k^2 \rho^{-1} W_b(k, u) \tilde{\eta}}{3 (\tilde{\eta}^2 + \omega^2)}. \quad (6.37b)$$

Here I use the notation $\chi_{\rho\bar{u}} = |\nabla \ln(\rho\bar{u})|$, and again signs are defined such that

$$a_{yy} = S [(a_{yy})_u^S + (a_{yy})_b^S] + \Omega [(a_{yy})_u^\Omega + (a_{yy})_b^\Omega], \quad (6.38)$$

with $\Omega > 0$ for anticyclonic rotation.

It is first worth noting the sign of each coefficient given in Eqs. (6.36a)-(6.37b). With $\chi_{\rho\bar{u}}, \chi_{\bar{b}} > 0$ it can be shown easily from the above expressions that

$$(a_{yy})_u^S > 0, \quad (a_{yy})_b^S < 0, \quad (a_{yy})_u^\Omega < 0, \quad (a_{yy})_b^\Omega > 0. \quad (6.39)$$

(Note that for the b components, it is necessary to integrate by parts over ω ; see App. D.3). The relations in Eq. (6.39) appear to also hold for $Pm \neq 1$ (although I have a proof of this only for the Ω coefficients). This consistent difference in sign between contributions is rather inconvenient for the application of SOCA results to stratified accretion disks. Since one expects $\chi_{\rho\bar{u}} < 0$ and $\chi_{\bar{b}} < 0$ (although possibly $\chi_{\bar{u}} > 0$) (Gressel, 2010; Bodo *et al.*, 2014), we are left with the situation where not only do the α effects due to u and b partially cancel, but also those due to rotation and velocity shear! Furthermore, as shown in Fig. 6.2, the relative contribution of each depends strongly on Pm . In particular, we see a dominance of $(a_{yy})_u$ over $(a_{yy})_b$ for $Pm \gtrsim 1$, but

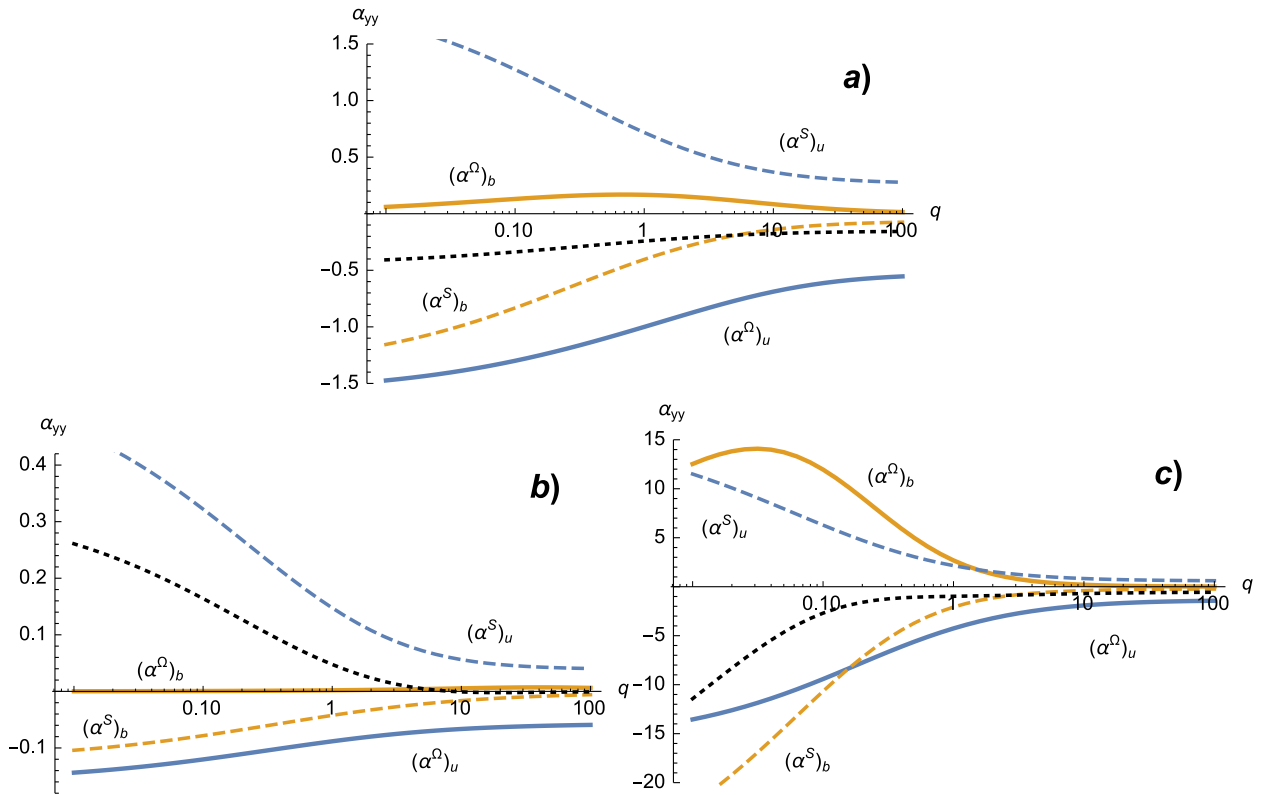


Figure 6.2: Transport coefficients $(a_{yy})_u^{\Omega}$ (solid, blue), $(a_{yy})_u^S$ (dashed, blue), $(a_{yy})_b^{\Omega}$ (solid, orange) and $(a_{yy})_b^S$ (dashed, orange) as a function of q for (a) $Pm = 1$, (b) $Pm = 10$, and (c) $Pm = 1/10$. Each coefficient is calculated using the form given in Eq. 6.31 for W , and normalized by $(\beta^{(0)})_u$ with the magnetic diffusion time, $\lambda_c^2/\bar{\eta}$, held constant (equivalently $\tau_c = 1/q$). The dotted (black) curve in each plot shows the total a_{yy} with equal kinetic and magnetic turbulence levels for Keplerian rotation, $\Omega = 2/3S$ [Eq. (6.38)], to illustrate the variability in these predictions.

this can reverse at low P_m . Similarly, the relative contributions due to velocity shear and rotation for the magnetic effect vary substantially with P_m , although the effect of shear seems generally more substantial. While the ratio of kinematic shear and rotation contributions may be somewhat more robust, the two are roughly equal in magnitude, $(a_{yy})_u^S \sim -(a_{yy})_u^\Omega$, and will approximately cancel for Keplerian rotation. Finally, it is worth noting that to complement these uncertainties, the signs of $\gamma^{(0)}$ seem to predict the *opposite* field migration pattern to the upwards transport seen in simulation. In particular, for $\chi_{\bar{b}} < 0$ and $\chi_{\bar{u}} > 0$, the kinematic and magnetic contributions both enforce $\gamma^{(0)} > 0$, leading to $\text{Im}\Gamma > 0$. However, in the use of the anelastic approximation, buoyancy effects are not included, although these would be expected to change this aspect of the calculation substantially (Kichatinov and Pipin, 1993; Rüdiger and Pipin, 2000), potentially even through large-scale instability (Rozyczka *et al.*, 1995).

Where does this leave us for understanding the dynamo in stratified accretion disks? We see that claims that SOCA predictions are *incorrect* for the stratified regions of accretion disks are unfounded. More accurately, one could say that SOCA predictions themselves are completely inconclusive, even in the kinematic regime, since each contribution – kinematic, magnetic, rotation, and velocity shear – has a tendency to cancel its partner. Such uncertainty seems at odds with the robust dynamo “butterfly diagram” seen across a wide variety accretion disk of simulations.

Of course, one possibility is that the SOCA calculation carried out here, keeping only the linear contributions due to Ω , S , and stratification, is not up to the task of calculating these coefficients, and in reality there *is* a robust α effect. For instance, in Rüdiger and Pipin (2000), the authors find that α_{yy} has the correct sign ($\alpha_{yy} < 0$) for magnetic fluctuations in a compressible turbulence model for Keplerian shear and moderate P_m [this is the sign opposite to that of Eq. (6.36b) but since their effect vanishes in the incompressible limit, one should have no reason to expect agreement]. While certainly a possibility, it would seem a little bizarre that a behavior that appears so robustly in simulation could show so much variability across different calculation methods or rely on nonlinear behavior of transport coefficients with Ω , S , or the stratification. A variety of other

possibilities might be imaginable, for instance a dynamo driven primarily by the magnetic shear-current effect up to relatively far from the mid-plane (Sec. 6.3), with upwards transport above this caused by a large-scale buoyancy instability (not included here due to the anelastic approximation). Another possibility could be that upwards field transport is caused by a small-scale magnetic helicity flux (Vishniac and Cho, 2001; Subramanian and Brandenburg, 2004) from the central shear-current dynamo causing a (helical) magnetic α effect. Such a process could look rather similar to a more standard α effect, although the basic cause of the dynamo would be entirely different (Gressel, 2010). I note that although the large-scale fields themselves are nonhelical, the $\mathcal{E} \cdot \mathbf{B}$ term driving the small-scale magnetic helicity (see Sec. 1.2) would lead to a magnetic α effect that could cause growth of the large-scale on the edges of the stratified region, potentially causing a butterfly pattern if this small-scale helicity was transported upwards. Note that magnetic helicity fluxes have been found to be important in unstratified global MRI turbulence (Ebrahimi and Bhattacharjee, 2014). Overall however, it seems that the underlying cause for the “butterfly diagram” in stratified disks remains unclear and more work will be needed to arrive at robust mean-field models of the process.

6.5 Discussion and conclusions

This chapter serves as an analytical confirmation of the results presented in the previous two chapters. Using perturbative calculations within the second-order correlation approximation, the EMF has been theoretically calculated in systems with mean velocity gradients, rotation, net helicity, and stratification. In addition to the standard kinematic dynamo, I include the possibility of a dynamo driven by small-scale *magnetic fluctuations*, as might arise from the small-scale dynamo or an instability. The main finding, in agreement with chapters 4 and 5, is that an off-diagonal resistivity coupled to the shear can cause a dynamo instability in the presence of magnetic fluctuations. As discussed, the potential importance of this effect lies in the interesting possibility of the small-

scale dynamo *enhancing* the growth of a large-scale field, as studied numerically in chapter 5. In some sense, this is the reverse of large-scale quenching (Kulsrud and Anderson, 1992; Blackman and Field, 2002); rather than the small-scale magnetic fluctuations inhibiting the large-scale field growth, they could actively aid field generation, with large-scale growth eventually halting due to nonlinear changes to the transport coefficients, possibly influenced by secondary quenching effects (Rogachevskii *et al.*, 2006).

Importantly, the prediction that the magnetic shear-current effect is able to excite a dynamo agrees with other transport coefficient calculation methods and simulations. In particular, the spectral τ approximation predicts the linear magnetic effect to be much stronger than the kinematic effect (see Fig. 3 of Rogachevskii and Kleeorin 2004), just as was found in this work using SOCA (Fig. 6.1). In addition, agreement is found with shear quasi-linear calculations (chapter 4, which is the magnetic version of the calculations in Singh and Sridhar 2011), as well as perturbative inhomogeneous shearing-wave calculations (Lesur and Ogilvie, 2008a). This suggests that the effect may be more robust than the kinematic shear-current effect and/or have less dependence on Reynolds numbers.

The work presented in this chapter was motivated primarily by improving understanding of the fundamental dynamo mechanisms in accretion disks. Consistent with the idea that two dynamo mechanisms might operate in disks (Blackman and Tan, 2004), their inner regions seem well suited to be explained by the magnetic shear current effect (Lesur and Ogilvie, 2008b) – magnetic fluctuations are generally stronger than kinetic fluctuations, rotation has the correct sign to enhance the kinematic dynamo, and the turbulence is essentially unstratified and nonhelical. All results discussed in Sec. 6.3 for the low- R_m regime have been confirmed numerically in chapter 4. Firstly, we observed the predicted qualitative change in the kinematic dynamo with the addition of rotation, due to the change in sign of the η_{yx} transport coefficient. Secondly, we observed the magnetically driven shear-current effect, both through direct driving of the induction equation (chapter 4), and at higher magnetic Reynolds number where magnetic fluctuations arise self-consistently though ex-

citation of a small-scale dynamo (chapter 5). The nonlinear saturation of these magnetically driven large-scale dynamos exhibits a pleasing resemblance to self-sustaining unstratified accretion disk turbulence simulations, with quasi-cyclic behavior of the large-scale B_y field.

Less clear have been our findings regarding the α effect as relevant to the stratified regions of accretion disks. In particular, α coefficients arising from rotation and shear, and those arising from kinetic and magnetic fluctuations, are each of opposite signs for anticyclonic rotation (Ω and $\nabla \times U$ antiparallel), and thus would tend to cancel. Furthermore, predictions about which of these terms dominate (thus determining the sign of the total α effect), depend strongly on the magnetic Prandtl number and the relative levels of kinetic and magnetic turbulence. I thus conclude that perturbative SOCA calculations *give no useful predictions* regarding the primary driver of the so-called “butterfly diagram” pattern of large-scale field evolution seen in self-sustaining stratified accretion disk simulations. Whether this is simply due to the inaccuracies of SOCA, or there is some other more exotic effect operating, remains to be seen.

Chapter 7

Conclusions and outlook

In this conclusion chapter, I briefly restate the central results of this thesis and consider possibilities for future work. The discussion is deliberately intended to be succinct, since conclusions are given at the end of each chapter separately. I refer the reader to Sec. 1.3 of the introduction for a more comprehensive overview of each chapter and their interrelation.

Much of the work in this thesis has revolved around exploration of the “magnetic shear-current” as a viable mechanism to drive large-scale dynamos in nonhelical shear flows. The effect is based on an off-diagonal turbulent resistivity η_{yx} , which enables the generation of radial magnetic fields from azimuthal fields. When coupled with the large-scale velocity shear (which generates azimuthal fields from radial fields), large dynamo instability can result if η_{yx} is of the required sign and sufficiently large (chapter 4). However, the magnetic shear-current effect is appealing not so much for this field generation mechanism, but because it raises the interesting possibility that the saturated state of the small-scale dynamo may *drive* large-scale field generation. Such behavior is in stark contrast to standard α -quenching theory, in which the small-scale magnetic field, growing over very short timescales, quenches large-scale field growth by canceling out the kinematic α effect. The dire predications that accompany such a cancellation have caused some researchers to question whether mean-field theory can reasonably explain large-scale field generation at all (Kul-

srud and Anderson, 1992; Cattaneo and Hughes, 2009). The magnetic shear-current effect is, in some sense, the *reverse* of this dynamo quenching: as the small-scale dynamo grows and saturates, creating a turbulent bath of magnetic fluctuations, large-scale dynamo action is enhanced rather than impaired (as shown numerically in chapter 5), with dynamo saturation arising later through nonlinear changes to the transport coefficients. Given the pervasive presence of large-scale shear flows in astrophysics, as well as the fact that the small-scale dynamo is always unstable above even moderate Reynolds numbers, the magnetic shear-current effect may turn out to have a significant impact on field generation across a wide variety of astrophysical objects.

In the introduction, I stated that one of our primary motivations was to improve understanding of the MRI dynamo. What has been achieved towards this goal? The magnetic shear-current effect seems highly plausible as a dynamo mechanism in the inner unstratified regions of accretion disks: simulations show that the turbulence has a strong magnetic component, and the Keplerian rotation is favorable for enhancing the kinematic contribution to the dynamo (chapter 4). In addition, there are a number of other indications that this is indeed the case. Firstly, from driven direct numerical simulation, we see that the nonlinear saturation of the magnetic shear-current effect can show cyclic behavior, with some resemblance to dynamo cycles in self-sustaining MRI turbulence (chapters 4 and 5). Secondly, the importance of the η_{yx} transport coefficient has been concluded previously from self-sustaining DNS (Lesur and Ogilvie, 2008b) (our suggestions are in some sense an extension of the dynamo proposed in that work to formal dynamo theory). Thirdly, the most significant observation is the similarity of the saturated state of CE2 calculations to MRI turbulence, in particular the strong dependence on magnetic Prandtl number (chapter 3). Since the magnetic shear-current effect is the *only* possible dynamo mechanism in these statistical calculations – incoherent effects are necessarily excluded completely and the kinematic shear-current effect is too weak – one is led to the conclusion that self-sustaining turbulence is likely to be also strongly influenced by this dynamo. Thus, as one of the central conclusions of this thesis, I would

tentatively state that the magnetic shear-current effect is the primary driver of the dynamo near the mid-plane of ionized accretion disks.

In addition to the magnetic shear-current effect, a number of subsidiary results have been presented. The most important of these, listed in their order of appearance, include:

The relationship between local and global linear MRI (chapter 2) – Through the use of non-modal stability theory, I have explicitly shown the connection between global eigenmodes and the local shearing box for both axisymmetric and non-axisymmetric modes. This illustrates that, in many cases, local stability approaches will be *more* relevant than global eigenmodes since the nonmodal structures can grow many orders of magnitude before the eigenmode predictions eventually become important. Thus we see that, from the linear standpoint, shearing box boundary conditions are a very natural choice for the study of the MRI. In addition, the nonmodal approach clarifies that the strong dependence of global non-axisymmetric eigenmodes on the chosen boundary conditions should not be a cause for concern, since shearing wave structures generically appear independently of this choice.

Fast linear MRI growth over all scales (chapter 2) – Over short timescales, all shearing wave MRI modes (k_y, k_z) grow at the same rate, which is the growth rate of the most unstable MRI eigenmode ($\gamma_{\text{MRI}} = q/2$). The contrast between this result and eigenmode predictions illustrates the importance of choosing a relevant timescale when evaluating the linear contribution to MRI turbulence, and suggests that linear drive could be important in turbulence over a wide range of scales, even when a number of spectrally unstable modes are present. In addition, a comparison between the growth of static structures and shearing waves gives some justification for why shearing waves are generically seen in the spatially dependent nonmodal calculations.

Prandtl number dependence of the saturated large-scale MRI dynamo (chapter 3) – Despite the very significant approximations in the derivation of the quasi-linear model, the saturated

state of the MRI dynamo bears a strong resemblance to nonlinear MRI turbulence. Most interesting is the non-intuitive dependence on P_m : at fixed magnetic dissipation, as the fluid dissipation is increased, the level of turbulence increases. The prevalence of this trend in the quasi-linear model illustrates the fundamental importance of the large-scale dynamo for this scaling in MRI turbulence. We have seen that the basic aspects of the trend can be explained through consideration of the electromotive force as a function of mean-field strength, so long as the effect of the radial magnetic field on the fluctuations is included. This can be seen as a simple extension to the model of Lesur and Ogilvie (2008a,b).

The importance of rotation for kinematic shear dynamos (chapter 4) – It has been shown conclusively that the low-Reynolds-number shear dynamos presented in Yousef *et al.* (2008a,b) are primarily driven by the stochastic- α effect. This mechanism involves temporal fluctuations in the dynamo α coefficient about zero, and is essentially that suggested by Vishniac and Brandenburg (1997) and Heinemann *et al.* (2011). However, rotation can qualitatively alter this dynamo (despite statements to the contrary in Yousef *et al.* 2008a), increasing its coherency and growth rate through the $\Omega \times \mathbf{J}$ effect (Krause and Rädler, 1980). This conclusion is completely compatible with the results of Yousef *et al.* (2008a,b), and nicely explains aspects of their measured growth rates.

The α effect in the stratified regions of accretion disks (chapter 6) – The lack of homogeneity in the stratified regions of disks enables a coherent α effect, which one might expect to be responsible for the upwards field migration and amplification seen in stratified MRI turbulence simulations (the “butterfly diagram”). However, using analytic calculations within the second-order correlation approximation (SOCA) it was shown that the four possible α effects – arising from combinations of shear and rotation, and kinetic and magnetic fluctuations – have the tendency to cancel each other. Furthermore, the prediction for which effect should dominate, thus determining the overall sign, depends strongly on P_m and the relative levels

of homogenous kinetic and magnetic fluctuations. We thus conclude that SOCA can make no prediction regarding the α effect in stratified regions of disks. While the inconclusive nature of this result may simply be related to inaccuracies in SOCA, it seems more likely that a fundamentally different mechanism is proving important in the stratified dynamo, for instance a large-scale buoyancy instability or fluxes of magnetic helicity.

Throughout the aforementioned studies, a variety of interesting and novel techniques have been applied to understanding the shear-current dynamo and MRI turbulence. Most notable are the statistical methods: direct statistical simulation (CE2), and the study of mean-field statistics using ensembles of direct numerical simulations. Given the inherent resolution limitations of simulations on even the most powerful computers, the extra information afforded by such methods – in particular in measurement accuracy – may prove critical in extrapolating results to regimes of high Reynolds numbers (Rempel *et al.*, 2010).

7.1 Outlook

Inevitably, a wide variety of questions have been left unanswered in this work. Here I outline a handful of those that I consider to be the most important, referring the reader to the conclusions of each chapter for more thorough discussion.

The magnetic shear-current effect at high Reynolds numbers – While I have given evidence for the excitation of the large-scale fields by the small-scale dynamo, the fate of such an effect at higher R_m remains entirely uncertain. Two effects may be important here: the first, a change of the transport coefficient with R_m for a given level of \mathbf{b}_0 fluctuations; the second, a change in the intensity of the small-scale dynamo with R_m and P_m . Understanding each of these in sufficient detail to extrapolate to astrophysical regimes is a very difficult problem, but is probably necessary to robustly assess the capacity of the magnetic shear-current effect

to drive large-scale dynamos in a variety of astrophysical scenarios (e.g., galactic dynamo, solar dynamo).

Nonlinear saturation of the magnetic shear-current effect – The saturation characteristics of the magnetic shear-current effect remain unclear, although a brief study was presented in chapter 3 (see also Rogachevskii and Kleeorin 2004). This saturation is likely to be fundamental to the cycles seen in unstratified nonlinear MRI simulations, and perhaps also to the time-dependent “butterfly diagram” seen in stratified disk simulations. Understanding the cause of the Prandtl number dependence of the saturation in more detail is of particular significance, since this appears to be fundamentally related to the similar dependence of MRI turbulence (chapter 3).

Self-sustaining MRI turbulence – The quasi-linear models cannot address the transition to self-sustaining turbulence due to the mean-field average. However, this transition, in particular its P_m dependence, is of fundamental importance for understanding MRI turbulence and its fate in astrophysically relevant regimes. A viable approach to tackle this problem may involve the use of the less restrictive azimuthal (rather than azimuthal and radial) average, as in Farrell and Ioannou (2012). This would enable quasi-linear “turbulence” to self-sustain in a highly simplified setting. Related to this, study of the transition to turbulence in hydrodynamic shear flows using the quasi-linear machinery could prove very rewarding. Of particular interest are the mechanisms that suppress subcritical transition as one moves away from the instability boundaries set by the Rayleigh criterion (Lesur and Longaretti, 2005).

The stratified MRI dynamo – The stratified MRI dynamo has been explored very little in this thesis, but is at least as important as the unstratified variety for formulating useful mean-field disk models (Blackman, 2012). The result in chapter 6 that there is no well-determined sign for the α effect is somewhat puzzling, and motivates study into other effects that could cause the rising patterns of field amplification seen in simulation. If indeed the central regions of

disks are primarily driven through the magnetic shear-current effect, it would be interesting to understand the cause of the significantly increased coherency in cycle periods after the addition of stratification (Simon *et al.*, 2012). Ideally, one might hope to formulate a simple one-dimensional mean-field model, containing only physically motivated effects, that could capture the differences and similarities between the stratified and unstratified MRI dynamos, and thus be used to construct observationally useful disk models that include the effects of self-consistent magnetic field generation.

Helicity effects in the MRI dynamo – Magnetic helicity and its transport are a cornerstone of modern dynamo theory (Brandenburg *et al.*, 2012) but have been explored very little in this thesis. Given that strong helicity fluxes have been found in unstratified global simulations (Ebrahimi and Bhattacharjee, 2014), it is critical to further explore these issues with both DNS and analytic models,¹ where analogies with previous work on “hyper-resistivity” in reversed field pinches may prove very helpful (Bhattacharjee and Hameiri, 1986; Boozer, 1986). In particular, vertical stratification is likely to be important since various additional contributions to the vertical helicity flux occur (Pipin, 2008), and these have yet not been systematically explored (to my knowledge). This subject is expected to be intimately related in various ways to the previous points on the saturation of the magnetic shear-current effect and the stratified MRI dynamo.

Extensions to the MHD model – The MHD model is far from accurate in many situations with low collisionality, and it is critical to understand how kinetic effects alter the fundamental physics. A simple approach that has been pursued in a variety of recent works, mostly related to protoplanetary disks, is to make modifications to the MHD induction equation. The most important effects include Hall MHD terms (Ebrahimi *et al.*, 2011; Kunz and Lesur, 2013), which are also fundamental for plasma experiments (Collins *et al.*, 2014), and am-

¹Some work has been done using toy analytic models for the shear-current effect, see Rogachevskii *et al.* 2006.

bipolar diffusion terms (Kunz and Balbus, 2004; Bai and Stone, 2013; Lesur *et al.*, 2014). Looking further, a fully kinetic description (Quataert *et al.*, 2015) may fundamentally alter the saturation characteristics of MRI turbulence. This subject is essentially unexplored at the present time due to the prodigious computational requirements, but will almost certainly become an important subfield in the future. Similarly, collisionless dynamos have hardly been studied, yet may contain a variety of interesting physics that diverges strongly from MHD predictions, with application across many astrophysical systems.

Of course, those subjects listed above only scratch the surface of interesting avenues for future work in this area.

Appendix A

Appendix: Nonmodal stability of the MRI

A.1 Global linear MHD equations

For reference, here I give the global linear MHD equations in the Orr-Sommerfeld variables [Eq. (2.17)], using the global equilibrium described in Sec. 2.3.1 (a Keplerian velocity profile has already been assumed). For simplicity, I have not included dissipation terms (i.e., set $\bar{\nu} = \bar{\eta} = 0$); these terms become very complex (especially with the $\bar{\nu}$ appearing in the background velocity profile) and the equilibrium is of mostly academic interest since compressibility is generally important in global domains. Note that when $\bar{\nu}$ and $\bar{\eta}$ are non-zero, derivatives up to fourth order in space appear in the equation for u . In practice, I derive these equations directly from the global nonlinear MHD equations [Eqs. (2.11)] in *Mathematica* and insert them directly into the Chebyshev eigenspectrum solver. It was found empirically that the global MHD equations in this form lead to a much cleaner numerical spectrum than in the original variables. This is very important for pseudo-mode calculations since a large number of eigenmodes are often needed to form an accurate pseudo-mode.

With $F \equiv mB_{0\theta} + k_z B_{0z}$, the equations are

$$\begin{aligned}
& \frac{\partial^3}{\partial t \partial r^2} u_r(r, t) + \frac{3m^2 + k_z^2 r^2}{r(m^2 + k_z^2 r^2)} \frac{\partial^2}{\partial t \partial r} u_r(r, t) + \left[\frac{m^2 - r^2 k_z^2}{r^2(m^2 + k_z^2 r^2)} - \left(\frac{m^2}{r^2} + k_z^2 \right) \right] \frac{\partial}{\partial t} u_r(r, t) \\
&= \frac{im}{r^{7/2}} \left(m^2 + k_z^2 r^2 - \frac{7m^2 + 3k_z^2 r^2}{4(m^2 + k_z^2 r^2)} \right) u_r(r, t) - \frac{im}{r^{5/2}} \frac{3m^2 + k_z^2 r^2}{m^2 + k_z^2 r^2} \frac{\partial}{\partial r} u_r(r, t) \\
&+ iF \left[\frac{(m^2 - k_z^2 r^2) + 4k_z^2 m r^2 B_{0\theta}/F}{r^2(m^2 + k_z^2 r^2)} - \left(k_z^2 + \frac{m^2}{r^2} \right) \right] B_r(r, t) + \frac{iF}{r} \frac{3m^2 + k_z^2 r^2}{m^2 + k_z^2 r^2} \frac{\partial}{\partial r} B_r(r, t) \\
&- \frac{im}{r^{3/2}} \frac{\partial^2}{\partial r^2} u_r(r, t) + iF \frac{\partial^2}{\partial r^2} B_r(r, t) - 2ik_z B_{0\theta} \eta(r, t) + \frac{2ik_z}{r^{3/2}} \zeta(r, t), \tag{A.1a}
\end{aligned}$$

$$\frac{\partial}{\partial t} \zeta(r, t) = iF \eta(r, t) + 2ik_z B_{0\theta} B_r(r, t) - \frac{ik_z}{2r^{3/2}} u_r(r, t) - \frac{im}{r^{3/2}} \zeta(r, t), \tag{A.1b}$$

$$\frac{\partial}{\partial t} B_r(r, t) = iF u_r(r, t) - \frac{im}{r^{3/2}} B_r(r, t), \tag{A.1c}$$

$$\frac{\partial}{\partial t} \eta(r, t) = -\frac{3ik_z}{2r^{3/2}} B_r(r, t) - iF \zeta(r, t) + \frac{im}{r^{3/2}} \eta(r, t). \tag{A.1d}$$

A.2 Conversion between global and shearing box equations

Here I outline the method used to obtain the shearing box parameters from global parameters at a chosen radius. The method is essentially that of Umurhan and Regev (2004) and involves non-dimensionalizing all variables and considering a small box centered at r_0 . Specifically, insert

$$r = r_0 (1 + \delta x) \tag{A.2}$$

into the global equations [Eqs. (A.1) including dissipation], where δ represents the size of the box compared to r_0 and x is the radial co-ordinate of the shearing box. Then, non-dimensionalize each variable according to the length scale δr_0 and the time-scale $r_0^{3/2}$; that is,

$$\begin{aligned} u_r &= \tilde{u}_r \frac{\delta}{r_0}, \quad B_r = \tilde{B}_r \frac{\delta}{r_0}, \quad \zeta = \tilde{\zeta} \frac{1}{r_0^{3/2}}, \quad \eta = \tilde{\eta} \frac{1}{r_0^{3/2}}, \quad k_z = \tilde{k}_z \frac{1}{r_0 \delta}, \quad m = \tilde{m} \frac{1}{\delta}, \\ B_{0z} &= \tilde{B}_{0z} \frac{\delta}{r_0}, \quad B_{0\theta} = \tilde{B}_{0\theta} \frac{\delta}{r_0^{3/2}}, \quad \bar{v} = \tilde{v} \delta^2 \sqrt{r_0}, \quad \bar{\eta} = \tilde{\eta} \delta^2 \sqrt{r_0}, \end{aligned} \quad (\text{A.3})$$

where the $\tilde{\cdot}$ indicates a non-dimensionalized quantity. Removing the background flow using

$$\frac{\partial}{\partial t} \rightarrow \frac{\partial}{\partial t} - i \frac{\mathbf{u}_0(r_0) m}{r_0 \delta}, \quad (\text{A.4})$$

and performing a series expansion in δ to first order, one obtains – after a substantial amount of algebra – the shearing box equations Eqs. (2.20).

This link between the global and local equations leads to a straightforward method for obtaining the relevant shearing box parameters at r_0 . With δ a necessary choice (representing the size of the shearing box in comparison to the radius), the local parameters are given by

$$\begin{aligned} k_y &= (m)_G \delta, \quad k_z = (k_z)_G \delta r_0, \quad B_{0z} = (B_{0z})_G \frac{\sqrt{r_0}}{\delta}, \\ B_{0y} &= (B_{0\theta})_G \frac{r_0^{3/2}}{\delta}, \quad \bar{v} = (\bar{v})_G \frac{1}{\delta^2 \sqrt{r_0}}, \quad \bar{\eta} = (\bar{\eta})_G \frac{1}{\delta^2 \sqrt{r_0}}, \end{aligned} \quad (\text{A.5})$$

where $(\cdot)_G$ represents a global quantity. It is also necessary to rescale time by a factor of $1/r_0^{3/2}$. As it transpires, the shearing wave equations are invariant under a rescaling by δ in exactly the way it appears in Eqs. (A.5), meaning the choice of δ is irrelevant and we can set it to 1 for simplicity.

A.3 Does the shearing box possess Floquet eigenmodes?

In the standard view prevalent in most of the MRI literature, non-axisymmetric eigenmodes are possible (and important) in global domains because of the time independence of the system, while the shearing box is limited to shearing-wave solutions since these are all that can be supported by the boundary conditions. The main purpose of chapter 2 has been to argue against the former point – while eigenmodes certainly exist, they may not be more important than localized shearing-wave solutions. In this appendix, I argue against the latter point; that eigenmode-like solutions should not exist for the shearing box. Indeed, the shearing box is a time-periodic system with period $T_{\text{SB}} = L_y / (qL_x)$, and thus one should expect eigenmodes of the *Floquet* type; that is solutions of the form,

$$U(\mathbf{x}, t) = U_P(\mathbf{x}, t) e^{\gamma t}. \quad (\text{A.6})$$

Here U represents all variables of the solution, $U_P(\mathbf{x}, t)$ is a T_{SB} periodic function in time, and γ a complex number. Such solutions are probably of no particular physical significance; however, the idea provides a nice closure to the discussion in chapter 2 (eigenmodes are usually considered in global domains, but shearing waves may be important; shearing waves are usually considered in the shearing box, but eigenmodes may be found). Note that Floquet theory fits seamlessly into the framework of nonmodal stability theory, as outlined in Schmid (2007), Sec. 3.3.

Consider the linear shearing-box system, written in the symbolic form

$$\partial_t U(t) = \mathcal{A}(t) U(t) \quad (\text{A.7})$$

where the operator $\mathcal{A}(t)$ satisfies, $\mathcal{A}(t) = \mathcal{A}(t + T_{\text{SB}})$. Floquet's theorem says that the fundamental solution matrix,

$$\partial_t \Phi(t) = \mathcal{A}(t) \Phi(t), \quad \Phi(0) = I \quad (\text{A.8})$$

can be written in the form

$$\Phi(t) = P(t) e^{Bt}, \quad (\text{A.9})$$

where $P(t)$ is periodic in time with the same period as $\mathcal{A}(t)$. Then, with coordinate change $U = P(t) \tilde{U}$, the system becomes

$$\partial_t \tilde{U} = B \tilde{U} \quad (\text{A.10})$$

for time-independent B , implying the existence of solutions to the original system of the form

$$U(t) = P(t) V_i e^{\gamma_i t} \quad (\text{A.11})$$

where γ_i and V_i are the eigenvalues and eigenvectors of the B matrix.

There are caveats to the above argument. Most importantly, for B to exist, the fundamental solution matrix $\Phi(t)$ must be invertible, since $e^{BT_{\text{SB}}} = \Phi(T_{\text{SB}})$. The steps leading to Eq. (A.10) also require the invertibility of $P(t)$, but this is implied by the invertibility of $\Phi(t)$. Thus we are left with the question: is $\Phi(t)$ invertible? In general, there is no obvious reason that it should not be; however, $\Phi(t)$ is not invertible in the special case in which \mathcal{A} is discretized using a finite number of Fourier modes. The reason is that the shearing wave,

$$U(x, t) = U(t) e^{iqk_y(t-t_0)x}, \quad (\text{A.12})$$

is an exact solution to the shearing box system Eq. (A.7). More precisely, the initial condition $U(0) = e^{ik_{x, \text{max}}x} = (0, 0, 0, \dots, 0, 1)$ evolves to $U(T_{\text{SB}}) = e^{i(k_{x, \text{max}} + 2\pi/L_x)x}$ by $t = T_{\text{SB}}$, which can obviously not be represented in any way by the finite number of Fourier modes. This leads to a singular matrix $\Phi(T_{\text{SB}})$. Nonetheless, this is a rather specific case due to the fact that a Fourier mode is advected to an another exact Fourier mode by $t = T_{\text{SB}}$, and it seems that a different discretization should allow a set of Floquet eigenmodes to be constructed (although perhaps this

would be numerically challenging since the fundamental solution matrices are likely to be close to singular). Presumably this could work with a finite-difference discretization (such as used in nonlinear shearing-box codes; see for example, Balbus and Hawley 1998), or by using a Chebyshev discretization in x . Since this seems to be a relatively substantial effort for a rather esoteric problem, I have not carried out such a calculation.

As some proof of principle that such solutions might exist, for the ideal hydrodynamic shearing box without rotation it is straightforward to construct special case Floquet solutions with purely imaginary γ . The equations of the system are

$$(\partial_x^2 + \partial_y^2 + \partial_z^2) \partial_t u = -iqx \partial_y (\partial_x^2 + \partial_y^2 + \partial_z^2) u, \quad (\text{A.13a})$$

$$\partial_t \zeta = iq \partial_z u - iqx \partial_y \zeta. \quad (\text{A.13b})$$

This has an exact shearing-wave solution

$$u_{n_x}(x, y, t) = \frac{e^{i\alpha y} e^{iq\alpha x t} e^{in_x k_{x0} x}}{\alpha^2 + (q\alpha t + n_x k_{x0})^2}, \quad \zeta = 0, \quad (\text{A.14})$$

for u with no z dependence and $k_{x0} = 2\pi/L_x$. Since these solutions decay to 0 sufficiently rapidly at $t = \pm\infty$, one can form the infinite sum of these shear waves separated in time by $T_{\text{SB}} = L_y / (qk_y L_x)$, to obtain a time-periodic solution satisfying the shearing-box boundary conditions,

$$u(\mathbf{x}, t) = \sum_{n_x=-\infty}^{\infty} \sigma^{n_x} u_{n_x}(\mathbf{x}, t), \quad (\text{A.15})$$

where σ is some complex number with $|\sigma| = 1$ that allows for $\gamma = i\omega$ (rather than $\gamma = 0$). Interestingly, this sum can be evaluated exactly in closed form in terms of β -functions and leads to a solution with a discontinuous derivative (the position of which depends on the phase factor σ – it is zero for $\sigma = 1$). While this discontinuity may be a little worrisome, eigenmodes of time-

independent fluid systems often develop discontinuities in the ideal limit, so this does not seem to constitute an obvious reason for discounting the solution.

Obviously, such a solution is of a very specific form, and its method of construction is not easily generalized to other cases; nonetheless, it does at least illustrate that such solutions can exist, and the presence of purely imaginary eigenvalues is expected in the ideal hydrodynamic case. Without calculating such solutions for the more complicated rotating MHD system, it is not clear how such modes would look, or whether unstable non-axisymmetric Floquet modes are possible. Given the presence of unstable non-axisymmetric modes when hard-wall boundaries are used (e.g., Fig. 2.3), there does not seem to be any *a-priori* reason to exclude the possibility. Interestingly in Brandenburg and Dintrans (2006) Fig. 4, the two highest-resolution runs appear to start growing exponentially towards the end of the calculation, which would be observed if a Floquet eigenmode were to start dominating. This could easily be a purely numerical effect however (for instance, aliasing of some form), and I do not mean to claim that this is credible evidence for the existence of unstable non-axisymmetric Floquet modes of the shearing box.

Appendix B

Appendix: The MRI dynamo

B.1 Derivation of the equation for $\mathcal{C}(t)$

In this appendix, I outline the derivation of the CE2 equation, Eq. (3.4b), governing the evolution of $\mathcal{C}(t)$ under the action of a linear operator $\mathcal{A}(t)$. I shall consider $\mathcal{A}(t)$ as given; any dependence on mean fields is subsumed within the operator's time dependence. More information can be found in Farrell and Ioannou (1993, 1994, 2003) and Tobias *et al.* (2011).

Consider the system

$$\partial_t u_i = \mathcal{A}_{ij}(t) u_j + \xi_i, \quad (\text{B.1})$$

where ξ is a driving noise. This equation could represent a suitably discretized form of the quasi-linear fluctuation equations. The solution is

$$u_i(t) = \int_0^t ds G_{ir}(t, s) \xi_r(s), \quad (\text{B.2})$$

where $G_{ir}(t, s)$ is the Green's function (in the case of time-independent \mathcal{A} , $G(t, s) = e^{\mathcal{A}(t-s)}$ for $t > s$ and 0 otherwise). We are interested in

$$C_{ij}(t) = \langle u_i(t) u_j^*(t) \rangle = \int_0^t ds \int_0^t ds' G_{ir}(t, s) G_{js}^*(t, s') \langle \xi_r(s) \xi_s^*(s') \rangle, \quad (\text{B.3})$$

which, using

$$\langle \xi_i(t) \xi_j^*(t') \rangle = Q_{ij}(t) \delta(t - t'), \quad (\text{B.4})$$

becomes

$$\int_0^t ds G_{ir}(t, s) G_{js}^*(t, s) Q_{ij}(s). \quad (\text{B.5})$$

We can then differentiate this in time to give

$$\begin{aligned} \partial_t C_{ij} &= \int_0^t ds \partial_t G_{ir}(t, s) G_{js}^*(t, s) Q_{ij}(s) \\ &\quad + \int_0^t ds G_{ir}(t, s) \partial_t G_{js}^*(t, s) Q_{ij}(s) + Q_{ij}(t) \\ &= (\mathcal{A}C + C\mathcal{A}^\dagger + Q)_{ij}, \end{aligned} \quad (\text{B.6})$$

using $\partial_t G_{ij}(t, s) = \mathcal{A}_{ir} G_{rj}(t, s)$ for $t > s$, and $G_{ij}(t, t) = \delta_{ij}$.

Appendix C

Appendix: Nonhelical shear dynamos

C.1 Stochastic- α shear dynamos: some notes on previously proposed mechanisms

There has been a wide variety of literature on stochastic- α dynamos in shear flows. Here, I consider the relationship between a number of these works, and explain some fundamental differences that would have important consequences for their observation in simulations. This discussion seems suitable for presentation as an appendix of chapter 4, since the primary purpose of this chapter has been to propose an alternative to the stochastic- α mechanism for non-helical shear dynamos.

At least two fundamentally different dynamo mechanisms are possible from fluctuations in the α effect with zero mean. The first – which has been explored for a variety of perspectives in Vishniac and Brandenburg (1997), Proctor (2007), Brandenburg *et al.* (2008a), Bushby and Proctor (2010), Heinemann *et al.* (2011), Richardson and Proctor (2012), Mitra and Brandenburg (2012), and McWilliams (2012) – has the property (discussed in Sec. 4.2) that $\langle \mathbf{B}(t) \rangle$ decays in time, and only $\langle \mathbf{B}^2 \rangle$ undergoes exponential instability. I shall term this the *incoherent stochastic- α mechanism*. (I remind the reader that $\langle \cdot \rangle$ refers to an ensemble average, while $\bar{\cdot}$ refers to the

mean-field average.) The second mechanism, which is in essence the Kraichnan-Moffat dynamo (Kraichnan, 1976; Moffatt, 1978), has been explored in the context of shear flows in Silant'ev (2000), Mitra and Brandenburg (2012), and Sridhar and Singh (2014), and does exhibit growth of $\langle \mathbf{B}(t) \rangle$. I shall term this the *coherent stochastic- α mechanism*. Since the requirements on mean-field evolution imposed by $\langle \mathbf{B}(t) \rangle = 0$ have been utilized as part of the argument for the prevalence of a coherent dynamo in chapters 4 and 5, it seems worth explaining in more detail the coherent stochastic- α mechanism and its relation to the incoherent variety.

In its absolute simplest form, the dynamo in Kraichnan (1976) and Sridhar and Singh (2014) can be described as resulting from

$$\partial_t \mathbf{B} = \nabla \times [\alpha(\mathbf{x}, t) \mathbf{B}] + \eta_T \nabla^2 \mathbf{B}, \quad (\text{C.1})$$

where $\alpha(\mathbf{x}, t)$ is a spatiotemporal fluctuating α -effect, assumed to arise from smaller-scale fluctuations, and η_T is the turbulent resistivity. One then specifies that $\langle \alpha \rangle = 0$, $\langle \alpha(\mathbf{x}, t) \alpha(\mathbf{x}', t') \rangle = 2\mathcal{A}(\mathbf{x} - \mathbf{x}') D(t, t')$, and forms the equation for $\langle \mathbf{B} \rangle$

$$\partial_t \langle \mathbf{B} \rangle = \nabla \times (\mathbf{V}_M \times \langle \mathbf{B} \rangle) + \eta_K \nabla^2 \langle \mathbf{B} \rangle, \quad (\text{C.2})$$

where $\eta_K \equiv \eta_T - \mathcal{A}(0)$, and $\mathbf{V}_M \equiv \int_0^\infty d\tau \langle \alpha(\mathbf{x}, \tau) \nabla \alpha(\mathbf{x}, 0) \rangle$. For sufficiently strong fluctuations in α , instability arises for $\langle \mathbf{B} \rangle$, because η_K becomes negative. Note that for such an instability, the *smallest* scales of the mean field grow the fastest. Sridhar and Singh (2014) give a variety of interesting extensions to this model, including the effects of nonzero α correlation time τ_α , and shear (which changes the dynamo only if $\tau_\alpha \neq 0$).

Why is it that this dynamo is mean field in the true sense – that is, $\langle \mathbf{B} \rangle$ grows exponentially – while this is not true for the incoherent stochastic- α dynamo? This question is important for understanding the shear dynamo, since a dynamo arising though this coherent stochastic- α mecha-

nism will have very different properties. While it seems that all previous treatments of the coherent stochastic- α dynamo have considered a spatiotemporal fluctuations in the α coefficient, this is not the fundamental difference. In particular, if we simply assert that $\alpha(\mathbf{x}, t) = \alpha(t)$ the dynamo can still exist with $\eta_K \equiv \eta_T - \mathcal{A}(0)$, although $\mathbf{V}_M = 0$. The answer to this question is given in Mitra and Brandenburg (2012) Sec. 3.3, where they examine the effects of mutual correlations between α coefficients. In particular (now considering specifically a horizontal mean-field average such that we have only a 2-D system), they find that in the presence of mutual *correlations* between α coefficients,

$$\langle \alpha_{ij}(t) \alpha_{kl}(t') \rangle = \mathcal{D}_{kl}^{ij} \delta(t - t'), \quad (\text{C.3})$$

the ensemble averaged mean-field $\langle \mathbf{B} \rangle = (\langle B_x \rangle, \langle B_y \rangle)$ satisfies the equation

$$\partial_t \langle \mathbf{B} \rangle = \begin{pmatrix} -k^2(\eta_T + \mathcal{D}_{yx}^{yx} - \mathcal{D}_{xx}^{yy}) & k^2(\mathcal{D}_{xy}^{yy} - \mathcal{D}_{yy}^{yx}) \\ -S + k^2(\mathcal{D}_{yx}^{xx} - \mathcal{D}_{xx}^{xy}) & -k^2(\eta_T + \mathcal{D}_{xy}^{xy} - \mathcal{D}_{yy}^{xx}) \end{pmatrix} \langle \mathbf{B} \rangle. \quad (\text{C.4})$$

Evidently, from Eq. (C.1), in the coherent stochastic- α mechanism, $\alpha_{xx}(t) = \alpha_{yy}(t)$, while $\alpha_{yx}(t) = \alpha_{xy}(t) = 0$. This implies $\mathcal{D}_{yy}^{xx} = \mathcal{D}_{xx}^{yy} = \mathcal{D}_{yy}^{yy}$, while all other \mathcal{D}_{kl}^{ij} vanish. Therefore we see exactly the same instability from Eq. (C.4), since $\eta_T - \mathcal{D}_{xx}^{yy}$ can be negative.

We thus find that the coherent stochastic- α mechanism requires the rather specific situation of *strong diagonal* α fluctuations, but *very weak off-diagonal* α fluctuations (since $\langle \alpha_{yx}(t) \alpha_{yx}(t') \rangle = \mathcal{D}_{yx}^{yx} \delta(t - t')$, and similarly for α_{xy}). While the exact result Eq. (C.4) is only valid for α with no spatial dependence, it seems almost certain that similar conclusions will hold if spatial variation is also included. Is it realistic for the correlation between α_{xx} and α_{yy} to greatly exceed the fluctuations in α_{yx} and α_{xy} (their difference must also overcome η_T)? Possibly, for instance if the fluctuations in α_{ij} arose purely from fluctuations in small-scale helicity, but this situation seems unlikely. In any case, more work, both numerical and analytical (e.g., inclusion of α_{yx} and α_{xy} in the much more thorough calculations of Sridhar and Singh 2014), would be needed to thoroughly assess this pos-

sibility. Overall, the confluence of factors that are unfavorable to the coherent stochastic- α dynamo – the requirement for very strong α fluctuations, the significantly adverse effect of off-diagonal α , and the fact that one would observe a mean field that grows much faster on the smallest scales – leads to the conclusion that this mechanism has probably not been observed in previous numerical experiments on shear dynamos.

Appendix D

Appendix: Analytic transport coefficients

D.1 Equations for $m^{(0)}$, $m^{(1)}$, $b^{(0)}$, $b^{(1)}$ in Fourier space

Here I give the set of perturbation equations for \mathbf{u} and \mathbf{b} in Fourier space, which result from the Fourier transform of Eq. (6.14). The method is outlined in RS06, so I give very little detail here. Since it is assumed that $U_i(\mathbf{x}) = U_{ij}x_j$, $\rho = \rho_0 + \chi_\rho \hat{g}_i x_i$, and $B_i(\mathbf{x}) = B_i + B_{ij}x_j$ the Fourier transforms can be carried out exactly using $\widehat{x_k \partial_l b_j} = -\delta_{lk} \hat{b}_j - k_l \partial_{k_k} \hat{b}_j$ (where $\hat{\cdot}$ denotes the Fourier transform). I have also neglected products of χ_ρ with B_{ij} . In the momentum equations, the projection operator $\delta_{ij} - k_i k_j / k^2$ is applied so as to remove the pressure.

Defining, as in RS06,

$$N_\nu = \frac{1}{i\omega - \nu k^2}, \quad E_\eta = \frac{1}{i\omega - \eta k^2}, \quad (\text{D.1})$$

the Fourier-space equations are as follows,

$$\begin{aligned}
m_i^{(0)} = N_\nu & \left[-U_{il}m_{0l} + U_{lk}k_l \frac{\partial m_{0i}}{\partial k_k} + 2\frac{k_i k_j}{k^2} m_{0l} U_{jl} - i\nu k_r \chi_\rho \hat{g}_r m_{0i} \right. \\
& + i\nu \frac{k_i k_j k_r}{k^2} \chi_\rho \hat{g}_r m_{0j} + 2\frac{k_r \Omega_r}{k^2} \varepsilon_{ijk} m_{0j} k_k + ik_r B_r b_{0i} \\
& \left. - ik_r B_r \frac{k_i k_j}{k^2} b_{0j} + B_{il} b_{0l} - B_{lk} k_l \frac{\partial b_{0i}}{\partial k_k} - 2\frac{k_i k_j}{k^2} b_{0l} B_{jl} \right], \tag{D.2}
\end{aligned}$$

$$\begin{aligned}
m_i^{(1)} = N_\nu & \left[-U_{il}m_l^{(0)} + U_{lk}k_l \frac{\partial m_i^{(0)}}{\partial k_k} + 2\frac{k_i k_j}{k^2} m_l^{(0)} U_{jl} - i\nu k_r \chi_\rho \hat{g}_r m_i^{(0)} \right. \\
& + i\nu \frac{k_i k_j k_r}{k^2} \chi_\rho \hat{g}_r m_j^{(0)} + 2\frac{k_r \Omega_r}{k^2} \varepsilon_{ijk} m_j^{(0)} k_k + ik_r B_r b_i^{(0)} \\
& \left. - ik_r B_r \frac{k_i k_j}{k^2} b_j^{(0)} + B_{il} b_l^{(0)} - B_{lk} k_l \frac{\partial b_i^{(0)}}{\partial k_k} - 2\frac{k_i k_j}{k^2} b_l^{(0)} B_{jl} \right], \tag{D.3}
\end{aligned}$$

$$\begin{aligned}
b_i^{(0)} = E_\eta & \left[\rho_0^{-1} \left(ik_r B_r m_{0i} - B_{ij} m_{0j} - B_{jk} k_j \frac{\partial m_{0i}}{\partial k_k} + B_i \chi_\rho \hat{g}_r m_{0r} \right. \right. \\
& \left. \left. + \chi_\rho \hat{g}_r B_j k_j \frac{\partial m_{0i}}{\partial k_r} \right) + U_{ij} b_{0j} + U_{jk} k_j \frac{\partial b_{0i}}{\partial k_k} \right], \tag{D.4}
\end{aligned}$$

$$\begin{aligned}
b_i^{(1)} = E_\eta & \left[\rho_0^{-1} \left(ik_r B_r m_i^{(0)} - B_{ij} m_j^{(0)} - B_{jk} k_j \frac{\partial m_i^{(0)}}{\partial k_k} + B_i \chi_\rho \hat{g}_r m_r^{(0)} \right. \right. \\
& \left. \left. + \chi_\rho \hat{g}_r B_j k_j \frac{\partial m_i^{(0)}}{\partial k_r} \right) + U_{ij} b_j^{(0)} + U_{jk} k_j \frac{\partial b_i^{(0)}}{\partial k_k} \right], \tag{D.5}
\end{aligned}$$

Here m_{0i} , b_{0i} etc. refer to the Fourier-space variables for simplicity of notation. As a first step in the calculation, Eqs. (D.2) and (D.4) are inserted into Eqs. (D.3) and (D.5) and expanded, neglecting those terms that contain $U_{ij}U_{rs}$, $U_{ij}\Omega_r$, $\Omega_i\Omega_j$, $U_{ij}\chi_\rho$, $\Omega\chi_\rho$, χ_ρ^2 , $B_i B_j$, $B_i B_{ij}$ and $B_{ij} B_{rs}$ as higher order in this perturbation expansion.

D.2 List of all transport coefficients

In this appendix, I list all transport coefficients $\alpha^{(0)}$, $\beta^{(0)}$, $\delta^{(\Omega)}$, \dots in the form of integrals over the isotropic velocity and magnetic correlation functions, $W_u(\mathbf{R}, k, \omega)$, $H_u(k, \omega)$, $W_b(\mathbf{R}, k, \omega)$, $H_b(k, \omega)$. This parallels Appendix B in RS06 and there is some overlap; however, for completeness I list all coefficients.

Analogous to the relations in Sec. 6.3 for the Cartesian case and RS06, I list the coefficient of $4\pi k^2 W_{u,b}$ or $4\pi k^2 H_{u,b}$ in the integrand of each transport coefficient; that is, $\tilde{\alpha}_H^{(\cdot)}$, $\tilde{\alpha}^{(\cdot)}$ or $\tilde{\beta}^{(\cdot)}$ in

$$\left(\alpha_H^{(\cdot)}\right)_{u,b} = 4\pi \int dk d\omega k^2 \tilde{\alpha}_H^{(\cdot)}(k, \omega) H_{u,b}(k, \omega), \quad (\text{D.6a})$$

$$\left(\alpha^{(\cdot)}\right)_{u,b} = 4\pi \int dk d\omega k^2 \tilde{\alpha}^{(\cdot)}(k, \omega) W_{u,b}(k, \omega), \quad (\text{D.6b})$$

$$\left(\beta^{(\cdot)}\right)_{u,b} = 4\pi \int dk d\omega k^2 \tilde{\beta}^{(\cdot)}(k, \omega) W_{u,b}(k, \omega). \quad (\text{D.6c})$$

I use the notation $\tilde{\eta} = k^2 \bar{\eta}$, $\tilde{\nu} = k^2 \bar{\nu}$, and $\nabla \ln a \equiv \chi_a \hat{\mathbf{g}}$ (e.g., $\nabla \ln \rho + \nabla \ln \bar{u} = \chi_{\rho \bar{u}} \hat{\mathbf{g}}$).

D.2.1 Nonhelical α coefficients

$$\left(\gamma^{(0)}\right)_u = \frac{\chi_{\bar{u}} \tilde{\eta}}{6(\tilde{\eta}^2 + \omega^2)}, \quad (\text{D.7})$$

$$\left(\gamma^{(0)}\right)_b = -\frac{\chi_{\bar{b}} \tilde{\nu}}{6\rho(\tilde{\nu}^2 + \omega^2)}, \quad (\text{D.8})$$

$$\left(\gamma^{(\Omega)}\right)_u = -\frac{\chi_{\rho \bar{u}} \omega^2}{3(\tilde{\eta}^2 + \omega^2)(\tilde{\nu}^2 + \omega^2)}, \quad (\text{D.9})$$

$$\left(\gamma^{(\Omega)}\right)_b = \frac{\chi_{\bar{b}}(\omega^2 - \tilde{\nu}^2)}{6\rho(\tilde{\nu}^2 + \omega^2)^2}, \quad (\text{D.10})$$

$$\left(\alpha_1^{(\Omega)}\right)_u = \frac{4\chi_{\rho\bar{u}}\tilde{\eta}(2\omega^2\tilde{\eta}(\tilde{\nu}^2 + \omega^2) + \tilde{\eta}^2(3\omega^2\tilde{\nu} + \tilde{\nu}^3) + \omega^2\tilde{\nu}(\tilde{\nu}^2 + 3\omega^2))}{15(\tilde{\eta}^2 + \omega^2)^2(\tilde{\nu}^2 + \omega^2)^2}, \quad (\text{D.11})$$

$$\left(\alpha_1^{(\Omega)}\right)_b = \frac{4\chi_{\bar{b}}\omega^2(\omega^2 - 3\tilde{\nu}^2)}{15\rho(\tilde{\nu}^2 + \omega^2)^3}, \quad (\text{D.12})$$

$$\begin{aligned} \left(\alpha_2^{(\Omega)}\right)_u &= \frac{\chi_{\rho\bar{u}}}{15} [2\omega^2\tilde{\eta}\tilde{\nu}(\omega^2 - 3\tilde{\nu}^2) + 3\omega^2\tilde{\eta}^2(\tilde{\nu}^2 + \omega^2) \\ &\quad + 2\tilde{\eta}^3\tilde{\nu}(\omega^2 - 3\tilde{\nu}^2) - 5\omega^4(\tilde{\nu}^2 + \omega^2)] \\ &\quad \times (\tilde{\eta}^2 + \omega^2)^{-2}(\tilde{\nu}^2 + \omega^2)^{-2}, \end{aligned} \quad (\text{D.13})$$

$$\left(\alpha_2^{(\Omega)}\right)_b = \frac{\chi_{\bar{b}}(3\omega^4 - 24\omega^2\tilde{\nu}^2 + 5\tilde{\nu}^4)}{30\rho(\tilde{\nu}^2 + \omega^2)^3}, \quad (\text{D.14})$$

$$\begin{aligned} \left(\alpha_1^{(W)}\right)_u &= \frac{\chi_{\rho\bar{u}}}{120} [4\tilde{\eta}^5(11\omega^2\tilde{\nu} + 5\tilde{\nu}^3) + 4\tilde{\eta}(11\omega^6\tilde{\nu} + 5\omega^4\tilde{\nu}^3) \\ &\quad + 8\tilde{\eta}^3(11\omega^4\tilde{\nu} + 5\omega^2\tilde{\nu}^3) + \tilde{\eta}^4(12\omega^2\tilde{\nu}^2 - \tilde{\nu}^4 + 13\omega^4) \\ &\quad - 4\tilde{\eta}^2(5\omega^4\tilde{\nu}^2 + 3\omega^2\tilde{\nu}^4 + 2\omega^6) + 5\omega^4\tilde{\nu}^4 - 5\omega^8] \\ &\quad \times (\tilde{\eta}^2 + \omega^2)^{-3}(\tilde{\nu}^2 + \omega^2)^{-2}, \end{aligned} \quad (\text{D.15})$$

$$\begin{aligned} \left(\alpha_1^{(W)}\right)_b &= \frac{\chi_{\bar{b}}}{120} [4\omega^2\tilde{\eta}\tilde{\nu}(\tilde{\nu}^2 + \omega^2)^2 + \tilde{\eta}^4(\tilde{\nu}^4 - 36\omega^2\tilde{\nu}^2 + 11\omega^4) \\ &\quad - 4\tilde{\eta}^3\tilde{\nu}(\tilde{\nu}^2 + \omega^2)^2 + 4\tilde{\eta}^2(-11\omega^4\tilde{\nu}^2 + 5\omega^2\tilde{\nu}^4 + 8\omega^6) \\ &\quad - 8\omega^6\tilde{\nu}^2 + 19\omega^4\tilde{\nu}^4 + 21\omega^8] (\tilde{\eta}^2 + \omega^2)^{-2}(\tilde{\nu}^2 + \omega^2)^{-3}\rho^{-1}, \end{aligned} \quad (\text{D.16})$$

$$\begin{aligned}
(\alpha_2^{(W)})_u &= \frac{\chi_{\rho\bar{u}}}{240} [-4\tilde{\eta}^5 (3\omega^2\tilde{\nu} + 5\tilde{\nu}^3) - 4\tilde{\eta} (3\omega^6\tilde{\nu} + 5\omega^4\tilde{\nu}^3) \\
&\quad + \tilde{\eta}^4 (44\omega^2\tilde{\nu}^2 + 13\tilde{\nu}^4 + 31\omega^4) - 8\tilde{\eta}^3 (3\omega^4\tilde{\nu} + 5\omega^2\tilde{\nu}^3) \\
&\quad - 28\tilde{\eta}^2 (5\omega^4\tilde{\nu}^2 + 3\omega^2\tilde{\nu}^4 + 2\omega^6) \\
&\quad + 5 (8\omega^6\tilde{\nu}^2 + 3\omega^4\tilde{\nu}^4 + 5\omega^8)] \\
&\quad \times (\tilde{\eta}^2 + \omega^2)^{-3} (\tilde{\nu}^2 + \omega^2)^{-2}, \tag{D.17}
\end{aligned}$$

$$\begin{aligned}
(\alpha_2^{(W)})_b &= \frac{\chi_{\bar{b}}}{240} [28\omega^2\tilde{\eta}\tilde{\nu} (\tilde{\nu}^2 + \omega^2)^2 - 28\tilde{\eta}^3\tilde{\nu} (\tilde{\nu}^2 + \omega^2)^2 \\
&\quad + \tilde{\eta}^4 (-12\omega^2\tilde{\nu}^2 + 7\tilde{\nu}^4 - 3\omega^4) \\
&\quad - 4\tilde{\eta}^2 (17\omega^4\tilde{\nu}^2 - 5\omega^2\tilde{\nu}^4 + 14\omega^6) \\
&\quad - 56\omega^6\tilde{\nu}^2 + 13\omega^4\tilde{\nu}^4 - 53\omega^8] (\tilde{\eta}^2 + \omega^2)^{-2} (\tilde{\nu}^2 + \omega^2)^{-3} \rho^{-1}, \tag{D.18}
\end{aligned}$$

$$\begin{aligned}
(\alpha^{(D)})_u &= \frac{\chi_{\rho\bar{u}}}{120} [12\omega^2\tilde{\eta}^2\tilde{\nu}^2 (\tilde{\nu}^2 + \omega^2) + 12\tilde{\eta}^5\tilde{\nu} (\omega^2 - \tilde{\nu}^2) \\
&\quad + 4\omega^4\tilde{\eta}\tilde{\nu} (\tilde{\nu}^2 + 7\omega^2) + 8\tilde{\eta}^3 (5\omega^4\tilde{\nu} - \omega^2\tilde{\nu}^3) + 5\omega^4\tilde{\nu}^4 - 5\omega^8 \\
&\quad - \tilde{\eta}^4 (20\omega^2\tilde{\nu}^2 + 9\tilde{\nu}^4 + 11\omega^4)] (\tilde{\eta}^2 + \omega^2)^{-3} (\tilde{\nu}^2 + \omega^2)^{-2}, \tag{D.19}
\end{aligned}$$

$$\begin{aligned}
(\alpha^{(D)})_b &= \frac{\chi_{\bar{b}}}{120} [-4\omega^2\tilde{\eta}\tilde{\nu} (6\omega^2\tilde{\nu}^2 + \tilde{\nu}^4 + 5\omega^4) \\
&\quad - \tilde{\eta}^4 (12\omega^2\tilde{\nu}^2 - 5\tilde{\nu}^4 + \omega^4) \\
&\quad + 4\tilde{\eta}^3\tilde{\nu} (6\omega^2\tilde{\nu}^2 + 5\tilde{\nu}^4 + \omega^4) \\
&\quad + 4\tilde{\eta}^2 (-3\omega^4\tilde{\nu}^2 + 3\omega^2\tilde{\nu}^4 + 2\omega^6) \\
&\quad + 7\omega^4\tilde{\nu}^4 + 9\omega^8] (\tilde{\eta}^2 + \omega^2)^{-2} (\tilde{\nu}^2 + \omega^2)^{-3} \rho^{-1}, \tag{D.20}
\end{aligned}$$

$$\begin{aligned}
(\gamma^{(W)})_u &= -\frac{\chi_{\rho\bar{u}}}{120} [-8\omega^6\tilde{\eta}\tilde{\nu} - 16\omega^4\tilde{\eta}^3\tilde{\nu} - 8\omega^2\tilde{\eta}^5\tilde{\nu} \\
&\quad -\tilde{\eta}^4(8\omega^2\tilde{\nu}^2 + \tilde{\nu}^4 + 7\omega^4) - 4\tilde{\eta}^2(7\omega^4\tilde{\nu}^2 + 3\omega^2\tilde{\nu}^4 + 4\omega^6) \\
&\quad + 12\omega^6\tilde{\nu}^2 + 5\omega^4\tilde{\nu}^4 + 7\omega^8] (\tilde{\eta}^2 + \omega^2)^{-3} (\tilde{\nu}^2 + \omega^2)^{-2}, \tag{D.21}
\end{aligned}$$

$$\begin{aligned}
(\gamma^{(W)})_b &= \frac{\chi_{\bar{b}}}{120} [4\tilde{\eta}^2(-3\omega^4\tilde{\nu}^2 + 2\omega^2\tilde{\nu}^4 + 3\omega^6) \\
&\quad - 8\omega^2\tilde{\eta}\tilde{\nu}(\tilde{\nu}^2 + \omega^2)^2 + \tilde{\eta}^4(-12\omega^2\tilde{\nu}^2 + 3\tilde{\nu}^4 + \omega^4) \\
&\quad + 5\omega^4\tilde{\nu}^4 + 11\omega^8] (\tilde{\eta}^2 + \omega^2)^{-2} (\tilde{\nu}^2 + \omega^2)^{-3} \rho^{-1}, \tag{D.22}
\end{aligned}$$

$$\begin{aligned}
(\gamma^{(D)})_u &= -\frac{\chi_{\rho\bar{u}}}{120} [9\tilde{\eta}^4(\omega^4 - \tilde{\nu}^4) + 8\tilde{\eta}^5(5\omega^2\tilde{\nu} + 6\tilde{\nu}^3) \\
&\quad + 8\tilde{\eta}(3\omega^6\tilde{\nu} + 4\omega^4\tilde{\nu}^3) + 16\tilde{\eta}^3(4\omega^4\tilde{\nu} + 5\omega^2\tilde{\nu}^3) \\
&\quad + 4\tilde{\eta}^2(13\omega^4\tilde{\nu}^2 + 3\omega^2\tilde{\nu}^4 + 10\omega^6) \\
&\quad + 5\omega^4(4\omega^2\tilde{\nu}^2 + \tilde{\nu}^4 + 3\omega^4)] \\
&\quad \times (\tilde{\eta}^2 + \omega^2)^{-3} (\tilde{\nu}^2 + \omega^2)^{-2}, \tag{D.23}
\end{aligned}$$

$$\begin{aligned}
(\gamma^{(D)})_b &= \frac{\chi_{\bar{b}}}{120} [-16\omega^2\tilde{\eta}\tilde{\nu}(3\omega^2\tilde{\nu}^2 + \tilde{\nu}^4 + 2\omega^4) \\
&\quad + \tilde{\eta}^4(12\omega^2\tilde{\nu}^2 + 19\tilde{\nu}^4 - 23\omega^4) \\
&\quad - 8\tilde{\eta}^3(3\omega^4\tilde{\nu} + 4\omega^2\tilde{\nu}^3 + \tilde{\nu}^5) + \tilde{\eta}^2(52\omega^4\tilde{\nu}^2 + 56\omega^2\tilde{\nu}^4 - 36\omega^6) \\
&\quad + 40\omega^6\tilde{\nu}^2 + 37\omega^4\tilde{\nu}^4 - 13\omega^8] (\tilde{\eta}^2 + \omega^2)^{-2} (\tilde{\nu}^2 + \omega^2)^{-3} \rho^{-1}, \tag{D.24}
\end{aligned}$$

D.2.2 β coefficients

$$(\beta^{(0)})_u = \frac{\tilde{\eta}}{3(\tilde{\eta}^2 + \omega^2)}, \tag{D.25}$$

$$(\beta^{(0)})_b = 0, \quad (\text{D.26})$$

$$(\delta^{(\Omega)})_u = -\frac{\omega^2}{3(\tilde{\eta}^2 + \omega^2)(\tilde{\nu}^2 + \omega^2)}, \quad (\text{D.27})$$

$$(\delta^{(\Omega)})_b = \frac{\tilde{\nu}^2 - \omega^2}{6\rho(\tilde{\nu}^2 + \omega^2)^2}, \quad (\text{D.28})$$

$$(\delta^{(W)})_u = \frac{\tilde{\eta}^2 - \omega^2}{12(\tilde{\eta}^2 + \omega^2)^2}, \quad (\text{D.29})$$

$$(\delta^{(W)})_b = \frac{\tilde{\nu}^2 - \omega^2}{12\rho(\tilde{\nu}^2 + \omega^2)^2}, \quad (\text{D.30})$$

$$(\kappa^{(\Omega)})_u = \frac{2\omega^2(11\tilde{\eta}^2 - 5\omega^2)}{15(\tilde{\eta}^2 + \omega^2)^2(\tilde{\nu}^2 + \omega^2)}, \quad (\text{D.31})$$

$$(\kappa^{(\Omega)})_b = \frac{9\tilde{\nu}^4 - 48\omega^2\tilde{\nu}^2 + 7\omega^4}{15\rho(\tilde{\nu}^2 + \omega^2)^3}, \quad (\text{D.32})$$

$$\begin{aligned} (\kappa^{(W)})_u = & \\ & \frac{\tilde{\eta}^4(23\omega^2 - \tilde{\nu}^2) + 12\tilde{\eta}^2(\omega^4 - \omega^2\tilde{\nu}^2) + 5\omega^4(\tilde{\nu}^2 + \omega^2)}{30(\tilde{\eta}^2 + \omega^2)^3(\tilde{\nu}^2 + \omega^2)}, \end{aligned} \quad (\text{D.33})$$

$$\begin{aligned} (\kappa^{(W)})_b = & \\ & \frac{3\tilde{\eta}^2(-12\omega^2\tilde{\nu}^2 + \tilde{\nu}^4 + 3\omega^4) - 20\omega^4\tilde{\nu}^2 + 15\omega^2\tilde{\nu}^4 + 13\omega^6}{30\rho(\tilde{\eta}^2 + \omega^2)(\tilde{\nu}^2 + \omega^2)^3}, \end{aligned} \quad (\text{D.34})$$

$$\begin{aligned} (\beta^{(D)})_u = & \frac{1}{30} \left[2\tilde{\eta}^5\tilde{\nu}(5\tilde{\nu}^2 + \omega^2) + 16\omega^2\tilde{\eta}^3\tilde{\nu}^3 + 5\omega^4(\tilde{\nu}^2 + \omega^2)^2 \right. \\ & + \tilde{\eta}(6\omega^4\tilde{\nu}^3 - 2\omega^6\tilde{\nu}) - \tilde{\eta}^4(10\omega^2\tilde{\nu}^2 + 3\tilde{\nu}^4 + 7\omega^4) \\ & \left. - 2\tilde{\eta}^2(8\omega^4\tilde{\nu}^2 + 3\omega^2\tilde{\nu}^4 + 5\omega^6) \right] (\tilde{\eta}^2 + \omega^2)^{-3} (\tilde{\nu}^2 + \omega^2)^{-2}, \end{aligned} \quad (\text{D.35})$$

$$\begin{aligned}
(\beta^{(D)})_b &= \frac{1}{10} [4\tilde{\eta}^3\tilde{\nu}^3(\tilde{\nu}^2 + \omega^2) + 4\tilde{\eta}^2(\omega^6 - 3\omega^4\tilde{\nu}^2) \\
&\quad - 4\omega^2\tilde{\eta}\tilde{\nu}(3\omega^2\tilde{\nu}^2 + \tilde{\nu}^4 + 2\omega^4) - 6\omega^6\tilde{\nu}^2 - \omega^4\tilde{\nu}^4 + 3\omega^8 \\
&\quad + \tilde{\eta}^4(-6\omega^2\tilde{\nu}^2 + \tilde{\nu}^4 + \omega^4)] (\tilde{\eta}^2 + \omega^2)^{-2} (\tilde{\nu}^2 + \omega^2)^{-3} \rho^{-1}, \tag{D.36}
\end{aligned}$$

$$\begin{aligned}
(\kappa^{(D)})_u &= \frac{1}{30} [2\tilde{\eta}^5\tilde{\nu}(5\tilde{\nu}^2 + \omega^2) + 16\omega^2\tilde{\eta}^3\tilde{\nu}^3 + \tilde{\eta}(6\omega^4\tilde{\nu}^3 - 2\omega^6\tilde{\nu}) \\
&\quad + \tilde{\eta}^4(10\omega^2\tilde{\nu}^2 + 3\tilde{\nu}^4 + 7\omega^4) + 2\tilde{\eta}^2(8\omega^4\tilde{\nu}^2 + 3\omega^2\tilde{\nu}^4 + 5\omega^6) \\
&\quad - 5\omega^4(\tilde{\nu}^2 + \omega^2)^2] (\tilde{\eta}^2 + \omega^2)^{-3} (\tilde{\nu}^2 + \omega^2)^{-2}, \tag{D.37}
\end{aligned}$$

$$\begin{aligned}
(\kappa^{(D)})_b &= \frac{1}{30} [-4\tilde{\eta}^3\tilde{\nu}^3(\tilde{\nu}^2 + \omega^2) + 4\omega^2\tilde{\eta}\tilde{\nu}(3\omega^2\tilde{\nu}^2 + \tilde{\nu}^4 + 2\omega^4) \\
&\quad + \tilde{\eta}^4(-6\omega^2\tilde{\nu}^2 - 3\tilde{\nu}^4 + 5\omega^4) + 4\tilde{\eta}^2(-7\omega^4\tilde{\nu}^2 - 4\omega^2\tilde{\nu}^4 + \omega^6) \\
&\quad - \omega^4(22\omega^2\tilde{\nu}^2 + 13\tilde{\nu}^4 + \omega^4)] (\tilde{\eta}^2 + \omega^2)^{-2} (\tilde{\nu}^2 + \omega^2)^{-3} \rho^{-1}, \tag{D.38}
\end{aligned}$$

Helical α coefficients

$$\left(\tilde{\alpha}_H^{(0)}\right)_u = \frac{2\tilde{\eta}}{3(\tilde{\eta}^2 + \omega^2)}, \tag{D.39}$$

$$\left(\alpha_H^{(0)}\right)_b = -\frac{2\tilde{\nu}}{3\rho(\tilde{\nu}^2 + \omega^2)}, \tag{D.40}$$

$$\left(\gamma^{(\Omega)}\right)_u = 0, \tag{D.41}$$

$$\left(\gamma^{(\Omega)}\right)_b = 0, \tag{D.42}$$

$$\left(\gamma_H^{(W)}\right)_u = \frac{\tilde{\eta}^2(\tilde{\nu}^2 + 3\omega^2) - \omega^2\tilde{\nu}^2 + \omega^4}{6(\tilde{\eta}^2 + \omega^2)^2(\tilde{\nu}^2 + \omega^2)}, \tag{D.43}$$

$$\left(\gamma_H^{(W)}\right)_b = \frac{\tilde{\eta}^2(\omega^2 - \tilde{\nu}^2) - \omega^2(3\tilde{\nu}^2 + \omega^2)}{6\rho(\tilde{\eta}^2 + \omega^2)(\tilde{\nu}^2 + \omega^2)^2}, \tag{D.44}$$

$$\begin{aligned}
\left(\alpha_H^{(D)}\right)_u &= -\frac{1}{15} \left[3\tilde{\eta}^4 (\omega^4 - \tilde{\nu}^4) + 4\tilde{\eta}^5 (5\omega^2\tilde{\nu} - 3\tilde{\nu}^3) \right. \\
&\quad - 8\omega^2\tilde{\eta}^3\tilde{\nu} (\tilde{\nu}^2 - 7\omega^2) + 4\omega^4\tilde{\eta}\tilde{\nu} (\tilde{\nu}^2 + 9\omega^2) \\
&\quad + 4\tilde{\eta}^2 (11\omega^4\tilde{\nu}^2 + 6\omega^2\tilde{\nu}^4 + 5\omega^6) \\
&\quad \left. - 5\omega^4 (4\omega^2\tilde{\nu}^2 + \tilde{\nu}^4 + 3\omega^4) \right] (\tilde{\eta}^2 + \omega^2)^{-3} (\tilde{\nu}^2 + \omega^2)^{-2}, \tag{D.45}
\end{aligned}$$

$$\begin{aligned}
\left(\alpha_H^{(D)}\right)_b &= -\frac{1}{15\rho} \left[\tilde{\eta}^4 (-24\omega^2\tilde{\nu}^2 + 7\tilde{\nu}^4 + \omega^4) \right. \\
&\quad - 4\tilde{\eta}^3 (3\omega^4\tilde{\nu} + 2\omega^2\tilde{\nu}^3 - \tilde{\nu}^5) + 4\tilde{\eta}^2 (-11\omega^4\tilde{\nu}^2 + 2\omega^2\tilde{\nu}^4 + 3\omega^6) \\
&\quad - 4\tilde{\eta} (11\omega^6\tilde{\nu} + 18\omega^4\tilde{\nu}^3 + 7\omega^2\tilde{\nu}^5) \\
&\quad \left. + \omega^4 (-20\omega^2\tilde{\nu}^2 + \tilde{\nu}^4 + 11\omega^4) \right] (\tilde{\eta}^2 + \omega^2)^{-2} (\tilde{\nu}^2 + \omega^2)^{-3}. \tag{D.46}
\end{aligned}$$

All of the listed nonhelical kinematic transport coefficients agree with those given in RS06, with one exception. This is the $(\beta^{(D)})_u$ coefficient, which contains a factor $1/30$, rather than $1/60$.

D.3 The sign of $(\eta_{yx})_b^S$

In this appendix, I argue that the sign of $(\eta_{yx})_b^S$ is always negative, given reasonable assumptions about the form of $W_b(k, \omega)$. I have not been able to find a general proof that this is the case due to the complexity of the expression Eq. (6.33b), but instead analyze the cases $\text{Pm} = 1$, $\text{Pm} \ll 1$, and $\text{Pm} \gg 1$ separately. In addition, plotting $(\eta_{yx})_b^S$ for the Gaussian W_b [Eq. (6.31)] across a range of Pm (e.g., Fig. 6.1) leads to the same conclusion for this specific W_b . [Note that $(\eta_{yx})_b^S$ depends nontrivially on only Pm and q when written in the dimensionless variables given in Eq. (6.32), meaning it is straightforward to observe positivity by plotting $(\eta_{yx})_b^S$ against q over a range of Pm .]

$P_m = 1$

Inserting $\nu = \eta$ into Eq. (6.33b) leads to

$$(\eta_{yx})_b^S = \int d\omega dk k^2 W_b(k, \omega) \frac{8\pi (\omega^2 - \tilde{\eta}^2) (3\tilde{\eta}^2 + \omega^2)}{15 (\tilde{\eta}^2 + \omega^2)^3}. \quad (\text{D.47})$$

An integration by parts in ω yields

$$(\eta_{yx})_b^S = \frac{4\pi}{15} \int d\omega dk \left[\frac{1}{\eta} \tan^{-1} \left(\frac{\omega}{\tilde{\eta}} \right) \frac{dW_b}{d\omega} + \frac{5\tilde{\eta}^2 + 3\omega^2}{(\tilde{\eta}^2 + \omega^2)^2} \omega \frac{dW_b}{d\omega} \right]. \quad (\text{D.48})$$

Under the reasonable assumptions that $\omega dW/d\omega \leq 0$ and $\tan^{-1}(\omega) dW/d\omega \leq 0$, each term in the integral must be negative. (Note that the $\tan^{-1}(\omega) dW/d\omega \leq 0$ condition, although it may appear less familiar, is just as restrictive as $\omega dW/d\omega \leq 0$, given the odd nature of the \tan^{-1} function.)

$P_m \ll 1$

Inserting $\eta = \nu/P_m$ into Eq. (6.33b), one carries out a series expansion about $P_m^{-1} = \infty$ of the resulting expression. The reason for this expansion (rather than the more obvious expansion about $P_m = 0$) is to enable study of the low P_m limit with large η , rather than that with $\nu \rightarrow 0$, since the SOCA loses applicability as $\nu, \eta \rightarrow 0$. The series expansion to first order in $1/P_m^{-1}$ is

$$(\eta_{yx})_b^S \approx -\frac{8\pi}{15} \int d\omega dk W_b k^2 \left[\frac{3\omega^2 \tilde{\nu}^2 + \tilde{\nu}^4 - 2\omega^4}{(\tilde{\nu}^2 + \omega^2)^3} + \frac{4\tilde{\nu}^2}{15 (\tilde{\nu}^2 + \omega^2)^2} \frac{1}{P_m^{-1}} + \dots \right]. \quad (\text{D.49})$$

The first term is independent of P_m , persisting as $\eta \rightarrow 0$, and the existence of this is not surprising given the fact that the dynamo can arise from the $\mathbf{B} \cdot \nabla \mathbf{b} + \mathbf{b} \cdot \nabla \mathbf{B}$ term in the induction equation. This term can be shown to be negative using the same integration by parts method used to obtain

Eq. (D.48), with the requirement $\omega dW/d\omega \leq 0$. The P_m -dependent second term is obviously negative due to the positive definiteness of the integrand.

$P_m \gg 1$

Inserting $\nu = P_m \eta$ into Eq. (6.33b), and carrying out a series expansion about $P_m = \infty$ (see previous paragraph), one obtains

$$(\eta_{yx})_b^S \approx \frac{16\pi}{15} \int d\omega dk W_b k^2 \left[\frac{1}{P_m} \frac{(\omega^2 - \tilde{\eta}^2)}{(\tilde{\eta}^2 + \omega^2)^2} + \dots \right]. \quad (\text{D.50})$$

As expected, there is no contribution to the transport as $\nu \rightarrow 0$. Again using integration by parts, one can straightforwardly prove negativity of the integral, provided $\omega dW/d\omega \leq 0$.

Appendix E

Appendix: The *VEST* package for tensor calculus in *Mathematica*

In this appendix, I give brief details of the *VEST* (Vector Einstein Summation Tools) package, which performs abstract vector calculus computations in *Mathematica*. Through the use of index notation, *VEST* is able to reduce three-dimensional scalar and vector expressions of a very general type to a well-defined standard form. In addition, utilizing properties of the Levi-Civita symbol, the program can derive types of multi-term vector identities that are not recognized by reduction, subsequently applying these to simplify large expressions. For the work presented in this thesis, the package proved very useful for automating the transport coefficient calculation presented in chapter 6. More details about the package, in particular its more advanced simplification capabilities, can be found in Squire *et al.* (2014).

E.1 Introduction

Many problems in the physical sciences and engineering involve substantial amounts of vector calculus; the manipulation of expressions involving derivatives of smooth scalar, vector and ten-

vector fields in 3-D Euclidean space. While multiple popular computer algebra systems include some basic native vector operations as well as external vector packages,¹ almost all emphasize the expansion of expressions into components. Although this can be an important tool, particularly when performing calculations in non-cartesian coordinates, the results obtained from this approach to simplification cannot be easily translated into a coordinate independent form. A natural way to overcome this problem is to encode the properties of vector operators such as \cdot , \times , and ∇ . Due to the nontrivial nature of these operators, expressions can often be greatly simplified without ever considering the underlying coordinate representation.

VEST (Vector Einstein Summation Tools), is designed to deal with such situations, and with a handful of additions, became a very practical tool for the calculation of turbulent transport coefficients given in chapter 6. Functions were designed to be simple and intuitive to use, in the hope it would be a practical tool for anyone working with vector calculus, both for simple checking of work and for more substantial computations. A thorough illustration of the capabilities of *VEST* can be found in Burby *et al.* (2013), which presents the first automated calculation of high-order guiding-center Lagrangians. Much of the functionality of *VEST* is made possible through the use of abstract index notation for internal manipulation, rather than standard vector notation. This allows *VEST* to *derive* vector identities, both through a systematic reduction to standard form and by inserting pairs of the Levi-Civita symbol, rather than relying on the relatively limited set found in standard reference (for instance, Huba 2009). The obvious advantage of this is that even for expressions and operations that are rarely used (e.g., higher order derivative tensors), a full simplification may still be performed without the necessity of hard-coding identities into the package. Of course, in principle one of the many existing abstract tensor manipulation packages designed for general relativistic calculations (e.g., MacCallum 2002; Wang 2013; Parker and Christensen 1994; Peeters 2007; Martín-García 2002–2012; Gouyet *et al.* 2008; Maple 2015) could be used for these types

¹For example, Mathematica (2015); Eastwood (1991); Yasskin and Belmonte (2010); Fiedler (1997); Wirth (1979); Liang and Jeffrey (2007); Qin *et al.* (1999); Maple (2015).

of computations; however, the increased generality required for curved spaces in any dimension necessitates features that would be very cumbersome for vector calculations (a possible exception is Gouyet *et al.* 2008, which is designed for continuum mechanics). For example, in Euclidean \mathbb{R}^3 there is never any need to store properties of the Riemann or torsion tensors and one may elect to use the identity metric. In addition, since the Levi-Civita symbol plays such a prominent role in vector calculus, it is desirable to have its expansions and contractions incorporated directly into routines. Indeed, the multi-term simplification functions are certainly the most novel feature of *VEST*. While such capabilities could have been added as an extension to an existing tensor manipulation package, with the addition of efficient tensor canonicalization functions in *Mathematica 9.0*, there seemed to be little to be gained through such an approach.

There are only a handful of previous software packages that are designed for working with abstract vector expressions. As well as some of the new functionality in *Mathematica 9.0* and functions in the *Maple Physics* package, the packages detailed in Fiedler (1997), Stoutemyer (1979), Wirth (1979), Qin *et al.* (1999), and Liang and Jeffrey (2007) include some abstract simplification capability (but only Liang and Jeffrey 2007 provides examples of simplifications that would be difficult to carry out by hand). Out of these previous packages, *VEST* is the first to work with general rules for gradient tensors and thus provide nontrivial simplifications of expressions involving gradient, divergence and curl. In addition, all of the vector algebra examples given in Liang and Jeffrey (2007) can be simplified, see Fig. E.1 for a selection of these. Note that all but one of the aforementioned examples are verified through reduction to standard form, without necessitating the use of the multi-term simplification capabilities of *VEST*. Utilization of these capabilities allows *VEST* to derive in real time many types of vector identities that have not (to my knowledge) appeared in any previous publications.

The remainder of the appendix is organized as follows. In Sec. E.2 I outline the foundations of the *VEST* package, including the use of abstract index notation and definition of a standard form. I then describe the function `ToCanonical`, which reduces any vector or scalar expres-

sion to standard form and is the main workhorse of the *VEST* package. Several relevant examples are given, illustrating various standard vector properties as well as more complex examples from the literature. While `ToCanonical` usually provides a thorough simplification, there are more complicated multi-term identities that are not recognized, and in section E.3 I explore some methods to provide further simplification of expressions. I briefly mention the function `FullSimplifyVectorForm`, which expands pairs of Levi-Civita symbols to generate identities for all terms in an expression (see Squire *et al.* 2014 for a more thorough description). A more general method of deriving vector identities based on symmetry properties is then given, with the idea that a similar technique will be implemented in a future version of *VEST*. Finally, in section E.4, I describe some additional tools provided in *VEST* with the aim of improving the usefulness of the package. These include: simple but very general input and output, explicit equality checking through expansion of sums, substitution capabilities, and automatic unit vector rule generation and simplification.

E.2 Index notation as a tool for vector calculus

While adequate for simple calculations, standard vector calculus notation [$\mathbf{A} \times \mathbf{B}$, $(\mathbf{b} \cdot \nabla) \mathbf{b}$, etc.] has numerous deficiencies when more complex expressions are involved. For instance, the meaning of the dot product can become ambiguous for higher rank tensors (e.g., derivatives) and seemingly disparate rules or "vector identities" (Huba, 2009) are needed to deal with specific cases of the cross product antisymmetry. To illustrate this latter point, although the exact correspondence between the identities $\nabla \times (\mathbf{a} \times \mathbf{b}) = \mathbf{a} \nabla \cdot \mathbf{b} - \mathbf{b} \nabla \cdot \mathbf{a} - (\mathbf{a} \cdot \nabla) \mathbf{b} + (\mathbf{b} \cdot \nabla) \mathbf{a}$ and $\mathbf{a} \times (\mathbf{b} \times \mathbf{c}) = \mathbf{b}(\mathbf{a} \cdot \mathbf{c}) - \mathbf{c}(\mathbf{a} \cdot \mathbf{b})$ is not entirely clear, both are simply expansions of the double cross product. In contrast, with a representation of vector objects in index notation using the Einstein summation convention, there is no trouble whatsoever with higher-rank tensors. In addition, many simple vector identities are an obvious consequence of the product rule and properties of

the Levi-Civita symbol, ε_{ijk} . This systemization makes index notation far more convenient for a computer algebra system. For the sake of input and output, it is straightforward (where possible) to convert between indexed and vector expressions using

$$\mathbf{a} \cdot \mathbf{b} \iff a_i b_i, \quad \nabla \cdot \mathbf{a} \iff a_{i,i}, \quad (\text{E.1a})$$

$$\mathbf{a} \times \mathbf{b} \iff \varepsilon_{ijk} a_j b_k, \quad \nabla \times \mathbf{a} \iff \varepsilon_{ijk} a_{k,j}, \quad (\text{E.1b})$$

$$\mathbf{a} \cdot \nabla \mathbf{b} \iff a_i b_{j,i}, \quad \nabla \mathbf{b} \cdot \mathbf{a} \iff a_i b_{i,j}, \quad (\text{E.1c})$$

$$\nabla \gamma \iff \gamma_{,j}, \quad (\text{E.1d})$$

for \mathbf{a} , \mathbf{b} vectors and γ a scalar. *VEST* includes functions to automatically perform the above conversions for both input and output. Note that, since by definition vector calculus is confined to Euclidean space, there is no need to distinguish between covariant and contravariant indices. I emphasize that this is not a restriction on a subsequent expansion into a curvilinear coordinate system, although an indexed expression cannot be interpreted in the literal sense (i.e., a sum over components) if a non-cartesian system is used. *VEST* also allows the use of a derivative with respect to a second coordinate (labelled v), since this functionality is useful in a variety of situations (for the transport calculation in chapter 6, this coordinate is used for $\partial/\partial k_i$ derivatives). For compactness, I shall notate this in a non-standard way with a semi-colon $\partial_v \mathbf{A} \iff A_{i;j}$, since it is not necessary to distinguish between the covariant and partial derivatives in Euclidean space.

E.2.1 Reduction to standard form

I now describe the `ToCanonical` function in *VEST*, which reduces expressions to the standard form defined by:

1. The expression is expanded into a sum of monomials.
2. There are no products inside partial derivatives and no nested derivatives.

3. Each term contains either no Levi-Civita symbols or one Levi-Civita symbol and no δ_{ij} (always possible for vector or scalar expressions).
4. The dummy indices in each monomial are reordered according to symmetry properties ensuring like terms appear as such. As a simple example of this type of reordering, $\varepsilon_{jik}b_ja_k$ becomes $\varepsilon_{ijk}a_jb_k$ due to the antisymmetry of ε_{ijk} .

Note that this is not a canonical form, since it is unique only for sufficiently simple expressions. The function name `ToCanonical` was chosen because the dummy reordering process (step 4) ensures that each monomial is in canonical form. Multi-term vector identities can lead to multiple polynomials being nontrivially equal after application of `ToCanonical`, motivating the implementation of *VEST*'s simplification functions (see Sec. E.3).

To bring an expression to the standard form defined above, `ToCanonical` uses the following sequence of steps:

1. Expand out products in partial derivatives and concatenate nested derivatives. For example,

$$(a_{i,j}b_j)_{,i} \xrightarrow{\text{expand}} (a_{i,j})_{,i} b_j + a_{i,j}b_{j,i} \xrightarrow{\text{concatenate}} a_{i,ij}b_j + a_{i,j}b_{j,i}.$$

2. Expand expression and find all dummy indices in each term. Check that these occur in pairs and free indices match across sum. Rename dummy indices in a consistent internal form so the procedure is not limited by the set number of user defined indices. Detailed information on the internal representation of objects and indices can be found in the tutorial supplied with *VEST*.

3. Expand pairs of Levi-Civita tensors according to

$$\varepsilon_{ijk}\varepsilon_{lmn} = \delta_{il}(\delta_{jm}\delta_{kn} - \delta_{jn}\delta_{km}) - \delta_{im}(\delta_{jl}\delta_{kn} - \delta_{jn}\delta_{kl}) + \delta_{in}(\delta_{jl}\delta_{km} - \delta_{jm}\delta_{kl}). \quad (\text{E.2})$$

4. Remove all δ_{ij} using $a_i\delta_{ij} = a_j$.

5. Apply user-defined rules. As a special case of this, rules associated to unit vectors are automatically derived and applied to relevant objects (see Sec. E.4).
6. Reorder dummy indices into a canonical form for each monomial in the expression. The problem of permuting indices can be very complex in large contractions and has historically been a major difficulty for tensor manipulation software, see for instance Martín-García (2008) and Manssur *et al.* (2002). *VEST* uses the *Mathematica* function `TensorReduce` (new in version 9.0), which has proven to be very reliable and efficient for our needs.
7. Print objects and dummy indices in a user-friendly output format (see Sec. E.4).

`ToCanonical` is relatively efficient and handles very large vector expressions with ease. As an example, a direct calculation of the guiding center Poisson tensor, which involves up to 1500 terms (after expansion of Levi-Civita symbols) and returns over 100 terms, takes approximately 15 seconds on a 2.26GHz Intel Core 2 Duo. If desired, parallelization would be straightforward.

The procedure detailed above effectively contains all of the most common vector identities (for instance all identities in Huba 2009), as well as many more complex identities. In Fig. E.1, I give some examples of the operation of `ToCanonical` on various vector expressions. Note that input and output can be in standard vector notation, indexed notation, or a mix of both. Several vector algebra examples have been taken from Liang and Jeffrey (2007), Cunningham (1969), Patterson (1968), and Stoutemyer (1979), with some examples involving gradients taken from Wimmel (1982).

E.3 Simplification through Levi-Civita expansions

The canonicalization of individual terms as carried out by `ToCanonical` does not recognize certain types of multi-term vector identities. In many cases, these can lead to substantial simplification of large expressions. Very few instances of this type of identity have been given in previous

Load package and define objects and indices.

```
<< VEST`
DefIndices[{i, j, k, l, p, q, r, s, m, n, t, u}];
DefObject[a, 1, {True, False}, "a"]
DefObject[b, 1, {True, False}, "b"]
DefObject[c, 1, {True, False}, "c"]
DefObject[d, 1, {True, False}, "d"]
DefObject[T, 2, {True, False}, "T", Symmetric[{1, 2}]]
DefObject[γ, 0, {True, False}, "γ"]
```

Some very simple canonicalization examples. Output can be printed in vector notation.

```
ToCanonical /@
{ b ⋅ a, -b ⋅ (c ⋅ a), div[γ a], div[curl[a]], curl[∇γ], γ a + curl[γ b], T[j, n] b[j] }
vectorForm /@ %
{-a_i b_j ε_{n i j}, -a_i b_j c_k ε_{k i j}, a_i γ_{,i} + a_{i,i} γ, 0, 0, -b_i ε_{n i j} γ_{,j} + a_n γ - ε_{n i j} b_{i,j} γ, b_i T_{n i}}
{-(a × b), -(c · (a × b)), (a · ∇γ) + γ (∇ · a), 0, 0, -(b × ∇γ) + (∇ × b) γ + a γ, b_i T_{n i}}
```

Some vector algebra examples from [Liang and Jeffrey 2007].

```
ToCanonical /@
{ a ⋅ (b ⋅ (c ⋅ d)) + b ⋅ (c ⋅ (d ⋅ a)) + c ⋅ (d ⋅ (a ⋅ b)) + d ⋅ (a ⋅ (b ⋅ c)) - (a ⋅ c) ⋅ (b ⋅ d),
  ((a ⋅ b) ⋅ (b ⋅ c)) ⋅ (c ⋅ a) - (a ⋅ (b ⋅ c)) (a ⋅ (b ⋅ c)),
  ((a ⋅ b) ⋅ c) ⋅ d + ((b ⋅ a) ⋅ d) ⋅ c + ((c ⋅ d) ⋅ a) ⋅ b + ((d ⋅ c) ⋅ b) ⋅ a }
{0, 0, 0}
```

Some identities involving ∇ from [Wimmel 1982].

```
vectorForm /@ ToCanonical /@ { (a ⋅ ∇b) ⋅ c + c ⋅ (∇b ⋅ a) - c ⋅ (a ⋅ curl[b]),
  (a ⋅ ∇b) ⋅ c - (c ⋅ ∇b) ⋅ a - (a ⋅ c) ⋅ curl[b],
  a ⋅ ∇(b ⋅ c) + c ⋅ ∇(b ⋅ a) - b ⋅ ∇(a ⋅ c) +
  (b ⋅ c) ⋅ curl[a] + (b ⋅ a) ⋅ curl[c] + (a ⋅ c) ⋅ curl[b] }
{0, 0, 2 (a · (∇b · c))}
```

Figure E.1: Various examples of the action of the *VEST* function `ToCanonical`.

literature; two examples are

$$\mathbf{d}(\mathbf{a} \cdot \mathbf{b} \times \mathbf{c}) - \mathbf{a}(\mathbf{b} \cdot \mathbf{c} \times \mathbf{d}) + \mathbf{b}(\mathbf{c} \cdot \mathbf{d} \times \mathbf{a}) - \mathbf{c}(\mathbf{d} \cdot \mathbf{a} \times \mathbf{b}) = 0, \quad (\text{E.3})$$

which is relatively well known, and

$$(\mathbf{a} \times \mathbf{c}) \cdot \nabla \mathbf{b} - \nabla \mathbf{b} \cdot (\mathbf{a} \times \mathbf{c}) - \mathbf{a}(\mathbf{c} \cdot \nabla \times \mathbf{b}) + \mathbf{c}(\mathbf{a} \cdot \nabla \times \mathbf{b}) = 0. \quad (\text{E.4})$$

There are in fact whole families of similar relations, including those involving more than one gradient tensors and more than four monomials.

Simplification of vector and tensor polynomials [e.g., Eqs. (E.3) and (E.4)] is provided by the *VEST* function `FullSimplifyVectorForm`. The basic mechanism is to insert products of Levi-Civita symbols using the identity

$$\frac{1}{2} \varepsilon_{irs} \varepsilon_{jrs} = \delta_{ij} \quad (\text{E.5})$$

into monomials, subsequently expanding out products of Levi-Civita symbols in a different orders. By generating a list of equivalent forms for each monomial and judiciously choosing forms from this list for each term in the polynomial, large simplifications can be found. Some identities found by `FullSimplifyVectorForm` have been quite nontrivial and apparently previously unpublished. Although these capabilities proved critical in other work (Burby *et al.*, 2013), because the final result of the calculation in chapter 6 involved scalar quantities, `FullSimplifyVectorForm` did not prove necessary for the work presented in this thesis. For this reason I refer to Squire *et al.* (2014) for details on these features of *VEST*.

E.3.1 More general methods for automatic generation of vector identities

While the method currently implemented in `FullSimplifyVectorForm` can easily and reliably generate many vector identities that have not appeared in previous literature, there are certain more complicated identities that cannot be recognized. Specifically, any nontrivial polynomial identity with no Levi-Civita symbols (i.e., involving *only* dot products) will not be identified by the above technique (I refer to Squire *et al.* 2014 for more explanation). Such relations are almost always rather long (an exception is when one or more of the vectors is a unit vector); however, they occur regularly in certain calculations – for example, the guiding center expansion at second order (Burby *et al.*, 2013) – and are usually very difficult to recognize. Application of such identities was also unnecessary for the work in this thesis; nonetheless, I include some details here because the method used to generate the relations is interesting, nonintuitive, and very general. The method encompasses previously unknown relations such as Eqs. (E.6) (see below), as well identities with cross-products [e.g., Eqs. (E.3) and (E.4)]. The hope is that simplification capabilities that rely on application of these identities will be included in a future release of *VEST*.

Let me start by giving an example. With up to two derivatives and without involving unit vector properties, the shortest such identity is given by

$$\begin{aligned}
0 = & (\mathbf{a}^2 \mathbf{c}^2 - (\mathbf{a} \cdot \mathbf{c})^2) \nabla \cdot \mathbf{b}^2 - (\mathbf{a}^2 \mathbf{c}^2 - (\mathbf{a} \cdot \mathbf{c})^2) b_{i,j} b_{j,i} + 2 \mathbf{a}^2 (\mathbf{c} \cdot \nabla \mathbf{b} \cdot \nabla \mathbf{b} \cdot \mathbf{c}) \\
& + 2 \mathbf{c}^2 (\mathbf{a} \cdot \nabla \mathbf{b} \cdot \nabla \mathbf{b} \cdot \mathbf{a}) - 2 (\mathbf{a} \cdot \mathbf{c}) (\mathbf{a} \cdot \nabla \mathbf{b} \cdot \nabla \mathbf{b} \cdot \mathbf{c} + \mathbf{c} \cdot \nabla \mathbf{b} \cdot \nabla \mathbf{b} \cdot \mathbf{a}) \\
& + 2 (\mathbf{a} \cdot \mathbf{c}) \nabla \cdot \mathbf{b} (\mathbf{a} \cdot \nabla \mathbf{b} \cdot \mathbf{c} + \mathbf{c} \cdot \nabla \mathbf{b} \cdot \mathbf{a}) + 2 (\mathbf{a} \cdot \nabla \mathbf{b} \cdot \mathbf{a}) (\mathbf{c} \cdot \nabla \mathbf{b} \cdot \mathbf{c}) \\
& - 2 (\mathbf{a} \cdot \nabla \mathbf{b} \cdot \mathbf{c}) (\mathbf{c} \cdot \nabla \mathbf{b} \cdot \mathbf{a}) - 2 \nabla \cdot \mathbf{b} (\mathbf{c}^2 (\mathbf{a} \cdot \nabla \mathbf{b} \cdot \mathbf{a}) + \mathbf{a}^2 (\mathbf{c} \cdot \nabla \mathbf{b} \cdot \mathbf{c})), \quad (\text{E.6})
\end{aligned}$$

for general vectors \mathbf{a} , \mathbf{b} and \mathbf{c} . For this collection of objects (two of each \mathbf{a} , $\nabla \mathbf{b}$ and \mathbf{c}), there also exists a slightly longer, very similar identity of 17 monomials. When unit vectors and/or more

derivative tensors are included, much shorter identities exist; for instance

$$-b_{i,j}b_{j,k}b_{k,i} + \frac{3}{2}b_{i,j}b_{j,i}\nabla \cdot \mathbf{b} - \frac{1}{2}(\nabla \cdot \mathbf{b})^3 = 0 \quad (\text{E.7})$$

is given in Littlejohn (1983) for a unit vector \mathbf{b} , and can also be derived through the method detailed in this section.² As another example, Eq. (E.6) reduces to 8 terms when \mathbf{a} or \mathbf{c} is set to \mathbf{b} and this is set as a unit vector.

The overall approach is based on the idea that antisymmetrization of an n -dimensional tensor over $n+1$ indices will automatically give a tensor polynomial that is identically zero. Such a polynomial is necessarily of relatively high rank, so the construction of interesting identities entails contracting over various pairs of indices. Note that almost all such contractions trivially canonicalize to zero and finding identities in this way by hand would be a very arduous task. The method is essentially an application of Lovelock's "dimensionally dependent identities" of the Riemann tensor (Lovelock, 1970) to tensor products of vectors and their gradients.

To be more precise, consider a general tensor $\mathcal{T}_{i_1 \dots i_k}$, where the i_k represent an arbitrary number of indices (note that I work in 3-D Euclidean space with all lower indices). For the cases I shall consider $\mathcal{T}_{i_1 \dots i_k}$, will be the product of vector objects, e.g., $a_i b_j c_k d_l \varepsilon_{rsq}$. Representing antisymmetrization by $[]$ around relevant indices, the identity

$$\mathcal{T}_{i_1 \dots i_{j-1} i_{j+1} \dots i_k [i_j \delta_{a_1}^{b_1} \delta_{a_2}^{b_2} \delta_{a_3}^{b_3}] = 0 \quad (\text{E.8})$$

must hold for for all $1 \leq j \leq k$, since the tensor is antisymmetric over four indices in three dimensions. In Eq. (E.8), δ_i^j is simply the standard Kronecker delta δ_{ij} ; I write it with an "up"

²Eq. (E.7) was derived in Littlejohn (1983) by noticing that it is nothing but the Cayley-Hamilton theorem for matrix $b_{i,j}$ satisfying $\det(b_{i,j}) = 0$. This method cannot be generalized to obtain other multi-term identities, but an interesting point is that the Cayley-Hamilton theorem is a simple consequence of the antisymmetrization procedure detailed in this section. Eq. (E.7) is the sole vector identity found in previous literature that cannot be recognized by the current version of `FullSimplifyVectorForm`.

index to more clearly show the antisymmetrization (note the non-standard use of this notation). One can also antisymmetrize over more indices of \mathcal{T} (and fewer δ_{ij}) if desired, but the resulting identity will involve only the relevant antisymmetric part of \mathcal{T} . Of course, in the case where \mathcal{T} is already antisymmetric in some set of indices (in our case due to ε_{ijk}), an identity involving the entirety of \mathcal{T} with fewer δ_{ij} can be obtained by antisymmetrizing over these indices. For example, with \mathcal{T} antisymmetric over $\{i_1, i_2, i_3\}$,

$$\mathcal{T}_{i_4 \dots i_k [i_1 i_2 i_3] \delta_{a_1}^{b_1}} = 0. \quad (\text{E.9})$$

This insight explains why vector identities that involve ε_{ijk} can be so much simpler than those that do not; any tensor with antisymmetry will naturally have identities with fewer terms than those without antisymmetry, since nontrivial identities in the form of Eq. (E.8) can be constructed with fewer indices.

The ideas of the previous paragraph can be used to automatically generate vector identities from a given set of vector objects. Although certainly not the most efficient method, a simple algorithm goes as follows:

1. For a given vector monomial, consider the tensor obtained by removing all contractions between dummy indices *e.g.*, for $a_i a_j b_i b_l b_j l b_k k$ this is $a_i a_j b_k b_l b_r s b_p q$.
2. Choose an index over which to antisymmetrize and form the polynomial given by Eq. (E.8). If one of the objects from step 1 is ε_{ijk} , construct Eq. (E.9) instead, antisymmetrizing over the indices of ε_{ijk} (the reason for this is simply to generate shorter identities). For instance, with the tensor example given in step 1, one could use $a_i a_j b_k b_l b_r s b_p [q \delta_a^b \delta_c^d \delta_e^f]$.
3. Contract the polynomial between index pairs. Aside from those contractions that are known *a priori* to give identically zero (see Edgar and Hoglund 2002) all possible contractions should be evaluated. For example, $a_i a_j b_k b_l b_r s b_p [q \delta_i^q \delta_r^j \delta_l^k]$ is the scalar formed by contraction

of the tensor given above between the index pairs

$\{\{1, 9\} \{2, 12\} \{3, 14\} \{4, 13\} \{5, 11\} \{6, 7\} \{8, 9\}\}$. If one wishes to generate only those identities involving the original scalar monomial (i.e., $a_i a_j b_l b_{j,l} b_{k,k}$ in the running example), consider only the set of contractions that have a possibility of generating this.

4. Canonicalize the resulting list of scalar or vector expressions to remove δ_{ij} and cancel relevant terms.

This procedure has been applied to various forms, systematically generating identities that involve a given set of objects, both with and without the Levi-Civita symbol. For instance, applying the method to the objects $\{\mathbf{a}, \mathbf{b}, \mathbf{c}, \mathbf{d}, \varepsilon\}$ (i.e., the tensor $a_i b_j c_k d_l \varepsilon_{rsq}$ at step 2) generates Eq. (E.3), Eq. (E.6) is generated with $\{\mathbf{a}, \mathbf{a}, \mathbf{c}, \mathbf{c}, \nabla \mathbf{b}, \nabla \mathbf{b}\}$, and Eq. (E.7) is generated with $\{\mathbf{b}, \mathbf{b}, \nabla \mathbf{b}, \nabla \mathbf{b}, \nabla \mathbf{b}\}$ (followed by an application of various unit vector identities). There are of course many other similar relations that are not listed here.

The *Invar* package Martín-García *et al.* (2007) uses a similar antisymmetrization-based method as part of its algorithm to generate scalar invariants of the Riemann tensor.

E.4 Additional *VEST* functionality

In addition to the functions described in Sections E.2 and E.3, *VEST* contains several other features than can be very useful when carrying out large calculations. In this section I briefly describe some of this functionality.

E.4.1 Intuitive and user friendly input and output

While very precise and straightforward to interpret, index notation can be inconvenient for the user, since expressions often look jumbled and confusing. As illustrated in Fig. E.1, *VEST* includes several features to facilitate user input and output, both in index and vector notation. Expressions

can be input in standard vector notation omitting indices (e.g., $\text{curl}[\mathbf{a}]$), full index notation, or a mix of both (e.g., $\text{div}[\mathbf{b}[\mathbf{i}]\mathbf{v}[\mathbf{i}]\mathbf{b}[\mathbf{j}]] + \mathbf{a} \cdot (\mathbf{T}[\mathbf{i}, \mathbf{j}]\mathbf{b}[\mathbf{j}])$). This allows for fast and reliable user input with the ability to represent more complex expressions when vector notation becomes ambiguous. In addition to coloring dummy index pairs so contractions are more immediately obvious, the function `vectorForm` prints expressions using vector notation where possible (up to first order derivatives); see Fig. E.1.

E.4.2 Checking expression equality

The function `CheckTensorZero` provides a very reliable check of whether an expression is identically zero. This is useful both for when one is not confident that `FullSimplifyVectorForm` has reached the shortest possible form and for rapid verification of results. The function works in a very straightforward way by expanding an expression into Cartesian coordinates, which amounts to explicitly evaluating all sums over dummy indices.

E.4.3 Substitutions

A very common application of a computer algebra package is the substitution of some explicit expression into a given form; i.e., given a specific a , calculate $f(a)$. While this is a very simple process for standard algebraic expressions, the task becomes more awkward when the substitution involves indexed expressions. To illustrate this, consider as a basic example the evaluation of

$$a_i a_{j,k} b_j b_k, \text{ with } a_i = b_j d_j d_i. \quad (\text{E.10})$$

There are two issues that arise if one attempts a naive substitution of a_i : first, the free index of $a_i = b_j d_j d_i$ must be replaced with the correct indices in $a_i a_{j,k} b_j b_k$; second, one must ensure that dummy indices in the substituted a_i do not conflict with those in $a_i a_{j,k} b_j b_k$. While these issues are

in principle not complicated, forcing the user to keep track of all indices would be a particularly inconvenient characteristic that would significantly reduce the utility of an index notation based package.

In *VEST* substitution of arbitrary expressions is handled through a new assignment operator $\stackrel{\text{ind}}{=}$, which automatically manages assignment of free indices and ensures dummies do not overlap. Rather than simply assigning an expression to the left hand side, $\stackrel{\text{ind}}{=}$ assigns a call to the function `FindDummies`, which is used in step 2 of `ToCanonical` (see Sec. E.2.1) and can generate a new set of indices at every call. After assignment with $\stackrel{\text{ind}}{=}$, an object can be used in exactly the same way as a standard indexed object without the user having to worry about its underlying structure. To illustrate with the example of Eq. (E.10), after assigning a $\stackrel{\text{ind}}{=} b[j]d[j]d[i]$, evaluating $a_i a_{j,k} b_j b_k$ in the standard way will generate a valid indexed expression.

These capabilities and the $\stackrel{\text{ind}}{=}$ operator were used extensively in the calculations presented in chapter 6.

E.4.4 Unit vectors and user defined rules

As examples earlier in the text have illustrated (e.g., Sec. E.3.1), unit vector identities can provide very substantial simplifications and it is important to make provision for these. Representing an arbitrary unit vector by b_i , *VEST* automatically generates identities by differentiating $b_i b_i = 1$ up to a user-specified order and applies these rules as part of `ToCanonical` and `FullSimplifyVectorForm`. A related feature is the ability for the user to define rules that are applied as part of `ToCanonical`. This is very useful both when nontrivial relationships between objects need to be identified (e.g., $\varepsilon_{ijk} D_{jl} \hat{g}_l B_k = (\hat{g} \cdot \mathbf{D}) \times \mathbf{B}$ was used to extract scalar transport coefficients in chapter 6) and when working with expressions that involve nontrivial scalar expressions in the denominator.

Bibliography

- R. Alexander (2008), “From discs to planetesimals: Evolution of gas and dust discs,” *New Astron. Rev.* **52**, 60–77.
- ALMA Partnership *et al.* (2015), “First results from high angular resolution ALMA observations toward the HL Tau region,” arXiv.org [1503.02649v3](https://arxiv.org/abs/1503.02649v3) .
- X.-N. Bai, and J. M. Stone (2013), “Wind-driven accretion in protoplanetary disks. I. Suppression of the magnetorotational instability and launching of the magnetocentrifugal wind,” *Astrophys. J.* **769**, 76–97.
- N. A. Bakas, and P. J. Ioannou (2009), “Modal and nonmodal growths of inviscid planar perturbations in shear flows with a free surface,” *Phys. Fluids* **21**, 024102 (14 pages).
- S. A. Balbus, and J. F. Hawley (1991), “A powerful local shear instability in weakly magnetized disks. I - Linear analysis. II - Nonlinear evolution,” *Astrophys. J.* **376**, 214–233.
- S. A. Balbus, and J. F. Hawley (1992), “A powerful local shear instability in weakly magnetized disks. IV. Nonaxisymmetric perturbations,” *Astrophys. J.* **400**, 610–621.
- S. A. Balbus, and J. F. Hawley (1998), “Instability, turbulence, and enhanced transport in accretion disks,” *Rev. Mod. Phys.* **70**, 1 (53 pages).
- S. A. Balbus, and J. F. Hawley (2006), “An exact, three-dimensional, time-dependent wave solution in local Keplerian flow,” *Astrophys. J.* **652**, 1020–1027.
- A. Bhattacharjee, and E. Hameiri (1986), “Self-consistent dynamolike activity in turbulent plasmas,” *Phys. Rev. Lett.* **57**, 206–209.
- A. Bhattacharjee, and Y. Yuan (1995), “Self-consistency constraints on the dynamo mechanism,” *Astrophys. J.* **449**, 739–744.
- E. Blackman, and G. Field (2002), “New dynamical mean-field dynamo theory and closure approach,” *Phys. Rev. Lett.* **89**, 265007 (4 pages).
- E. G. Blackman (2012), “Accretion disks and dynamos: toward a unified mean field theory,” *Physica Scripta* **86**, 058202 (23 pages).

- E. G. Blackman, and A. Brandenburg (2002), “Dynamic nonlinearity in large-scale dynamos with shear,” *Astrophys. J.* **579**, 359–373.
- E. G. Blackman, and J. C. Tan (2004), “Coronae & outflows from helical dynamos, compatibility with the MRI, and application to protostellar disks,” *Astrophys. Space Sci.* **292**, 395–406.
- O. M. Blaes (2004), “Course 3: Physics fundamentals of luminous accretion disks around black holes,” in *Accretion Discs, Jets and High Energy Phenomena in Astrophysics*, edited by V. Beskin, G. Henri, F. Menard, *et al.*, pp. 137–185, [astro-ph/0211368](#).
- J. W. S. Blokland, E. van der Swaluw, R. Keppens, and J. P. Goedbloed (2005), “Magneto-rotational overstability in accretion disks,” *Astron. Astrophys.* **444**, 337–346.
- G. Bodo, F. Cattaneo, A. Mignone, and P. Rossi (2014), “On the convergence of magnetorotational turbulence in stratified isothermal shearing boxes,” *Astrophys. J.* **787**, L13–L17.
- G. Bodo, A. Mignone, F. Cattaneo, P. Rossi, and A. Ferrari (2008), “Aspect ratio dependence in magnetorotational instability shearing box simulations,” *Astron. Astrophys.* **487**, 1–5.
- S. Boldyrev, F. Cattaneo, and R. Rosner (2005), “Magnetic-field generation in helical turbulence,” *Phys. Rev. Lett.* **95**, 255001 (4 pages).
- A. Bonanno, and V. Urpin (2008), “Non-axisymmetric instability of axisymmetric magnetic fields,” *Astron. Astrophys.* **488**, 1–7.
- A. Bondeson, R. Iacono, and A. Bhattacharjee (1987), “Local magnetohydrodynamic instabilities of cylindrical plasma with sheared equilibrium flows,” *Phys. Fluids* **30**, 2167–2180.
- A. H. Boozer (1986), “Ohm’s law for mean magnetic fields,” *J. Plasma Phys.* **35**, 133–139.
- F. Bouchet, C. Nardini, and T. Tangarife (2013), “Kinetic theory of jet dynamics in the stochastic barotropic and 2D Navier-Stokes equations,” *J. Stat. Phys.* **153**, 572–625.
- A. Brandenburg (2008), “The dual role of shear in large-scale dynamos,” *Astron. Nachr.* **329**, 725–731.
- A. Brandenburg (2009), “Large-scale dynamos at low magnetic Prandtl numbers,” *Astrophys. J.* **697**, 1206–1213.
- A. Brandenburg, and B. Dintrans (2006), “Nonaxisymmetric stability in the shearing sheet approximation,” *Astron. Astrophys.* **450**, 437–444.
- A. Brandenburg, A. Nordlund, R. F. Stein, and U. Torkelsson (1995), “Dynamo-generated turbulence and large-scale magnetic fields in a Keplerian shear flow,” *Astrophys. J.* **446**, 741–754.
- A. Brandenburg, K. H. Rädler, M. Rheinhardt, and P. J. Käpylä (2008a), “Magnetic diffusivity tensor and dynamo effects in rotating and shearing turbulence,” *Astrophys. J.* **676**, 740–751.

- A. Brandenburg, K.-H. Rädler, M. Rheinhardt, and K. Subramanian (2008b), “Magnetic quenching of α and diffusivity tensors in helical turbulence,” *Astrophys. J.* **687**, L49–L52.
- A. Brandenburg, and D. Sokoloff (2002), “Local and nonlocal magnetic diffusion and alpha-effect tensors in shear flow turbulence,” *Geophys. Astrophys. Fluid Dyn.* **96**, 319–344.
- A. Brandenburg, D. Sokoloff, and K. Subramanian (2012), “Current status of turbulent dynamo theory. from large-scale to small-scale dynamos,” *Space Sci. Rev.* **169**, 123–157.
- A. Brandenburg, and K. Subramanian (2005), “Astrophysical magnetic fields and nonlinear dynamo theory,” *Phys. Rep.* **417**, 1–209.
- V. Bratanov, F. Jenko, D. R. Hatch, and M. Wilczek (2013), “Nonuniversal power-law spectra in turbulent systems,” *Phys. Rev. Lett.* **111**, 075001 (4 pages).
- K. A. Brucker, J. C. Isaza, T. Vaithianathan, and L. R. Collins (2007), “Efficient algorithm for simulating homogeneous turbulent shear flow without remeshing,” *J. Comp. Phys.* **225**, 20–32.
- J. W. Burby, J. Squire, and H. Qin (2013), “Automation of the guiding center expansion,” *Phys. Plasmas* **20**, 072105 (13 pages).
- P. J. Bushby, and M. R. E. Proctor (2010), “The influence of α -effect fluctuations and the shear-current effect upon the behaviour of solar mean-field dynamo models,” *Mon. Not. R. Astron. Soc.* **409**, 1611–1618.
- K. M. Butler, and B. F. Farrell (1993), “Optimal perturbations and streak spacing in wall-bounded turbulent shear flow,” *Phys. Fluids A* **5**, 774–777.
- E. Camporeale (2012), “Nonmodal linear theory for space plasmas,” *Space Sci. Rev.* **172**, 397–409.
- S. Candelaresi, A. Hubbard, A. Brandenburg, and D. Mitra (2011), “Magnetic helicity transport in the advective gauge family,” *Phys. Plasmas* **18**, 012903 (11 pages).
- F. Cattaneo, and D. W. Hughes (2009), “Problems with kinematic mean field electrodynamics at high magnetic Reynolds numbers,” *Mon. Not. R. Astron. Soc.* **395**, L48–L51.
- F. Cattaneo, and S. M. Tobias (2014), “On large-scale dynamo action at high magnetic Reynolds number,” *Astrophys. J. Lett.* **789**, 70–80.
- S. Chandrasekhar (1960), “The stability of non-dissipative Couette flow in hydromagnetics,” in *Proceedings of the National Academy of Sciences of the United States of America*, pp. 253–257.
- C. Collins, M. Clark, C. M. Cooper, K. Flanagan, I. V. Khalzov, M. D. Nornberg, B. Seidlitz, J. Wallace, and C. B. Forest (2014), “Taylor-Couette flow of unmagnetized plasma,” *Phys. Plasmas* **21**, 042117 (8 pages).
- C. Cossu, G. Pujals, and S. Depardon (2008), “Optimal transient growth and very large-scale structures in turbulent boundary layers,” *J. Fluid Mech.* **619**, 79–94.

- A. Courvoisier, D. W. Hughes, and M. R. E. Proctor (2010), “A self-consistent treatment of the electromotive force in magnetohydrodynamics for large diffusivities,” *Astron. Nachr.* **331**, 667–670.
- J. Cunningham (1969), *Vectors* (Heinemann Educational Books Ltd, London).
- C. Curry, and R. E. Pudritz (1996), “On the global stability of magnetized accretion discs - III. Non-axisymmetric modes,” *Mon. Not. R. Astron. Soc.* **281**, 119–136.
- C. Curry, R. E. Pudritz, and P. G. Sutherland (1994), “On the global stability of magnetized accretion disks. I. Axisymmetric modes,” *Astrophys. J.* **434**, 206–220.
- S. W. Davis, J. M. Stone, and M. E. Pessah (2010), “Sustained magnetorotational turbulence in local simulations of stratified disks with zero net magnetic flux,” *Astrophys. J.* **713**, 52–65.
- J. Dongarra, B. Straughan, and D. Walker (1996), “Chebyshev tau-QZ algorithm methods for calculating spectra of hydrodynamic stability problems,” *Appl. Num. Math.* **22** (4), 399 – 434.
- C. Donnelly (2013), *Shearing Waves and the MRI Dynamo in Stratified Accretion Discs*, Ph.D. thesis (Cambridge University).
- J. W. Eastwood (1991), “ORTHOVEC: version 2 of the REDUCE program for 3-D vector analysis in orthogonal curvilinear coordinates,” *Comp. Phys. Comm.* **64** (1), 121–122.
- F. Ebrahimi, and A. Bhattacharjee (2014), “Helicity-flux-driven α effect in laboratory and astrophysical plasmas,” *Phys. Rev. Lett.* **112**, 125003 (4 pages).
- F. Ebrahimi, B. Lefebvre, C. B. Forest, and A. Bhattacharjee (2011), “Global hall-MHD simulations of magnetorotational instability in a plasma Couette flow experiment,” *Phys. Plasmas* **18**, 062904 (13 pages).
- S. B. Edgar, and A. Høglund (2002), “Dimensionally dependent tensor identities by double antisymmetrization,” *J. Math. Phys.* **43**, 659–677.
- B. F. Farrell, and P. J. Ioannou (1993), “Stochastic forcing of the linearized Navier-Stokes equations,” *Phys. Fluids A* **5**, 2600–2609.
- B. F. Farrell, and P. J. Ioannou (1994), “Variance maintained by stochastic forcing of non-normal dynamical systems associated with linearly stable shear flows,” *Phys. Rev. Lett.* **72**, 1188–1192.
- B. F. Farrell, and P. J. Ioannou (1996), “Generalized stability theory. Part II: Nonautonomous operators,” *J. Atmos. Sci.* **53**, 2041–2053.
- B. F. Farrell, and P. J. Ioannou (2003), “Structural stability of turbulent jets,” *J. Atmos. Sci.* **60**, 2101–2118.
- B. F. Farrell, and P. J. Ioannou (2009), “A stochastic structural stability theory model of the drift wave–zonal flow system,” *Phys. Plasmas* **16**, 112903 (11 pages).

- B. F. Farrell, and P. J. Ioannou (2012), “Dynamics of streamwise rolls and streaks in turbulent wall-bounded shear flow,” *J. Fluid Mech.* **708**, 149–196.
- B. F. Farrell, and P. J. Ioannou (2014), “Statistical state dynamics: a new perspective on turbulence in shear flow,” *Zonal Jets*, 1–23.
- B. Fiedler (1997), “Vectan 1.1,” Manual Math. Inst., Univ. Leipzig.
- M. Flock, N. Dzyurkevich, H. Klahr, N. Turner, and T. Henning (2011), “Large-scale azimuthal structures of turbulence in accretion disks: Dynamo triggered variability of accretion,” *Astrophys. J.* **744**, 144–158.
- M. Flock, T. Henning, and H. Klahr (2012), “Turbulence in weakly ionized protoplanetary disks,” *Astrophys. J.* **761**, 95–103.
- B. Friedman, and T. A. Carter (2014), “Linear technique to understand non-normal turbulence applied to a magnetized plasma,” *Phys. Rev. Lett.* **113**, 025003 (4 pages).
- M. Frigo, and S. G. Johnson (2005), “The design and implementation of FFTW3,” in *Proceedings of the IEEE*.
- S. Fromang (2010), “MHD simulations of the magnetorotational instability in a shearing box with zero net flux: the case $Pm = 4$,” *Astron. Astrophys.* **514**, L5–L9.
- S. Fromang, and J. Papaloizou (2007), “MHD simulations of the magnetorotational instability in a shearing box with zero net flux. I. The issue of convergence,” *Astron. Astrophys.* **476**, 1113–1122.
- S. Fromang, J. Papaloizou, G. Lesur, and T. Heinemann (2007), “MHD simulations of the magnetorotational instability in a shearing box with zero net flux. II. The effect of transport coefficients,” *Astron. Astrophys.* **476**, 1123–1132.
- C. W. Gardiner (2004), *Handbook of Stochastic Methods for Physics, Chemistry, and the Natural Sciences* (Springer Verlag).
- C. Gissinger, J. Goodman, and H. Ji (2012), “The role of boundaries in the magnetorotational instability,” *Phys. Fluids* **24**, 074109 (15 pages).
- C. Gissinger, H. Ji, and J. Goodman (2011), “Instabilities in magnetized spherical Couette flow,” *Phys. Rev. E* **84**, 026308 (10 pages).
- J. P. Goedbloed, R. Keppens, and S. Poedts (2010), *Advanced Magnetohydrodynamics, With Applications to Laboratory and Astrophysical Plasmas* (Cambridge University Press).
- J. Goodman, and G. Xu (1994), “Parasitic instabilities in magnetized, differentially rotating disks,” *Astrophys. J.* **432**, 213–223.

- J. F. Gouyet, R. Cabrera, and D. Park (2008), “**Tensorial 4.0 and TContinuumMechanics 2.0**,” .
- O. Gressel (2010), “A mean-field approach to the propagation of field patterns in stratified magnetorotational turbulence,” *Mon. Not. R. Astron. Soc.* **405**, 41–48.
- A. V. Gruzinov, and P. H. Diamond (1994), “Self-consistent theory of mean-field electrodynamics,” *Phys. Rev. Lett.* **72**, 1651–1653.
- G. Guennebaud, B. Jacob, *et al.* (2010), “Eigen v3,” <http://eigen.tuxfamily.org>.
- A. Guha, and G. A. Lawrence (2014), “A wave interaction approach to studying non-modal homogeneous and stratified shear instabilities,” *J. Fluid Mech.* **755**, 336–364.
- J. F. Hawley, C. F. Gammie, and S. A. Balbus (1995), “Local three-dimensional magnetohydrodynamic simulations of accretion disks,” *Astrophys. J.* **440**, 742–763.
- J. F. Hawley, C. F. Gammie, and S. A. Balbus (1996), “Local three-dimensional simulations of an accretion disk hydromagnetic dynamo,” *Astrophys. J.* **464**, 690–703.
- J. F. Hawley, S. A. Richers, X. Guan, and J. H. Krolik (2013), “Testing convergence for global accretion disks,” *Astrophys. J.* **772**, 102–117.
- T. Heinemann, J. C. McWilliams, and A. A. Schekochihin (2011), “Large-scale magnetic field generation by randomly forced shearing waves,” *Phys. Rev. Lett.* **107**, 255004 (4 pages).
- T. Heinemann, and J. C. B. Papaloizou (2009), “The excitation of spiral density waves through turbulent fluctuations in accretion discs - I. WKB theory,” *Mon. Not. R. Astron. Soc.* **397**, 52–63.
- B. Hof, J. Westerweel, T. M. Schneider, and B. Eckhardt (2006), “Finite lifetime of turbulence in shear flows,” *Nature* **443**, 59–62.
- R. Hollerbach, and G. Rüdiger (2005), “New type of magnetorotational instability in cylindrical Taylor-Couette flow,” *Phys. Rev. Lett.* **95**, 124501 (4 pages).
- R. Hollerbach, V. Teeluck, and G. Rüdiger (2010), “Nonaxisymmetric magnetorotational instabilities in cylindrical Taylor-Couette flow,” *Phys. Rev. Lett.* **104**, 044502 (4 pages).
- H. Hotta, M. Rempel, and T. Yokoyama (2015), “Efficient small-scale dynamo in the solar convection zone,” *Astrophys. J.* **803**, 42–56.
- J. D. Huba (2009), “NRL Plasma Formulary,” Supported by the Office of Naval Research.
- A. Hubbard, and A. Brandenburg (2012), “Catastrophic quenching in $\alpha\omega$ dynamos revisited,” *Astrophys. J.* **748**, 51–60.
- A. Hubbard, F. Del Sordo, P. J. Käpylä, and A. Brandenburg (2009), “The α effect with imposed and dynamo-generated magnetic fields,” *Mon. Not. R. Astron. Soc.* **398**, 1891–1899.

- P. J. Ioannou, and A. Kakouris (2001), “Stochastic dynamics of Keplerian accretion disks,” *Astrophys. J.* **550**, 931–943.
- H. Ji (1999), “Turbulent dynamos and magnetic helicity,” *Phys. Rev. Lett.* **83**, 3198–3201, [astro-ph/0102321](#).
- H. Ji, M. Burin, E. Scharfman, and J. Goodman (2006), “Hydrodynamic turbulence cannot transport angular momentum effectively in astrophysical disks,” *Nature* **444**, 343–346.
- H. Ji, J. Goodman, and A. Kageyama (2001), “Magnetorotational instability in a rotating liquid metal annulus,” *Mon. Not. R. Astron. Soc.* **325**, 1–5.
- A. Johansen, A. Youdin, and H. Klahr (2009), “Zonal flows and long-lived axisymmetric pressure bumps in magnetorotational turbulence,” *Astrophys. J.* **697**, 1269–1289.
- B. M. Johnson (2007), “Magnetohydrodynamic shearing waves,” *Astrophys. J.* **660**, 1375–1385.
- P. J. Käpylä, and M. J. Korpi (2011), “Magnetorotational instability driven dynamos at low magnetic Prandtl numbers,” *Mon. Not. R. Astron. Soc.* **413**, 901–907.
- E. Kersalé, D. W. Hughes, G. I. Ogilvie, and S. M. Tobias (2006), “Global magnetorotational instability with inflow. II. The nonlinear development of axisymmetric wall modes,” *Astrophys. J.* **638**, 382–390.
- E. Kersalé, D. W. Hughes, G. I. Ogilvie, S. M. Tobias, and N. O. Weiss (2004), “Global magnetorotational instability with inflow. I. Linear theory and the role of boundary conditions,” *Astrophys. J.* **602**, 892–903.
- L. L. Kichatinov, and V. V. Pipin (1993), “Mean-field buoyancy,” *Astron. Astro.* **274**, 647–652.
- L. L. Kichatinov, and G. Rüdiger (1992), “Magnetic-field advection in inhomogeneous turbulence,” *Astron. Astrophys.* **260**, 494–498.
- J. Kim, P. Moin, and R. Moser (1987), “Turbulence statistics in fully developed channel flow at low Reynolds number,” *J. Fluid Mech.* **177**, 133–166.
- O. N. Kirillov, and F. Stefani (2013), “Extending the range of the inductionless magnetorotational instability,” *Phys. Rev. Lett.* **111**, 061103 (4 pages).
- L. L. Kitchatinov, and G. Rüdiger (2010), “Nonaxisymmetric modes of MRI in dissipative Keplerian disks,” *Astron. Astrophys.* **513**, L1–L4.
- N. Kleeorin, and I. Rogachevskii (2007), “New mechanism of generation of large-scale magnetic field in a sheared turbulent plasma,” *Planet. Space Sci.* **55**, 2315–2318.
- E. Knobloch (1992), “On the stability of magnetized accretion discs,” *Mon. Not. R. Astron. Soc.* **255**, 25–28.

- G. Kowal, K. Otmianowska-Mazur, and M. Hanasz (2005), “Calculation of dynamo coefficients in cosmic-ray driven dynamo experiment,” *The Magnetized Plasma in Galaxy Evolution*, 171–176.
- R. H. Kraichnan (1971), “An almost-Markovian Galilean-invariant turbulence model,” *Journal of Fluid Mechanics* **47**, 513–524.
- R. H. Kraichnan (1976), “Diffusion of weak magnetic fields by isotropic turbulence,” *J. Fluid Mech.* **75**, 657–676.
- F. Krause, and K. H. Rädler (1980), *Mean-field magnetohydrodynamics and dynamo theory* (Oxford: Pergamon Press).
- J. H. Krolik (1999), *Active Galactic Nuclei, From the Central Black Hole to the Galactic Environment* (Princeton University Press).
- R. M. Kulsrud, and S. W. Anderson (1992), “The spectrum of random magnetic fields in the mean field dynamo theory of the galactic magnetic field,” *Astrophys. J.* **396**, 606–630.
- M. W. Kunz, and S. A. Balbus (2004), “Ambipolar diffusion in the magnetorotational instability,” *Mon. Not. R. Astron. Soc.* **348**, 355–360.
- M. W. Kunz, and G. Lesur (2013), “Magnetic self-organization in hall-dominated magnetorotational turbulence,” *Mon. Not. R. Astron. Soc.* **434**, 2295–2312.
- H. N. Latter, S. Fromang, and O. Gressel (2010), “MRI channel flows in vertically stratified models of accretion discs,” *Mon. Not. R. Astron. Soc.* **406**, 848–862.
- H. N. Latter, P. Lesaffre, and S. A. Balbus (2009), “MRI channel flows and their parasites,” *Mon. Not. R. Astron. Soc.* **394**, 715–729.
- M. Lee, N. Malaya, and R. D. Moser (2013), “Petascale direct numerical simulation of turbulent channel flow on up to 786k cores,” in *the International Conference for High Performance Computing, Networking, Storage and Analysis* (ACM Press, New York, New York, USA) pp. 1–11.
- N. Leprovost, and E.-J. Kim (2008), “Analytical theory of forced rotating sheared turbulence: The parallel case,” *Phys. Rev. E* **78**, 036319 (12 pages).
- G. Lesur, M. W. Kunz, and S. Fromang (2014), “Thanatology in protoplanetary discs. The combined influence of ohmic, hall, and ambipolar diffusion on dead zones,” *Astron. Astrophys.* **566**, 56–73.
- G. Lesur, and P. Y. Longaretti (2005), “On the relevance of subcritical hydrodynamic turbulence to accretion disk transport,” *Astron. Astrophys.* **444**, 25–44.

- G. Lesur, and P. Y. Longaretti (2007), “Impact of dimensionless numbers on the efficiency of magnetorotational instability induced turbulent transport,” *Mon. Not. R. Astron. Soc.* **378**, 1471–1480.
- G. Lesur, and P. Y. Longaretti (2011), “Non-linear energy transfers in accretion discs MRI turbulence. I. Net vertical field case,” *Astron. Astrophys.* **528**, 17–27.
- G. Lesur, and G. I. Ogilvie (2008a), “Localized magnetorotational instability and its role in the accretion disc dynamo,” *Mon. Not. R. Astron. Soc.* **391**, 1437–1450.
- G. Lesur, and G. I. Ogilvie (2008b), “On self-sustained dynamo cycles in accretion discs,” *Astron. Astrophys.* **488**, 451–461.
- S. Liang, and D. J. Jeffrey (2007), “Rule-based simplification in vector-product spaces,” *Towards Mechanized Mathematical Assistants, Lecture Notes in Artificial Intelligence*, 116–127.
- Y. Lithwick (2007), “Nonlinear evolution of hydrodynamical shear flows in two dimensions,” *Astrophys. J.* **670**, 789–804.
- R. Littlejohn (1983), “Variational principles of guiding centre motion,” *J. Plasma Phys.* **29**, 111–125.
- W. Liu, J. Goodman, I. Herron, and H. Ji (2006), “Helical magnetorotational instability in magnetized Taylor-Couette flow,” *Phys. Rev. E* **74**, 056302 (11 pages).
- P. Y. Longaretti, and G. Lesur (2010), “MRI-driven turbulent transport: the role of dissipation, channel modes and their parasites,” *Astron. Astrophys.* **516**, 51–62.
- D. Lovelock (1970), “Dimensionally dependent identities,” *Math. Proc. Camb. Phil. Soc.* **68**, 345–350.
- A. Lundbladh, D. S. Henningson, and A. V. Johansson (1992), “An efficient spectral integration method for the solution of the Navier-Stokes equations,” *NASA STI/Recon Technical Report N* **93**, 29009.
- M. A. H. MacCallum (2002), “Computer algebra in general relativity,” *Int. J. Mod. Phys. A* **17**, 2707–2710.
- S. M. Mahajan, and V. Krishan (2008), “Existence of the magnetorotational instability,” *Astrophys. J.* **682**, 602–607.
- G. R. Mamatsashvili, G. D. Chagelishvili, G. Bodo, and P. Rossi (2013), “Revisiting linear dynamics of non-axisymmetric perturbations in weakly magnetized accretion discs,” *Mon. Not. R. Astron. Soc.* **435**, 2552–2567.
- L. R. U. Manssur, R. Portugal, and B. Svaiter (2002), “Group-theoretic approach for symbolic tensor manipulation,” *Int. J. Mod. Phys. C* **13**, 859–879.

- Maple (2015), “Maple Waterloo Software inc.” See <http://www.maplesoft.com>.
- J. Marston (2012), “Planetary atmospheres as nonequilibrium condensed matter,” *Annu. Rev. Condens. Matter Phys.* **3**, 285–310.
- J. B. Marston, E. Conover, and T. Schneider (2008), “Statistics of an unstable barotropic jet from a cumulant expansion,” *J. Atmos. Sci.* **65**, 1955–1966.
- J. M. Martín-García (2002–2012), “Efficient tensor computer algebra,” .
- J. M. Martín-García (2008), “*xPerm*: fast index canonicalization for tensor computer algebra,” *Comp. Phys. Comm.* **179**, 597–603.
- J. M. Martín-García, R. Portugal, and L. Manssur (2007), “The *Invar* tensor package,” *Comp. Phys. Comm.* **177** (8), 640 – 648.
- Mathematica (2015), *Mathematica, Version 10.0* (Wolfram Research Inc., Champaign, Illinois).
- J. C. McWilliams (2012), “The elemental shear dynamo,” *J. Fluid Mech.* **699**, 414–452.
- H. Meheut, F. Casse, P. Varniere, and M. Tagger (2010), “Rossby wave instability and three-dimensional vortices in accretion disks,” *Astron. Astrophys.* **516**, 31–40.
- H. Meheut, S. Fromang, G. Lesur, M. Joos, and P.-Y. Longaretti (2015), “Angular momentum transport and large eddy simulations in magnetorotational turbulence: the small Pm limit,” *Astron. Astrophys.* **579**, 117–129.
- D. Mitra, and A. Brandenburg (2012), “Scaling and intermittency in incoherent α -shear dynamo,” *Mon. Not. R. Astron. Soc.* **420**, 2170–2177.
- H. K. Moffatt (1978), *Magnetic Field Generation in Electrically Conducting Fluids* (Cambridge University Press).
- H. K. Moffatt, and M. R. E. Proctor (1982), “The role of the helicity spectrum function in turbulent dynamo theory,” *Geophys. Astrophys. Fluid Dyn.* **21**, 265–283.
- B. Mukhopadhyay, N. Afshordi, and R. Narayan (2005), “Bypass to turbulence in hydrodynamic accretion disks: an eigenvalue approach,” *Astrophys. J.* **629**, 383–396.
- G. I. Ogilvie, and J. E. Pringle (1996), “The non-axisymmetric instability of a cylindrical shear flow containing an azimuthal magnetic field,” *Mon. Not. R. Astron. Soc.* **279**, 152–164.
- J. S. Oishi, and M.-M. Mac Low (2011), “Magnetorotational turbulence transports angular momentum in stratified disks with low magnetic Prandtl number but magnetic Reynolds number above a critical value,” *Astrophys. J.* **740**, 18–29.
- J. C. B. Papaloizou, and J. E. Pringle (1985), “The dynamical stability of differentially rotating discs. II,” *Mon. Not. R. Astron. Soc.* **213**, 799–820.

- J. C. B. Papaloizou, and C. Terquem (1997), “On the stability of an accretion disc containing a toroidal magnetic field: the effect of resistivity,” *Mon. Not. R. Astron. Soc.* **287**, 771–789.
- K. Park, and E. G. Blackman (2012), “Simulations of a magnetic fluctuation driven large-scale dynamo and comparison with a two-scale model,” *Mon. Not. R. Astron. Soc.* **423**, 2120–2131.
- J. B. Parker, and J. A. Krommes (2013), “Zonal flow as pattern formation,” *Phys. Plasmas* **20**, 100703 (4 pages).
- L. Parker, and S. Christensen (1994), *MathTensor: A system for doing tensor analysis by computer* (Addison-Wesley, Reading, MA).
- E. Patterson (1968), *Solving problems in vector algebra* (Oliver and Boyd Ltd, Edinburgh-London).
- K. Peeters (2007), “Cadabra: a field-theory motivated symbolic computer algebra system,” *Comp. Phys. Comm.* **176** (8), 550–558.
- M. E. Pessah, and J. Goodman (2009), “On the saturation of the magnetorotational instability via parasitic modes,” *Astrophys. J.* **698**, L72–L76.
- M. E. Pessah, and D. Psaltis (2005), “The stability of magnetized rotating plasmas with superthermal fields,” *Astrophys. J.* **628**, 879–901.
- V. V. Pipin (2008), “The mean electro-motive force and current helicity under the influence of rotation, magnetic field and shear,” *Geophys. Astrophys. Fluid Dyn.* **102**, 21–49.
- A. Pouquet, U. Frisch, and J. Leorat (1976), “Strong MHD helical turbulence and the nonlinear dynamo effect,” *J. Fluid Mech.* **77**, 321–354.
- M. R. E. Proctor (2007), “Effects of fluctuation on $\alpha\omega$ dynamo models,” *Mon. Not. R. Astron. Soc. Lett.* **382**, L39–L42.
- H. Qin, W. Tang, and G. Rewoldt (1999), “Symbolic vector analysis in plasma physics,” *Comp. Phys. Comm.* **116**, 107–120.
- E. Quataert, T. Heinemann, and A. Spitkovsky (2015), “Linear instabilities driven by differential rotation in very weakly magnetized plasmas,” *Mon. Not. R. Astron. Soc.* **447**, 3328–3341.
- K. H. Rädler, N. Kleeorin, and I. Rogachevskii (2003), “The mean electromotive force for MHD turbulence: The case of a weak mean magnetic field and slow rotation,” *Geophys. Astrophys. Fluid Dyn.* **97**, 249–268.
- K.-H. Rädler, and R. Stepanov (2006), “Mean electromotive force due to turbulence of a conducting fluid in the presence of mean flow,” *Phys. Rev. E* **73**, 056311 (15 pages).
- S. C. Reddy, P. J. Schmid, and D. S. Henningson (1993), “Pseudospectra of the Orr-Sommerfeld operator,” *Siam J. Appl. Math.* **53**, 15–47.

- O. Regev, and O. M. Umurhan (2008), “On the viability of the shearing box approximation for numerical studies of MHD turbulence in accretion disks,” *Astron. Astrophys.* **481**, 21–32.
- R. A. Remillard, and J. E. McClintock (2006), “X-ray properties of black-hole binaries,” *Annu. Rev. Astron. Astrophys.* **44**, 49–92.
- E. L. Rempel, G. Lesur, and M. R. E. Proctor (2010), “Supertransient magnetohydrodynamic turbulence in Keplerian shear flows,” *Phys. Rev. Lett.* **105**, 044501 (4 pages).
- M. Rheinhardt, and A. Brandenburg (2010), “Test-field method for mean-field coefficients with MHD background,” *Astron. Astrophys.* **520**, 28–45.
- K. J. Richardson, and M. R. E. Proctor (2012), “Fluctuating $\alpha\omega$ dynamos by iterated matrices,” *Mon. Not. R. Astron. Soc. Lett.* **422**, L53–L56.
- F. Rincon, G. I. Ogilvie, and M. R. E. Proctor (2007), “Self-sustaining nonlinear dynamo process in Keplerian shear flows,” *Phys. Rev. Lett.* **98**, 254502 (4 pages).
- F. Rincon, G. I. Ogilvie, M. R. E. Proctor, and C. Cossu (2008), “Subcritical dynamos in shear flows,” *Astron. Nachr.* **329**, 750–761.
- A. Riols, F. Rincon, C. Cossu, G. Lesur, P. Y. Longaretti, G. I. Ogilvie, and J. Herault (2013), “Global bifurcations to subcritical magnetorotational dynamo action in Keplerian shear flow,” *J. Fluid Mech.* **731**, 1–45.
- A. Riols, F. Rincon, C. Cossu, G. Lesur, G. I. Ogilvie, and P. Y. Longaretti (2015), “Dissipative effects on the sustainment of a magnetorotational dynamo in Keplerian shear flow,” *Astron. Astrophys.* **575**, 14–20.
- I. Rogachevskii, and N. Kleeorin (2003), “Electromotive force and large-scale magnetic dynamo in a turbulent flow with a mean shear,” *Phys. Rev. E* **68**, 036301 (12 pages).
- I. Rogachevskii, and N. Kleeorin (2004), “Nonlinear theory of a “shear-current” effect and mean-field magnetic dynamos,” *Phys. Rev. E* **70**, 046310 (15 pages).
- I. Rogachevskii, N. Kleeorin, and E. Liverts (2006), “Nonlinear shear-current dynamo and magnetic helicity transport in sheared turbulence,” *Geophys. Astrophys. Fluid Dyn.* **100**, 537–557.
- M. S. Rosin, and A. J. Mestel (2012), “Quasi-global galactic magnetorotational instability with Braginskii viscosity,” *Mon. Not. R. Astron. Soc.* **425**, 74–86.
- M. Rozyczka, N. Joung Turner, and P. Bodenheimer (1995), “A simple model for a buoyancy-driven dynamo in accretion discs,” *Mon. Not. R. Astron. Soc.* **276**, 1179–1184.
- G. Rüdiger (1990), “The alpha-effect in galaxies is highly anisotropic,” *Geophys. Astrophys. Fluid Dyn.* **50**, 53–66.

- G. Rüdiger, R. Hollerbach, and L. L. Kitchatinov (2013), *Magnetic Processes in Astrophysics, Theory, Simulations, Experiments* (John Wiley & Sons).
- G. Rüdiger, and L. L. Kitchatinov (1993), “Alpha-effect and alpha-quenching,” *Astron. Astrophys.* **269**, 581–588.
- G. Rüdiger, and L. L. Kitchatinov (2006), “Do mean-field dynamos in nonrotating turbulent shear-flows exist?” *Astron. Nachr.* **327**, 298–303.
- G. Rüdiger, and V. V. Pipin (2000), “Viscosity-alpha and dynamo-alpha for magnetically driven compressible turbulence in Kepler disks,” *Astron. Astrophys.* **362**, 756–761.
- R. Z. Sagdeev, and A. Galeev (1969), *Nonlinear Plasma Theory* (W. A. Benjamin).
- A. Salhi, T. Lehner, F. Godeferd, and C. Cambon (2012), “Magnetized stratified rotating shear waves,” *Phys. Rev. E* **85**, 026301 (18 pages).
- A. A. Schekochihin, A. B. Iskakov, S. C. Cowley, J. C. McWilliams, M. R. E. Proctor, and T. A. Yousef (2007), “Fluctuation dynamo and turbulent induction at low magnetic Prandtl numbers,” *New J. Phys.* **9**, 300–324.
- P. J. Schmid (2007), “Nonmodal stability theory,” *Ann. Rev. Fluid Mech.* **39**, 129–162.
- J. Schumacher (2004), “Relation between shear parameter and Reynolds number in statistically stationary turbulent shear flows,” *Phys. Fluids* **16**, 3094–3104.
- M. Seilmayer, V. Galindo, G. Gerbeth, T. Gundrum, F. Stefani, M. Gellert, G. Rüdiger, M. Schultz, and R. Hollerbach (2014), “Experimental evidence for nonaxisymmetric magnetorotational instability in a rotating liquid metal exposed to an azimuthal magnetic field,” *Phys. Rev. Lett.* **113**, 024505 (4 pages).
- N. I. Shakura, and R. A. Sunyaev (1973), “Black holes in binary systems. Observational appearance,” *Astron. Astrophys.* **24**, 337–355.
- Y. Shen, J. M. Stone, and T. A. Gardiner (2006), “Three-dimensional compressible hydrodynamic simulations of vortices in disks,” *Astrophys. J.* **653**, 513–524.
- J. Shi, J. H. Krolik, and S. Hirose (2010), “What is the numerically converged amplitude of magnetohydrodynamics turbulence in stratified shearing boxes?” *Astrophys. J.* **708**, 1716–1727.
- N. A. Silant’ev (2000), “Magnetic dynamo due to turbulent helicity fluctuations,” *Astron. Astrophys.* **364**, 339–347.
- J. B. Simon, K. Beckwith, and P. J. Armitage (2012), “Emergent mesoscale phenomena in magnetized accretion disc turbulence,” *Mon. Not. R. Astron. Soc.* **422**, 2685–2700.
- J. B. Simon, J. F. Hawley, and K. Beckwith (2011), “Resistivity-driven state changes in vertically stratified accretion disks,” *Astrophys. J.* **730**, 94–113.

- N. K. Singh, and N. Jingade (2015), “Numerical studies of dynamo action in a turbulent shear flow. I.” *Astrophys. J.* **806** (1), 118.
- N. K. Singh, and S. Sridhar (2011), “Transport coefficients for the shear dynamo problem at small Reynolds numbers,” *Phys. Rev. E* **83**, 056309 (10 pages).
- D. R. Sisan, N. Mujica, W. A. Tillotson, Y.-M. Huang, W. Dorland, A. B. Hassam, T. M. Antonsen, and D. P. Lathrop (2004), “Experimental observation and characterization of the magnetorotational instability,” *Phys. Rev. Lett.* **93**, 114502 (4 pages).
- K. A. Sorathia, C. S. Reynolds, J. M. Stone, and K. Beckwith (2012), “Global simulations of accretion disks. I. Convergence and comparisons with local models,” *Astrophys. J.* **749**, 189–213.
- J. Squire, and A. Bhattacharjee (2014a), “Magnetorotational instability: Nonmodal growth and the relationship of global modes to the shearing box,” *Astrophys. J.* **797**, 67–82.
- J. Squire, and A. Bhattacharjee (2014b), “Nonmodal growth of the magnetorotational instability,” *Phys. Rev. Lett.* **113**, 025006 (5 pages).
- J. Squire, and A. Bhattacharjee (2015a), “Statistical simulation of the magnetorotational dynamo,” *Phys. Rev. Lett.* **114**, 085002 (4 pages).
- J. Squire, and A. Bhattacharjee (2015b), “Generation of large-scale magnetic fields by small-scale dynamo in shear flows,” ArXiv e-prints [arXiv:1506.04109](https://arxiv.org/abs/1506.04109) [astro-ph.SR] .
- J. Squire, and A. Bhattacharjee (2015c), “Coherent nonhelical shear dynamos driven by magnetic fluctuations at low Reynolds numbers,” ArXiv e-prints [arXiv:1507.03154](https://arxiv.org/abs/1507.03154) [astro-ph.HE] .
- J. Squire, and A. Bhattacharjee (2015d), “Electromotive force due to magnetohydrodynamic fluctuations in sheared rotating turbulence,” ArXiv e-prints [arXiv:1508.01566](https://arxiv.org/abs/1508.01566) [astro-ph.HE] .
- J. Squire, J. Burby, and H. Qin (2014), “*VEST*: Abstract vector calculus simplification in *Mathematica*,” *Comp. Phys. Comm.* **185**, 128–135.
- S. Sridhar, and N. K. Singh (2010), “The shear dynamo problem for small magnetic Reynolds numbers,” *J. Fluid Mech.* **664**, 265–285.
- S. Sridhar, and N. K. Singh (2014), “Large-scale dynamo action due to fluctuations in a linear shear flow,” *Mon. Not. R. Astron. Soc.* **445**, 3770–3787.
- S. Sridhar, and K. Subramanian (2009), “Shear dynamo problem: Quasilinear kinematic theory,” *Phys. Rev. E* **79**, 045305 (4 pages).
- K. Srinivasan, and W. R. Young (2012), “Zonostrophic instability,” *J. Atmos. Sci.* **69**, 1633–1656.

- F. Stefani, T. Gundrum, G. Gerbeth, G. Rüdiger, M. Schultz, J. Szklarski, and R. Hollerbach (2006), “Experimental evidence for magnetorotational instability in a Taylor-Couette flow under the influence of a helical magnetic field,” *Phys. Rev. Lett.* **97**, 184502 (4 pages).
- D. Stoutemyer (1979), “Symbolic computer vector analysis,” *Comput. Math. Appl.* **5**, 1–9.
- K. Subramanian, and A. Brandenburg (2004), “Nonlinear current helicity fluxes in turbulent dynamos and alpha quenching,” *Phys. Rev. Lett.* **93**, 205001 (4 pages).
- K. Subramanian, and A. Brandenburg (2006), “Magnetic helicity density and its flux in weakly inhomogeneous turbulence,” *Astrophys. J. Lett.* **648**, L71–L74.
- C. Terquem, and J. C. B. Papaloizou (1996), “On the stability of an accretion disc containing a toroidal magnetic field,” *Mon. Not. R. Astron. Soc.* **279**, 767–784.
- A. G. Tevzadze, G. D. Chagelishvili, and J. P. Zahn (2008), “Hydrodynamic stability and mode coupling in Keplerian flows: local strato-rotational analysis,” *Astron. Astrophys.* **478**, 9–15.
- The HDF Group (2010), “Hierarchical data format version 5,” <http://www.hdfgroup.org/HDF5>.
- S. Tobias, and J. Marston (2013), “Direct statistical simulation of out-of-equilibrium jets,” *Phys. Rev. Lett.* **110**, 104502 (4 pages).
- S. M. Tobias, and F. Cattaneo (2014), “Shear-driven dynamo waves at high magnetic Reynolds number,” *Nature* **497**, 463–465.
- S. M. Tobias, K. Dagon, and J. B. Marston (2011), “Astrophysical fluid dynamics via direct statistical simulation,” *Astrophys. J.* **727**, 127–138.
- L. N. Trefethen, and M. Embree (2005), *Spectra and Pseudospectra*, The Behavior of Nonnormal Matrices and Operators (Princeton University Press).
- L. N. Trefethen, A. E. Trefethen, S. C. Reddy, and T. A. Driscoll (1993), “Hydrodynamic stability without eigenvalues,” *Science* **261**, 578–584.
- O. M. Umurhan, and O. Regev (2004), “Hydrodynamic stability of rotationally supported flows: Linear and nonlinear 2D shearing box results,” *Astron. Astrophys.* **427**, 855–872.
- V. Urpin (1999), “Mean electromotive force and dynamo action in a turbulent flow,” *Astron. Astrophys.* **347**, L47–L50.
- V. Urpin (2002), “Mean electromotive force in turbulent shear flow,” *Phys. Rev. E* **65**, 026301 (8 pages).
- S. I. Vainshtein, and L. L. Kichatinov (1983), “The macroscopic magnetohydrodynamics of inhomogeneously turbulent cosmic plasmas,” *Geophys. Astrophys. Fluid Dyn.* **24**, 273–298.

- E. P. Velikhov (1959), “Stability of an ideally conducting liquid flowing between rotating cylinders in a magnetic field,” *Zhur. Eksptl’i. Teoret. Fiz.* **36**, 995.
- E. T. Vishniac, and A. Brandenburg (1997), “An incoherent alpha-omega dynamo in accretion disks,” *Astrophys. J.* **475**, 263–274.
- E. T. Vishniac, and J. Cho (2001), “Magnetic helicity conservation and astrophysical dynamos,” *Astrophys. J.* **550**, 752–760.
- Y. Wang (2013), “MathGR: a tensor and GR computation package to keep it simple,” ArXiv e-prints [arXiv:1306.1295 \[cs.MS\]](https://arxiv.org/abs/1306.1295) .
- H. K. Wimmel (1982), “Extended standard vector analysis with applications to plasma physics,” *Eur. J. Phys.* **3**, 223–229.
- M. C. Wirth (1979), “Symbolic vector and dyadic analysis,” *Siam J. Comput.* **8**, 306–319.
- P. B. Yasskin, and A. Belmonte (2010), *CalcLabs with Maple commands for multivariable calculus, fourth edition* (Brooks/Cole, Cengage Learning, Belmont, CA).
- P. A. Yecko (2004), “Accretion disk instability revisited,” *Astron. Astrophys.* **425**, 385–393.
- N. Yokoi (2013), “Cross helicity and related dynamo,” *Geophys. Astrophys. Fluid Dyn.* **107**, 114–184.
- A. Yoshizawa, and N. Yokoi (1993), “Turbulent magnetohydrodynamic dynamo for accretion disks using the cross-helicity effect,” *Astrophys. J.* **407**, 540–548.
- T. A. Yousef, T. Heinemann, F. Rincon, A. A. Schekochihin, N. Kleeorin, I. Rogachevskii, S. C. Cowley, and J. C. McWilliams (2008a), “Numerical experiments on dynamo action in sheared and rotating turbulence,” *Astron. Nachr.* **329**, 737–749.
- T. A. Yousef, T. Heinemann, A. A. Schekochihin, N. Kleeorin, I. Rogachevskii, A. B. Iskakov, S. C. Cowley, and J. C. McWilliams (2008b), “Generation of magnetic field by combined action of turbulence and shear,” *Phys. Rev. Lett.* **100**, 184501 (4 pages).
- V. V. Zhuravlev, and D. N. Razdoburdin (2014), “A study of the transient dynamics of perturbations in Keplerian discs using a variational approach,” *Mon. Not. R. Astron. Soc.* **442**, 870–890.